DTIC

Stepped Tip Gap Effects on a Transonic
Axial-Flow Compressor Rotor

DISSERTATION

Donald W. Thompson B.S., M.S.
Major, USAF

AFIT/DS/ENY/97-5

DTIC QUALITY INSPECTED 2

DEPARTMENT OF THE AIR FORCE

AIR UNIVERSITY

AIR FORCE INSTITUTE OF TECHNOLOGY

Wright-Patterson Air Force Base, Ohio

19970805 025

AFIT/DS/ENY/97-5

**Stepped Tip Gap Effects on a Transonic
Axial-Flow Compressor Rotor**

DISSERTATION

**Donald W. Thompson B.S., M.S.
Major, USAF**

AFIT/DS/ENY/97-5

DTIC QUALITY INSPECTED 3

Disclaimer

The views expressed in this dissertation are those of the author and do not reflect the official policy or position of the United States Air Force, the Department of Defense, or the United States Government.

Stepped Tip Gap Effects on a Transonic Axial-Flow Compressor Rotor

DISSERTATION

Presented to the Faculty of the Graduate School of Engineering

of the Air Force Institute of Technology

Air Education and Training Command

In Partial Fulfillment for the Degree of

Doctor of Philosophy

Specialization in: Aeronautical and Astronautical Engineering

Donald W. Thompson B.S., M.S.

Major, USAF

Air Force Institute of Technology
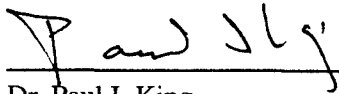
Wright-Patterson AFB, Ohio

June, 1997

Stepped Tip Gap Effects on a Transonic Axial-Flow Compressor Rotor

Donald W. Thompson B.S., M.S.

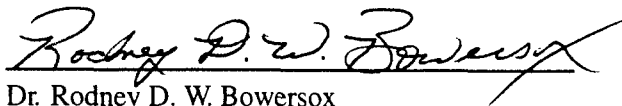### Major, USAF

Approved:

_____

Dr. Paul I. King
Committee Chairman
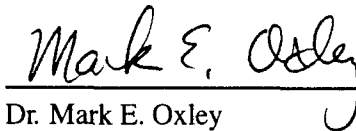
25 Jun 97
Date

_____

Dr. Rodney D. W. Bowersox
Committee Member

25 Jun 97
Date

_____

Dr. Mark E. Oxley
Committee Member

25 Jun 97
Date

_____

Dr. Won B. Roh
Dean's Representative

25 June 97
Date

Accepted:

_____

Dr. Robert A. Calico
Dean, School of Engineering

Dedication

I dedicate this work to my wife and best friend, Rachelle, whose love and support made this journey possible. With a warm heart and kind soul, she gave comfort and aid to our Air Force friends and families during the most tragic and desperate days of their lives. To me, she gave unending support and understanding during the deepest and darkest moments of this endeavor. She is a true blessing to the world, and I am fortunate to share my life and love with her.

This work is also dedicated to the memory of Colonel Robert Wolf, Lieutenant Colonel Mark McGeehan, Lieutenant Colonel Arthur "Bud" Holland, and Lieutenant Colonel Ken Houston whose lives were tragically cut short while serving their country. Together we strived in earnest to erase the bonds of tyranny from our world, and we placed our lives on the line in defense of these convictions and the precious freedom we enjoy. These men have joined the ranks of "Fame's Favored Few" from the once mighty 325th Bomb Squadron which gave us a heritage of vigilance and a legacy of peace. May the spirit of these airmen, warriors, patriots, and noble leaders kindle and forever reside in the hearts and minds of all officers, and may their inspiration wisely guide us in our national, military, and personal endeavors. Rest in peace, Gentlemen. Alley Oop!

Finally, I dedicate this work to the Holy Trinity: the grand engineer of the universe; my friend and teacher, Jesus Christ; and the guiding spirit that fills me with energy, dreams, and ideas. May this small work be used to help fix the problems in our world.

<div align="right">Don Thompson</div>

Acknowledgments

I first want to thank my research advisor, Dr. Paul I. King, for his direction and support during this endeavor. I would also like to thank the committee members, Dr. Bowersox and Dr. Oxley, for their time and effort during the course work, qualification examinations, and research phases of the program. Special thanks are due to Dr. Doug Rabe for sponsoring this research and participating in many discussions supporting this effort.

I would also like to thank Chuck Elrod and Norm Poti for providing the time, equipment, and personnel required to conduct the experimental portion of this research at the Wright Laboratories Compressor Research Facility. The complexity of the facility and its data acquisition process requires the expertise of many highly talented engineers and technicians. I am deeply grateful to each for the support provided. I would also like to thank the machinists at the AFIT Model Shop for their timely and precise support in manufacturing critical test equipment.

Finally, I would like to thank Dr. Chunill Hah of the NASA Lewis Research Center for the generation of the computational fluid dynamics results which were critical to the success of this effort.

Table Of Contents

List of Figures

List of Tables

Nomenclature

English Symbols

Symbol	Definition
A	Frontal Area of the Rotor Passage Inlet (m^2)
A_0	Magnitude of a Planar Surge Wave
A_{jm}	Magnitude of a Rotating Modal Wave
b_x	Bias Error of a Measured or Calculated Quantity
C	Absolute Air Velocity (m/sec)
C_a	Axial Flow Velocity (m/sec)
C_p	Specific Heat at Constant Pressure (J/kg-K)
C_v	Specific Heat at Constant Volume (J/kg-K)
C_θ	Absolute Tangential Air Velocity (m/sec)
c_1	Closure Coefficient
c_2	Closure Coefficient
c_3	Closure Coefficient
c_4	Closure Coefficient
c_μ	Closure Coefficient
df_x	Degrees of Freedom of a Measured or Calculated Quantity
e	Specific Internal Energy (J/kg)
e_t	Specific Total Internal Energy (J/kg)
F_i	Indicial Component of Body Force (N)
F_{SL}	Thrust at Sea Level (N)
f	Closure Coefficient

g	Gravitational Acceleration (m/sec^2)
g_c	Unit Correction Coefficient (ft-lbm/lbf-sec^2)
h	Static Enthalpy (J/kg)
h_0	Stagnation Enthalpy (J/kg)
K	Turbulent Kinetic Energy
k	Coefficient of Thermal Conductivity (J/m-sec-K)
k_T	Turbulent Coefficient of Thermal Conductivity (J/m-sec-K)
k_{eff}	Effective Coefficient of Thermal Conductivity (J/m-sec-K)
l	Mixing Length (m)
M	Mach Number
MFP	Mass Flow Parameter (m-K$^{\frac{1}{2}}$/N)
m	Mode of a Rotating Wave
$\dot{m}$	Mass Flow Rate (kg/sec)
$\dot{m}_c$	Corrected Mass Flow Rate (kg/sec)
N	Rotor Rotational Speed (revolutions / minute)
N_c	Corrected Rotor Rotational Speed (revolutions / minute)
N_T	Number of Circumferential Stall Sensors
n	Index Counter
P	Static Pressure (N/m^2)
P_0	Stagnation Pressure (N/m^2)
P_A	Added Static Pressure (N/m^2)
P_D	Differenced Static Pressure (N/m^2)
PR	Pressure Ratio
Pr	Prandtl Number ($\frac{C_p \mu}{k}$)

Pr_T	Turbulent Prandtl Number ($\frac{C_p \mu_T}{k_T}$)
R	Specific Gas Constant (J/kg-K)
r	Radial Location from Rotation Axis (m)
r_h	Rotor Hub Radius (m)
r_t	Rotor Tip Radius (m)
Re	Reynolds Number ($\frac{\rho u x}{\mu}$)
S	Wing Surface Area (m^2)
S_1	Sutherland's Constant
S_2	Sutherland's Constant
s_x	Precision Error of a Measured or Calculated Quantity
T	Static Temperature (K)
T_0	Stagnation Temperature (K)
t_{95}	Probability of Student-t distribution with 95% Confidence
U_m	Blade Velocity at Rotor Mean Radius (m/sec)
U_x	Uncertainty of a Measured or Calculated Quantity
u	Local Velocity (m/sec)
u_i	Indicial Velocity Component
u^*	Friction Velocity
V	Relative Air Velocity (m/sec)
W_{TO}	Aircraft Weight at Takeoff (N)
$\dot{W}$	Work Rate Done by a Compressor Rotor (J/sec)
ΔW	Specific Power Input to Rotor (J/kg)
x	Axial Location (m)
x_i	Indicial Coordinate

Greek Symbols

Symbol	Definition
α	Absolute Air Angle (degrees)
β	Relative Air Angle (degrees)
β_i	Initial Weight Fraction
δ	Referenced Pressure Ratio
δ_{ij}	Kronecker Delta
ε	Turbulent Energy Dissipation
ε_{ijk}	Permutation Symbol
γ	Ratio of Specific Heats ($\frac{C_p}{C_v}$)
η	Isentropic Efficiency
μ	Viscosity of Fluid (kg/m-sec)
μ_T	Turbulent Viscosity of Fluid (kg/m-sec)
μ_{eff}	Effective Viscosity of Fluid (kg/m-sec)
ν	Kinematic Viscosity of Fluid (m^2/sec)
π	Trigonometric Identity
ρ	Static Density of Air (kg/m^3)
σ_ε	Effective Prandtl Number for Turbulent Dissipation
σ_k	Effective Prandtl Number for Turbulent Kinetic Energy
θ	Referenced Temperature Ratio
τ_{ij}	Viscous Stress Tensor
Ω_j	Angular Rotation Vector (radians/sec)
ω	Rotor Rotational Speed (radians/sec)

ω_x	Error of a Measured or Calculated Quantity
$\frac{\partial}{\partial x}$	Partial Derivative

Subscripts

Symbol	Definition
1	Rotor Inlet (Leading Edge)
2	Rotor Exit (Trailing Edge)
s	Constant Entropy Value
SL	Standard Sea Level Value

Decorations

Symbol	Definition
$\overline{()()()}$	Reynolds Time-Averaged Quantity
$\overline{()}$	Reynolds Mean Quantity
$()'$	Reynolds Fluctuating Quantity
$\widetilde{()}$	Reynolds Mass-Weighted Mean Quantity
$()''$	Reynolds Mass-Weighted Fluctuating Quantity

Abbreviations

Abbreviation	Definition
ADI	Alternating Direction Implicit
ADLARF	Advanced Damping Low Aspect Ratio Fan
AFIT	Air Force Institute of Technology
AMRAAM	Advanced Medium Range Air-to-Air Missile

ASCII	American Standard Code for Information Interchange
BCM	Best Cruise Mach Number
CAP	Combat Air Patrol
CARL	Compressor Aerodynamics Research Laboratory
CFD	Computational Fluid Dynamics
CRF	Compressor Research Facility
DFT	Discrete Fourier Transform
FANS	Favre-Averaged Navier-Stokes Equations
FAST	Flow Analysis Software Toolkit
FDE	Finite Difference Equation
Hz	Hertz (cycles per second)
IHPTET	Integrated High Performance Turbine Engine Technology
J	Joule (N-m)
K	Degrees Kelvin
kg	Kilogram
kPa	KiloPascals
LE	Leading Edge
lbf	Pound of Force
lbm	Pound of Mass
MISS	Mission Analysis Software Package
m	Meters
mm	Millimeters (10^{-3}m)
μm	Micrometers (10^{-6}m)
nm	Nanometers (10^{-9}m)

N	Newton (kg-m/sec^2)
NASA	National Aeronautics and Space Administration
NS	Near-Stall
ONX	On-Design Jet Engine Software Package
Pa	Pascal (N/m^2)
PDE	Partial Differential Equation
PE	Peak Efficiency
PS	Pressure Surface
RANS	Reynolds-Averaged Navier-Stokes Equations
revs	Revolutions
RMS	Root-Mean-Square
RPM	Revolutions per Minute
sec	Second
SFT	Spatial Fourier Transform
SS	Suction Surface
STP	Sea-Level Standard Temperature and Pressure
TE	Trailing Edge
TKE	Turbulent Kinetic Energy

AFIT/DS/ENY/97-5

Abstract

The effects of stepped tip gaps and clearance levels on the performance, flowfield, and stall characteristics of a transonic axial-flow compressor rotor were experimentally and numerically determined. A theory and mechanism for relocation of blockage in the rotor tip region was developed. A two-stage compressor with no inlet guide vanes was tested in the Wright Laboratories Compressor Research Facility located at Wright-Patterson Air Force Base, Ohio. The first-stage rotor was unswept and was tested for an optimum tip clearance with variations in stepped gaps machined into the casing near the aft tip region of the rotor. Nine casing geometries were investigated consisting of three step profiles at each of three clearance levels. For small and intermediate clearances, stepped tip gaps were found to improve pressure ratio, efficiency, and flow range for most operating conditions. At 100% design rotor speed, stepped tip gaps produced a doubling of mass flow range with as much as a 2.0% increase in mass flow and a 1.5% improvement in efficiency. The flowfield characteristics associated with performance improvements were experimentally and numerically analyzed. Stepped tip gaps were found to have no significant effect on the stall characteristics of the rotor; the stability characteristics attributable to tip geometry were determined by the clearance over the forward portion of the rotor blade. This study provides guidelines for engineers to improve compressor performance for an existing design by applying an optimum casing profile.

Stepped Tip Gap Effects on a Transonic Axial-Flow Compressor Rotor

Chapter 1 - Introduction

Propulsion systems for aircraft have evolved for decades. Using propellers driven by internal combustion engines, the Wright Flyer changed the world with the first successful demonstration of controlled, powered flight. As aeronautical science matured, the power and efficiency of propeller systems rapidly improved, and aircraft flew higher, faster, and farther. However, pilots and engineers soon found propeller-driven aircraft to have practical aerodynamic limits that prevented their use in higher and faster flight regimes. A larger flight envelope would require development of a substantially new and different propulsion system — this regime would belong to the turbojet engine.

Whittle's revolutionary invention of the turbojet engine (Scott [80] ; Hawthorne [41]) in the 1930s introduced the basic technology that would prove to be the mainstay of modern aviation. The concept of the jet engine was theorized long before Whittle, but he was the first to envision and apply the compressor-turbine pair to produce a viable jet propulsion system. Despite initially adverse publicity, the turbojet engine eventually gained widespread acceptance for military and commercial aviation. Variations of the basic concept produced the turbofan and turboprop engines which allowed the compressor-turbine propulsion system also to compete in the lower and slower flight regimes traditionally reserved for internal combustion-driven propeller systems. Improvements in thrust and efficiency allowed the turbojet engine to become the dominant propulsion system for the jet age.

The evolutionary process of the jet engine continues today. The turbojet engine can now propel aircraft to altitudes and airspeeds for which the compressor-turbine pair is no longer necessary for sustained airbreathing propulsion; such is the concept and regime of ramjet and scramjet en-

gines (Heiser and Pratt [42]). In another application, ultrahigh bypass turbofan engines are being studied for use on many commercial aircraft (Brines [14]). Additionally, thrust vectoring of turbojet exhaust promises substantial performance improvement for fighter aircraft (Ashley [10]). All of these research programs share the gas turbine-driven jet engine as the focal point.

Evolutionary improvement of basic turbojet technology will benefit the propulsion systems for essentially every region of the atmospheric flight envelope, and any improvement will be compounded by the quantities of jet engines employed. Although jet engine hardware has existed for years, a complete understanding of the physical processes occurring internally is lacking. Since continued evolution requires thorough understanding of the processes involved, jet engine components and the physics of their operation are the focus of ongoing research.

1.1 Program for Improvement — IHPTET

A current initiative guiding the research of jet engine components is the Integrated High Performance Turbine Engine Technology (IHPTET) program (Grier [34] ; Valenti [87]). This joint venture between U.S. government and industry began in 1988, and it calls for doubling the thrust-to-weight ratio of 1987 turbine engine technology by the year 2003. The IHPTET program aims for similar results in three classes of engines (Valenti [87]): 1) turbojet and turbofans used in most military and large transport aircraft, 2) turboshafts and turboprops used in helicopters and small transport aircraft, and 3) expendable engines used in missiles and drones. Fortunately, due to similar technology between classes, efforts aimed at one class of engine are often applicable to the others.

The IHPTET program is to accomplish its mission in three phases, with each phase contributing approximately one-third of the proposed overall improvement. The first phase, completed in 1991, resulted in the F119 engine which is the powerplant for the U.S. Air Force's next generation F-22

2

fighter. The second phase is scheduled to be completed by 1997, and the final phase will close the program in 2003. The program may produce radically different and innovative engine technology.

A logical approach for doubling the thrust-to-weight ratio of an engine is to reduce its weight by half while maintaining the same amount of thrust. Since the compressor comprises most of the mass of an engine, steps at reducing the number of stages and the number of blades per stage are obvious objectives. However, the compressor must still deliver the same mass flow with the same pressure rise as its larger counterpart; its work requirements are unchanged. Therefore, the smaller compressor becomes highly loaded, with associated physical limitations and flow phenomena. A look at compressor theory will help explain these effects and some of the relevant problems facing the IHPTET program.

1.2 Elementary Theory of Compressor Work

From an application of the first law of classical thermodynamics (i.e., conservation of energy) for an open system, the work rate done by a compressor rotor on a thermally and calorically perfect gas is expressed as

$$\dot{W} = \dot{m}(h_{02} - h_{01}) = \dot{m}C_p(T_{02} - T_{01}) \tag{1}$$

where $\dot{m}$ is the mass flow rate, h_{01} and h_{02} are the stagnation enthalpies at the rotor inlet and exit, respectively, C_p is the specific heat at constant pressure, and T_{01} and T_{02} are the stagnation temperatures at the rotor inlet and exit, respectively.

From the conservation of angular momentum for simplified two-dimensional mean-radius uniform flow, the Euler pump equation (Cohen et al. [17]) relates work rate to the key factors of the compression process

$$\dot{W} = \dot{m}(U_{m2}C_{\theta 2} - U_{m1}C_{\theta 1}) \tag{2}$$

3

where U_{m1} and U_{m2} are the blade velocities at the rotor mean radius for the rotor inlet and exit, respectively, and $C_{\theta 1}$ and $C_{\theta 2}$ are the absolute tangential air velocities at the rotor inlet and exit, respectively. After dividing Equation 2 through by mass flow and using known relations for geometry (see Figure 1), the specific power input for a rotor with constant axial velocity, $C_{a1} = C_{a2} = C_a$, and negligible change in mean radius is

$$\Delta W = \frac{\dot{W}}{\dot{m}} = U_m C_a (\tan \beta_1 - \tan \beta_2) \tag{3}$$

where β_1 and β_2 are the relative air angles at the rotor inlet and exit, respectively.
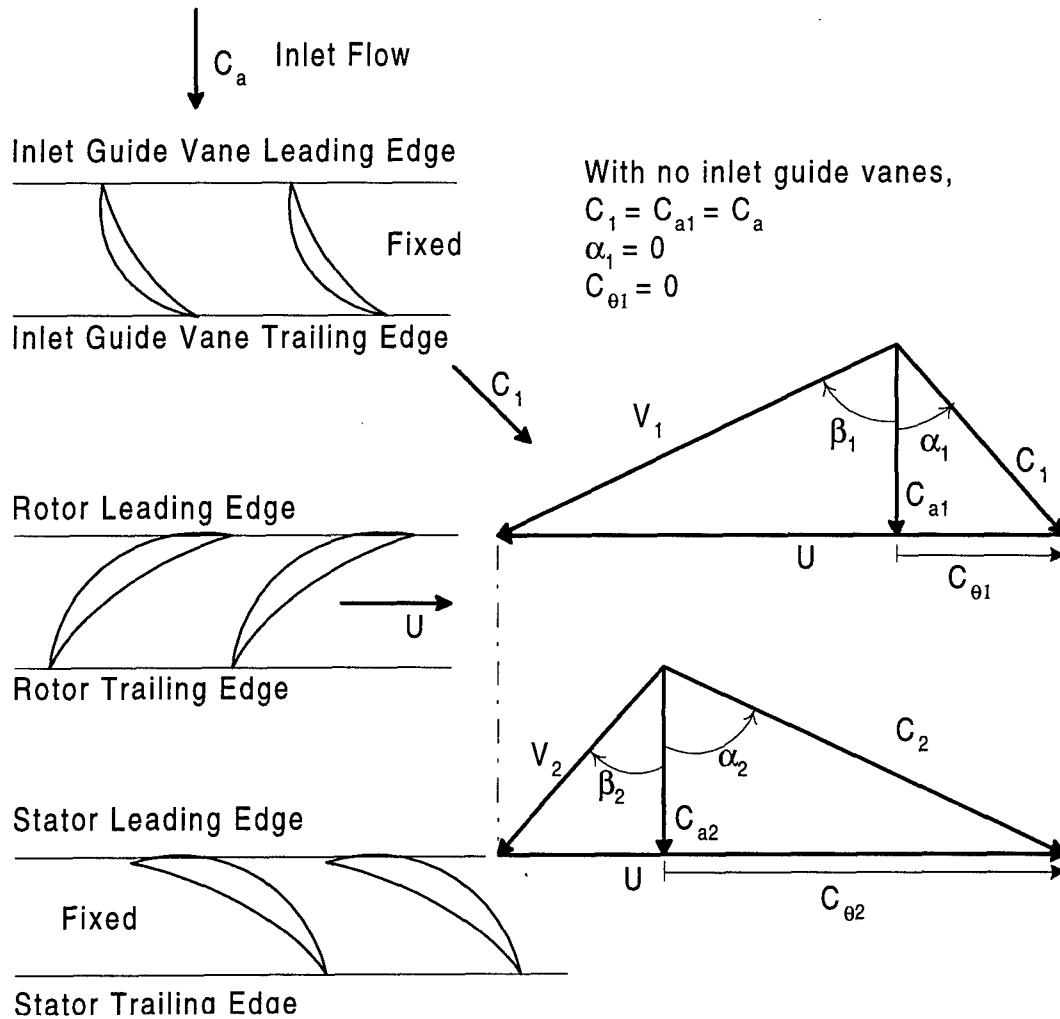
Figure 1. Velocity Diagram for Single Stage Compressor

4

According to Equation 3, to maximize compressor work capacity, the rotor should operate at high rotational speed, large axial flow velocity, and the greatest permissible flow turning angle. Recognizing these basic factors and exploiting them, engineers made giant leaps in turbojet engine capabilities. For example, *Aviation Week and Space Technology* (Aboulafia [4]) reports the following progression of thrust-to-weight ratios. In the early 1950s, turbojet thrust-to-weight ratios of 3.5 were common. By the 1960s, the typical F-4 fighter had turbojet engines with thrust-to-weight ratios of 4.5; similarly, the engines used in larger aircraft such as the B-52H had thrust-to-weight ratios of 4.4. However, by 1987 the engines powering the U.S. front-line fighters had achieved thrust-to-weight ratios of 7.0 or greater. Doubling this capacity by the year 2003 is an ambitious task as compressors have evolved into machines where compressibility effects, flow choking, and blade stall are severely limiting factors.

1.3 Limiting Factors — Transonic Flow and Stall

The flow velocity relative to the blade, V_1 and V_2 in Figure 1, depends on the axial flow velocity and the rotor speed. The axial flow velocity, C_a, is a function of the mass flow, $\dot{m}$, static density, ρ, and frontal area, A, at the rotor inlet.

$$\dot{m} = \rho C_a A \tag{4}$$

To achieve a large axial velocity, large mass flow per unit frontal area is desired. The frontal area of a compressor is a function of the rotor tip, r_t, and hub, r_h, radii.

$$A = \pi(r_t^2 - r_h^2) \tag{5}$$

With a constant rotor hub radius, a reduced frontal area requires a reduced rotor tip radius which aids in reducing the weight of the compressor. These features create a condition of high throughflow; however, a reduced radius also results in a slower mean blade speed which must be countered with increased rotational speed.

As rotor rotational speed and throughflow are increased, the threshold of sonic relative flow is often exceeded. For this condition, the airflow relative to the rotor travels faster than the localized speed of sound at various locations along the rotor blade. The flow will tend to be supersonic at the blade tips, subsonic near the hub, with an inherent transonic flow regime bridging the extremes. Rotors designed to operate at these flow conditions are termed transonic.

Compressibility effects are significant for transonic compressors. Flow disturbances cause oblique and normal shock waves to form near the tips and leading edges of rotor blades and within blade passages. These discontinuities, when interacting with other flow features near the engine casing, produce blockage which inhibits mass flow through the compressor and effects losses in the flow passage. These interactions are very complex and not completely understood, and they will be addressed in detail in Chapter 2.

Due to the losses associated with the complex interactions of transonic and supersonic flow, it is desirable to delay the onset of these flows as much as possible. As done with aircraft wings, rotor blades can be swept to lessen the effects of transonic flow in compressors. The Air Force and Navy are currently pursuing swept compressor blades to reduce shock losses in their next generation engines (Valenti [87]). However, to obtain more work from the rotor with less hardware, a practical limit is reached where the flow is sonic regardless of sweep. Therefore, it is important to recognize that increased rotor speed and axial velocity often result in transonic flow which creates additional problems that must be dealt with during design.

Transonic compressor designs must also consider performance during inevitable off-design operation since these conditions can adversely affect the loading of rotor blades. Increasing the rotation rate without an increase in mass flow has the inherent effect of increasing the flow incidence angle of the rotor as seen in Figure 2. Since the trailing edge relative air angle varies little with change in incidence (Cohen et al. [17] ; Hill and Peterson [43]), increased rotor speed results in a

6
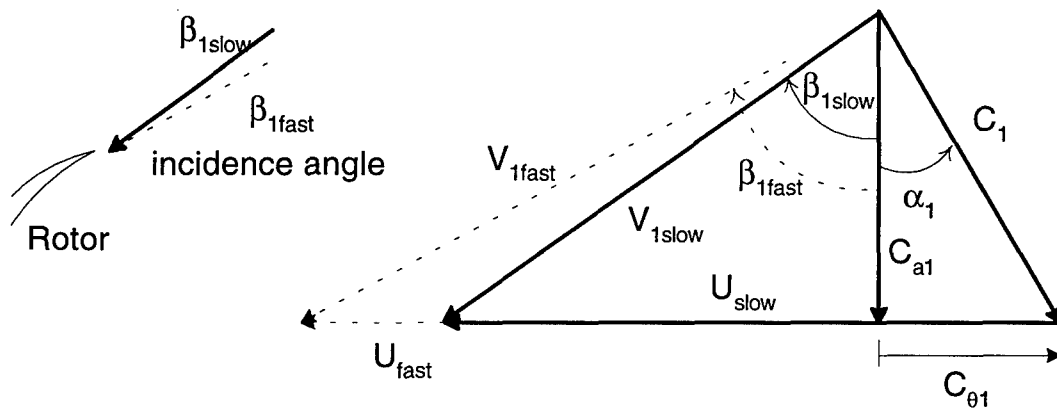
Figure 2. Effect of Rotor Speed on Incidence Angle

larger flow turning angle. Generally, this increase is acceptable provided the flow has not already been excessively turned.

Turning angle is directly associated with stall as a limiting factor for compressor performance and work capacity. As the turning angle (i.e., loading) is increased, an adverse pressure gradient is created on the suction surface of the blade. This adverse pressure gradient causes flow separation of the attached boundary layer (Hill and Peterson [43]). Separation begins at the blade trailing edge and progresses to the leading edge with increased angle-of-attack. When too much flow turning is attempted, a critical turning angle is achieved wherein the flow separates at the leading edge of the blade and full stall occurs. Transonic rotor blades also are susceptible to shock-induced boundary layer separation; the adverse pressure gradient across a shock wave that is normal to the suction surface of a blade induces flow separation and stall. For any case, the loading of the blade is limited by stall.

1.4 Operating Range and Performance

Stall and other performance measures are explained in a macroscopic sense with a compressor map. A typical map for a single-stage transonic compressor is shown in Figure 3.

7
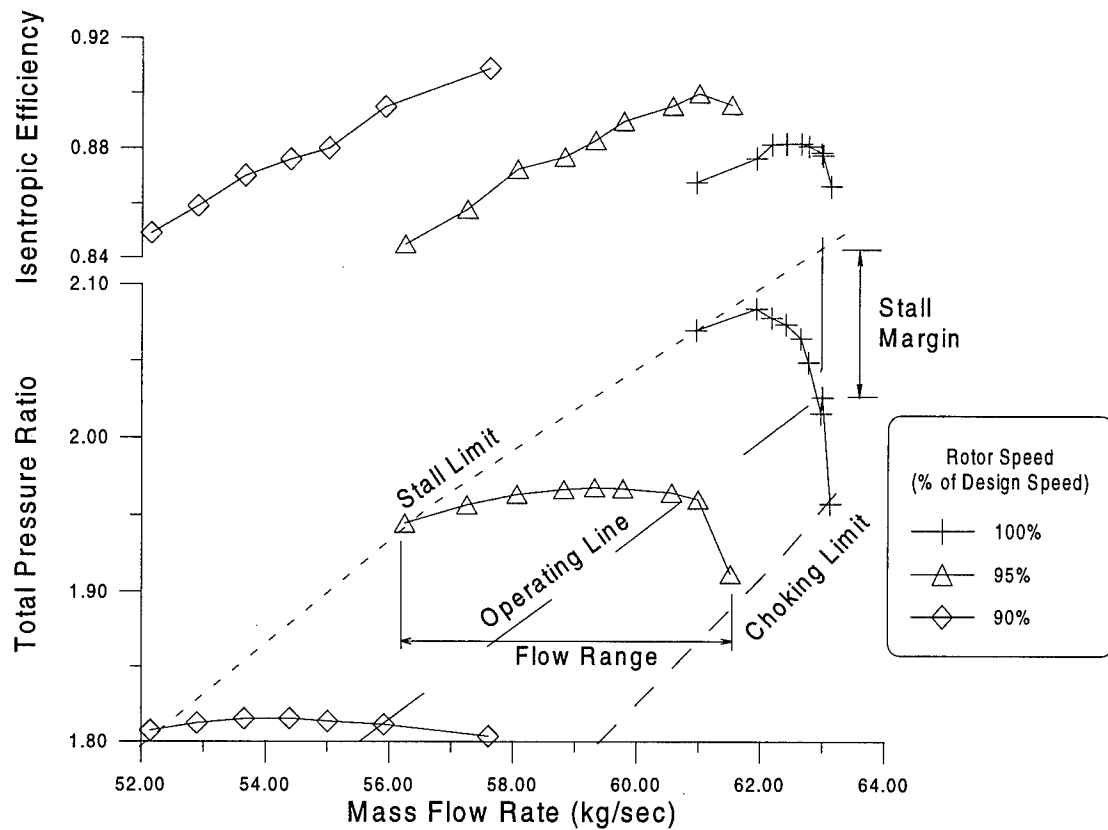
Figure 3. Transonic Compressor Map [Adapted from Wennerstrom et al. [95]]

Note that as mass flow is decreased along any constant rotor speed line, a stall limit is approached. Likewise, if the mass flow is increased with rotor speed held constant, the choking limit is approached. The difference between these two mass flow extremes is designated the flow range of operation for a given speed. Similarly, the stall limit is approached for an increase in rotor speed with mass flow held constant. The difference between the stalling and design pressure ratios as a fraction of the design pressure ratio at a constant mass flow is traditionally defined as the stall margin. This margin permits excursions beyond design rotor speed (hence loading and pressure ratio) at a constant mass flow.

8

Additional trends of a transonic compressor can be identified with a compressor map. If both mass flow and rotor speed are increased, the total pressure ratio of the compressor increases as previously discussed. Unfortunately, the flow range decreases with increasing rotor speed. For the extreme case of fast rotor speed with large mass flow, the compressor operates in a small flow range between stall and choking. Such is the case for many modern transonic compressors. Notice also that peak efficiency tends to decrease with increased rotor speed. This decrease is primarily due to blockage and losses associated with the complex transonic flow interactions in the tip region mentioned earlier.

The operating regime for transonic compressors appears to be at odds with efficiency and tolerance for off-design conditions. Ultimately, a design is sought that combines the desirable characteristics of large work capacity (i.e., large $\dot{m}/A$, rotor speed, and pressure ratio) with ample flow range and stall margin while operating at peak efficiency. A design having these attributes is elusive. Solving this problem is the subject of current research.

1.5 Current Research Focus — Definition of Problem

Rotors have progressed into realms where transonic flow, shock waves, choking, and stall are of serious concern. These factors must be understood and surmounted if doubling compressor capacity is to be achieved. Many ingenious ideas have been tried to squeeze extra thrust from turbomachinery; Wennerstrom [94] gives an excellent summary of these efforts. Additionally, a large volume of information is available from testing of low-speed compressors and two-dimensional cascades; the details of those studies are beyond the scope of this dissertation. However, Day and Freeman [27] state that low-speed testing is an effective means of obtaining insight into the behavior of high-speed machines, so relevant studies in low-speed compressors will be included where additional insight is necessary.

9

From the numerous past and current research efforts, one thing is clearly evident — one of the main factors influencing compressor capabilities is the clearance between the rotor tip and the engine casing. The flowfield in the vicinity of the rotor tip is known to be a source of flow disturbance that strongly affects the physics and losses in compressors (Cumpsty [22] ; Freeman [32] ; Lakshminarayana [55] ; Lakshminarayana et al. [58] ; Moyle [67] ; Peacock[69]). Tip clearance flow interactions effect regions of blockage which alter the throughflow and hence the choking, stall, and overall performance characteristics of the compressor. When a compressor is transonic, these effects are magnified and can be a large source of pressure loss and performance degradation. Understanding tip clearance effects is key to the IHPTET program.

1.5.1 Thesis Statement

This dissertation focuses on tip gap effects in transonic axial-flow compressors to support the primary goal of relocating the inherent tip region blockage to benefit compressor performance. In particular, it addresses the effect of tip clearance size and geometry on blockage, stall, efficiency, pressure rise, and flow range of a modern prototype compressor, the Advanced Damping Low Aspect Ratio Fan (ADLARF). The problem is addressed from a system performance perspective in addition to the detailed study of the tip region flowfield associated with stall, peak efficiency, and choking. Stepped tip gap configurations are evaluated to determine their effectiveness in altering the blockage for improved compressor performance.

The background necessary to understand the aerodynamics of the tip region is presented in Chapter 2; the theory associated with blockage relocation is developed in Chapter 3. The experimental and computational details associated with this research are presented in Chapter 4 and Chapter 5, respectively. The results of this research regarding the effects of tip geometry on rotor performance, flowfield and stall characteristics are detailed, respectively, in Chapters 6, 7, and 8. In

10

Chapter 9, conclusions are drawn regarding the effects of tip geometry on transonic rotor operation, and recommendations are given for future research and compressor designs.

1.5.2 Research Objectives

As a result of the discussion in the previous sections, the objectives of this research were to:

1. Expand the experimental data available in the open literature for transonic axial-flow compressor rotors.

2. Determine the effects of tip clearance on performance, flowfield, and rotor stall characteristics; evaluate the possible existence of an optimum tip gap.

3. Determine the effects of stepped tip gaps on performance, flowfield, and rotor stall characteristics.

4. Identify key geometric bounds and candidates deserving additional study and optimization for future numerical and analytical models.

5. Provide guidance to compressor designers that will aid the IHPTET program goal of doubling thrust-to-weight ratio of turbojet engines.

1.6 Summary

In this chapter, the factors influencing the evolution of turbojet engines and compressors were introduced, and compressor performance was explained with elementary theory. Finally, the problem of this dissertation was stated, and the research objectives were defined. In the following chapter, the background of research leading to this dissertation is discussed.

Chapter 2 - Background

2.1 Overview of Tip Gap Aerodynamics

The flowfield in the tip region of axial-flow compressors has been studied for decades. The flow is a three-dimensional phenomenon comprised of the complex interactions between the tip leakage vortex, the turbulent endwall and blade boundary layers, and often times shock waves distorted by radial and rotational effects. Suder and Celestina [86] , Puterbaugh [71] , Puterbaugh and Brendel [72] , Cybyk et al. [24] , and Sellin et al. [81] provide detailed characterization of these flow structures and their interactions.

The rotor tip clearance is a major factor controlling the level of interaction of the various flow phenomena in the tip region, but loss effects also extend beyond that region. Large pockets of low-energy fluid are created by the interacting flows, and these pockets alter the flow throughout the rotor cavity. Altered flow often creates greater adverse pressure gradients on the suction surfaces of rotor blades which lead to flow separation and stall.

Flow separation and overall performance are interrelated. Blade loading and mass flow range are limited by stall, an advanced case of flow separation; efficiency is also degraded by partial flow separation. If separation can be mitigated or controlled, compressor performance and work capacity will improve. Therefore, tip gap effects on blockage, flow separation, and performance merit detailed examination. A look at the flowfield in the tip region will illuminate the key factors and processes of tip gap aerodynamics.

2.2 Tip Region Flowfield and Interactions

Several flow phenomena exist in the tip region of a compressor rotor. Boundary layers exist on the blades and on the engine casing. These flow regions interact with the tip leakage vortex generated when air escapes from the pressure side to the suction side of a blade through the tip

12

gap. Many times, these flows are further complicated by interacting with oblique and normal shock waves protruding into the passage.

2.2.1 Boundary Layers

The characteristics of endwall and blade boundary layers is well documented (Abdalla and Soundranayagam [2] ; Bettner and Elrod [12] ; Lakshminarayana and Popovski [56] ; Smith [82] ; Wagner et al. [90] ; Wagner et al. [91] ; Zhang and Lakshminarayana [103]). These areas of high viscosity and low kinetic energy fluid are present immediately adjacent to the flow surfaces. Outside of these layers, the flow is essentially inviscid. The thickness of these layers increases with axial coordinate to produce a ducting of flow away from the engine casing and an inherent low-velocity wake aft of the rotor blade trailing edge. The endwall boundary layer of the tip region can extend from 5 to 35 percent of span for a first-stage rotor (Wagner et al. [91]). Likewise, blade boundary layers can extend pitchwise up to ten percent of chord length (Lakshminarayana and Popovski [56]).

Boundary layers play a relatively larger role in slow-speed machines than in transonic compressors due to Reynold's number effect. Reynolds number, Re, is defined by Incropera and De-Witt [46] as the ratio of inertial forces to viscous forces.

$$\mathrm{Re} \equiv \frac{\rho u x}{\mu} \tag{6}$$

where ρ, u, and μ are the static density, local velocity, and viscosity of the fluid, respectively, at an axial location, x. As velocity increases, Reynolds number increases and inertial forces become dominant over viscous forces. Boundary layers are the result of viscous fluid shear adjacent to a surface having a no-slip boundary condition. In high-speed compressors, inertial forces are dominant over viscous forces, so boundary layers have less influence than they do in slow-speed flows. Boundary layers are still present in high-speed flows, but they are generally turbulent with inher-

ently increased momentum transport and vortical action. In high-speed compressors, leakage vortices and shocks are the dominant influences in the tip region.

2.2.2 Tip leakage Vortex

The existence of tip leakage vortices and their influence is also well-documented (Lakshminarayana [54] ; Lakshminarayana [55] ; Lakshminarayana et al. [57] ; Inoue and Kuroumaru [47] ; Inoue and Kuroumaru [49] ; Kang and Hirsch [51] ; Moyle [67] ; Stauter [83] ; Storer and Cumpsty [84]). Tip leakage vortices are large contributors to low-energy fluid in the tip region. A leakage vortex is produced when a jet of high-velocity air leaks through the tip gap from the high-pressure to the low-pressure side of the blade. After transiting the gap, the fluid rolls up into a vortex with a low axial velocity core. This core penetrates deeply into the rotor passage and is a considerable source of flow blockage.

2.2.3 Shock Waves

Compressibility effects in the form of shock waves become extremely influential for transonic compressors. Oblique shock waves tend to form near the blade leading edge, and shock waves normal to the flow typically span the tip gap. As expected from compressible flow theory (Anderson [7]), fluid decelerates across a shock wave creating a zone with lower kinetic energy. This process adds to the flow blockage in the tip region.

Efforts by Epstein et al. [31] and Wennerstrom and Puterbaugh [96] to characterize the three-dimensional shock patterns and associated losses in transonic rotors had limited success. Epstein found through modeling and experimentation that the three-dimensional nature of shocks produce large radial pressure gradients and strong radial flows downstream of the shock termination; however, he could not generalize his results since these effects were not identified in other rotors. Similarly, Wennerstrom was unsuccessful in resolving the disparity between his calculated shock losses

14

and those from experiment. Later, Rabe et al. [75] found that shock waves cannot be studied in isolation of endwall effects; aerodynamics in this region require complex models.

2.2.4 Flowfield Interactions and Loading Effects

Hoping to simplify the problem, engineers prefer to model each of the tip region flow features independently, but separating and tallying the contribution of the various types of flows in the tip region is a daunting task. In the past, as explained by Kerrebrock [52], the sum of the losses calculated for each viscous flow type fell short of the actual losses existing in transonic compressors. He attributed the discrepancy to the unfavorable interaction of viscous flow with the shock system and a lack of understanding of the physical processes. Subsequently, Dring and Joslyn [28, 29] showed that the combined effects can be studied with throughflow analysis, but this approach lacks sufficient detail to characterize and improve compressor designs. Detailed analysis is needed.

The use of Computational Fluid Dynamics (CFD) is valuable in merging and understanding the qualitative models for the various types of flow in the tip region. It is particularly valuable when compressible flow modeling is necessary, as is the case for transonic flow compressors. To build accurate models, precise measurements of the flowfield in the tip region are necessary. Collecting this data requires high-speed facilities and precision instruments, so it has been restricted to a handful of engine manufacturers and government research laboratories. Nevertheless, using experimental data and/or numerical modeling, several studies have addressed the interaction of flows in the tip region.

Sellin et al. [81] explored the tip shock structure in transonic flows. They used three rotors in their study. A highly loaded straight-bladed rotor built to reduce shock losses (Law and Wadia [61]; Wadia and Law [89]) was used as the baseline rotor. The second rotor (designated as Rotor 4) also was straight-bladed and was nearly identical to the baseline rotor except for less flow turning. The

third rotor had a swept leading edge. The baseline rotor was run with a tip clearance of approximately 0.85mm (0.8% tip chord) while the other two rotors were run with a tip clearance of 0.53mm (0.5% tip chord).

Sellin et al. [81] found that two shock systems exist in the tip region for open throttle flow (near choking): an oblique shock emanates from the leading edge and intersects the suction surface of the adjoining blade aft of the mid-chord point; a second normal shock wave spans the passage from approximately 25 percent axial chord on the pressure surface to approximately 75 percent axial chord on the suction surface (Figure 4). With greater throttling (i.e., decreased mass flow), the secondary normal shock weakens and moves forward in the passage (Figure 5). The secondary shock ceases to exist for flows below peak efficiency mass flow. Likewise, the oblique shock at the leading edge strengthens as it becomes more normal with decreased mass flow. As the flow is throttled to the near-stall point (Figure 6), the leading edge shock becomes a detached bow shock that impinges the adjacent blade suction surface at near midchord. Sellin et al. also found strong evidence of a tip leakage vortex that increases in strength and influence with increased loading. A large zone of blockage is created as the tip leakage vortex passes through the leading edge shock. The shock-vortex interaction creates curvature in the shock with a weakened localized pressure gradient and shock-induced growth of the tip leakage vortex. Thus, a pronounced area of low-velocity fluid exists immediately downstream of the interaction as the shock-expanded vortex continues to grow circumferentially and radially as it moves through the passage. Interestingly, they also found very similar flow patterns in the cascade plane for the three rotors tested; Figures 4, 5, and 6, depicting the baseline rotor, are representative of the macroscopic flowfields for all three rotors.
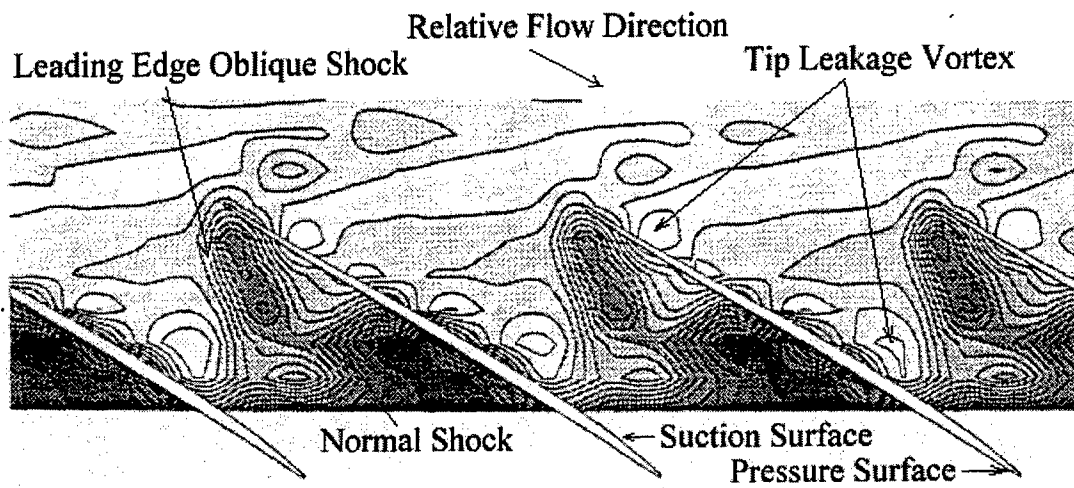
Figure 4. Rotor Tip Region Flowfield (Open Throttle) [Adapted from Sellin et al. [81]]
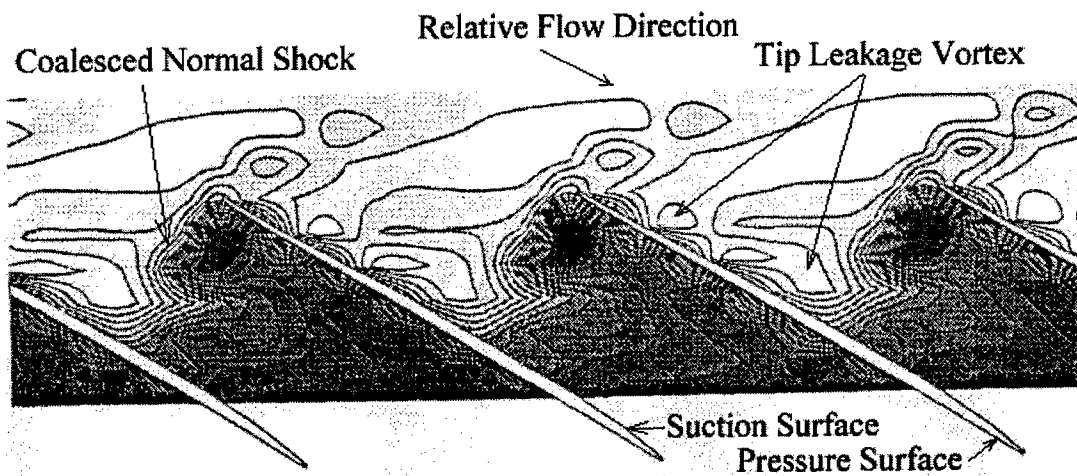
Figure 5. Rotor Tip Region Flowfield (Peak Efficiency) [Adapted from Sellin et al. [81]]
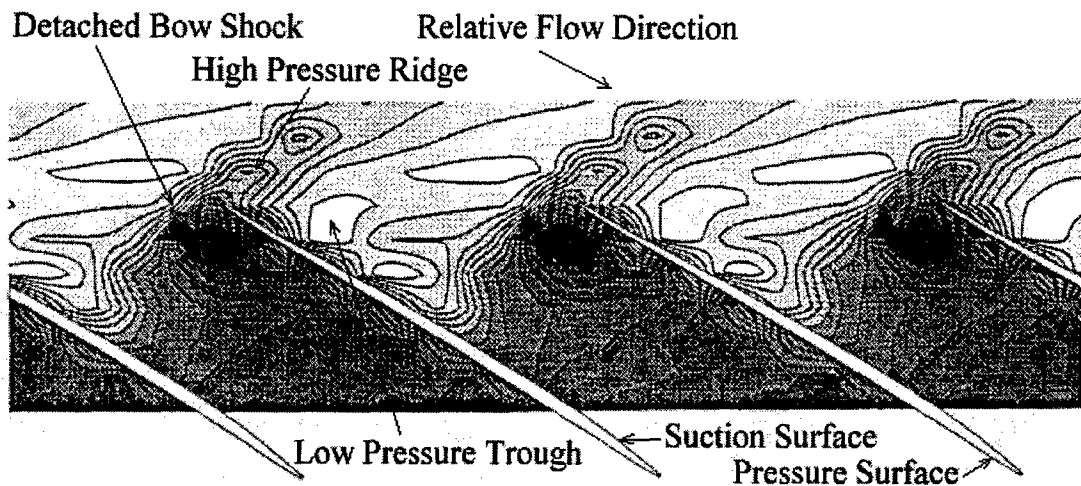
Figure 6. Rotor Tip Region Flowfield (Near-Stall) [Adapted from Sellin et al. [81]]

Copenhaver et al. [18] confirmed these results with additional experimental and numerical studies of the best performing straight-bladed rotor (Rotor 4) from the earlier study of Sellin et al. [81] . The tip clearance for these tests was unspecified. They found excellent agreement between experimental data and numerical predictions; thus accurate computational fluid dynamic modeling was validated. In addition to the flow structures mentioned previously, they found a smaller vortex-like flow forming coincident with the smaller secondary normal shock (Figure 4).

Suder and Celestina [86] used a Navier-Stokes solver to detail the velocity and energy levels of the flow near the tip of the NASA Stage 37 rotor. They found no significant differences in the qualitative interactions taking place for the two tip gaps studied (0.356mm equating to 0.6% tip chord, and 0.584mm being 1.0% tip chord). Likewise, from experimental measurements of the NASA Stage 37 transonic rotor operating with tip clearance of 0.400mm (0.7% tip chord), they produced quite detailed flow paths and vector diagrams clearly illustrating the flowfield effects in the tip region (Figures 7 and 8). They found that after the tip leakage vortex passes through the shock (sometimes referred to as the post-shock vortex), its path (dotted lines in Figures 7 and 8)

18
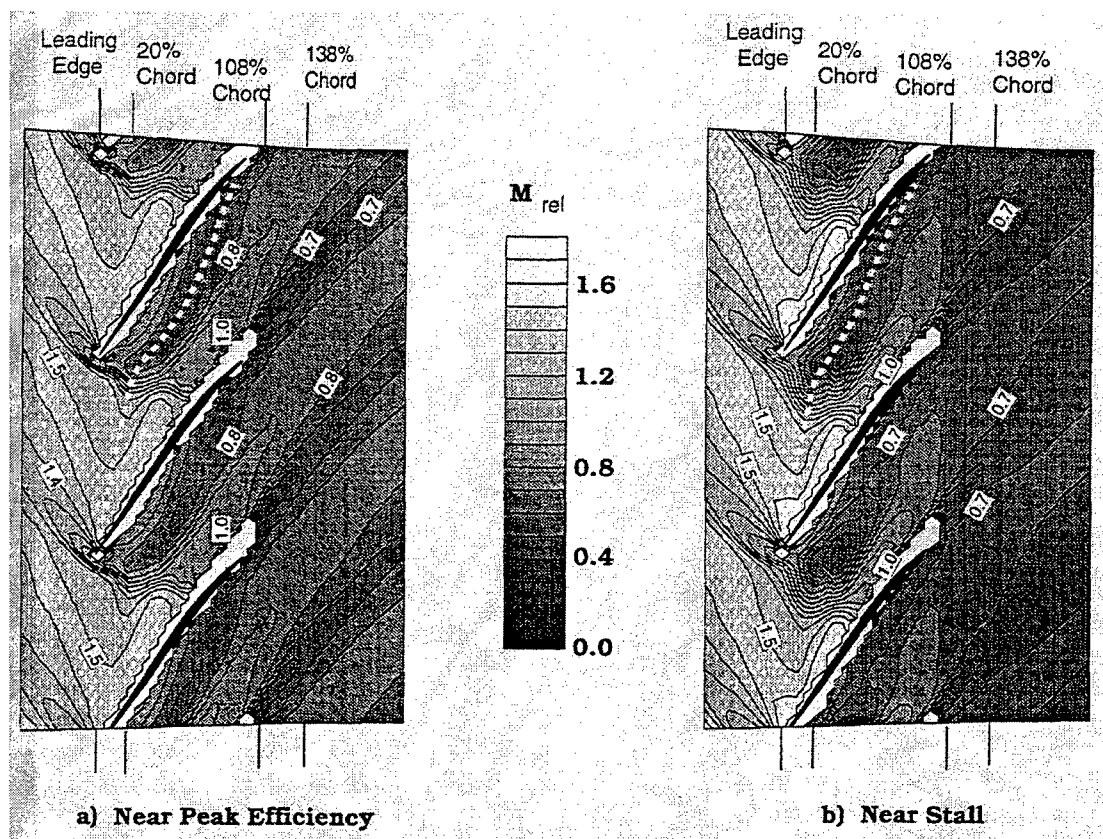
Figure 7. Measured Relative Mach Number [Extracted from Suder and Celestina [86]]

moves faster toward the pressure surface of the adjacent blade than is predicted by numerical analysis. Moreover, as seen in Figure 7, this path impacts the blade pressure surface before reaching the trailing edge. The vortex then merges with the rotor wake. The interaction profile along the vortex path is seen in Figure 9. In Figure 9b, the blockage produced by the shock-vortex interaction has moved forward in the passage with increased throttling, and the axial Mach numbers in the interaction region are less than half of the diffused and recovered values seen at the rotor trailing edge. This blockage extends radially up to 20 times the tip clearance height. Suder and Celestina suggested that alternative blade or casing treatments might alleviate the shock-vortex interaction.

19
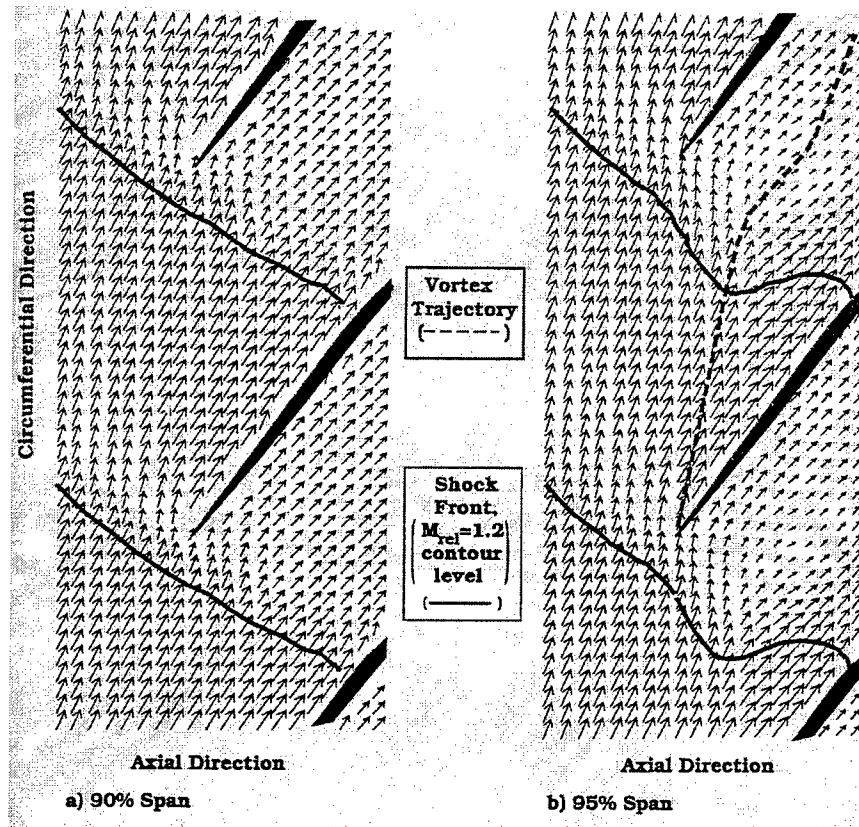
Figure 8. Measured Relative Velocity Vectors [Extracted from Suder and Celestina [86]]
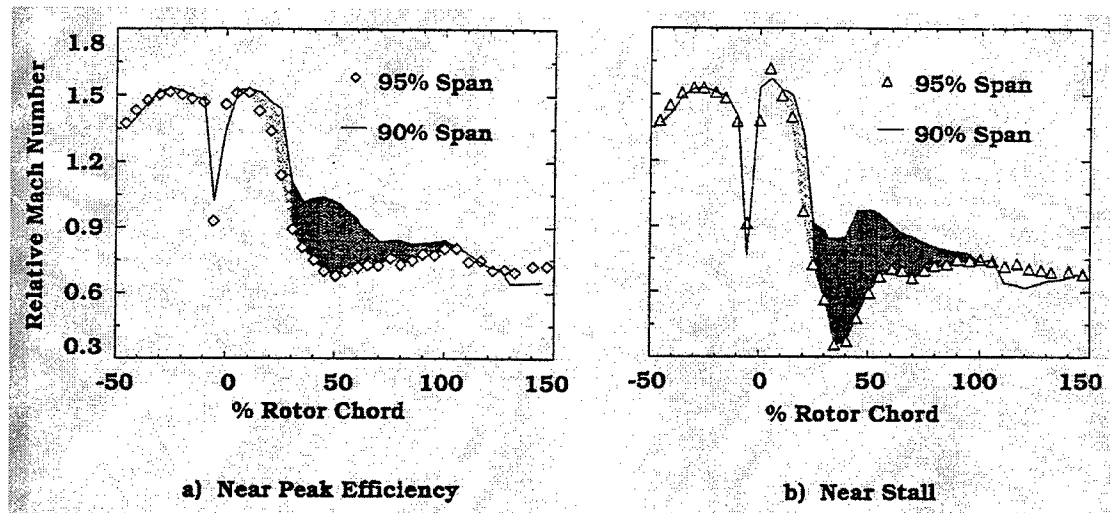
Figure 9. Measured Relative Mach Number Along Vortex Trajectory [Extracted from Suder and Celestina [86]]

20

Another intensive study of the tip clearance flow was performed by Puterbaugh [71] . He concluded with five key findings:

1. *The clearance flow-shock interaction has an unsteady component.* The unsteadiness is localized downstream of the passage shock near mid-pitch and is postulated to result from rotor relative shock movement.

2. *The post-shock vortex has a wake-like nature.* A deep velocity defect as well as a relatively constant static pressure distribution in the pitch-radial plane were identified.

3. *The injection of mass via the clearance flow plays an important role in the clearance flow-shock interaction process.* The low-velocity core of the upstream vortex (the tip leakage vortex generated over the forward portion of one blade prior to encountering the leading edge bow shock of the adjacent blade) has a significant impact on the overall interaction.

4. *The vortical character of the vortex upstream of the shock is not a significant factor in driving the interaction.*

5. *The interaction between the clearance flow and the shock is fundamentally the result of the change in momentum brought about by the shock-induced pressure rise. The interaction can therefore be viewed as an inviscid problem.*

More recently, Russler et al. [79] and Cybyk et al. [24] characterized through experiment and computation the flow structure of the Advanced Damping Low Aspect Ratio Fan (ADLARF) rotor. As seen in Figures 10 and 11, the flow in the tip region is similar to that found by Sellin et al. [81] (Figures 4, 5, and 6), and Suder and Celestina [86] (Figure 7). Note in Figure 10 the apparent path of the tip leakage vortex emanating from the leading edge of the blade and terminating at the trailing edge pressure surface of the adjoining blade. The low-energy vortex path and regions of stagnation are clearly seen in Figure 11.
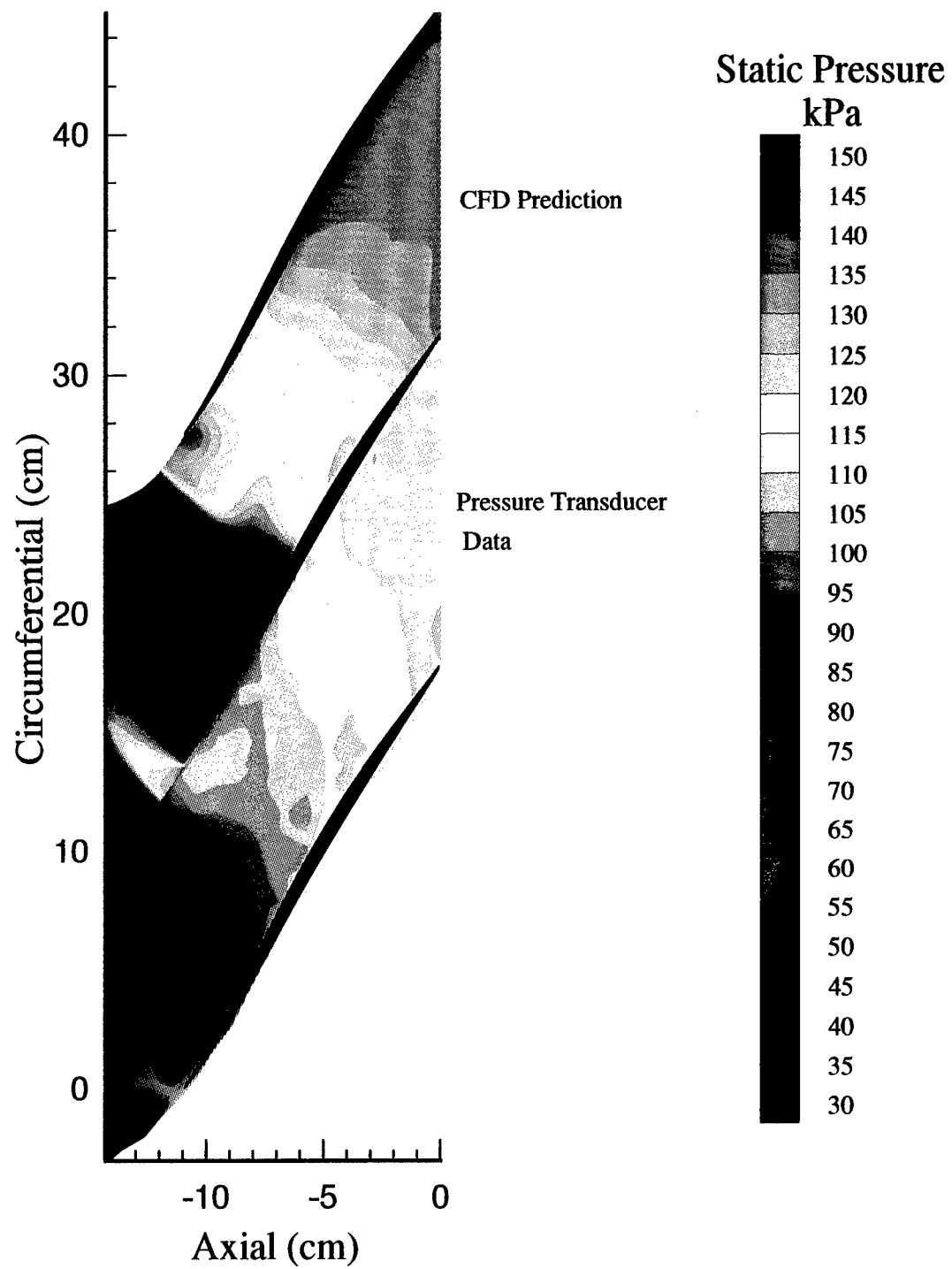
Figure 10. Static Pressure of ADLARF Rotor (Peak Efficiency, 85% Design Rotor Speed, 100% Span) [Extracted from Russler et al. [79]]
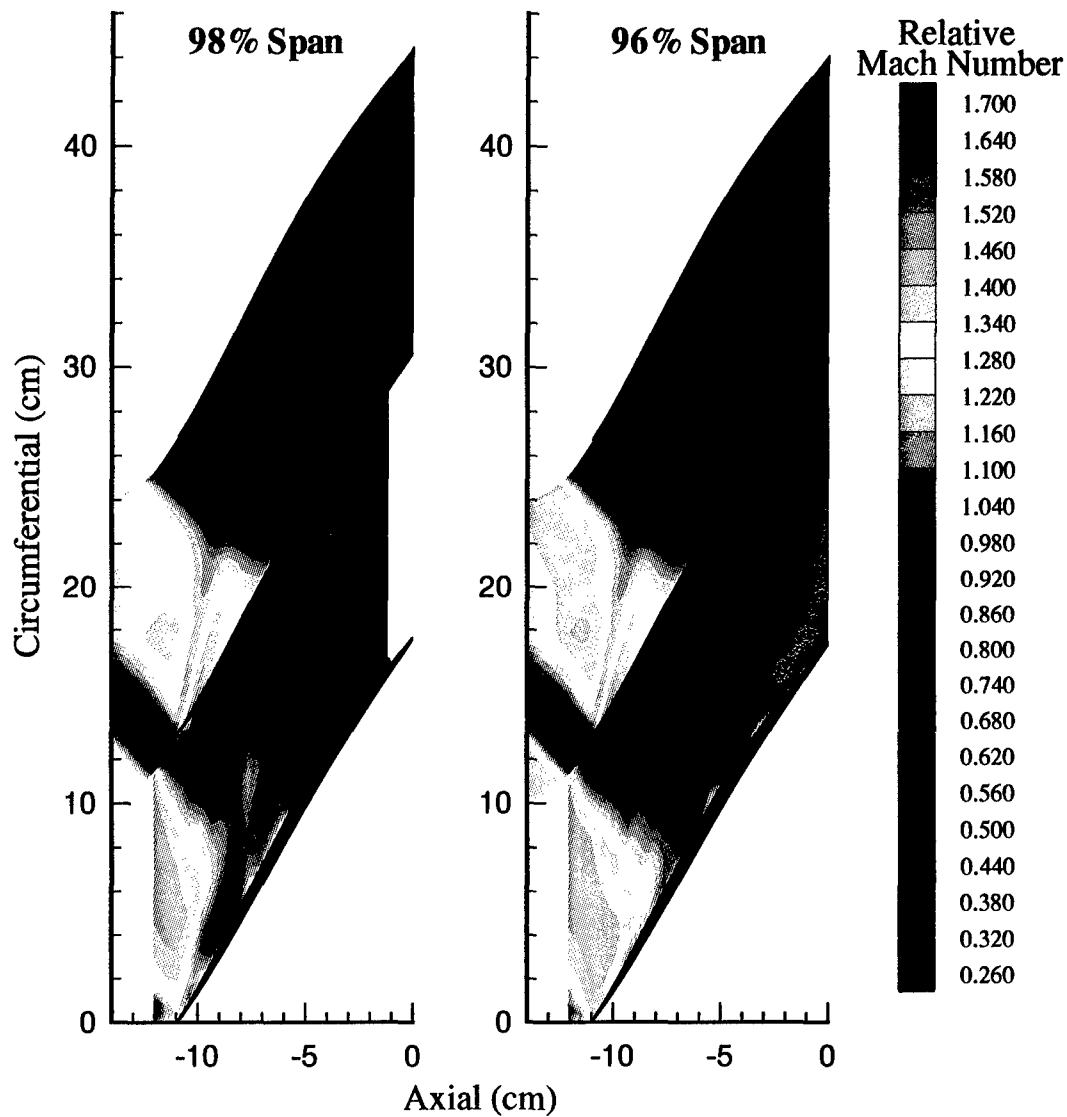
Figure 11. Relative Mach Number of ADLARF Rotor (Peak Efficiency, 85% Design Rotor Speed) [Extracted from Russler et al. [79]]

As the mass flow is throttled to near-stall, the leading edge shock becomes detached from the blade to form a normal bow shock (Figure 12), causing the vortex path to impinge upon the adjacent blade further upstream from the trailing edge (Figure 13). At 80% span (Figure 14), the low-velocity fluid is seen to parallel the curvature of the blades; the direct effects of the leakage vortex on the flow path are no longer evident even for the near-stall condition.

23
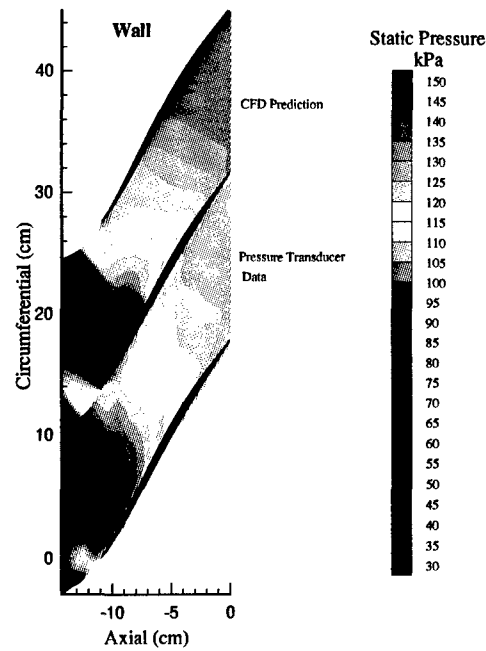
Figure 12. Static Pressure of ADLARF Rotor (Near-Stall, 85% Design Rotor Speed, 100% Span) [Extracted from Russler et al. [79]]
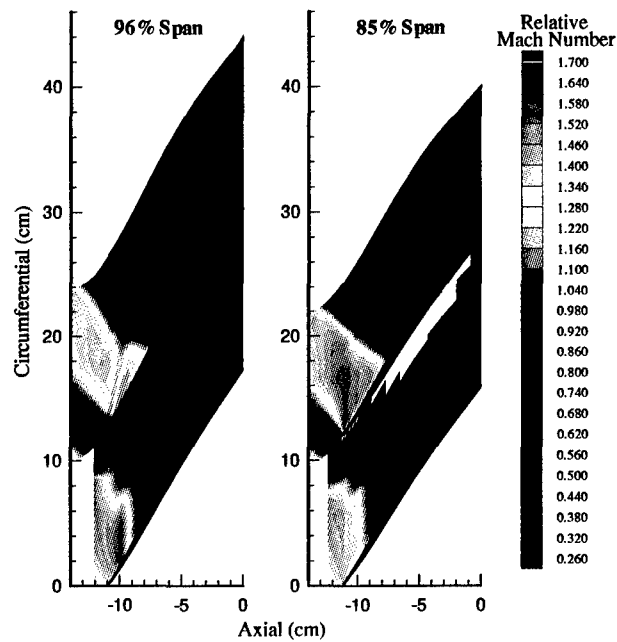
Figure 13. Relative Mach Number of ADLARF Rotor (Near-Stall, 85% Design Rotor Speed) [Extracted from Russler et al. [79]]
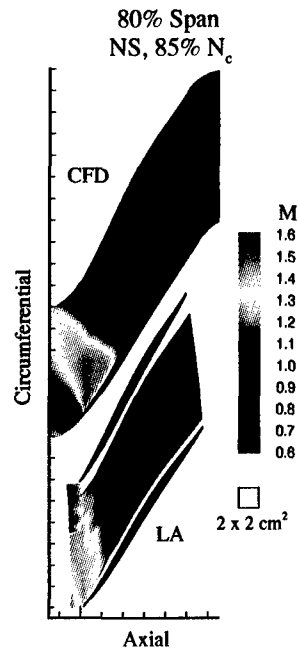
Figure 14. Relative Mach Number for ADLARF Rotor (Near-Stall, 85% Design Rotor Speed, 80% Span) [Extracted from Cybyk et al. [24]]

The radial profiles of efficiency (Figure 15) and total pressure ratio (Figure 16) confirm that the blockage created by the interactions engulfs the outer 20 percent of the span. For the near-stall condition (dotted line in Figures 15 and 16), a rapid drop in efficiency occurs near the tip where the largest interactions occur. This drop in efficiency is associated with the large wake created by the low-energy vortex impinging on the adjacent blade and merging with the blade boundary layer. Some of the inefficiency can also be attributed to flow separation on the suction surface which occurs during excessive turning as evidenced by the large total pressure ratio near the tip in Figure 16. Figure 17 shows the effect of the blockage on flow turning in the tip region as evidenced by the large absolute flow angles in the rotor exit plane; in this case, the leakage vortex impinging on the adjacent blade causes the main flow to divert closer to the suction surface near the tip resulting in greater absolute flow angle. This increased absolute flow angle (decreased relative flow angle, see

25
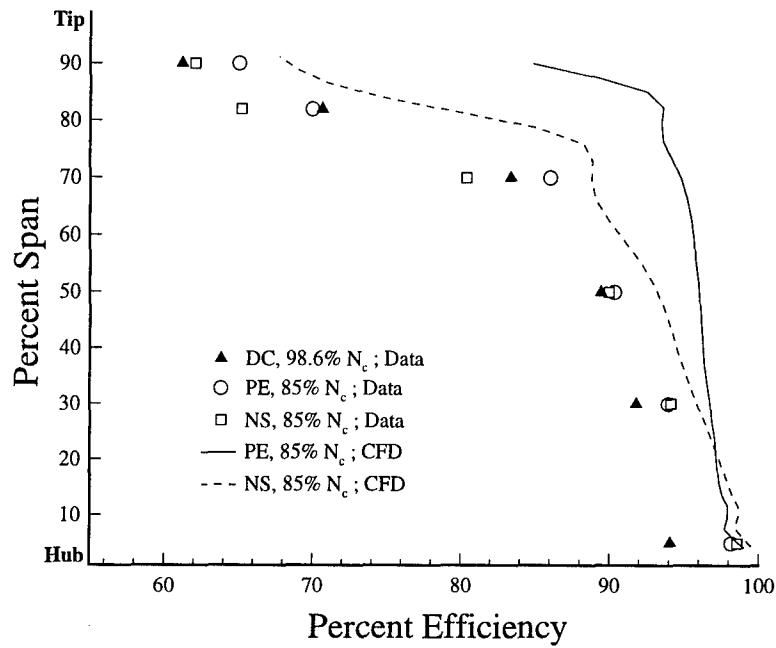
Figure 15. Adiabatic Efficiency Profile of ADLARF Rotor (85% Design Rotor Speed, 110% Axial Chord) [Extracted from Cybyk et al. [24]]
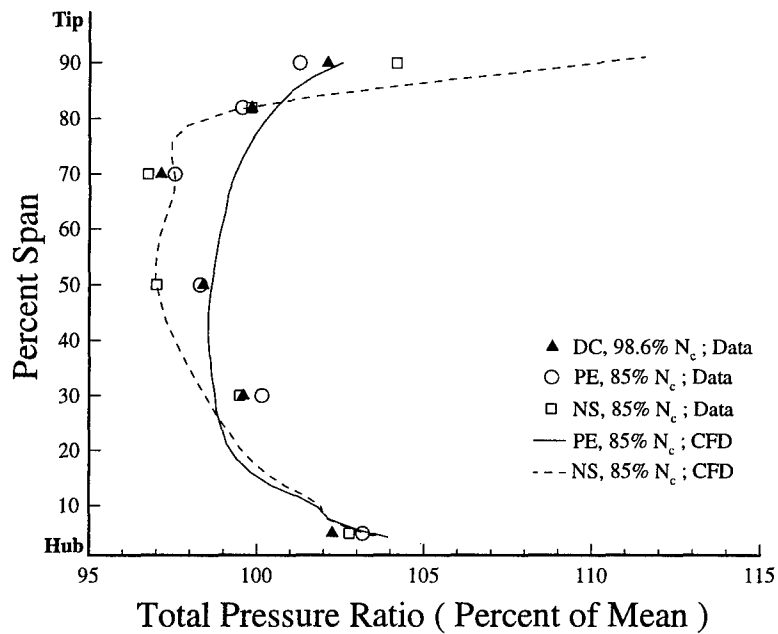
Figure 16. Total Pressure Profile of ADLARF Rotor Wake (85% Design Rotor Speed, 110% Axial Chord) [Extracted from Cybyk et al. [24]]

Figure 1) at the rotor trailing edge gives increased turning which can result in flow separation and stall. Thus, Figure 17 indicates the tip region to be the area of stall cell initiation.
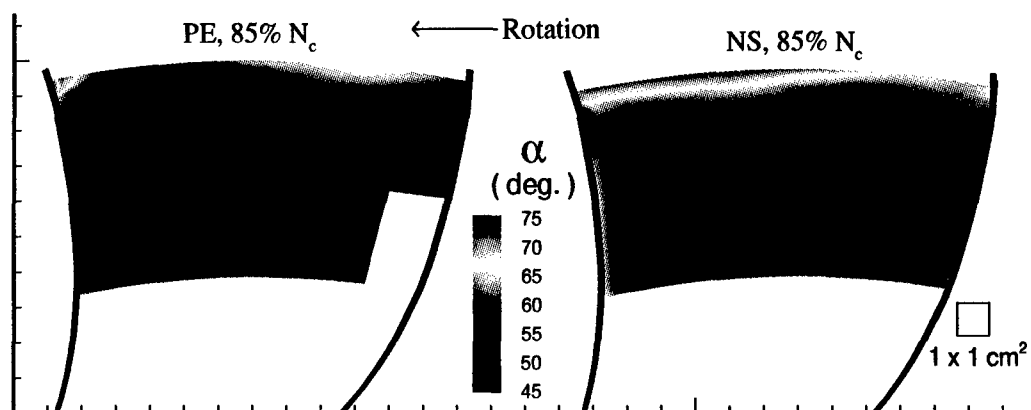
Figure 17. Measured Absolute Flow Angles of ADLARF Rotor Wake (85% Design Rotor Speed, 100% Chord) [Extracted from Cybyk et al. [24]]

The research described above provides a clear picture of the flow interactions in the tip region, and the complementary findings may be applied to all transonic rotors. In addition to being a source of blockage and losses in compressors, the flowfield interactions in the tip region are also key factors influencing the initiation and development of rotor stall.

2.2.5 Rotating Stall

Rotating stall initiation and propagation have been the focus of numerous experimental studies with low-speed compressors (Inoue et al. [48] ; Longley and Hynes [63] ; McDougall et al. [65] ; Wilson and Freeman [100]) as well as high-speed machines (Boyer et al. [13] ; Copenhaver and Okiishi [20] ; Gorrell and Russler [33] ; Hoying [45]). In each study, the stall process was highly repeatable, and the tip region was noted to be the most probable source of stall initiation. These experiments substantiate Jackson's [50] analysis of the stall process. Jackson noted that stall inception is not random, and he found overwhelming evidence that a low-energy stall cell forms at a very

27

small distance from the rotor tip. Higher energy fluid diverts around this cell, creating an increased angle-of-attack on the adjacent blade and a reduced angle-of-attack on the stalled blade (Figure 18).
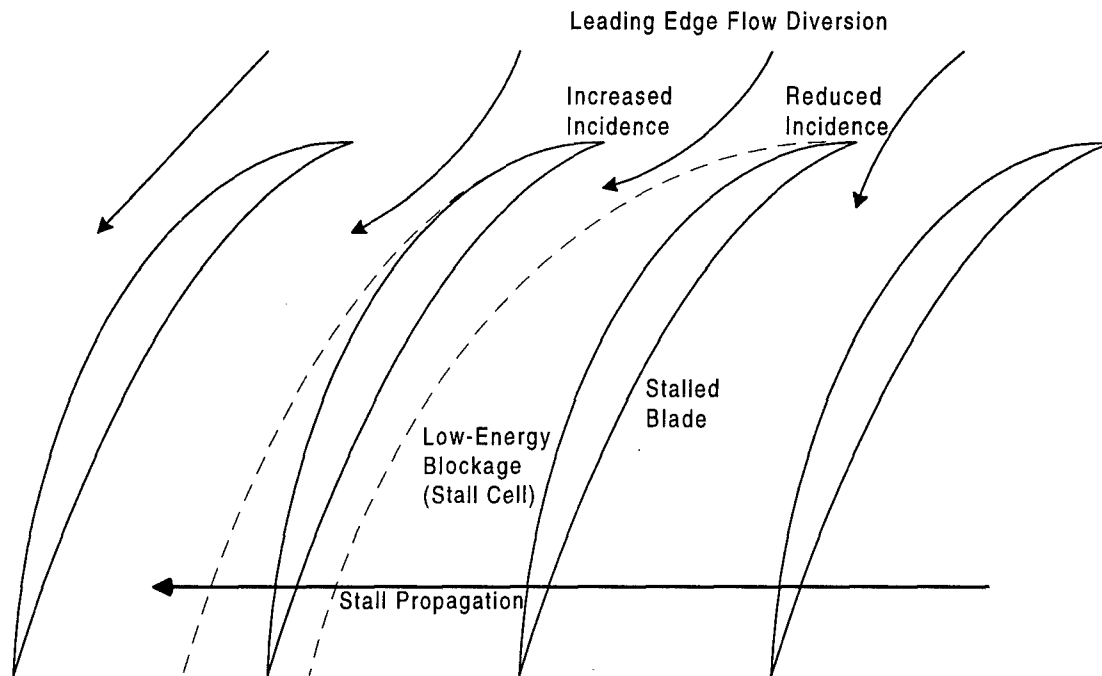
Figure 18. Rotating Stall Propagation Through a Rotor

The adjacent blade then stalls, and the original stalled blade becomes unstalled. Thus, propagation of the stall cell results as described by Emmons et al. [30] and supported by others (Day and Cumpsty [26] ; Cumpsty and Greitzer [23] ; Day [25] ; Longley [62]). This propagation is opposite to the rotation of the rotor, but since its steady rate is approximately half that of the rotor, in the absolute frame, the stall cell appears to move in the same direction as the rotor at half the rotor speed. The stall cell also elongates circumferentially and grows radially as it propagates and merges with other stall cells initiated by the same process (and in many cases, the same blade at the same circumferential location). The stall cell quickly expands in three dimensions to form a fully developed full-span rotating stall cell.

Since the tip gap regulates the degree of interaction of the tip region flows, it obviously has an affect on the formation of the low-energy stall cell. Therefore, with the structure of tip flows described earlier in mind, a look at the effects of changing tip gap on compressor performance and stability is in order.

2.3 Experimental and Numerical Studies of Tip Gap Effects

The issue of the existence of an optimum tip gap for transonic rotors has been marked with conflicting data. Some research (Moore [66] ; Copenhaver et al. [19]) indicates the optimum gap to be the minimum possible (zero would be best), while other experiments (Wennerstrom [93] ; Freeman [32]) have found a nonzero clearance to give the best performance. The explanation for these seemingly contradictory results requires examination of an extensive database. Unfortunately, the experimental database exploring this topic is small and often disjointed or is a secondary by-product of results from other research of transonic flow. The large database from low-speed two-dimensional cascade tests gives little assistance since cascade data lack radial flow effects and, with rare exception (Peter and King [70] ; Yaras and Sjolander [101, 102]), the moving wall effects that complicate the tip gap flow. Transonic flows are much more complicated than low-speed flows; shock waves are distorted by radial flow and moving wall effects. An adequate accounting for these effects requires transonic flows to be studied in rotating machinery for which the existing data set is small.

Theoretical approaches have often been used to explore the effects of variations in tip clear-ance. Numerous studies (Hah [35] ; Chen et al. [15] ; Adamczyk et al. [5] ; Crook et al. [21] ; Kunz et al. [53] ; Hall et al. [40] ; Basson and Lakshminarayana [11]) have aided the evolution of com-putational fluid dynamic (CFD) models, but because of the limited experimental data set to validate these simulations, it is not clear that all the necessary factors for accurate modeling have been in-

29

cluded. Therefore, the experimental data available in the open literature needs to be expanded to encompass a wider variety of transonic rotors and operating conditions; specifically, additional testing is needed to address and generalize the problem of an optimum tip gap for transonic rotors. A review of the existing experimental and numerical studies addressing tip gap variation in axial flow rotors will be helpful.

2.3.1 Effects on Overall Performance

In 1982, Moore [66] investigated the effects of four tip clearances on the performance of a single-stage NASA transonic research rotor. Running tip clearances ranged from 0.021 centimeters (0.445% tip chord) to 0.138 centimeters (2.923% tip chord). He found that the stage performance in terms of efficiency and total pressure ratio decreased with increasing tip gap; the efficiency dropped 5.1 percentage points while the total pressure ratio fell 6.6 percent over the range of clearances. Likewise, the stall margin of the smallest clearance was 15.5 percent greater than that of the largest clearance. The effects of tip clearance were not confined to the rotor tip region; instead, they were most evident in the outer 30 percent of span. He also noted an apparent shift of flow through the rotor blades with changes in clearance. Although not stated, the optimum tip gap for his study can be concluded to be a zero clearance.

Freeman [32] investigated the effects of extremely narrow tip clearance in a rotating transonic compressor at Whittle Laboratories in the early 1980s. Varying the clearance from zero to eleven percent of chord by using paper seals on the blades, he found that a reduction in peak pressure rise occurred near stall for tip clearances less than approximately 1.2 percent of chord. The best efficiency occurred for the zero clearance. Based on peak pressure rise capability alone (efficiency was not considered), Freeman concluded that an optimum tip gap (1.2% chord) existed, but it was not practicably achievable. A practical limit of rotor tip gap is set by the machining precision and

the level of nonhomogeneous thermal and centrifugal expansion of the metal comprising the rotor. The design tip clearance must allow for these variations; otherwise, asymmetric distortions can result in damage caused by rotor tips striking the engine casing. Putting these material restrictions aside, Freeman's test demonstrated the likely existence of an optimum nonzero tip clearance based on aerodynamic experiment.

From a separate series of tests (Wennerstrom et al. [95] ; Law et al. [59] ; Law et al. [60] ; Wennerstrom [93]) performed at Wright Aeronautical Laboratories from 1977 to 1984, Wennerstrom [93] found that the best efficiency resulted from the use of an intermediate tip clearance (Figure 19) during tests of a transonic rotor developed by Wright Laboratories. The tests were conducted with running tip clearances of 0.41mm (0.415% tip chord), 0.66mm (0.675% tip chord), and 0.92mm (0.935% tip chord). The 0.675% gap gave a 0.7 percent increase in efficiency over the 0.415% gap throughout the overlapping range of operation. Unfortunately, the optimum tip gap for efficiency did not correspond to the optimum for pressure ratio and mass flow. For clearances larger than 0.415% tip chord, pressure ratio decreased approximately three percent at design conditions (62.642 lbm/sec at 20,150 RPM). However, for the lower two-thirds of the mass flow range, the pressure ratio for the larger clearances held a nearly constant value of approximately 2.06 which was only one percent less than that of the 0.415% gap. Wennerstrom also found that an increased tip gap yields a beneficial increased mass flow range for the compressor stage, but the maximum mass flow is lower for a given speed line. His results demonstrated that the tip gap yielding improved performance for one measure may adversely affect other performance measures.
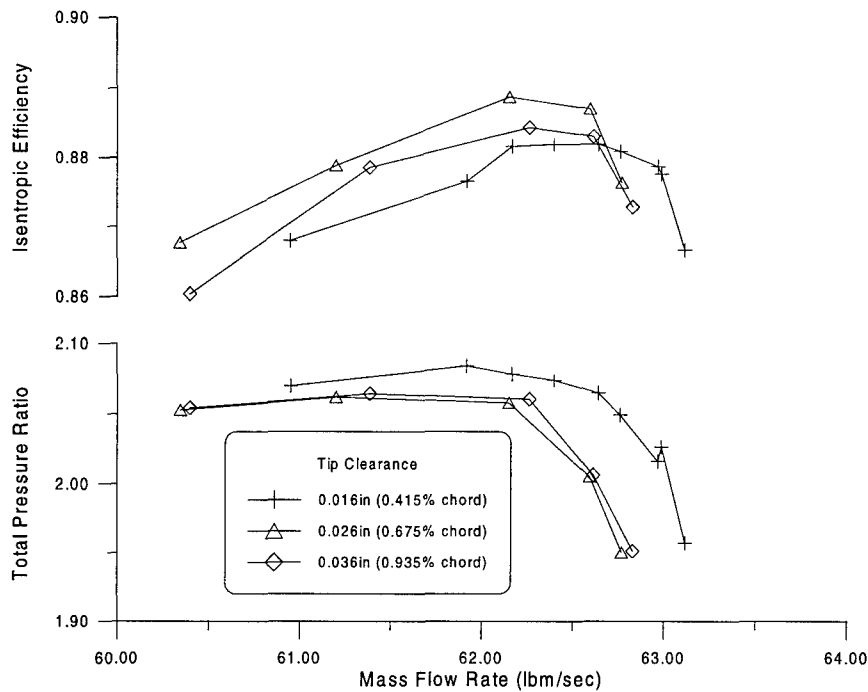
Figure 19. Effect of TipClearance Change at 100% Design Rotor Speed (Adapted from Wenner-strom [93]]

In 1993, Adamczyk et al. [5] conducted a series of numerical simulations to evaluate the effect of tip clearance on the NASA Rotor 67 (described by Strazisar et al. [85]). The analyses were performed with tip clearances of 0.0%, 0.25%, 0.75%, and 1.25% tip chord with the rotor simulated to operate at 100% design speed. Pressure ratio was found to decrease with increased tip clearance (see Table 1) with the maximum pressure ratio occurring for a zero tip clearance, but the maximum efficiency occurred for a nonzero clearance (0.25% tip gap). These results followed the trends of Wennerstrom [93] in which the optimum clearance for pressure ratio did not coincide with that for maximum efficiency. However, contrary to Wennerstrom, Adamczyk found that mass flow range decreased with increased clearance. These results demonstrated that theoretical modeling (albeit, semi-empirical and numerical) could duplicate some of the performance trends associated with optimum tip gaps.

32

Table 1. Summary of Tip Gap Effects on the Performance of Transonic Axial Flow Rotors [Data Taken from Moore [66] , Freeman [32] , Wennerstrom [93] , Adamczyk et al. [5] , and Copenhaver et al. [19]]

Investigator	Tip Gap (mm)	Percent of Tip Chord	Maximum Isentropic Efficiency	Maximum Pressure Ratio	Mass Flow Range (kg/sec)	Choking Mass Flow (kg/sec)	Remarks
Moore	0.210	0.445	0.866	1.793	2.090	29.55	
	0.620	1.313	0.844	1.715	1.020	29.42	Pressure ratio and efficiency
	1.000	2.118	0.832	1.675	0.870	29.18	decrease with increased tip gap
	1.380	2.923	0.815	1.674	0.810	28.96	(Tip Chord = 47.22mm)
Freeman	0.000	0.000	0.910	0.600		not given	Efficiency peaks at zero tip gap
	not given	1.200	0.903	0.770		not given	Pressure rise peaks at intermediate tip gap
	not given	4.000	0.899	0.630		not given	(Pressure Rise Coefficient
	not given	6.000	0.883	0.560		not given	used in lieu of Pressure Ratio)
	not given	11.000	0.859	0.520		not given	(Tip Chord = unknown)
Wennerstrom	0.410	0.415	0.882	2.065	0.984	28.63	Pressure ratio peaks at smallest tip gap
	0.660	0.675	0.887	2.005	1.115	28.47	Efficiency peaks at intermediate tip gap
	0.920	0.935	0.883	2.007	1.103	28.50	(Tip Chord = 98.0mm)
Adamczyk	0.000	0.000	0.913	1.740	4.820	33.22	Pressure ratio peaks at zero tip gap
et al.	1.016	0.250	0.916	1.730	3.160	33.25	Efficiency peaks at intermediate tip gap
	3.048	0.750	0.909	1.690	1.030	32.95	
	5.080	1.250	0.903	1.660	1.130	33.28	(Tip Chord = 406.4mm)
Copenhaver	0.000	0.000	not given	not given	1.650	28.35	Numerical--Efficiency decrease with zero gap
et al.	0.280	0.270	0.940	2.050	1.500	28.40	Experiment
	1.050	1.000	0.905	2.000	1.300	27.80	Numerical
	1.960	1.870	0.865	1.900	1.000	26.90	Experiment
							(Tip Chord = 105.0mm)

In 1994, Copenhaver et al. [19] found no benefit of increased tip gap when conducting tests on a backward swept transonic research compressor at the Wright Laboratories Compressor Aerodynamics Research Laboratory. Two running tip clearances, with the smallest being an average 0.28 millimeters (0.27% mean chord) and the larger being 1.96 millimeters (1.87% mean chord), were evaluated at design speed. The rotor was also tested at 90% and 95% of design speed. The larger tip clearance gave a 30 percent reduction in mass flow range and a smaller mass flow rate at stall inception. Pressure ratio and efficiency also decreased with increasing tip gap. However, they also found that for the 90% speed condition, the mass flow rate at stall inception decreased with decreased tip clearance—this agreed with previous studies of low-speed subsonic compressors (Freeman [32]). Copenhaver also performed a numerical analysis paralleling his experiment in which he found that efficiency and stall margin decreased when the tip clearance was reduced to zero at design speed. Although this result was consistent with the findings of Wennerstrom [93] and Adamczyk et al. [19] , Copenhaver concluded that an optimum tip gap was not indicated.

2.3.2 Effects on Stability

Adamczyk et al. [5] extended their numerical study to evaluate the role of tip clearance in high-speed fan stall. Their findings illuminated several key aspects of the tip region flow. Adamczyk found the strong interaction between the tip leakage vortex and the passage shock system to be consistent with Jackson's [50] experimental studies and the likely cause of stall cell development. With decreased tip clearance, the shock-vortex interaction near the blade leading edge was reduced, resulting in a large stable operating range. Adamczyk reasoned that the increased operating range was a consequence of reduced tip region blockage which is the genesis of stall cells. In the same study, Adamczyk modeled three different partial clearance configurations. The first configuration consisted of zero tip clearance from the blade leading edge to 50% chord, with a tip clearance

of 1.25% chord over the aft potion of the blade. The second configuration consisted of zero tip clearance from the blade leading edge to 29% chord, with a tip clearance of 1.25% chord from 29% chord to the blade trailing edge. The third configuration consisted of a tip clearance of 1.25% chord from the blade leading edge to 50% chord, with zero tip clearance over the aft portion of the blade. Adamczyk found that zero tip clearance confined to the forward portion of the blade was sufficient to suppress the shock-vortex interaction, leading to a reduction of end-wall loss and blockage in the forward portion of the blade and an increase in operating range. Adamczyk also found that the tip clearance (or lack of it) over the forward portion of the blade is far more important than that over the aft portion of the blade in establishing peak pressure rise of the fan. Thus, Adamczyk concluded that it is the clearance over the forward portion of the fan blade that controls the flow process leading to stall.

As alluded to earlier in Section 2.2.4, Puterbaugh [71] and Puterbaugh and Copenhaver [73] found an unsteadiness in the shock-vortex interaction zone assumed to be caused by shock movement with varying inlet flow conditions and turbulence. Tip gap can affect the susceptibility of the flow to inlet variations or disturbances through the generation of tip region blockage; reduced passage flow area resulting from tip region blockage yields a corresponding increase in throughflow (see Section 1.3 and Equation 4) which directly affects the formation of shock waves (will be addressed in Section 2.4). In this manner, blockage can magnify deviations of the inlet flow. Since blockage is a function of tip gap, tip clearance affects the susceptibility of the flow to unsteadiness. Momentary or impulsive flow deviations are possibly acceptable, but prolonged or rapidly varying disturbances can be a significant source of unsteadiness to the flow. Suspecting this unsteadiness to be a cause of compressor stall, the Wright Laboratories Compressor Aerodynamics Research Laboratory is fully investigating its effects. Some preliminary results have been obtained (Puterbaugh and Copenhaver [73]), and their research is continuing.

2.4 Interpretation of Previous Results

For each study discussed in the previous sections, some form of performance change was evident as a result of the variation of tip clearance. The effects were not always consistent (see Table 1), but tip clearance was seen to have significant influence on compressor performance and stability. It is possible that the disparity of the results may be a consequence of the inherent errors associated with experimental testing and numerical modeling. It is more likely that the blockage generated as a result of tip clearance flow interactions is utilized better by some rotor designs than others to optimize performance. Some interpretation of the limited data set regarding tip clearance effects on rotor performance is possible.

For the four most recent studies of tip clearance effects (see Table 1 regarding Freeman [32] , Wennerstrom [93] , Adamczyk et al. [5] , and Copenhaver et al. [19]), either pressure ratio or efficiency was found to decrease as the tip clearance was reduced below a threshold value for each rotor[1]. It is possible that the earlier tests conducted by Moore [66] did not achieve a tip clearance below the threshold value for that rotor to witness performance degradation, or it is possible that the tip clearances Moore used straddled the clearance range where improved efficiency or pressure ratio was witnessed by Freeman [32] , Wennerstrom [93] , and Adamczyk et al. [5] . Likewise, Copenhaver's experimental tests may have missed the intermediate tip clearance range where the results of Freeman, Wennerstrom, and Adamczyk suggest an optimum gap to reside (see Table 1).

Although most studies indicated that mass flow range decreased with increased clearance (Table 1), Wennerstrom's test showed that a larger tip gap could increase the mass flow range (Figure 19 and Table 1). More importantly, Wennerstrom's results came from experimental testing rather than from numerical simulation, and his experiments were the only tests which validated the efficiency

---

[1]It should be noted that Copenhaver et al. [19] found a decrease in efficiency below a threshold tip clearance only in their numerical study and not in their experimental tests; however, their experimental study consisted of only two tip clearances which prevents valid identification of trends.

trends (i.e., improved efficiency for an intermediate tip clearance) of the numerical approaches. It is possible that the numerical studies did not accurately model all aspects of the tip region flow processes. Additionally, Wennerstrom's results were consistent with the elementary compressor theory of Chapter 1; with a larger tip gap, the mass flow associated with choking and stall on the same rotor speed line decreased (Table 1). In the following paragraphs, conservation of mass and a knowledge of shock-vortex interaction mentioned earlier is used to explain this decrease in mass flow.

With an increased tip gap over the axial length of the rotor, the size and strength of the tip leakage vortex is increased, thereby creating a larger zone of low-energy fluid downstream of the shock-vortex interaction (Puterbaugh [71] ; Puterbaugh and Brendel [72]). This larger pocket of low-energy air produces a larger region of blockage to the flow. The larger blockage effectively reduces the area of the channel causing the high-energy mainstream flow to be diverted around the low-energy blockage. To satisfy continuity, the essentially inviscid mainstream flow must accelerate to a greater velocity through the reduced passage. This process affects the choking limit; if the main flow is nearly sonic (i.e., near the choked mass flow limit) prior to the tip clearance increase, the increased tip gap will cause the mainstream flow to accelerate to sonic velocity and create shock waves that choke the passage near the blade trailing edge. Therefore, choking will occur at a lesser mass flow for the larger tip clearance.

Increased tip gap also lowers the stall limit mass flow. Since the mainstream axial velocity increases with greater tip gap as discussed in the previous paragraph, the incident air angle of the rotor (with no inlet guide vanes) decreases for the main portion of the span (Figure 2). Recall that when the rotor speed is fixed, stall requires a decrease in mass flow (Figure 1) from the normal operating point. If the flow is near stall prior to the gap increase, an increased gap requires a further decrease in mass flow to attain the incident air angle at which stall occurs. Thus, increasing the tip gap causes the rotor to stall at a lesser mass flow for a given speed.

37

For the theoretical case discussed in the preceding paragraphs (and that of Wennerstrom's [93]), the entire mass flow range of the rotor shifts to a lesser mass flow with an increased tip gap, and the flow range also may increase for the larger tip clearance. However, as seen in Table 1 regarding Moore, Adamczyk et al., and Copenhaver et al., the reduction of mass flow range with increased tip clearance indicates that another factor is involved for the stall condition. The increased blockage generated as a result of a larger tip clearance heightens the instability of the tip region (Adamczyk et al. [5] , Jackson [50]). This instability causes stall to initiate near the rotor tip at a greater mass flow than would cause stall in the main portion of the span. In this manner, a decreased mass flow range could result from an increased tip clearance.

The results discussed in Section 2.3.1 and summarized in Table 1 suggest to the author that the blockage generated in the tip region is utilized differently by one compression system than by another. A variation of the tip clearance does not have consistent affect on all rotors. Occasionally, the idea of an optimum tip gap is introduced when some facet of performance is found to improve with the variation of rotor tip clearance. Others contend the optimum tip clearance is the smallest possible size. The common thread linking these tests is the blockage generated as a result of tip region flow interaction.

From simple observation, blockage is not always a bad thing. Blockage can have a beneficial sealing effect near the rotor blade tips, an effect which the author calls an "aerodynamic seal." The blockage produced by the interactions in the tip region creates zones of low-velocity fluid that divert the main flow away from this area. By removing air from the tip region, additional tip region losses in the form of leakage flow through the tip gap are averted, and rotor work efficiency is increased. Some tip losses are unavoidable in achieving this diversion effect.

For a compressor designed for the optimum tip clearance, there is just sufficient interaction and blockage to aerodynamically seal the endwall. Furthermore, though this sealing yields apparently

38

the best efficiency and pressure rise, a more optimum casing geometry with even greater performance improvements may exist. Thus, if thoroughly understood, the interactions can be further tailored to provide the desired tip sealing without adversely affecting the passage throughflow area. A simple approach for tailoring the interactions to achieve these goals is presented in the next chapter.

2.5 Summary

In this chapter, the aerodynamics associated with the rotor tip region was presented. The rotor tip clearance was shown to be a major factor influencing the shock-vortex interaction in the tip region. This interaction was shown to be a source of low-energy blockage to the flow which affects the performance of the rotor passage. Previous studies exploring the effects of tip clearance on rotor performance and stability were presented; the results from these studies were compared and interpreted with relevant compressor theory and experimental evidence. The concept of an aerodynamic seal created from tip region blockage was presented. In the next chapter, a method of flowfield manipulation to relocate tip region blockage for improved rotor performance is presented.

Chapter 3 - Theory of Blockage Relocation

As described in the previous chapters, the most detrimental effects to highly loaded transonic compressor performance are losses associated with the rotor tip region. Losses in the form of flow separation, stall, and reduced rotor work efficiency are the result of flow blockage created by the interaction of tip region flows. Despite efforts to eliminate blockage, it will always remain as a consequence of flow physics. Therefore, the main focus of this study was to relocate the blockage to benefit compressor performance. Achieving this relocation using simple means requires thorough understanding of fundamental concepts.

3.1 Fundamental Concepts

The tip gap influences the level of interaction of the various tip region flow elements; consequently, the amount of blockage in the tip region is a function of tip gap. Experimental evidence (Adamczyk et al. [5] ; Freeman [32] ; Wennerstrom [93]) suggests that shock-vortex interaction near the rotor tip can generate sufficient blockage to create aerodynamic sealing of the tip region. This sealing can yield improved efficiency and pressure rise capability of the compressor, but it may also block more of the flow area than is desired. Any reduction in flow area alters the throughflow of the compressor, resulting in reduced mass flow at stall and choke and in some instances a slightly reduced pressure ratio. Through proper design, the tip region interactions can be tailored to achieve beneficial aerodynamic sealing without adversely affecting the compressor flow area, resulting in performance improvement.

3.2 ADLARF Flowfield.

Designing the necessary interactions requires analysis of the tip region flowfield. Referring to Figures 15 and 16 for the ADLARF rotor, the size of the blockage cell at the rotor trailing edge appears to be larger than would seem practical to seal the tip region. The vortex expands radially

and pitchwise with axial coordinate to engulf the outer 20 percent of span at the trailing edge. This blockage creates the undesirable effect of reducing the flow area. A mechanism that allows manipulation of the blockage to seal the tip region yet increases the passage flow area is needed. A stepped tip gap provides this mechanism.

3.3 Hypothesis - Flowfield Manipulation

Since the tip leakage vortex impacts the adjacent blade pressure surface (Cybyk et al. [24] ; Suder and Celestina [86]), a larger tip gap near the point of impact can alter the path and extent of the blockage. Opening the channel creates a path of lesser resistance for the flow by providing more throughflow area to relieve the blockage. As the flow is drawn into the increased area, it entrains the vortex blocking the flow[2]. Since the fluid in the outer fringe of the blockage is accelerating as a result of entrainment, the extent of the blockage normal to the flow is lessened, and the zone of acceleration results in the blockage being swept with the flow. The low-velocity blockage entrained by the flow thereby elongates the vortex and draws the vortex closer to the annulus casing. The primary flow going through the increased clearance will thus include the low-energy fluid of the blockage. Once the flow enters the tip gap, interaction with the viscous boundary layer will help dissipate the strength of the vortex to form a medium-energy ring of air that encompasses the outer casing near the rotor trailing edge. Despite increased flow through the gap, the passage blockage will be smaller in radial extent thereby creating a larger flow area for the compressor. Thus, the blockage in the tip region is rearranged to provide a more open passage for the main flow which yields improved overall performance.

---

[2]Entrainment of the blockage results from the viscous interaction of two fluids at different velocities (White [98]). A free shear layer exists in the region between these two flow velocities, and in this region, some of the low-velocity fluid accelerates to merge with the higher speed main flow. The intensity of free shear interaction is a function of the fluid viscosity and the velocity defect between the main flow and the blockage.

A larger tip gap near the trailing edge of the rotor may also help to dissipate the blockage immediately aft of the leading edge shock by providing a reduced adverse pressure gradient in the tip region. A vortex expands in an adverse pressure gradient; this is particularly true when a tip leakage vortex passes through the extreme pressure gradient of the leading edge shock (Puterbaugh [71]). An increased tip clearance near the rotor trailing edge reduces the adverse pressure gradient in the tip region thereby inhibiting growth of the post-shock vortex. The decreased pressure gradient also causes the flow to accelerate axially near the rotor casing. This increased axial velocity will entrain the low-velocity vortex. This mechanism helps to attenuate the blockage along the length of the rotor, creating a larger passage flow area.

The placement and size of the stepped tip gap is crucial. It is desirable to reduce the extent of the blockage without excessive mass leakage through the increased clearance. With a modification of the casing in the region where the vortex impacts the trailing edge of the adjacent blade (Figure 20), the desired effect of entraining the blockage into the gap to create an aerodynamic seal can be achieved. For the rotor used in these experiments, at peak efficiency operation, the vortex center impacts the adjacent blade at approximately 90% axial chord (Figure 11), and for near-stall operation, the impact zone on the pressure surface of the adjacent blade is centered approximately at 70% axial chord (Figure 13). To ensure these zones were encompassed, initial tests had stepped tip gaps starting in the region of 80% and 60% axial chord.
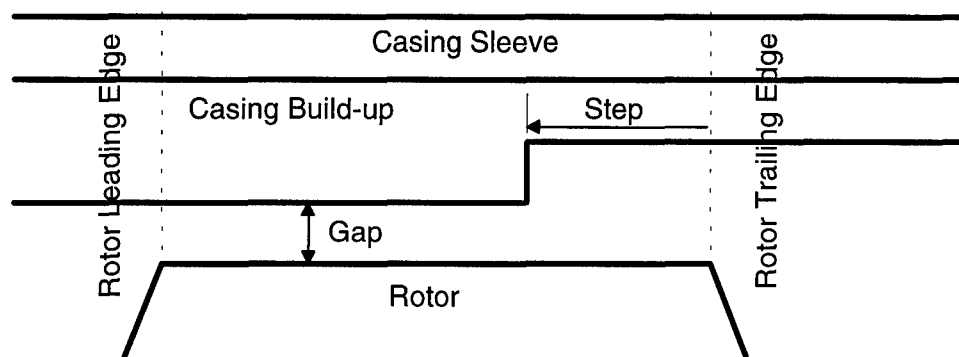
Figure 20. Stepped Tip Gap Profile

The size of the increased gap must also be considered; the depth of the step should be no larger than necessary to generate the entrainment. Lacking sufficient data dealing with the entrainment of complex geometric flows, the author arbitrarily chose to constrain the size of the increased clearance to a value no greater than twice the nominal tip clearance. The nominal tip clearance was limited to the range of values in which the phenomena associated with aerodynamic sealing had already been demonstrated or numerically predicted (see Sections 2.3.1 and 2.4). The upper limit of running tip clearance for which pressure ratio improvement was noted was 1.2% tip chord (referring to Freeman in Table 1); the lower limit of clearance for which efficiency improvement was calculated was 0.25% tip chord (referring to Adamczyk et al. in Table 1). These gaps may be practicably achievable in modern transonic compressors that have greater tip chords than the rotors of previous tests; the tip chord on the ADLARF rotor is approximately 208mm. Desiring to make the clearance increments as small as possible, the author chose to use running tip clearances within the range of 0.25% to 1.2% tip chord. Therefore, the initial tests of the ADLARF rotor had nominal running tip clearances ranging from 0.66mm (0.32% tip chord) to 2.08mm (1.0% tip chord).

3.4 Summary

In this chapter, the theory of blockage relocation to achieve aerodynamic sealing of the AD-LARF rotor was presented. Stepped tip gaps were introduced as a simple means to accomplish this relocation. The details of the experiment which tested the author's hypothesis of aerodynamic sealing and blockage relocation are presented in the next chapter.

EQUIPMENT, PROCEDURES, AND MODELS

Chapter 4 - Experimental Test Facility and Data Acquisition

This series of tests was conducted in the Wright Laboratories Compressor Research Facility described by Reitz [76] and an informational pamphlet [1] . This highly-automated facility is capable of mapping the performance parameters of a full-scale transonic compressor throughout its operating regime and will accommodate hardware to extract specific flowfield measurements during a test. Details relating exclusively to this series of tests are described in the following sections.

4.1 Compressor and First-Stage Rotor

The research facility was configured to test an unswept transonic two-stage axial-flow research compressor described by Russler et al. [79] . The first stage rotor (Figure 21), with key parameters listed in Table 2, was tested without inlet guide vanes. The outer casing (Figure 22) was removed, modified, and replaced after each run without disturbing the rotor.

Table 2. Rotor Geometry

Parameter	Value
Number of Blades	16
Rotor Tip Radius (cm)	35.24
Blade Tip True Chord (cm)	20.79
Blade Tip Axial Chord (cm)	10.56
Hub-to-tip Ratio at Leading Edge	0.33
Hub-to-tip Ratio at Trailing Edge	0.62
Tip Solidity (true chord / pitch)	1.50
Design Rotational Speed (RPM)	13288
Design Mass Flow [100% RPM, STP] (kg/sec)	71.66
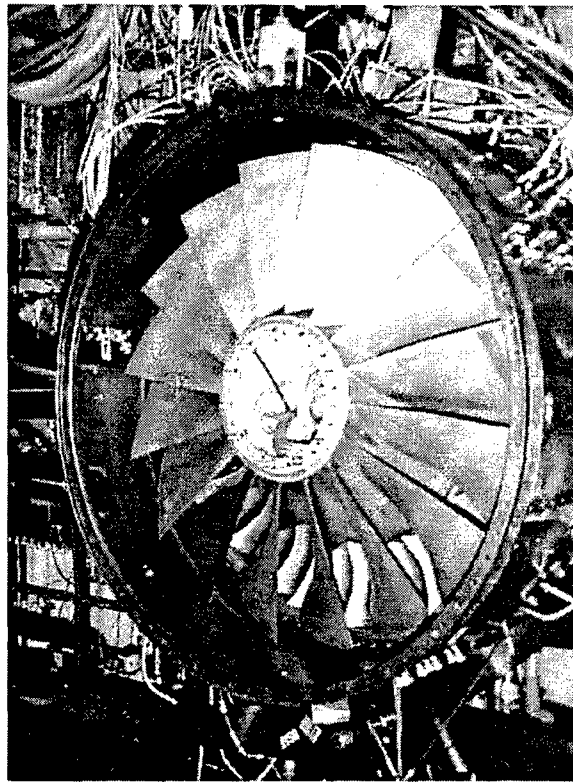
Figure 21. ADLARF Transonic First Stage Rotor
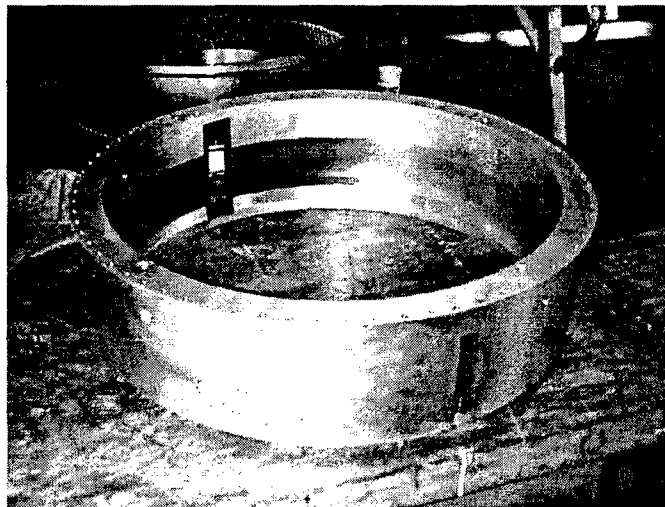
Figure 22. First Stage Rotor Casing

4.2 Casing Configurations

Nine casing configurations comprised of three step profiles at each of three clearance levels were tested in this series. The rotor annulus casing was machined to provide the sequence of geometries shown in Figure 23. The clearance levels were designed to encompass the zones that previous research (Wennerstrom [93] ; Freeman [32] ; Copenhaver et al. [19]) had indicated for an optimum tip clearance. The depth of each step corresponded to the subsequent desired clearance level. Locating the steps at 58% and 86% axial chord eased integration with hardware constraints of the research facility.

4.3 Instrumentation

A rotor's performance is usually measured in terms of its pressure ratio, efficiency, and mass flow. To understand performance changes, the associated flowfield must be discerned, but flowfield measurements must not disrupt the flow. Key aspects of the flowfield often can be identified with static pressure measurements along the rotor casing and with nonintrusive laser-probing of the interior flowfield. Likewise, the stalling characteristics of a rotor are usually determined by nonintrusive measurement of the rotating pressure waves associated with stall. Since rotor tip clearance influences performance, flowfield, and stalling features, the tip gap size must also be quantifiable for the various operating conditions and casing configurations. To attain these quantities, the following instrumentation was used.

4.3.1 Performance Measures

Performance quantities were derived from total pressure and total temperature measurements upstream of the rotor leading edge and downstream of the trailing edge. The upstream total temperature was the average from 49 thermocouples located in the airflow stilling chamber. Two radial rakes of 5 total pressure probes each mounted in the compressor's straight inlet duct provided the average

48

RUNNING TIP CLEARANCES

Axial Tip Chord: -12% 0% 58% 86% 100% 108%

Case A - Baseline
Small gap (0.66mm, 0.318% tip chord)
No steps
0.61mm
0.28mm 0.51mm 0.66mm
Rotor

Case B
Small gap (0.66mm, 0.318% tip chord)
Aft step of 0.53mm (0.256% tip chord) at 86% axial chord
0.61mm
1.14mm
0.28mm 0.51mm 1.19mm
Rotor

Case C
Small gap (0.66mm, 0.318% tip chord)
Forward step of 0.53mm (0.256% tip chord) at 58% axial chord
0.51mm 1.14mm
0.28mm 1.04mm 1.19mm
Rotor

Case D
Medium gap (1.19mm, 0.574% tip chord)
No steps
1.14mm
0.53mm 1.19mm
0.81mm 1.04mm
Rotor

Case E
Medium gap (1.19mm, 0.574% tip chord)
Aft step of 0.89mm (0.428% tip chord) at 86% axial chord
1.04mm 2.03mm
0.53mm 2.08mm
0.81mm 1.14mm
Rotor

Case F
Medium gap (1.19mm, 0.574% tip chord)
Forward step of 0.89mm (0.428% tip chord) at 58% axial chord
1.04mm 2.03mm
0.53mm 2.08mm
0.81mm 1.93mm
Rotor

Case G
Large gap (2.08mm, 1.002% tip chord)
No steps
1.93mm
2.08mm
1.42mm
1.70mm 2.03mm
Rotor

Case H
Large gap (2.08mm, 1.002% tip chord)
Aft step of 0.59mm (0.281% tip chord) at 86% axial chord
1.93mm 2.62mm
1.42mm 2.67mm
1.70mm 2.03mm
Rotor

Case I
Large gap (2.08mm, 1.002% tip chord)
Aft step of 1.73mm (0.831% tip chord) at 86% axial chord
1.93mm 3.76mm
1.42mm 3.81mm
1.70mm 2.03mm
Rotor
LE TE

CASING LEADING EDGE

Notes: 1. All running clearances are for 100% design speed.
2. Clearances increase approximately linearly at 0.03mm per 5% decrease in rotor speed in the range from 100% to 85% RPM.

Figure 23. Rotor Casing Geometry

49

total pressure of the upstream air. To measure the downstream variables, sensors were mounted on the leading edges of three first-stage stator vanes positioned approximately 120 degrees apart; each vane had pairs of collocated total pressure and temperature sensors spanning seven radial positions extending over the range from 10% to 94% span. The sensors were aligned with the stator vane leading edge angle, which followed a predefined schedule as a function of rotor speed. This same schedule was used for each test. Static pressure sensors in the inlet bellmouth provided the input for mass flow computation; consistency was verified by a comparison of the calculated bellmouth mass flow with the mass flow derived from the inlet pressure rakes and the downstream venturi. The mass flows presented in the figures included in this dissertation were corrected for temperature and pressure (see Appendix A). Mass flow through the compressor was controlled with a discharge throttling valve set by the facility operator.

Calibration of the instruments in the performance data collection system was accomplished prior to the first test. To maintain consistency, calibration was not performed between tests; however, a validity check (a tolerated comparison to a calibration input) of each data collection channel was accomplished prior to and after each subsequent test. A data channel found to be outside of designated tolerance was flagged for removal during data averaging.

4.3.2 Casing Pressure Measurement

Differential static pressure measurements at the casing were made with a linear array of 16 Kulite brand high-response pressure transducers mounted in a specially designed block that extended axially beyond the leading and trailing edges of the rotor. The block, segmented at the 58% and 86% rotor axial chord planes (Figure 24), was mounted in a slot in the casing; each segment was adjusted with shims to ensure the faces were flush with the casing inner surface and matched any steps. Each of the transducers was capable of measuring pressure fluctuation frequencies up to 100 kHz. The

50

calibration and operation of the transducers is described by Russler [78] and Russler et al. [79] .

These nonintrusive measurements yielded the static pressure distribution of the blade passages near

the rotor tip.
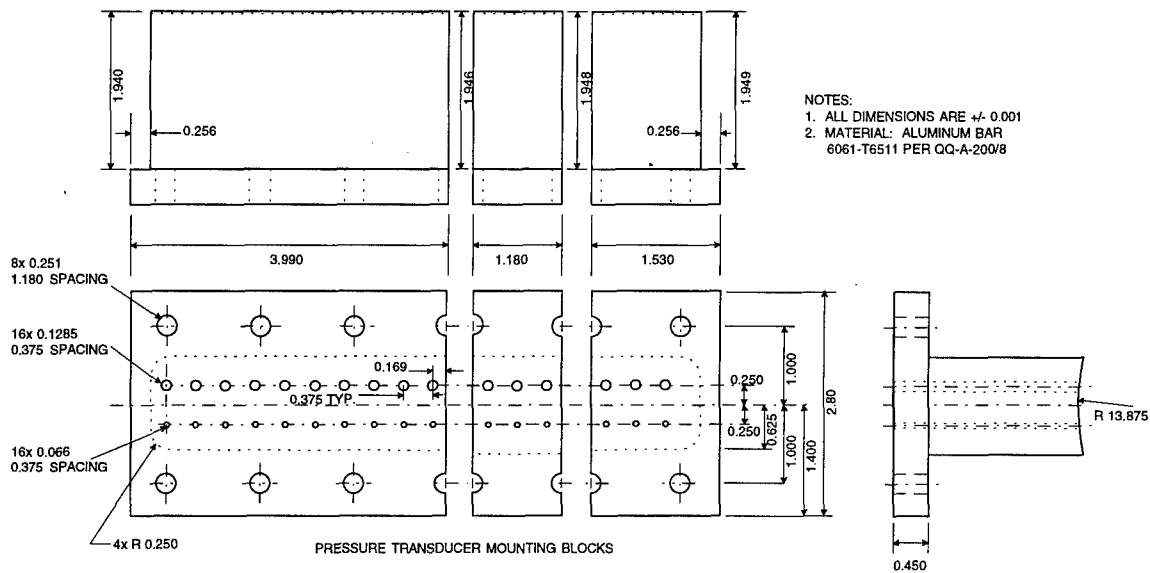
Figure 24. Pressure Transducer Mounting Block

4.3.3 Velocity Measurement

Nonintrusive measurements were also made to discern the velocity patterns in the tip region

of each flow passage at various spanwise locations. A laser velocimetry probe measured flow

velocities through a transparent window in the casing. Like the pressure transducer block, the laser

window frame was designed and segmented to match the inner contour of the casing as closely

as possible including any stepped tip gaps (Figure 25). Mounted within this frame were three flat

12.7mm thick plates of fused silica. The frame also incorporated a series of holes along the side

of the silica from front to rear; distilled water was injected through these holes to wash the laser

window whenever a drop in data acquisition rate was observed.

51

NEW LASER WINDOW

0.256

7.687

NOTES:
1. Aft windows are comprised of inner and outer shells of aluminum casing salvaged from old window.
2. All salvaged pieces must be cut so that final milled surfaces align with mounting centerholes at the specified dimensions ±0.001 inches.
3. Mounting hole diameters are 0.251 ±0.004 inches

0.770   1.180
          typical

FRONT

0.251±0.004 DIAM

0.251±0.004 DIAM
OLD HOLES FROM
SALVAGE

Salvaged Metal Block   Salvaged Window   Salvaged   Salvaged Window/
                                                Window   Metal Block

REAR

3.118   3.750

2.360

3.130   2.360   1.180   1.530

8.200

0.491

Figure 25. Laser Window with Stepped Gap Capabilities

The laser system, described by Cybyk et al. [24] and Russler et al. [79], was comprised of four beams configured to discern axial and tangential velocities. Central to this system was a five watt argon ion laser that generated two blue (488nm wavelength) and two green (514nm wavelength) light beams. The beams were passed through a 150m long fiber optic bundle to the optical head which transmitted the beams at set angles through the laser window. The optical head also served as the receiver for on-axis backscatter light detection; the returning detected light signals also were routed through the fiber optic bundle to the data acquistion equipment. The optical head was mounted in an angular rotator affixed to a three-axis traversing table in the test chamber. Positioning accuracy

of the traversing table was 0.025mm in each of three directions, and the angular rotator had an accuracy of 0.01 degrees. Characteristics of the laser system are summarized in Table 3.

Table 3. Laser System Properties

Parameter	Blue Beams	Green Beams
Light Wavelength (nm)	488	514
Average Power (watts)	0.16	0.30
Beam Crossing Angle (degrees)	3.9	3.9
Fringe Spacing (μm)	3.53	3.72
Volume Diameter (μm)	117.2	117.2
Probe Volume Length (mm)	1.7	1.7
Light Collection Angle (degrees)	8.2	8.2
Fringe Shift Range (MHz)	40-100	40-100

Calibration of the laser system was accomplished before the first test, and this calibration was maintained throughout the testing series. Also, prior to each test, laser beam alignment was checked and repositioned as necessary. The blue beam was inoperative for this series of tests; therefore, the green beam was used to acquire both the axial and tangential components of velocity. This acquisition process required the optical head to be rotated 90 degrees between measurements at each steady-state operating condition. Seeding the flow with trace particles of atomized glycerin (0.8μm mean diameter) was accomplished with a Laskin particle generator (Rabe and Sabroske [74]) in the airflow stilling chamber located 7.5m upstream of the compressor inlet. These particles provided the reflective means for achieving the Doppler effect essential to the laser velocimetry process. The accuracy of the laser system is summarized in Table 4.

Table 4. Laser System Accuracy

Parameter	Accuracy
Absolute Velocity (percent)	1.5
Absolute Flow Angle (degrees)	1.25
Axial Resolution (percent axial chord)	3.0
Circumferential Resolution (percent pitch)	3.3

4.3.4 Stall Precursor Measurement

Stall precursor signals were measured with 8 Kulite brand high-response pressure transducers located at 45 degree increments along the circumference of the rotor casing at the rotor leading edge. The sensors, capable of measuring differential pressures up to 100kPa with an accuracy of 0.31kPa in the frequency range from 0 to 100 kHz, measured static pressure through 0.4mm taps in the outer case. These sensors measured the time-variant magnitude and frequencies of pressure signals associated with the onset of rotating stall and surge.

4.3.5 Clearance Measurement

The nonrotating tip clearances were verified before each run using gauged shims. Also, during each test, electrical capacitance proximity probes measured the running tip clearances near the leading and trailing edges of the rotor. The compiled tip gap data for the test series is shown in Figure 23.

4.4 Data Collection and Analysis

Data collection and analysis were performed at the Wright Laboratories Compressor Research Facility (CRF) and the Air Force Institute of Technology (AFIT).

4.4.1 Performance Data

Collection and preliminary processing of performance data was accomplished using custom written Test Article Data Analysis software on the CRF's VS4 computer. The processes for calculating mass flow and efficiency are shown in Appendix A. Several utility programs were developed

54

to extract processed information from the VS4's uniquely complex database structure. The resulting sets of data were stored in ASCII standard format on standard media for subsequent analysis on AFIT computer systems.

The uncertainty of the CRF performance data collection system was unknown prior to this series of tests; therefore, extensive analysis of its inherent errors was required. In accordance with the Air Force standard handbook for uncertainty analysis of gas turbine engines (Abernethy and Thompson [3]), the author developed the methods and software necessary to evaluate the measurement errors and propagation of those errors during analysis. The necessary changes, consuming almost two thousand man-hours from Battelle Memorial Institute software programmers and the author, required eight months to implement.

Sample calculations for the uncertainty analysis of the CRF performance data system are seen in Appendix B. The uncertainty of the performance data is shown in Table 5. Data are presented for only the 100 percent design rotor speed at peak efficiency mass flow for each casing configuration; the uncertainty for slower rotor speeds are less than those shown here.

Table 5. Uncertainty of ADLARF First-Stage Rotor Performance

Casing Configuration	Mass Flow Rate kg/sec	Pressure Ratio	Efficiency
A	0.277	0.002	0.009
B	0.302	0.002	0.007
C	0.306	0.002	0.006
D	0.344	0.002	0.008
E	0.279	0.002	0.006
F	0.292	0.002	0.007
G	0.278	0.002	0.006
H	0.310	0.002	0.006
I	0.361	0.002	0.008

The repeatability of test results were also verified. Prior to each test, the rotor was operated at idle speed for a minimum of thirty minutes. This warm-up period allowed the rig and measurement

instruments to reach a consistent steady-state operating condition. Each test then began with a steady-state data check at 90 percent design rotor speed and mass flow for peak efficiency; this check was also repeated as the last action of each test to verify consistency of the CRF data system for that test. Moreover, a consistent sequence and pacing of changes to the operating conditions of the rotor were maintained throughout the testing series. Furthermore, the baseline casing configuration (small gap, no step) was tested as the first and last test in the series. These efforts verified the highly repeatable nature of the CRF system and this test series.

4.4.2 Casing Pressure Data

Acquisition and preliminary processing of rotor tip region pressure data were accomplished using the CRF's ADA computer. The static pressure sensors were calibrated before each test, and the calibration constants were stored for subsequent processing. Each of the 16 signals was amplified to maximize the 5.0 volt sampling capability of the digitizing equipment, and each signal was low-pass filtered at 30 kHz using an eight–pole Butterworth analog filter to eliminate aliasing during the digitizing process. Each gained and filtered signal was sampled at 7500 samples-per-second in real time during compressor steady-state operation, and this information was stored in raw binary format. The database was analyzed using CRF custom software to produce a binary database of two-dimensional pressure distributions created by time-averaging the signal from each transducer for each independent passage. This database was converted into standard ASCII format for further processing on AFIT computers.

4.4.3 Velocity Data

Velocity information for each test was collected using the laser velocimeter during compressor steady-state operation, and this data was stored in raw binary format. Preliminary processing of laser flowfield data was accomplished on the CRF's DVL computer. During processing, the data

from the 16 separate blade passages were ensemble-averaged to create a three-dimensional velocity distribution of a single representative passage. The database for each test was stored in ASCII standard format for additional processing on AFIT computers.

4.4.4 Stall Precursor Data

The fluctuating voltage signals produced by the stall precursor sensors were simultaneously recorded on analog tape. The signals were amplified during playback to maximize the 5.0 volt sampling capability of the digitizing equipment, and each signal was low-pass filtered at 800 Hz using an eight–pole Butterworth analog filter to eliminate aliasing during the digitizing process. Each amplified and filtered analog signal was sampled at 2500 samples-per-second using an analog-to-digital converter with an accuracy of 0.0025 volts; this sample rate was chosen to satisfy the Nyquist criteria (Newland [68]) of using a sampling rate of at least twice the maximum expected frequency of a signal. The digital data was stored in binary form on the CRF's ADA computer, and it was subsequently converted to ASCII standard format. Software created by the author was used for subsequent signal processing.

4.5 Summary

In this chapter, the equipment used in the experimental portion of this dissertation was described. Also, the processes used for data acquisition and analysis were discussed. The data collected from the test series comprised the experimental aspect of this research. Theoretical modeling of tip gap effects on rotor performance and flowfield also was accomplished using Computational Fluid Dynamics; details of the computational analysis are presented in the next chapter.

Chapter 5 - Computational Fluid Dynamic Modeling

Computational modeling of the flow processes occurring within the ADLARF transonic rotor was accomplished at NASA Lewis Research Center to augment the experimentally acquired data. This modeling allowed analysis of an interior flowfield that was difficult or impossible to experimentally measure with nonintrusive instruments. The model used here was a simplified implementation of the fully compressible three-dimensional Favre-Averaged Navier-Stokes equations (FANS).

5.1 Requirements

For a flowfield model to be useful, it should accurately describe the real effects of the elements within the flow. Consequently, the complexity of the flowfield and its operating parameters dictate the complexity of the model. Theoretical models are produced by applying the laws of conservation of mass, momentum, and energy to a particular environment. Some insight into the nature of the flow is necessary to include relations that model particular effects. For this study of the flow within a transonic compressor, the following criteria were considered:

1. *Three-Dimensional Geometry.* Flows within transonic turbomachinery are inherently three-dimensional. Although many flows can be described by quasi-one-dimensional equations, capturing the spatial effects of complex flow geometries and interactions near the rotor tip requires three-dimensional spatial models.

2. *Compressibility Effects.* Transonic compressors have shocks which must be modeled with compressible flow theory. This theory requires the physical laws to be expressed in conservation form to accurately model density variations.

3. *Viscous Effects.* Boundary layers, wakes, flow entrainment, and dissipation require modeling the viscous behavior of fluids. Many analyses treat a flowfield as two independent flows; the main passage flow is assumed inviscid, and the boundary layer flow is assumed viscous. Such analyses also require the flow to be matched at the interface boundaries which may be extremely difficult for three-dimensional flows. Treating the entire flowfield as a viscid medium gives a more realistic model of the flowfield, and it avoids the matching problems associated with viscid-inviscid models. Therefore, viscous effects are modeled throughout the flowfield for this study.

4. *Turbulence.* High Reynolds Number flows associated with transonic compressors are

58

inherently turbulent; therefore, turbulent effects are necessary for accurate modeling.

5. *Robustness.* A good model is equally applicable to the entire domain of operating conditions, and it can handle various boundary conditions. Robustness is needed for comparative analyses of various casing geometries.

The author chose to use a model developed by Hah [37] . This model satisfied the requirements listed above, and during previous tests (Cybyk et al. [24] ; Russler et al. [79] ; Hah et al. [39]), it had demonstrated success in qualifying the flowfield of the ADLARF rotor. The details of this model are described below.

5.2 Governing Equations

The following partial differential equations mathematically model the flow within a transonic compressor. Each equation represents the conservation of an intrinsic transport property (mass, momentum, energy) with Reynold's mass-weighted time-averaging (Anderson et al. [6] ; Wilcox [99]) applied to account for turbulent fluctuation of the flow variables. As a group, these equations are known as the Favre-Averaged Navier-Stokes equations applicable to unsteady compressible viscous turbulent flows. Their derivation is detailed by Anderson et al. [6] . The equations are expressed in differential conservation-law form using Einstein indicial notation (Cartesian summation convention described by Aris [9]).

5.2.1 Conservation of Mass

$$\frac{\partial}{\partial t}(\overline{\rho}) + \frac{\partial}{\partial x_i}(\overline{\rho}\widetilde{u}_i) = 0 \tag{7}$$

5.2.2 Conservation of Momentum

Newton's second law applied to a rotating control volume takes the form

$$\frac{\partial}{\partial t}(\overline{\rho}\widetilde{u}_i) + \frac{\partial}{\partial x_j}(\overline{\rho}\widetilde{u}_i\widetilde{u}_j) + 2\overline{\rho}\varepsilon_{ijk}\Omega_j\widetilde{u}_k = -\frac{\partial \overline{P}}{\partial x_i} + \frac{\partial}{\partial x_j}\left[\mu\overline{\tau}_{ij} - \overline{\rho u_i'' u_j''}\right] + F_i \tag{8}$$

59

The first term in Equation 8 represents the time-varying mean component of momentum. The second term represents the change in momentum of fluid convected through a differential control volume. The third term accounts for the body force due to Coriolis acceleration of a rotating reference frame (White [97]). The fourth term represents the change in momentum due to pressure forces acting normal to the control volume surfaces. The fifth term accounts for the change in momentum due to viscous laminar and turbulent shear forces acting tangential to the control volume surfaces. The last term accounts for all other body forces imposed on the flow including radial acceleration forces of the control volume.

By employing the Boussinesq approximation in which the turbulent shear stress is represented as the product of the turbulent viscosity and the mean viscous stress tensor,

$$-\overline{\rho u_i'' u_j''} = \mu_T \overline{\tau}_{ij} \tag{9}$$

Equation 8 becomes

$$\frac{\partial}{\partial t}\left(\overline{\rho}\widetilde{u}_i\right) + \frac{\partial}{\partial x_j}\left(\overline{\rho}\widetilde{u}_i\widetilde{u}_j\right) + 2\overline{\rho}\varepsilon_{ijk}\Omega_j\widetilde{u}_k = -\frac{\partial \overline{P}}{\partial x_i} + \frac{\partial}{\partial x_j}\left[\mu_{eff}\overline{\tau}_{ij}\right] + F_i \tag{10}$$

where the effective viscosity is the sum of the laminar and turbulent (eddy) viscosities

$$\mu_{eff} = \mu + \mu_T \tag{11}$$

and the mean viscous stress tensor is given by

$$\overline{\tau}_{ij} = \frac{\partial \widetilde{u}_i}{\partial x_j} + \frac{\partial \widetilde{u}_i}{\partial x_i} - \frac{2}{3}\frac{\partial \widetilde{u}_k}{\partial x_k}\delta_{ij} \tag{12}$$

5.2.3 Conservation of Energy

For an adiabatic differential control volume, the energy balance using the Boussinesq approximation is

$$\frac{\partial}{\partial t}\left(\overline{\rho}\widetilde{e}_t\right) + \frac{\partial}{\partial x_j}\left(\overline{\rho}\widetilde{u}_j\widetilde{e}_t\right) = \frac{\partial}{\partial x_j}\left[k_{eff}\frac{\partial \widetilde{T}}{\partial x_j}\right] - \frac{\partial}{\partial x_j}\left(\overline{P}\widetilde{u}_j\right) + \widetilde{u}_iF_i + \frac{\partial}{\partial x_j}\left[\widetilde{u}_i\mu_{eff}\overline{\tau}_{ij}\right] \tag{13}$$

where the total internal energy per unit mass (i.e., specific total internal energy) includes specific

internal energy and kinetic energy (potential energy is neglected)

$$\widetilde{e}_t = \widetilde{e} + \frac{1}{2}\widetilde{u}_i\widetilde{u}_i \tag{14}$$

and the effective coefficient of thermal conductivity is

$$k_{eff} = k + k_T \tag{15}$$

5.2.4 Transport Properties

The coefficient of viscosity, μ, is related to static temperature via the kinetic theory of gases;

Sutherland's approximation (Anderson et al. [6]) for viscosity is

$$\mu = S_1\frac{T^{\frac{3}{2}}}{T + S_2} \tag{16}$$

where S_1 and S_2 are constants for a given gas. For air, $S_1 = 1.458 \times 10^{-6}\text{kg/(m-sec}\sqrt{\text{K}})$ and

$S_2 = 110.4\text{K}$.

Using the definition of the Prandtl Number (the dimensionless ratio of momentum to thermal

diffusion)

$$\text{Pr} \equiv \frac{\mu C_p}{k} \tag{17}$$

the coefficient of thermal conductivity of the fluid is expressed as a function of viscosity:

$$k = \frac{C_p\mu}{\text{Pr}} \tag{18}$$

Extending Equation 18 to apply to turbulent thermal conductivity and assuming a calorically perfect

gas (i.e., C_p = constant), Equation 15 is expressed in terms of laminar and turbulent viscosities:

$$k_{eff} = C_p\left[\left(\frac{\mu}{\text{Pr}}\right) + \left(\frac{\mu_T}{\text{Pr}_T}\right)\right] \tag{19}$$

Additionally, experimental studies (White [98]) have shown that the laminar and turbulent Prandtl

Numbers, Pr and Pr_T respectively, are approximately constant for most gases; therefore, for air, it is

customary to assume $\text{Pr} \approx 0.7$ and $\text{Pr}_T \approx 0.9$. The turbulent viscosity, μ_T, which includes the net

effects of turbulence, is a much more difficult transport property to quantify, and its semi-empirical model will be addressed in Section 5.3 dealing with turbulence modeling.

5.2.5 Perfect Gas State Equation

The use of the transport property relations, Equations 16 and 19, in association with the governing laws, Equations 7, 10, and 13, yields five scalar equations (one continuity, three momentum, and one energy) with seven unknown quantities ($\overline{\rho}$, $\overline{P}$, $\widetilde{e}$, $\widetilde{T}$, and three velocity components). Four of these quantities, $\overline{\rho}$, $\overline{P}$, $\widetilde{e}$, and $\widetilde{T}$, are thermodynamic variables representing the state of the gas. However, according to the state postulate of thermodynamics (Reynolds [77]), the local thermodynamic state for the compression process (one reversible work mode) is fixed by any two independent thermodynamic variables. Therefore, two of the unknown thermodynamic variables are expressed in terms of the other two unknowns using the perfect gas equation of state

$$P = \rho R T \tag{20}$$

and the additional perfect gas definitions:

$$e = C_v T \qquad h = C_p T \qquad \gamma = \frac{C_p}{C_v} \qquad C_v = \frac{R}{\gamma - 1} \qquad C_p = \frac{\gamma R}{\gamma - 1} \tag{21}$$

Therefore, for a perfect gas, static pressure and static temperature are expressed in terms of static density and specific internal energy:

$$\overline{P} = (\gamma - 1)\,\overline{\rho}\widetilde{e} \tag{22}$$

$$\widetilde{T} = \frac{(\gamma - 1)\,\widetilde{e}}{R} \tag{23}$$

For air, the ratio of specific heats is $\gamma_{air} = 1.4$, and the specific gas constant is $R_{air} = 287\text{J/kg-K}$.

5.3 Turbulence Modeling

The governing equations were developed from the conservation laws of mass, momentum, and energy, and they permit simplified turbulence modeling with the introduction of turbulent viscosity and turbulent thermal conductivity. However, these turbulent quantities are semi-empirical and can

be modeled with various levels of complexity and associated accuracy. Accurate modeling requires examination of the factors which affect turbulence. As seen in Equation 8, the turbulent shear stress, $-\overline{\rho u_i'' u_j''}$, is proportional to the kinetic energy of turbulent fluctuations; therefore, kinetic energy is the focal point for essentially every turbulence model. A theoretical turbulent kinetic energy (TKE) equation, representing the transport of kinetic energy through a control volume, can be derived from the momentum equation (White [98]). However, White states that the terms in this equation are so complex that they cannot be computed from first principles. Simplified modeling is required for each of the terms in the theoretical TKE equation. Consequently, modeling turbulent kinetic energy is a semi-empirical process, and numerous forms of the TKE equation (Anderson et al. [6] ; White [98] ; Wilcox [99]) exist. Furthermore, the one-equation TKE model for turbulence has been fraught with disappointing results.

The turbulent modeling process can be improved by coupling a semi-empirical TKE equation with a second equation. The dissipation of turbulent energy is particularly important to any TKE model; therefore, an equation modeling this dissipation is often paired with the TKE to produce the $K - \varepsilon$ turbulence model. The $K - \varepsilon$ model used in this analysis is an extension of Chien's [16] model incorporating low Reynold's Number effects.

5.3.1 Turbulent Kinetic Energy

The turbulent kinetic energy, K, is found from the following PDE.

$$\frac{\partial}{\partial t}\left(\overline{\rho}\overline{K}\right) + \frac{\partial}{\partial x_i}\left(\overline{\rho}\widetilde{u}_i\overline{K}\right) = \frac{\partial}{\partial x_i}\left(\frac{\mu_{eff}}{\sigma_k}\frac{\partial \overline{K}}{\partial x_i}\right) - \overline{\rho u_i'' u_j''}\widetilde{u}_{i,j} - \overline{\rho}\widetilde{\varepsilon} - \frac{2\mu \overline{K}}{l^2} \tag{24}$$

5.3.2 Energy Dissipation

Turbulent energy dissipation, ε, is modeled using the following relation.

$$\frac{\partial}{\partial t}\left(\overline{\rho}\widetilde{\varepsilon}\right) + \frac{\partial}{\partial x_i}\left(\overline{\rho}\widetilde{u}_i\widetilde{\varepsilon}\right) = \frac{\partial}{\partial x_i}\left(\frac{\mu_{eff}}{\sigma_\varepsilon}\frac{\partial \widetilde{\varepsilon}}{\partial x_i}\right) + c_1\frac{\rho\widetilde{\varepsilon}}{\overline{K}}\left(\overline{u_i'' u_j''}\widetilde{u}_{i,j}\right) - \frac{\rho\widetilde{\varepsilon}}{\overline{K}}\left(c_2 f\widetilde{\varepsilon} + \frac{2\nu\overline{K}\exp\left(-c_4 u^* l/\nu\right)}{l^2}\right)$$

$$\tag{25}$$

63

5.3.3 Turbulent Viscosity

The turbulent eddy viscosity for this model takes the form of

$$\mu_T = c_\mu \left(\frac{\overline{K}^2}{\widetilde{\varepsilon}} \right) (1 - \exp\left(-c_3 u^* l/\nu\right)) \tag{26}$$

5.3.4 Closure Coefficients

The turbulence model requires the following closure coefficients.

$$f = 1 - \frac{0.4}{1.8} \exp\left(-\left(\overline{K}^2/6\nu\widetilde{\varepsilon}\right)^2\right) \tag{27}$$

$$c_\mu = 0.09, \ c_1 = 1.35, \ c_2 = 1.8, \ \sigma_k = 1.0, \ \sigma_\varepsilon = 1.3, \ c_3 = 0.0115, \ c_4 = 0.5 \tag{28}$$

5.4 Finite Difference Approximations

The partial differential equations (PDEs) for the conservation laws and turbulence model are nonlinear; furthermore, the unsteady compressible Favre-Averaged Navier-Stokes equations (Equations 7, 10, and 13) are a mixed set of hyperbolic-parabolic equations. The steady-state form of the equations can be obtained by eliminating the time-dependent derivatives in Equations 7, 10, and 13. However, numerical solutions of the steady-state PDEs are difficult because the steady-state FANS equations are a mixed set of hyperbolic-elliptic equations which require different numerical solution techniques. The numerical solution of hyperbolic equations requires a marching technique within the cone of dependence whereas elliptic equations require relaxation techniques. This combination makes the solution to this equation set difficult because the numerical implementation must be a mixed marching and relaxation method. Such methods are time and memory intensive, and the large number of calculations can lead to a reduction of accuracy. Therefore, the unsteady form of the FANS equations are used to simplify the solution process.

A pseudo-time-dependent numerical approach is the standard method to obtain a steady-state solution to the compressible Navier-Stokes equations. The steady-state flow distribution is obtained by marching (iterating) the parabolic solution in time (or time-like coordinate) until convergence is

attained. Moreover, the approach is equally applicable to subsonic, supersonic, or mixed subsonic-supersonic flow. This approach requires the unsteady (long term transient) form of the original PDEs, Equations 7, 10, 13, 24, and 25, to be represented by finite difference equations.

For this study, a fully conservative control-volume approach was used to generate the finite difference equations. This approach assured that the discretized finite difference equation exactly satisfied the physical law represented by the original PDE. The finite difference equations were formulated in terms of the three Cartesian components of momentum ($\rho \widetilde{u}_i$), the specific total internal energy ($\widetilde{e}_t$), turbulent kinetic energy ($\overline{K}$), and energy dissipation rate ($\widetilde{\varepsilon}$). A third-order accurate interpolation scheme was used for the discretization of convection terms, and central difference relations were used for diffusion terms. The overall scheme was second-order accurate.

5.4.1 Numerical Scheme

Flow variables were solved in sequence according to the following process. The momentum fluxes through the control volume at a new pseudo-time increment were estimated with a semi-implicit quadratic upwind prediction method; these predictions, based on the previous time increment, determined the coefficients used in the subsequent correction process. The iteration produced an intermediate momentum distribution and an associated static pressure distribution. The intermediate solution did not satisfy global continuity since it was based on the static pressure distribution at the previous time step; therefore, corrective measures were required for the momentum distribution to satisfy global continuity. Pressure-implicit splitting, a two-step method that combines the momentum and continuity equations, was applied to correct the static pressure and momentum distributions. The combination of the continuity and momentum equations, Equations 7 and 10, produced a Poisson-like equation. An Alternating Direction Implicit (ADI) relaxation method (Anderson et al. [6]) was employed to solve each combined continuity-momentum equation in sequence.

During the first correction step, the convection terms were neglected, and intermediate static pressure and momentum distributions were obtained. During the second correction step, convection terms were included as the adjusted static pressure and momentum distributions were calculated from the intermediate distributions. The corrected static pressure and momentum flux distributions were used to calculate the density field. Also, the adjusted fluxes were used in ADI iteration to sequentially determine the total internal energy, turbulent kinetic energy, and energy dissipation of the flowfield. The residual errors of the resulting flow variables were integrated over the entire domain, and when the errors were reduced by four orders of magnitude from their initial values, the solution was considered converged. The state of the converged flowfield was saved in terms of five primary quantities: density, three Cartesian components of momentum, and total internal energy. Specific details of this numerical scheme are given by Hah [36] , Hah and Wennerstrom [37] , and Hah [38] .

5.4.2 Computational Grid

An I-grid was used to discretize the rotor flow passage. The grid consisted of 49 nodes in the pitchwise direction, 150 nodes in the streamwise direction, and up to 50 nodes in the spanwise direction. The blade, approximately centered in the grid, was represented by 6 pitchwise nodes, 96 streamwise nodes, and 35 spanwise nodes; the tip clearance accounted for the balance (5 to 15) of the spanwise grid points. The grid was devised to match the geometric variations of the experimental study. The general curvilinear computational grid was generated with an elliptic grid generation method, and good orthogonality was maintained across the computational domain.

5.4.3 Boundary Conditions

Dirichlet boundary conditions were specified for the domain. The distributions of total temperature, total pressure, and inlet flow angle were fixed at the inflow boundary. At the outflow boundary, coincident with the leading edge of the first stage stator, the static pressure at the rotor tip

was fixed at 189,500Pa, and all unknown variables were extrapolated. Radial equilibrium was not applied at the outflow boundary since it is not a valid condition for this flow. Experimental values of turbulent kinetic energy were used at the inflow boundary.

5.4.4 Implementation

. The numerical scheme with associated boundary conditions and grid was implemented by Dr. Chunill Hah on a CRAY-XMP computer at NASA Lewis Research Center. The author provided the geometric data and specified the operating conditions for each numerical simulation. Five solutions were obtained corresponding to cases A, D, E, F, and G in Figure 23, and each solution required one to two hours of computing time using a single processor. Subsequent processing of the solutions was accomplished by the author using NASA Flow Analysis Software Toolkit (FAST) (Walatka et al. [92]) and custom utility programs written by the author.

5.5 Summary

In this chapter, a theoretical model for the flow process within a transonic compressor was detailed. This model was based on the mass-weighted Reynold's Averaged Navier-Stokes Equations for turbulent compressible viscous flow. The numerical scheme used to implement this model was discussed. In the following chapters, the results of the experimental and numerical analyses are presented.

RESULTS

Chapter 6 - Performance Results

A variation of the tip clearance and the use of stepped tip gaps generated marked differences in rotor performance. Generally, while a variation of clearance levels produced large differences in performance, the inclusion of stepped tip gaps produced new performance improvements.

For each casing configuration, performance (pressure, temperature, and velocity) data were collected as the rotor was tested throughout the mass flow range at each of 100%, 95%, 90%, and 85% corrected design speeds (corrected for nonstandard inlet total temperature). This data was put into the form of a compressor map; these rotor maps are seen in Appendix C. From the rotor maps, data were extracted to make the comparisons shown in the following sections.

6.1 Effect of Tip Clearance on Rotor Performance

6.1.1 Effect of Tip Clearance on Stall Margin

To calculate the effects on stall margin, the stall line for each configuration was first determined from a least-squares linear-fit through the four stall conditions corresponding to each rotor speed (Figure 26 and Appendix C). From such a line, the stalling pressure ratio at any mass flow can be determined. The stall margin for each configuration was calculated as the ratio of the difference between the curve-fitted stall pressure ratio and pressure ratio at peak efficiency to the pressure ratio at peak efficiency.

The effect of clearance on stall margin can be seen in Figure 27. For 85% and 90% rotor speed, stall margin decreased with increased clearance; however, for 95% and 100% speed conditions, the medium tip clearance (no steps) produced the largest stall margin. These results suggest that the medium tip clearance is the best compromise of stall margin for a design in which operation at 100% rotor speed is important.
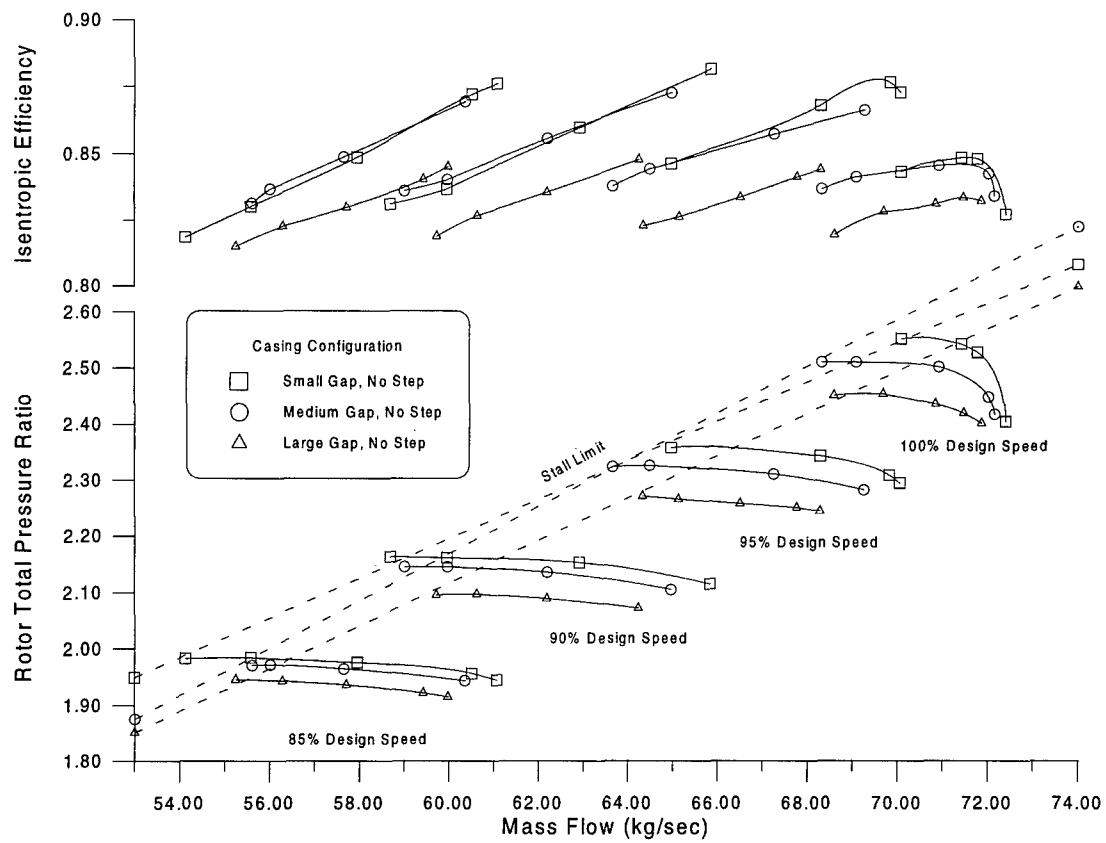
69

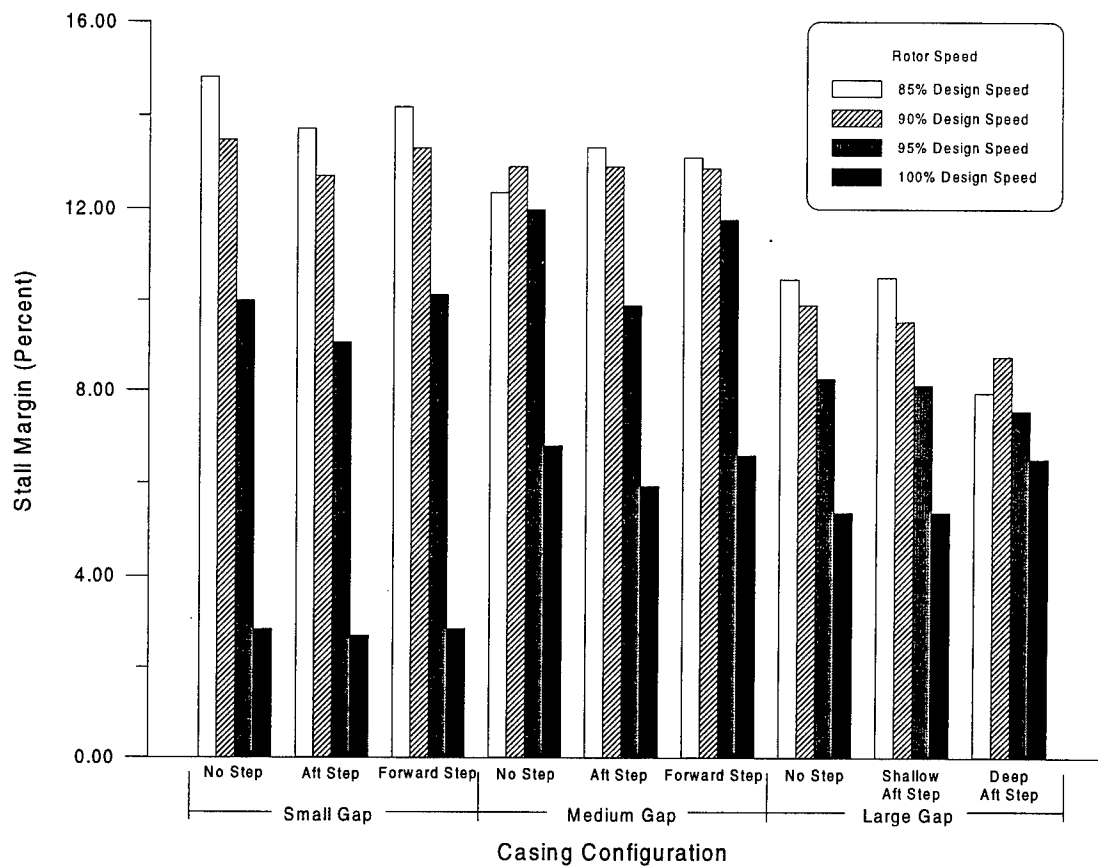Figure 26. Rotor Map of Clearance Level (No Steps) Configurations

Figure 27. Stall Margin for Casing Configurations and Speeds

6.1.2 Effect of Tip Clearance on Pressure Ratio

For all rotor speeds, the small clearance yielded the greatest pressure ratio; pressure ratio decreased with increased (no step) tip gap (Figure 26). The uncertainties of pressure ratio, efficiency, and mass flow corresponding to the 100% rotor speed line are shown in Table 5. As seen in Figures 28 through 31, the steady-state circumferentially averaged pressure ratio (normalized by the passage averaged pressure ratio) in the outer half of span decreased with increased clearance, whereas, it increased nearer the hub. This shift is due to blockage created in the tip region which diverts the main flow to the inner span creating greater throughflow and work nearer the hub. However, the greater work near the hub did not completely balance the work lost near the rotor tip, resulting in an overall reduction of total pressure for the passage (Figure 26). Additional evidence of the effects of blockage on flowfield diversion will be shown in the next chapter dealing with flowfield characteristics.

6.1.3 Effect of Tip Clearance on Efficiency

Efficiency also tended to decrease with increased clearance, with a significant decrease occurring for the large (1.002% tip chord) tip gap (Figure 26). Differences in efficiency were minimal between the small (0.318% tip chord) and medium (0.574% tip chord) gaps, with the medium gap giving slightly improved efficiency in the lower mass flow region near stall for each speed line. As seen in Figures 28 through 31, efficiency in the outer portion of span[3] decreased with larger tip gap and was essentially unchanged for the inner span. Thus, it is the outer span region which contributes most to changes in overall efficiency.

---

[3] Spanwise efficiencies were calculated using Equations 36 and 37 shown in Appendix A. In these equations, the circumferentially averaged values of total pressure and total temperature measured at each spanwise location were used for the exit condition; the inlet condition used the passage averaged total temperature and total pressure.
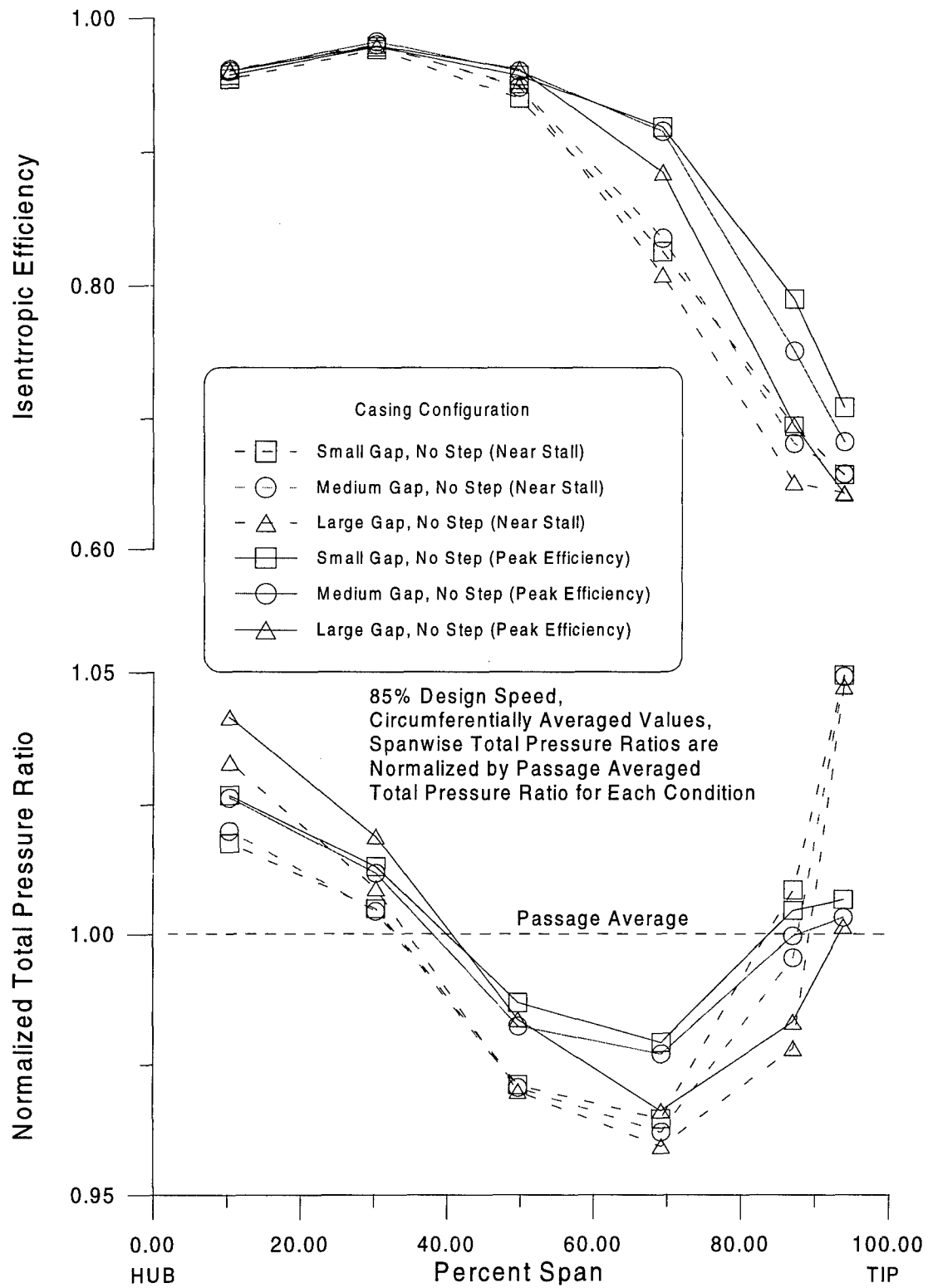
72

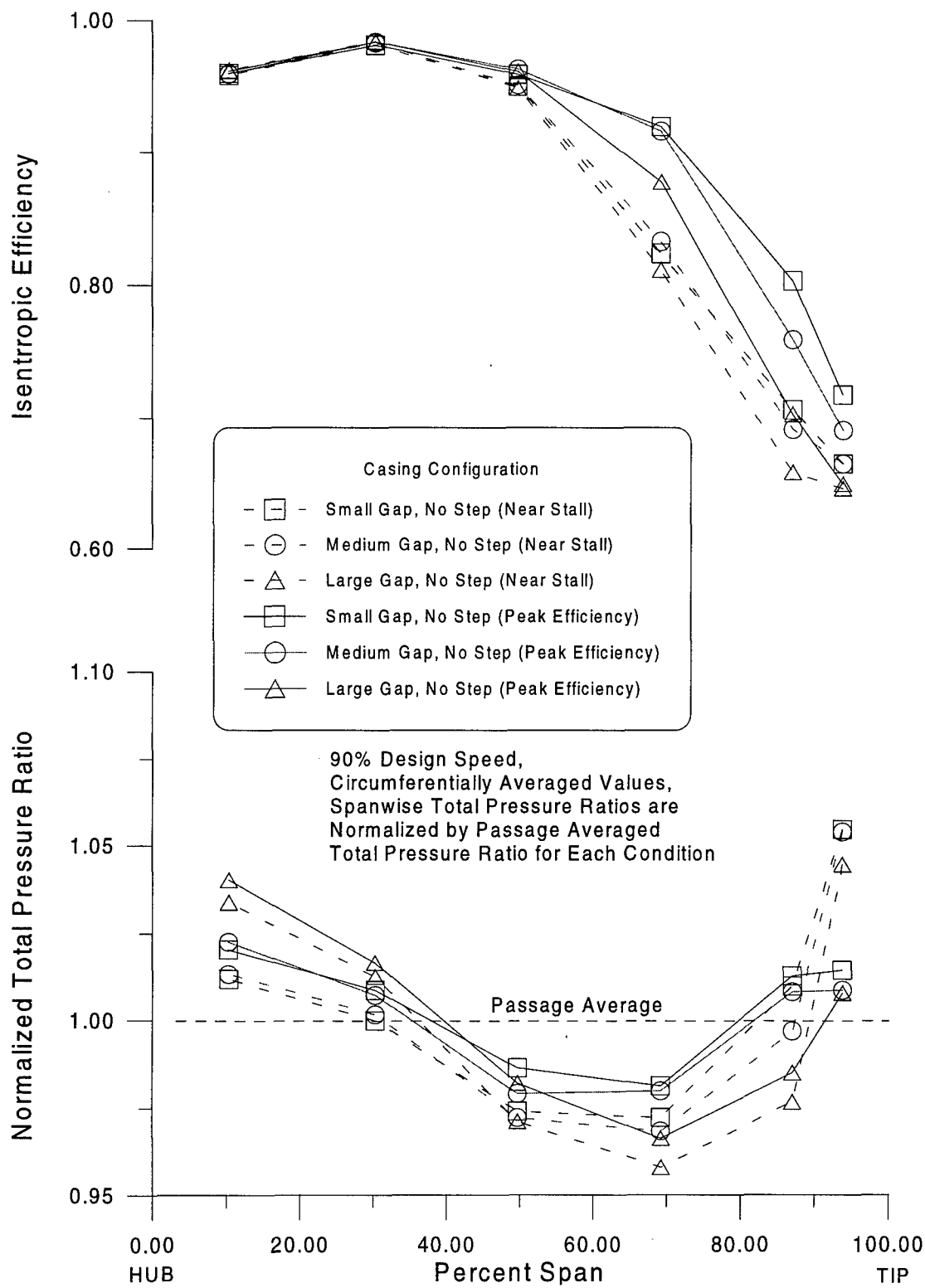Figure 28. Clearance Effects on Spanwise Rotor Performance (85% Design Speed)

73

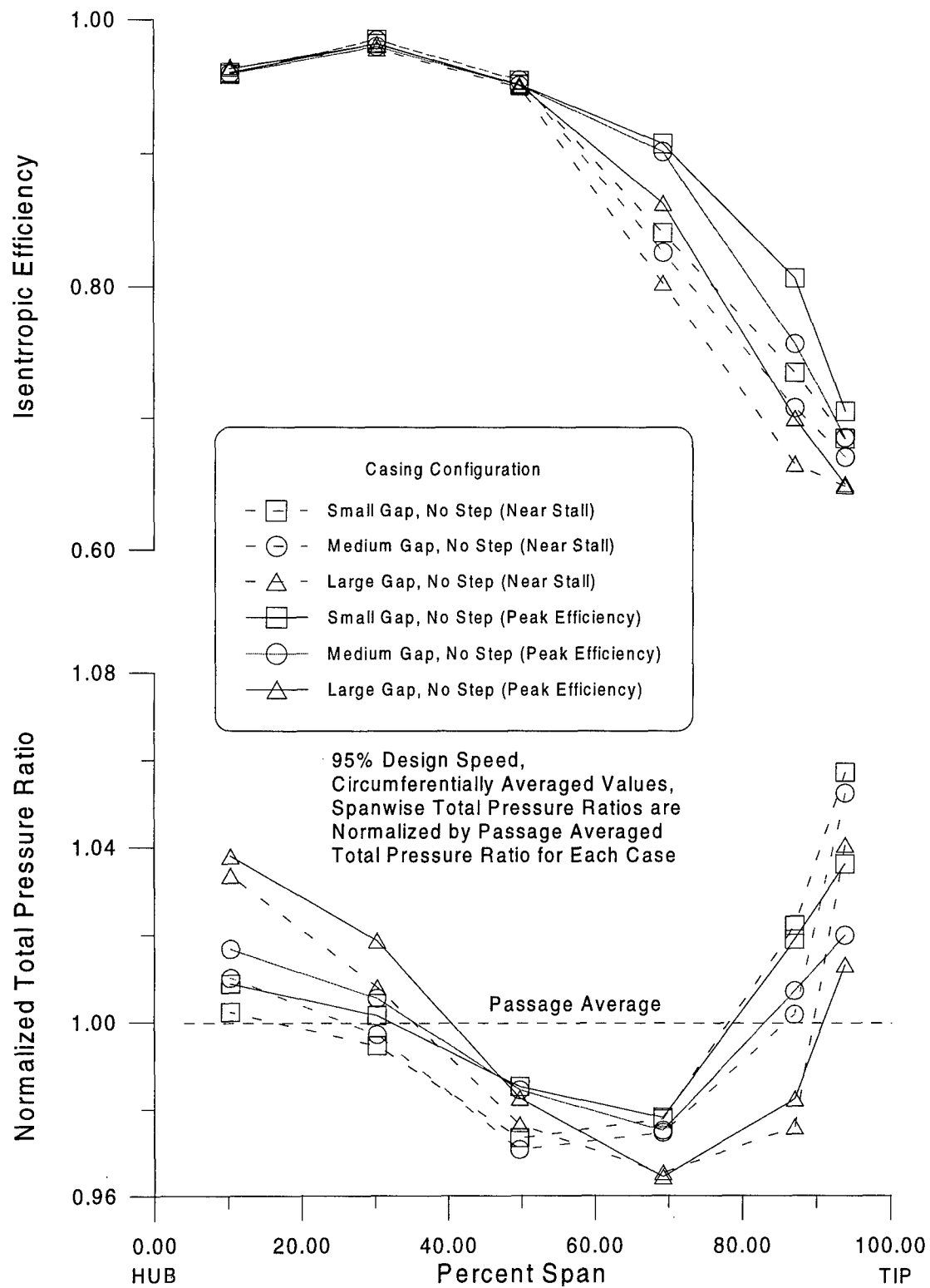Figure 29. Clearance Effects on Spanwise Rotor Performance (90% Design Speed)

74

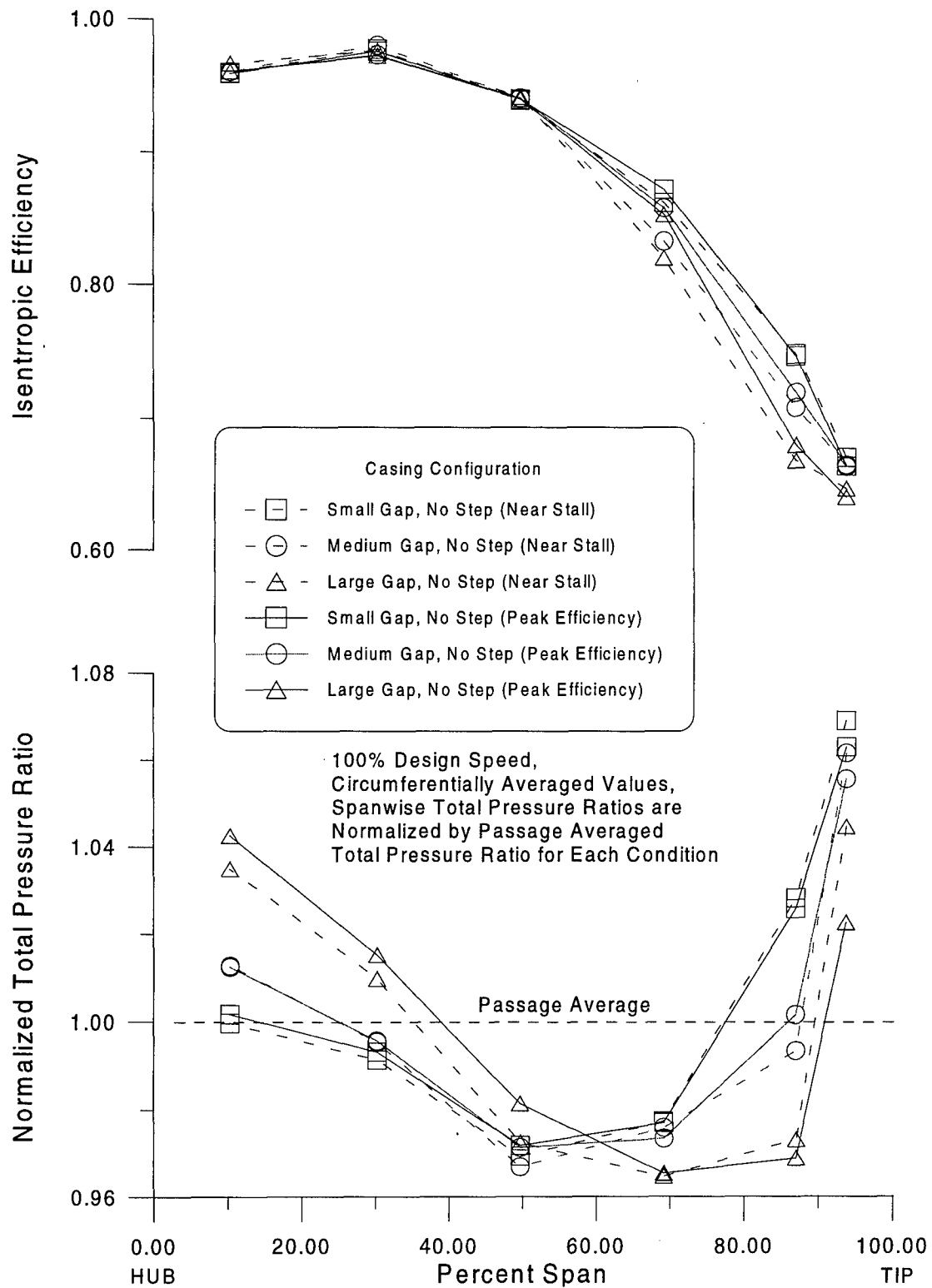Figure 30. Clearance Effects on Spanwise Rotor Performance (95% Design Speed)

75

Casing Configuration

- – ⊟ – Small Gap, No Step (Near Stall)
- – ⊖ – Medium Gap, No Step (Near Stall)
- – △ – Large Gap, No Step (Near Stall)
- ⊞ Small Gap, No Step (Peak Efficiency)
- ○ Medium Gap, No Step (Peak Efficiency)
- △ Large Gap, No Step (Peak Efficiency)

100% Design Speed,
Circumferentially Averaged Values,
Spanwise Total Pressure Ratios are
Normalized by Passage Averaged
Total Pressure Ratio for Each Condition

Passage Average

Figure 31. Clearance Effects on Spanwise Rotor Performance (100% Design Speed)

76

6.1.4 Effect of Tip Clearance on Mass Flow Range

For rotor speeds of 90% or less, mass flow range decreased with increased tip gap (Figure 26). For the 100% speed line, larger clearances gave increased flow range, with the medium clearance producing the largest gain. At the slower 95% speed, the medium clearance also yielded increased mass flow range over the small gap, but the large gap resulted in a significant loss of flow range. In all cases, the maximum mass flow attainable was reduced with increasing clearance. These results indicate the optimum tip gap to maximize flow range for high speed operation resides in an intermediate running clearance range between 0.318% and 1.002% tip chord; for the slower speeds, the smallest tip gap possible optimizes mass flow range. It should be noted that a maximized mass flow range does not necessarily coincide with the condition for maximum mass flow capability.

6.2 Effect of Stepped Tip Gap on Rotor Performance

6.2.1 Effect of Stepped Tip Gap on Stall Margin

No significant changes in stall margin were introduced with the use of stepped tip gaps (Figure 27). Any differences are within the error introduced by the definition of the stall line–a least-squares linear-fit through the four stall conditions corresponding to each rotor speed. Again, the stall margin is mainly affected by the overall tip clearance, with the medium tip clearance generally being the best compromise for a design in which operation at 100% rotor speed is important.

6.2.2 Effect of Stepped Tip Gap on Pressure Ratio

The effects of stepped tip gaps on rotor total pressure ratio and efficiency are seen in Figures 32 through 35. These segmented rotor maps provide detailed comparisons by speed for all configurations tested. Total pressure ratio and efficiency are steady-state passage-averaged quantities calculated as shown in Appendix A. The uncertainties of pressure ratio, efficiency, and mass flow corresponding to the 100% rotor speed line are shown in Table 5.
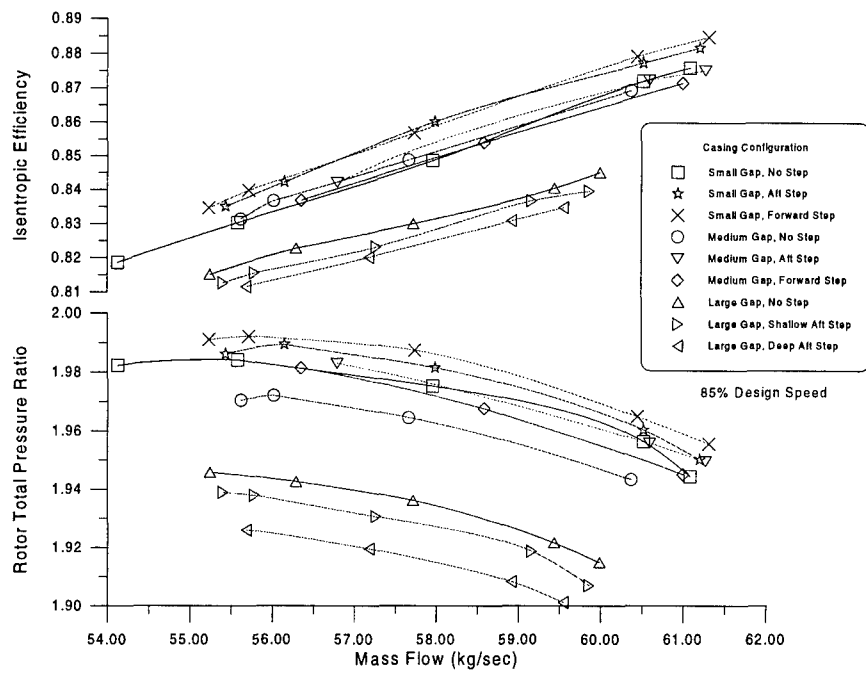
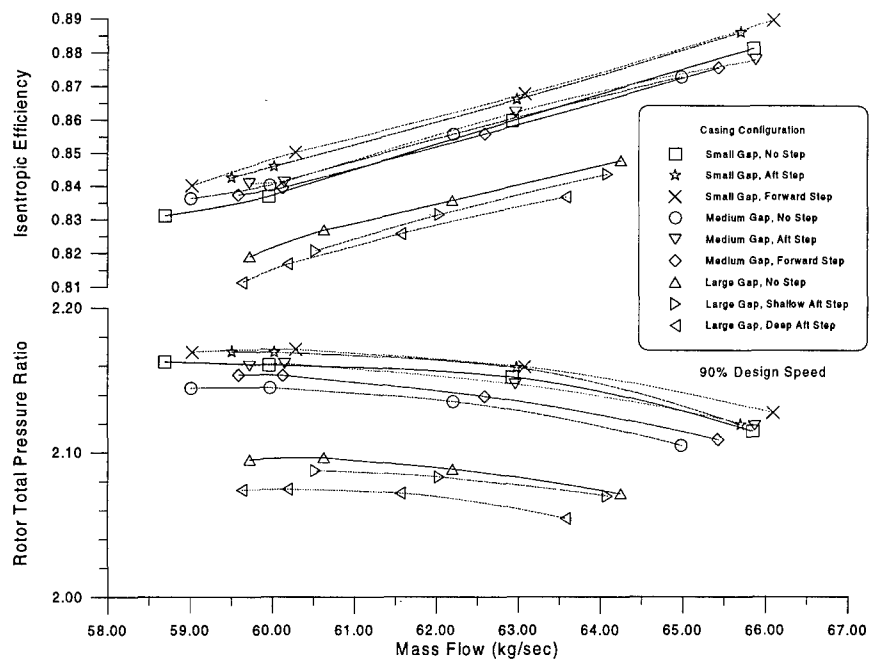77

Figure 32. Rotor Map for 85% Design Speed

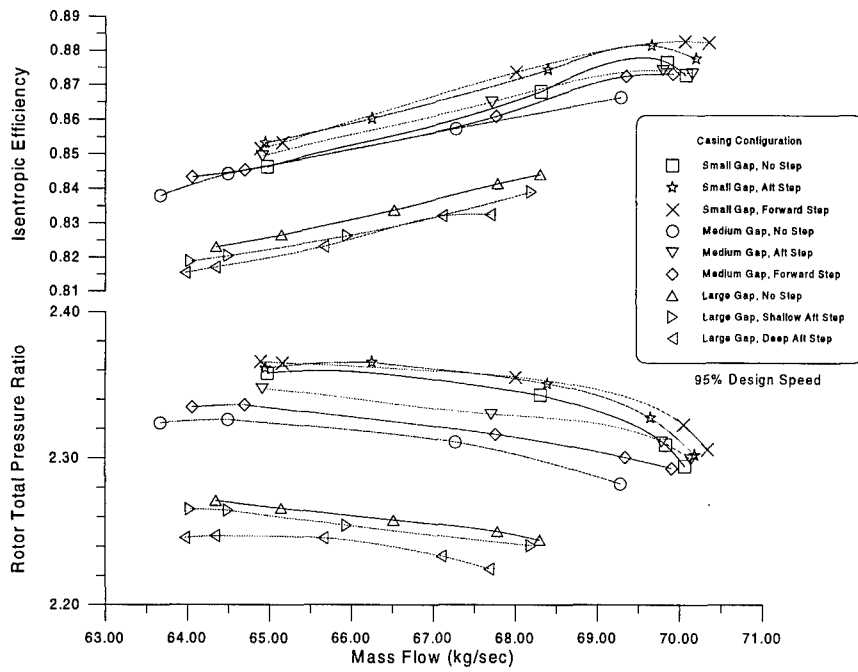Figure 33. Rotor Map for 90% Design Speed
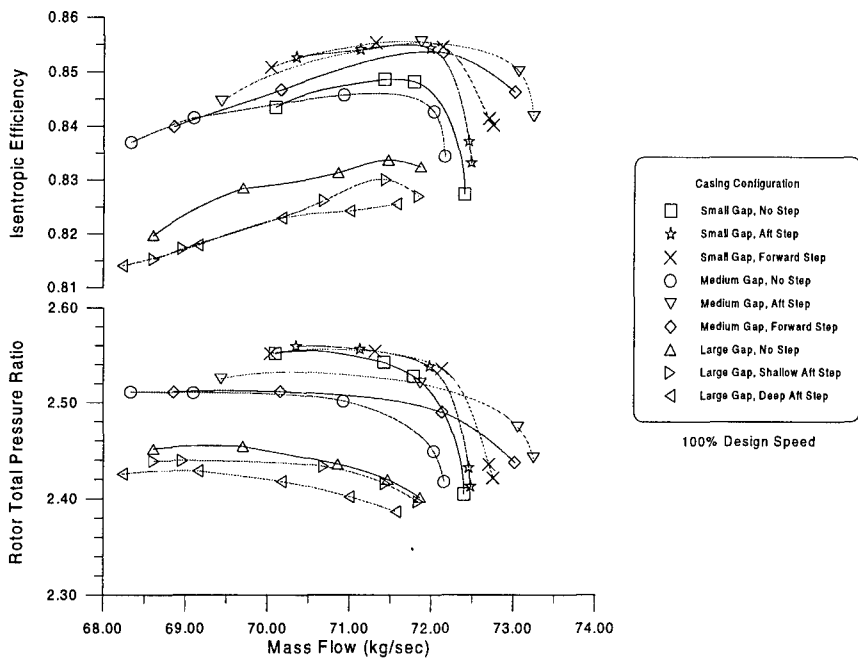
78

Figure 34. Rotor Map for 95% Design Speed

Figure 35. Rotor Map for 100% Design Speed

79

The inclusion of stepped tip gaps with the small and medium clearances gave increased pressure ratio throughout the mass flow range for all rotor speeds (Figures 32, 33, 34, 35); furthermore, the small clearance with forward step location gave the greatest pressure ratio of all cases tested. However, for the largest tip clearance level of 1.002% tip chord, pressure ratio decreased throughout the mass flow range for all rotor speeds. It was seen that the axial location of the step giving the greatest improvement depended mainly on the clearance level. For the small clearance level of 0.318% tip chord, the forward step of 0.256% tip chord at 58% axial chord produced the greatest improvement. This relation held true for all speeds except in the low mass flow range at 100% design speed (Figure 35). For the medium clearance level of 0.574% tip chord, the aft step at 86% axial chord clearly produced the better pressure ratio throughout the mass flow range. As evidenced in Figures 36 through 39, pressure ratio decreased in the outer 40% of span when stepped gaps were used, but this loss was countered with improved performance in the inner 60% of span to produce an average gain in pressure ratio across the span.

Only the aft step location was tested for the large clearance level (1.002% tip chord). Unlike for the small and medium clearances, a stepped gap for the large clearance degraded pressure ratio throughout mass flow range. A deeper step (0.831% tip chord) at this clearance caused an even greater degradation of pressure ratio. The author feels it is doubtful that any step for this larger clearance will improve performance.
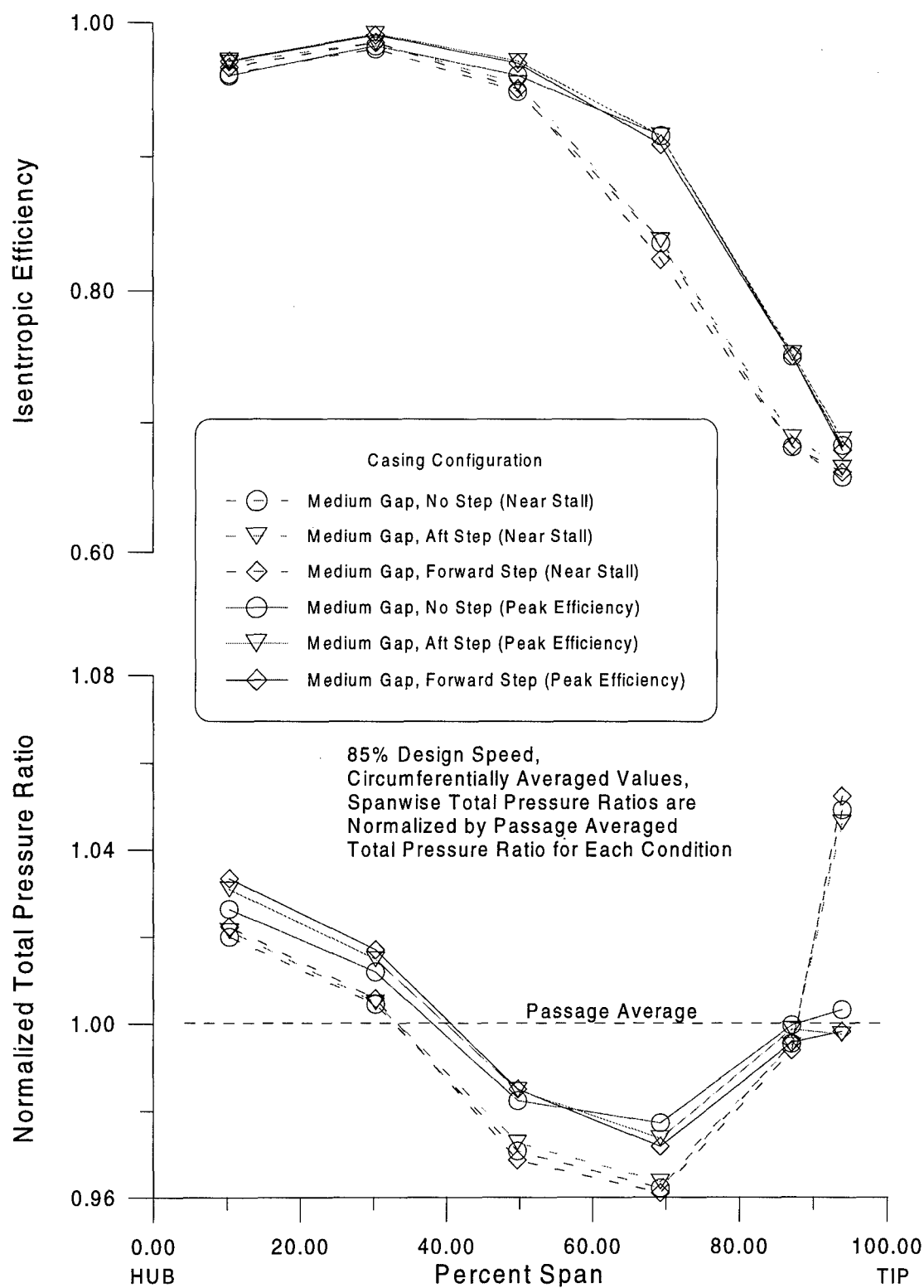
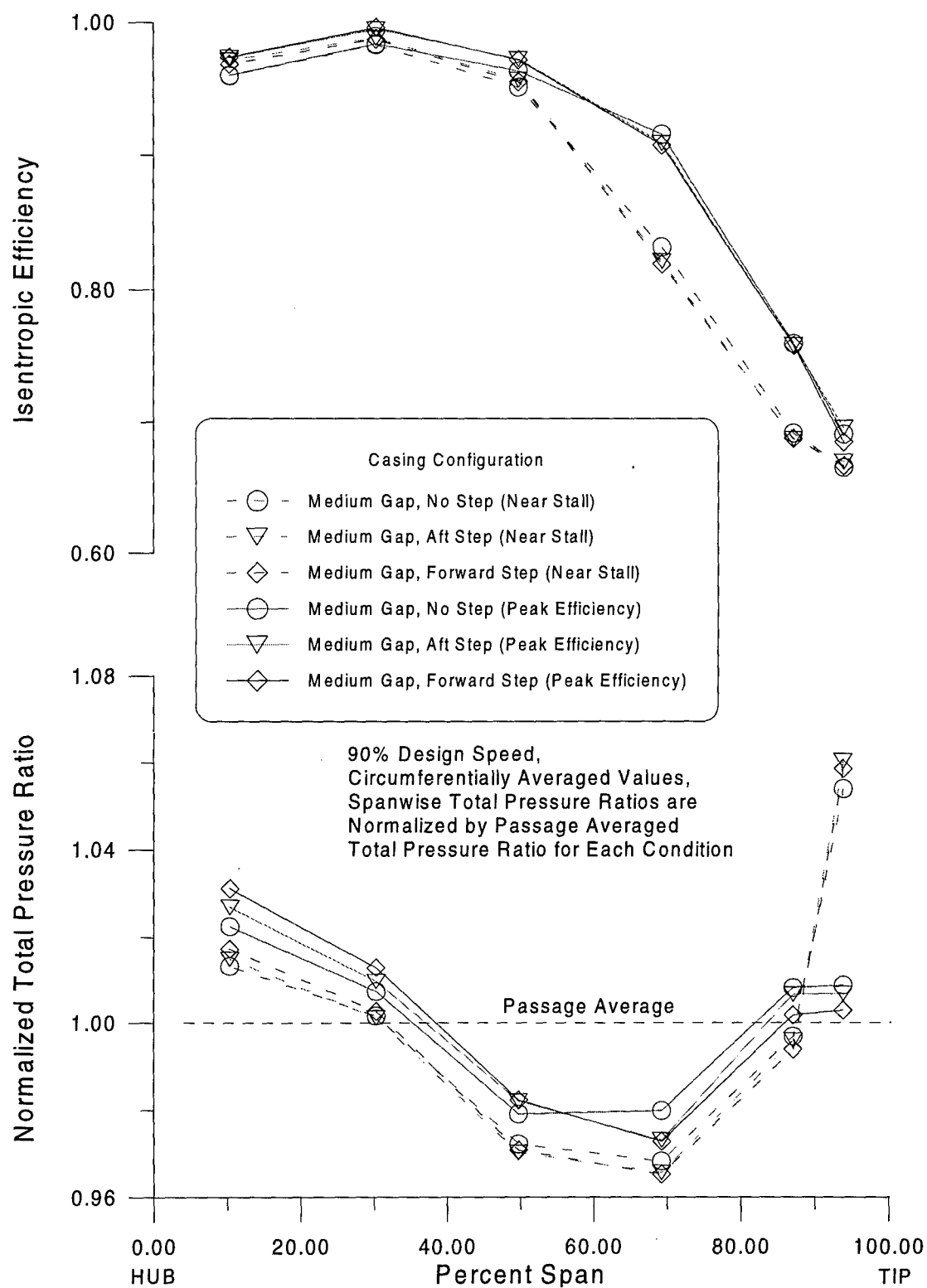Figure 36. Stepped Tip Gap Effects on Spanwise Rotor Performance (85% Design Speed, Medium Clearance)

81

Figure 37. Stepped Tip Gap Effects on Spanwise Rotor Performance (90% Design Speed, Medium Clearance)
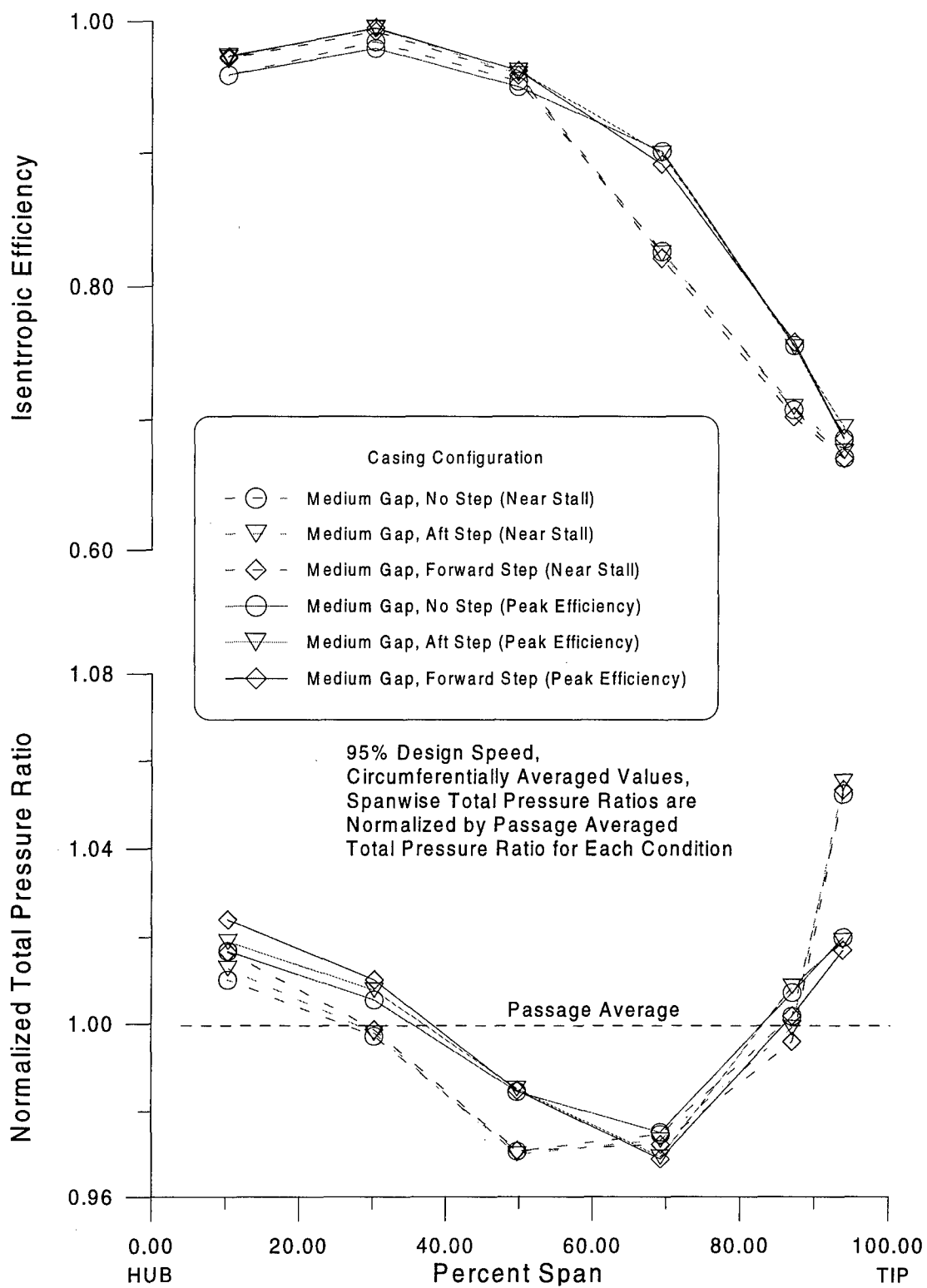
82

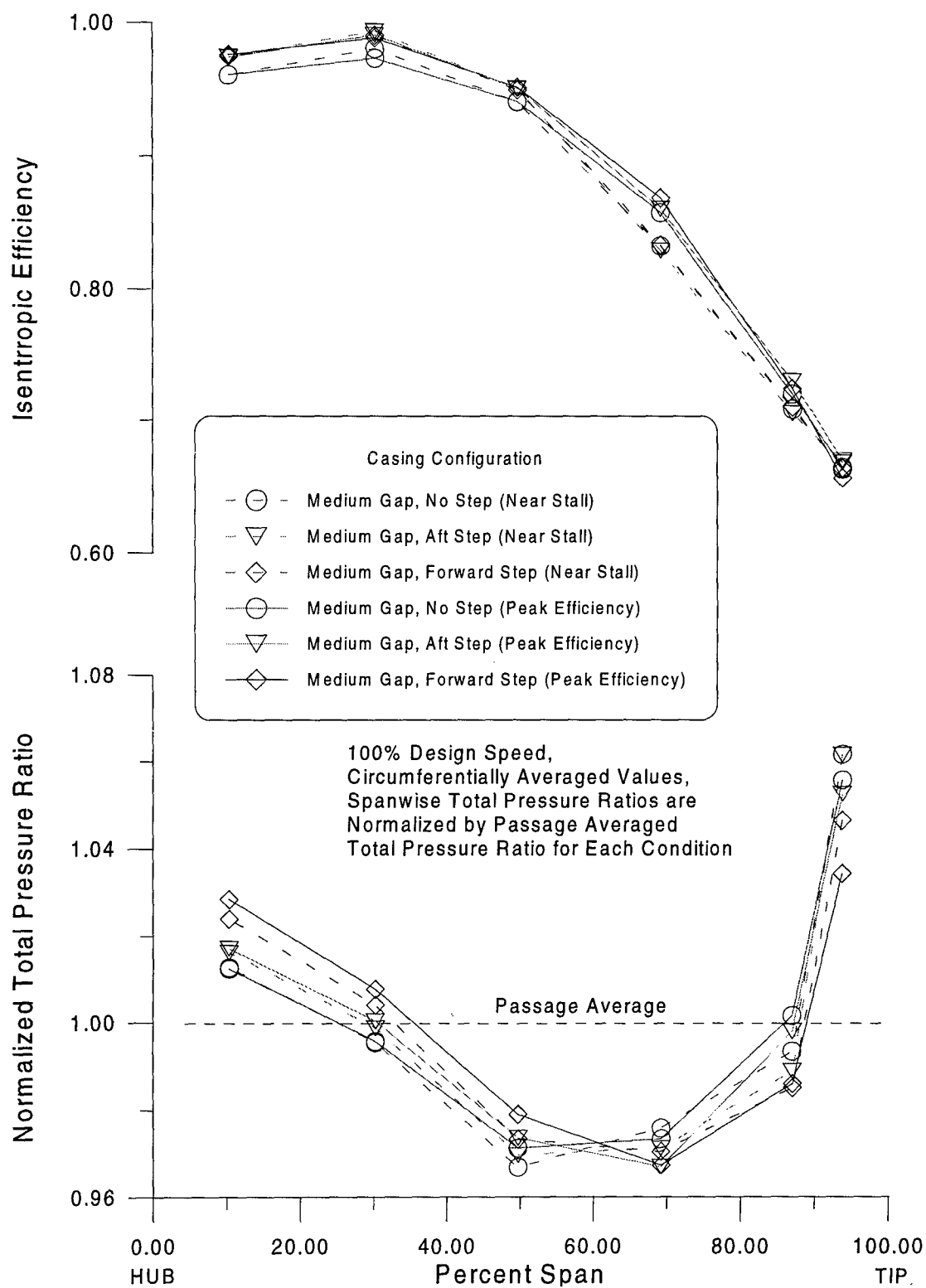Figure 38. Stepped Tip Gap Effects on Spanwise Rotor Performance (95% Design Speed, Medium Clearance)

83

Figure 39. Stepped Tip Gap Effects on Spanwise Rotor Performance (100% Design Speed, Medium Clearance)

84

6.2.3 Effect of Stepped Tip Gap on Efficiency

As with pressure ratio, efficiency tended to increase when stepped gaps were employed for the small and medium clearance levels but tended to decrease for the large clearance level. Again, for the small clearance level, the forward step at 58% axial chord gave the largest increase in efficiency throughout the mass flow range for all rotor speeds tested (Figures 32, 33, 34, 35). For the medium clearance level, though minimal changes in efficiency occurred for 90% and 85% design speeds, at 95% and 100% speeds, stepped tip gaps produced significant gains in efficiency throughout the mass flow range, with the greatest change occurring for the aft step at 86% axial chord. As seen in Figures 36 through 39, stepped gaps increased efficiency across the entire span for those cases that showed an overall efficiency improvement. Again, as with pressure ratio, efficiency decreased when stepped tip gaps were used with the large clearance level at all rotor speeds, with the deeper step being the worst.

6.2.4 Effect of Stepped Tip Gap on Mass Flow Range

The effects of stepped tip gaps on mass flow range can be seen in Figures 32 through 35. With the small clearance, mass flow range improvement was only achieved at the two faster rotor speeds by using stepped gaps, with the best results occurring for the forward step location. With the medium clearance level, flow range improvement was increased at all speeds by using a stepped gap. The forward step location gave improvement for the two fastest rotor speeds, and the aft step gave improvement for the two slowest speeds tested. With the large clearance level, there were no significant improvements in mass flow range at any speed or aft step depth; in most cases, the mass flow range decreased.

The effects of stepped tip gaps on the upper limit of mass flow are also seen in Figures 32 through 35. Only for the medium gap did significant increases occur in the upper limit mass flow

for all conditions; for the small and large gaps, only minor increases or decreases occurred with stepped gaps. Moreover, the configuration yielding the greatest mass flow capability for all rotor speeds was the medium clearance level with aft axial step location. In summary, only the medium gap yielded increases in both mass flow range and mass flow capability by using steps.

6.3 Second-Stage Effects on Performance

The preceding results were obtained by modifying the casing geometry for only the first-stage rotor; the second-stage of the compressor was unaltered. Consequently, performance improvement provided by a modified first-stage rotor casing may have been limited by the unaltered second-stage of the compressor. Therefore, the beneficial effects of stepped tip gaps on performance improvement may be greater than indicated by these tests.

6.4 Mission Performance - Sensitivity Analysis

As seen in the rotor map for 100% rotor speed (Figure 35), the pressure ratio for the medium tip clearance cases was less than that for the small tip clearance cases; however, when stepped tip gaps were used, the isentropic efficiency for the medium clearance cases was greater than that for the small clearance cases. Such trade-offs made it necessary to evaluate the sensitivity of overall turbojet engine performance to tip gap geometry. A representative fighter aircraft engine and mission were used for the sensitivity analysis; the mission and analysis techniques are described in Appendix D. As the comparative measure, the total fuel burned during a mission was calculated based on the experimentally determined isentropic efficiency and pressure ratio at 100% design rotor speed (13288 RPM) and design mass flow (71.66 kg/sec) for each casing configuration.

Mission analyses yielded the sensitivity of fuel economy to casing configuration shown in Table 6. The fuel use factor is the amount of fuel used for each case divided by the fuel used for Case A. For aircraft mission planning, it is more common to express fuel economy by the reciprocal

86

Table 6. Fuel Economy Sensitivity to Casing Configuration

Casing Configuration	Fuel Used lbm	Fuel Use Factor	Fractional Variation	Range Factor
A (Small Gap, No Step)	13679	1.0000	0.0	1.0
B (Small Gap, Aft Step)	13645	0.9975	-0.0025	1.0025
C (Small Gap, Forward Step)	13640	0.9971	-0.0029	1.0029
D (Medium Gap, No Step)	13672	0.9995	-0.0005	1.0005
E (Medium Gap, Aft Step)	13634	0.9967	-0.0033	1.0033
F (Medium Gap, Forward Step)	13641	0.9972	-0.0028	1.0028
G (Large Gap, No Step)	13730	1.0037	+0.0037	0.9963
H (Large Gap, Shallow Aft Step)	13756	1.0056	+0.0056	0.9944
I (Large Gap, Deep Aft Step)	13766	1.0064	+0.0064	0.9936

of the fuel use factor, the range factor. Range factor is the ratio of the range (distance traveled) that would be achieved with the use of a particular case to the range that would be achieved with the use of the reference case (Case A) for the same amount of fuel. A medium (unstepped) tip clearance was found to yield better fuel economy than a small (unstepped) clearance, and stepped tip gaps improved the fuel economy over the unstepped configurations at both the small and medium clearance levels.

6.5 Summary

In this chapter, the effects of tip clearance and stepped tip gaps on rotor performance were detailed. A variation of tip clearance was found to produce large differences in performance, whereas stepped tip gaps produced new performance improvement. In the next chapter, the effects of tip clearance and stepped tip gap on flowfield characteristics are linked to the performance trends shown in this chapter.

Chapter 7 - Flowfield Characteristics

The change in performance with the variation of tip geometry presented in the previous chapter is the result of the amount and distribution of blockage in the rotor tip region. The results presented in this chapter confirm that flowfield manipulation is possible with the use of stepped tip gaps as discussed in Chapter 3. The tip region static pressure distributions and the laser wake data provide insight into the structure of the flow and the effects of clearance geometry. Computational fluid dynamic modeling provides additional insight into the flow structures within the rotor passage. In the following sections, detailed flowfield characterizations for each casing configuration tested are presented, and significant effects of varying casing geometry on the flowfield of the ADLARF rotor are addressed.

7.1 Tip Region Static Pressures

Tip region static pressure distributions along the rotor casing were collected for each casing configuration at 100% corrected rotor speed and mass flow rates corresponding to near choke, peak efficiency, and near-stall. These distributions, seen in Figures 40 through 57, detail the flowfield passage between the suction surface of a rotor blade and the pressure surface of an adjacent rotor blade near the rotor tip. For each case of steady-state operating condition, the static pressure was normalized by the stagnation pressure at the rotor inlet; flow unsteadiness was defined to be simply the standard deviation of the time-averaged pressure measurements at each point in the passage.

The flowfield elements in each pressure cascade plot of Figures 40, 42, 44, 46, 48, 50, 52, 54, and 56 were easily identified. Also, the interaction of the flowfield elements was evident in each pressure unsteadiness cascade plot of Figures 41, 43, 45, 47, 49, 51, 53, 55, and 57. For example, as seen in the static pressure distributions associated with Case D (Figure 46), concentrated
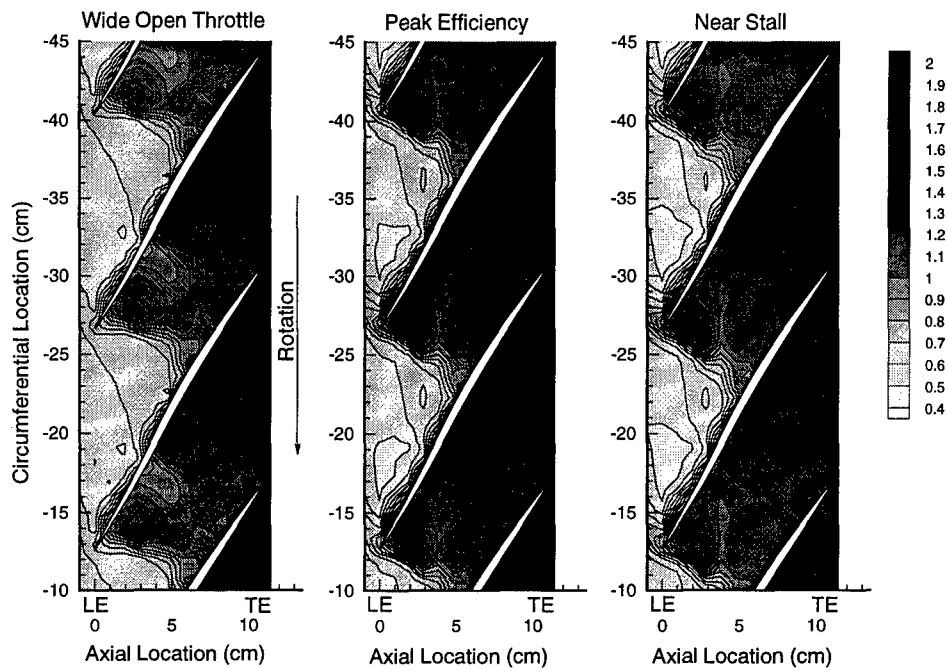
88

Figure 40. Normalized Static Pressure at the Rotor Endwall (Case A, 100% Design Rotor Speed)
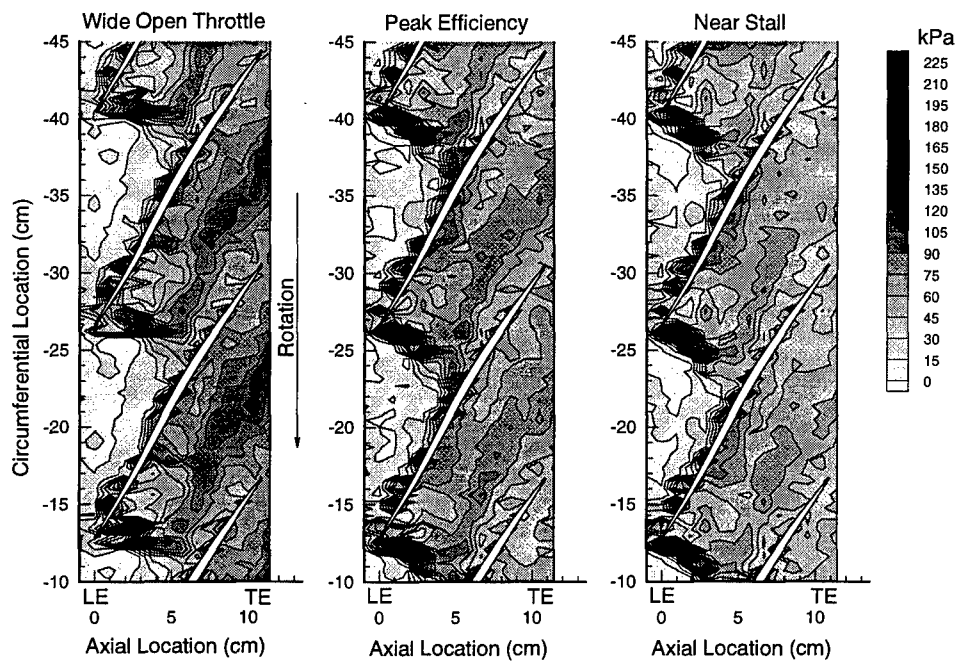

Figure 41. Rotor Tip Region Pressure Unsteadiness (Case A, 100% Design Rotor Speed)
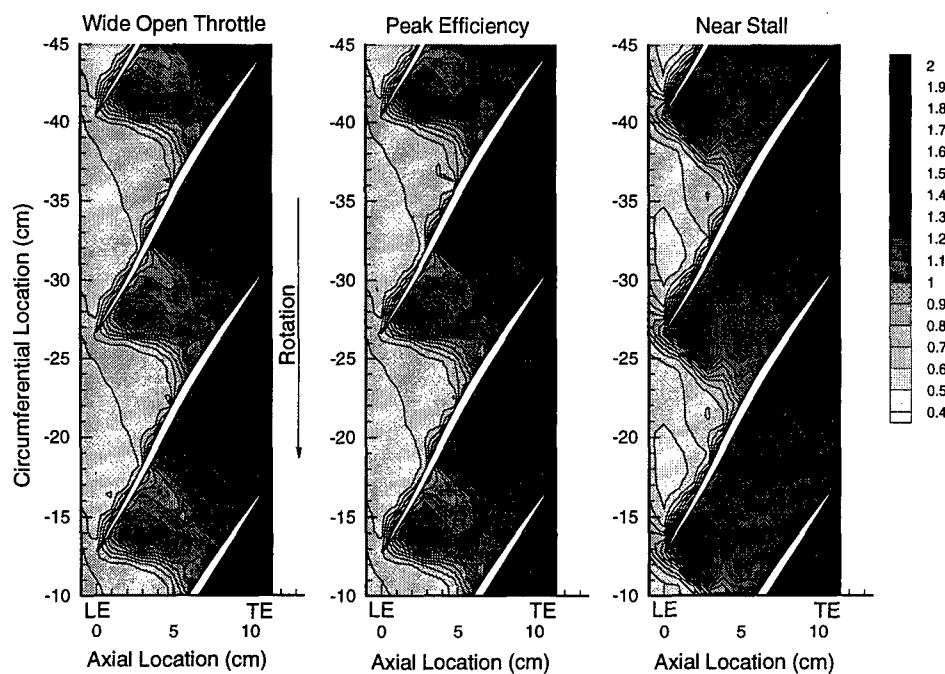
Figure 42. Normalized Static Pressure at the Rotor Endwall (Case B, 100% Design Rotor Speed)
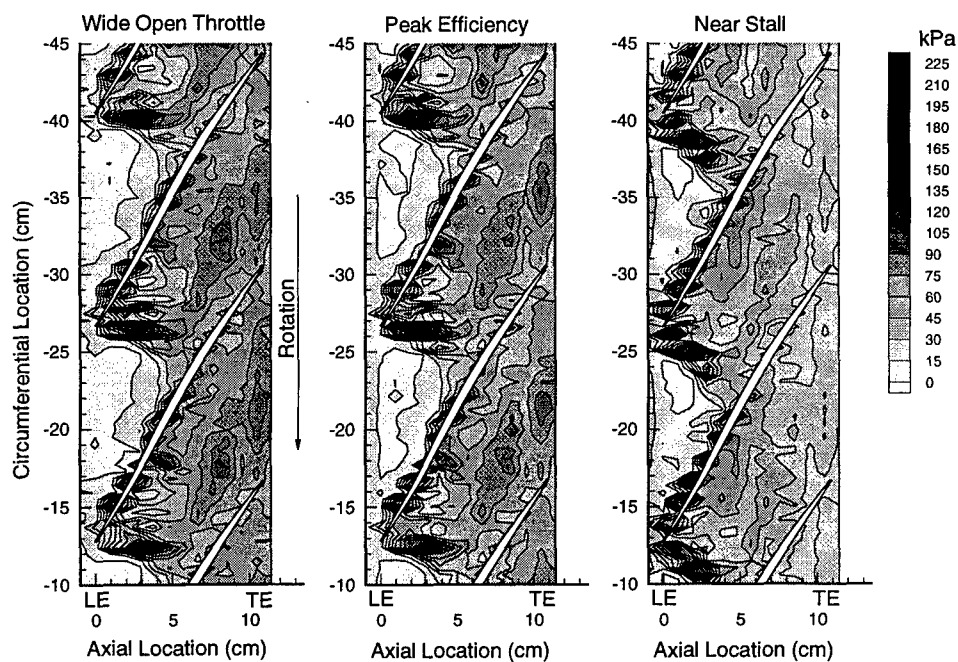

Figure 43. Rotor Tip Region Pressure Unsteadiness (Case B, 100% Design Rotor Speed)
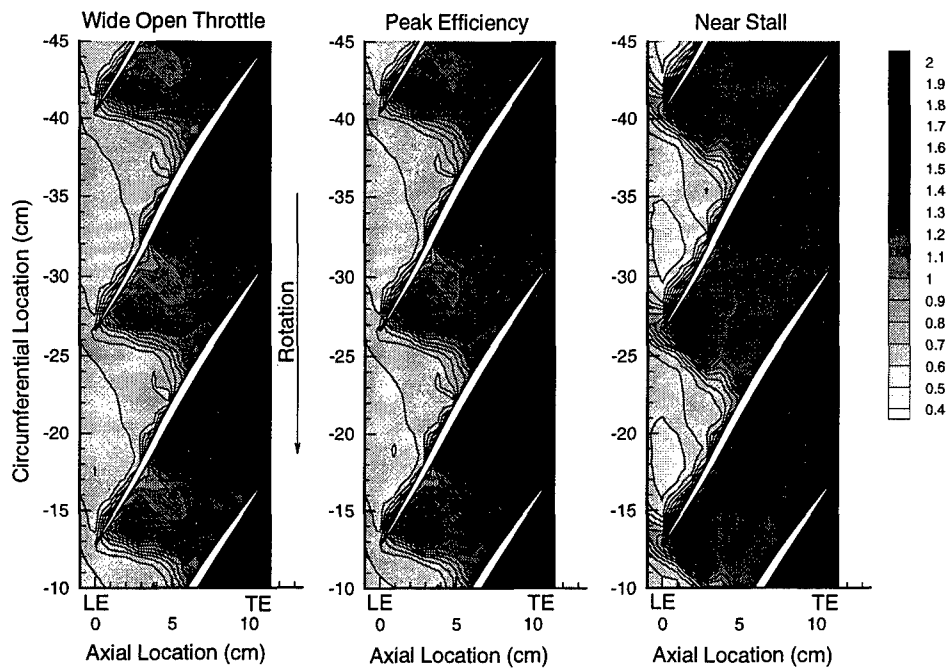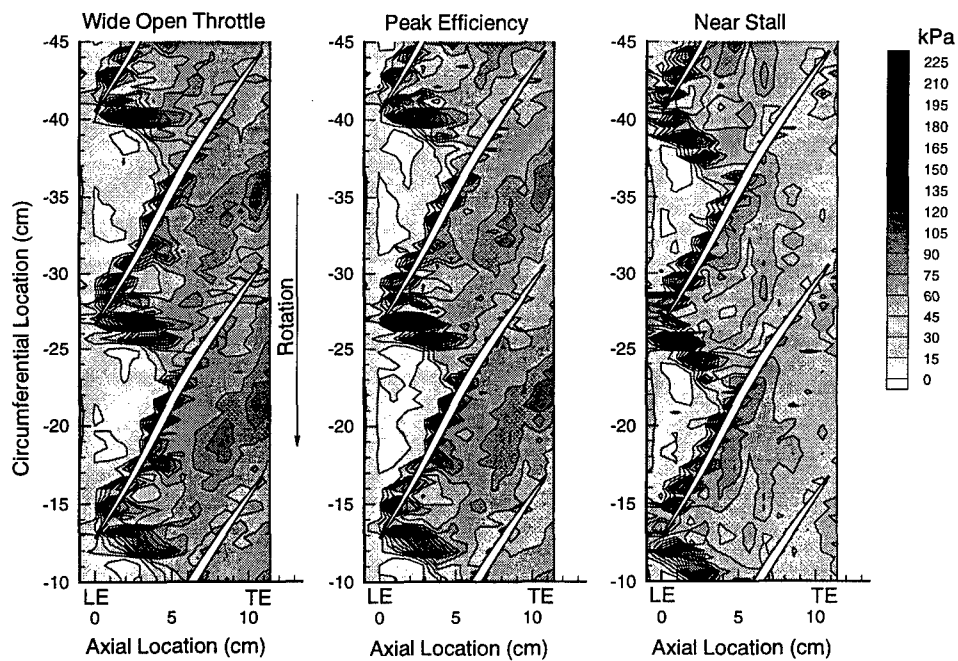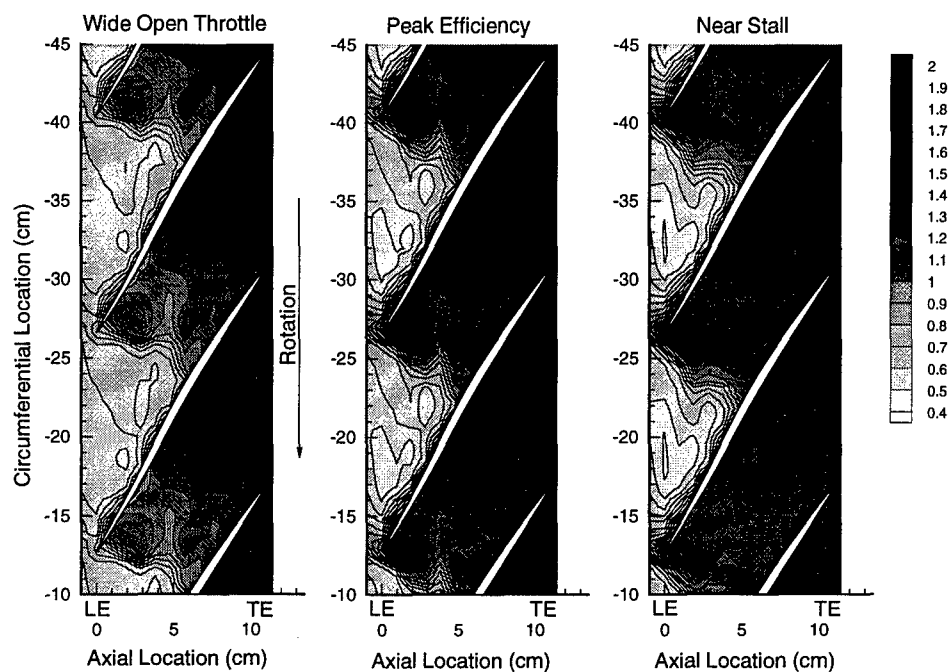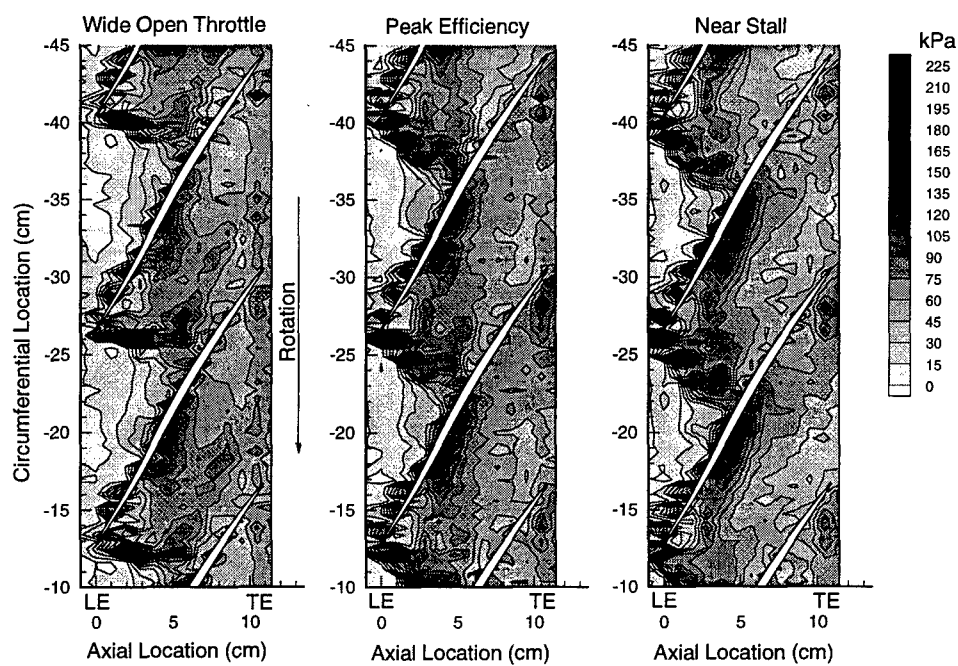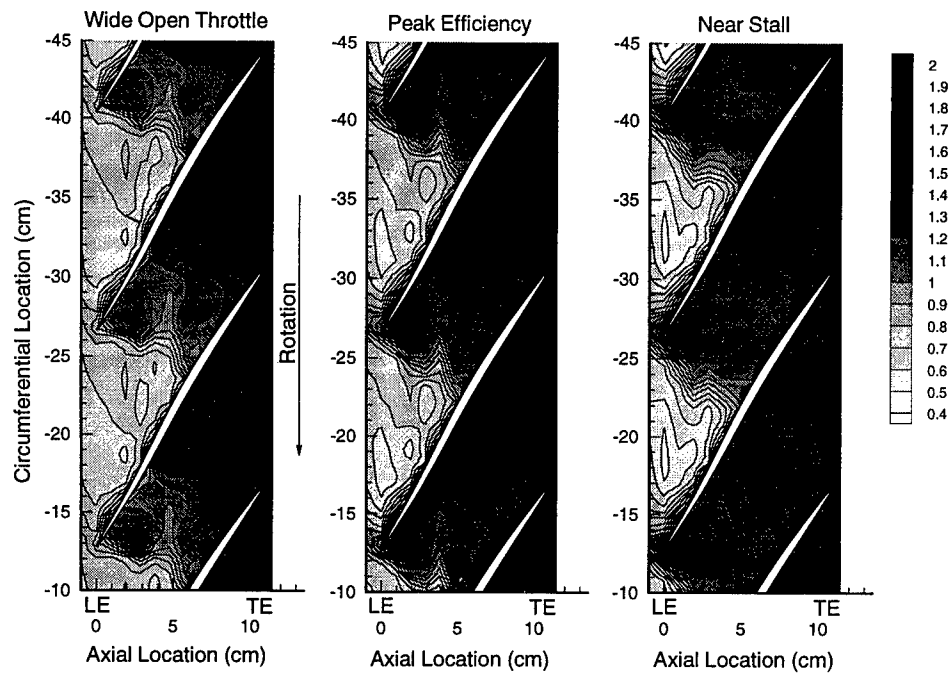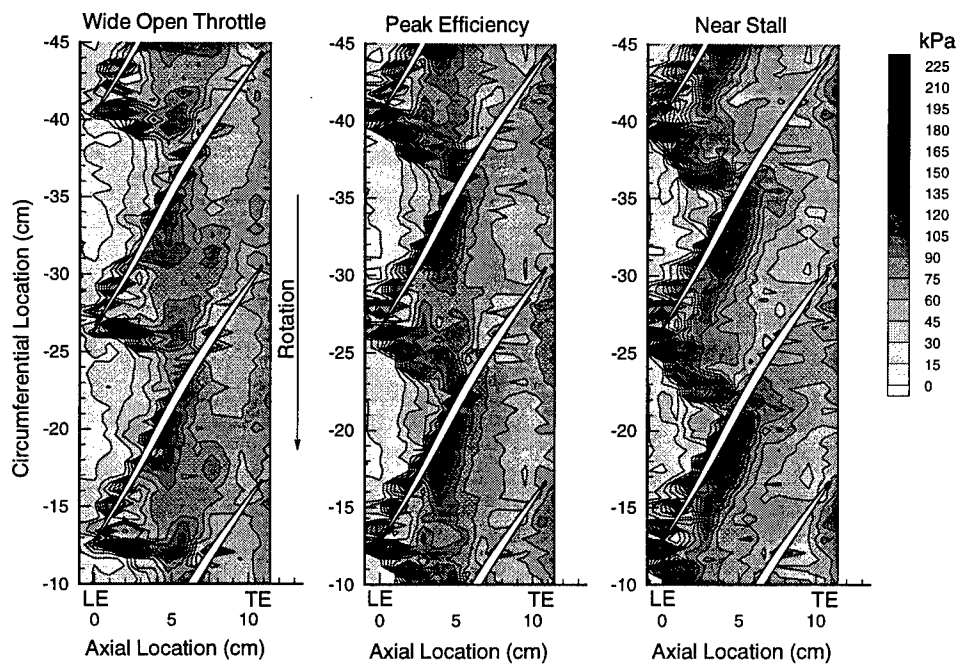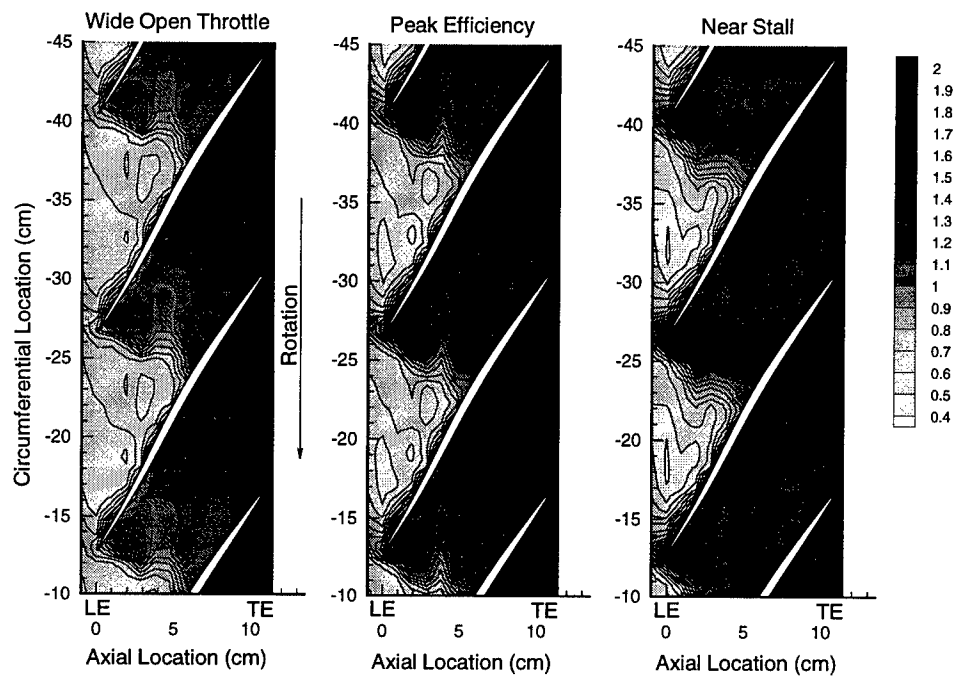
Figure 44. Normalized Static Pressure at the Rotor Endwall (Case C, 100% Design Rotor Speed)
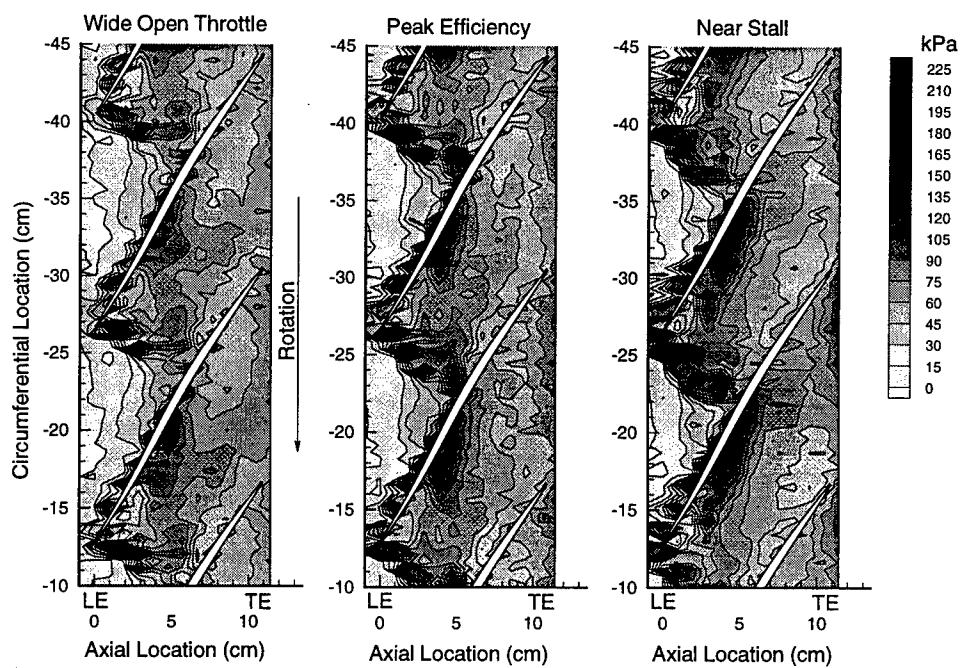

Figure 45. Rotor Tip Region Pressure Unsteadiness (Case C, 100% Design Rotor Speed)
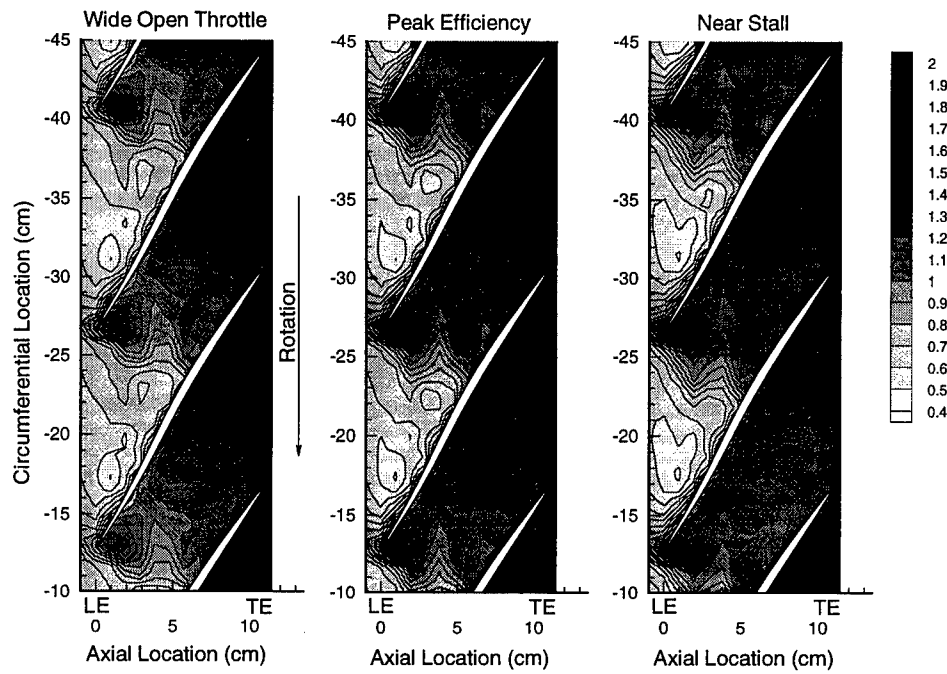
91

Figure 46. Normalized Static Pressure at the Rotor Endwall (Case D, 100% Design Rotor Speed)

Figure 47. Rotor Tip Region Pressure Unsteadiness (Case D, 100% Design Speed)

92

Figure 48. Normalized Static Pressure at the Rotor Endwall (Case E, 100% Design Rotor Speed)

Figure 49. Rotor Tip Region Pressure Unsteadiness (Case E, 100% Design Rotor Speed)

Figure 50. Normalized Static Pressure at the Rotor Endwall (Case F, 100% Design Rotor Speed)
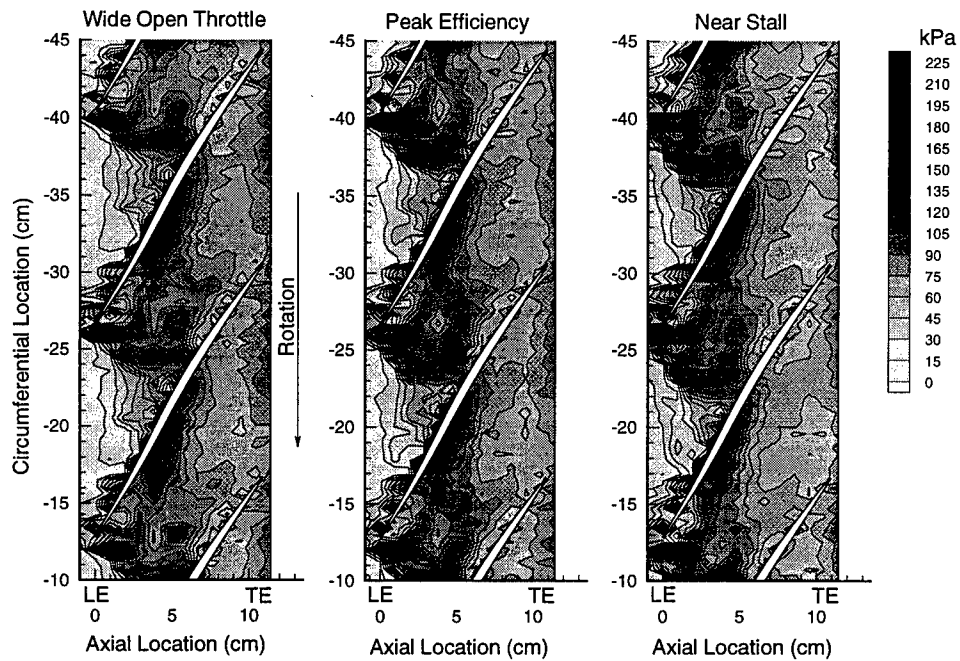

Figure 51. Rotor Tip Region Pressure Unsteadiness (Case F, 100% Design Rotor Speed)

Figure 52. Normalized Static Pressure at the Rotor Endwall (Case G, 100% Design Rotor Speed)

Figure 53. Rotor Tip Region Pressure Unsteadiness (Case G, 100% Design Rotor Speed)
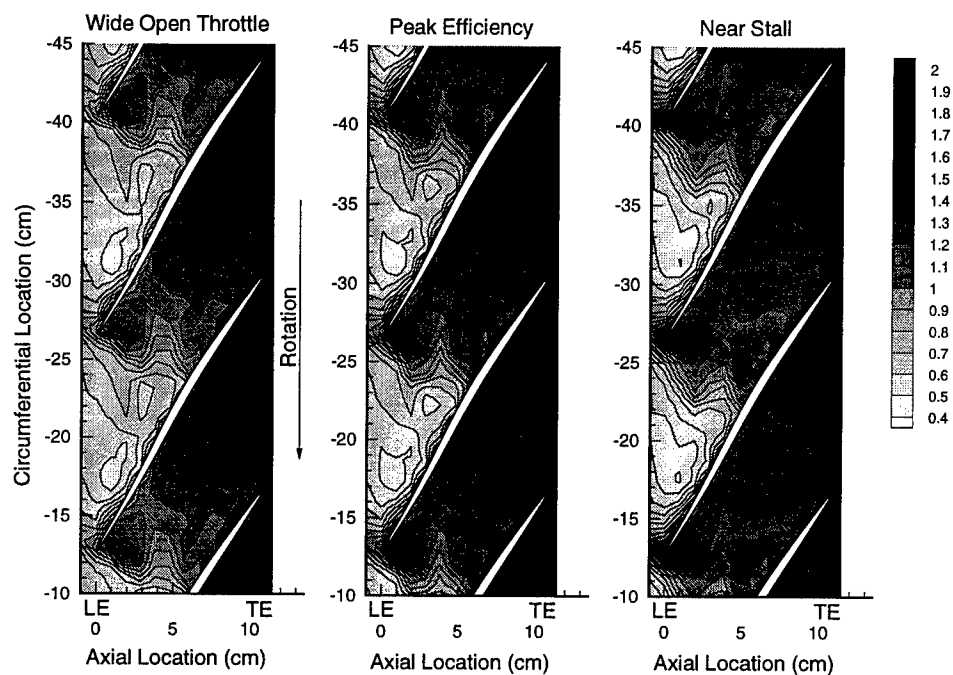
Figure 54. Normalized Static Pressure at the Rotor Endwall (Case H, 100% Design Rotor Speed)
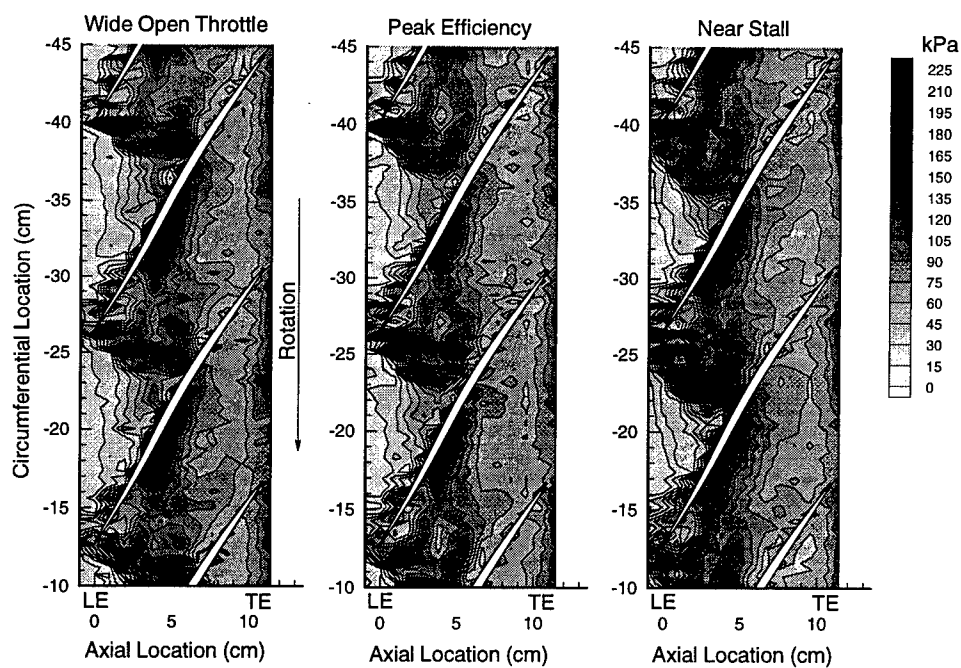

Figure 55. Rotor Tip Region Pressure Unsteadiness (Case H, 100% Design Rotor Speed)
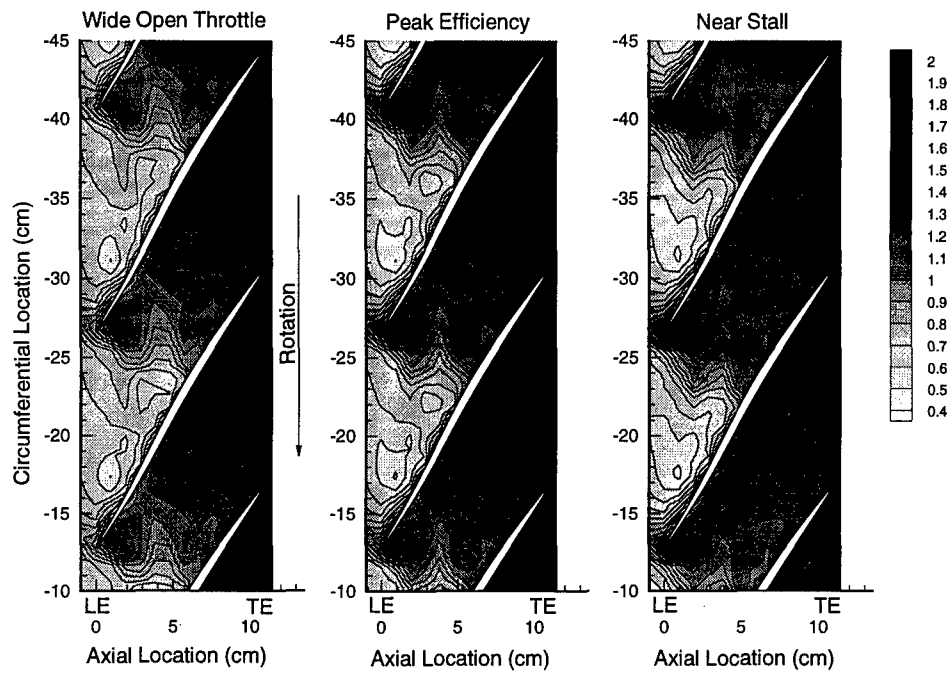
96

Figure 56. Normalized Static Pressure at the Rotor Endwall (Case I, 100% Design Rotor Speed)
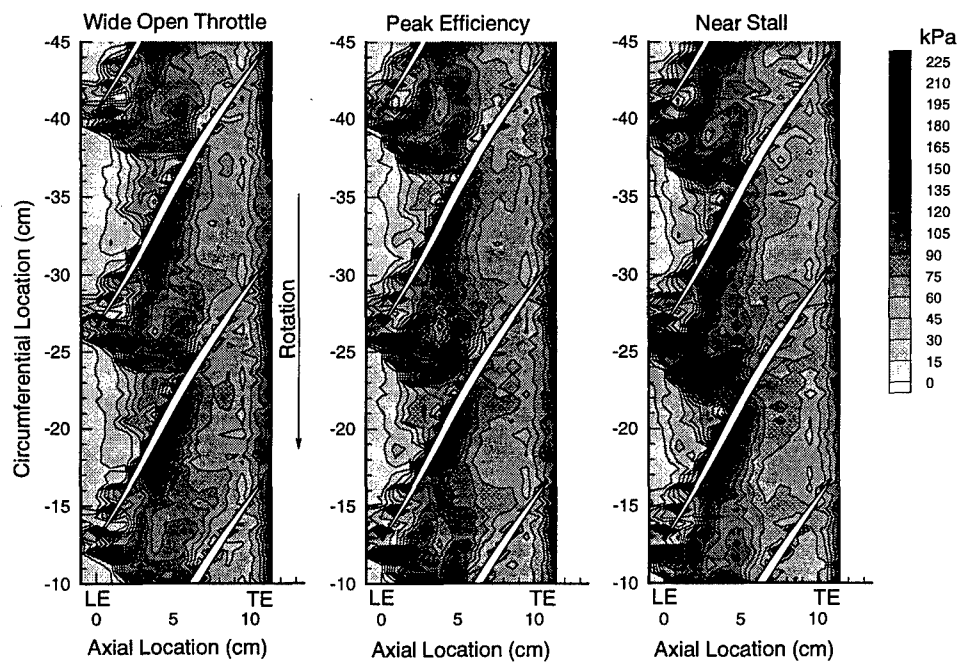

Figure 57. Rotor Tip Region Pressure Unsteadiness (Case I, 100% Design Rotor Speed)

pressure gradients near the leading edge were characteristic of the leading edge shock. As mass flow was throttled from wide open throttle (i.e., near choking) to near-stall, this leading edge oblique shock moved forward in the passage to become a detached normal bow shock during the near-stall condition. For each throttle position, the trough of lower pressure emanating from the rotor leading edge and adjacent to the suction surface of the blade was caused by the tip leakage vortex; the vortex interacted with the shock to form a zone of blockage (increased static pressure) immediately downstream of the shock. This interaction zone was evidenced by increased flow unsteadiness for all throttle positions as seen in Figure 47. Such flow features were present in each cascade pressure plot for Cases A through I; the tip leakage vortex is more difficult to identify for the small tip clearance (Figures 40, 42, and 44) due to the inherently smaller amount of tip leakage flow. The interactions shown in Figures 40 through 57 were consistent with flowfield characterization studies conducted by Cybyk et al. [24] , Puterbaugh [71] , Puterbaugh and Brendel [72] , Puterbaugh and Copenhaver [73] , Russler et al. [78, 79] , and Suder and Celestina [86] . The comparisons of flowfield characteristics as a result of the variation of tip gap geometry are presented in Sections 7.4.1 and 7.5.1.

7.2 Rotor Exit Velocities

The velocity distribution of the rotor passage downstream (105% axial chord, 92% span) of the rotor trailing edge was measured using a laser velocimeter for each casing configuration during steady-state operation at 100% corrected rotor speed and mass flow rates associated with peak efficiency and near-stall. Velocity and flow angle profiles relative to the rotor at 105% axial chord and 92% span are shown for Cases A through I in Figures 58, 60, 62, 64, 66, 68, 70, 72, and 74. The velocity distribution for Case E (Figure 66) is suspected to be erroneous in the wake of the blade as evidenced by the increased velocity near the suction and pressure surfaces of the blade; however,

the velocity profile from approximately 10% to 75% passage is consistent with that of Case F (Figure 68). Therefore, the velocity profile for Case E (Figure 66) has been included for completeness despite its probable invalidity in the blade wake.

In addition to the velocity profiles, the specific power and velocity unsteadiness profiles at 105% axial chord and 92% span are shown for Cases A through I in Figures 59, 61, 63, 65, 67, 69, 71, 73, and 75. The specific power, a measure of the circumferential velocity imparted to the fluid by the rotor, was calculated from the Euler pump equation (Equation 2), without the use of inlet guide vanes (i.e., $C_{\theta 1} = 0$). The standard deviation of the ensemble-averaged velocity data (for example, see Figure 59) is a measure of the turbulence or unsteadiness of the flow. The comparisons of flowfield characteristics as a result of the variation of tip gap geometry are presented in Sections 7.4.2 and 7.5.2.
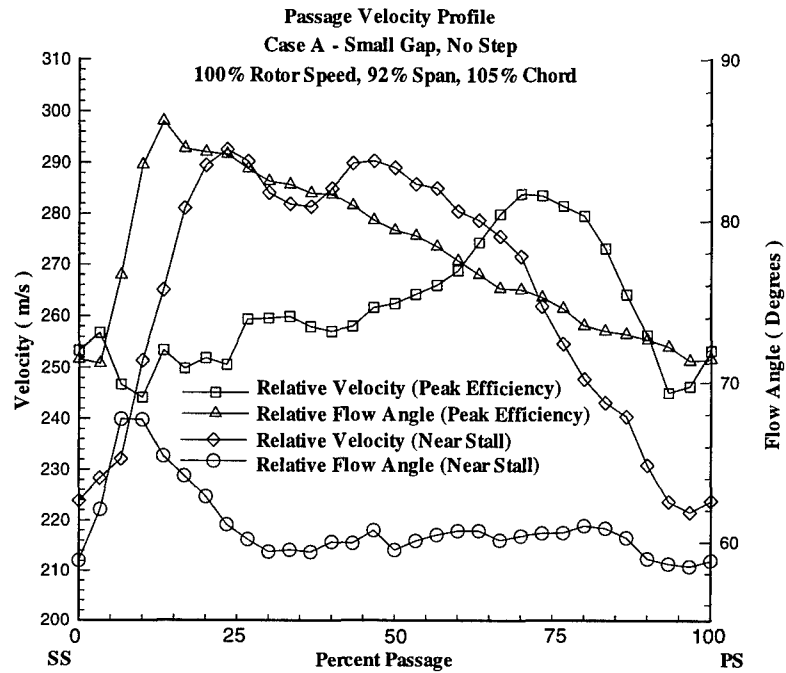
Passage Velocity Profile
Case A - Small Gap, No Step
100% Rotor Speed, 92% Span, 105% Chord

Figure 58. Measured Relative Velocity at Rotor Exit (Case A, 100% Design Rotor Speed)

Passage Specific Power and Velocity Unsteadiness Profiles
Case A - Small Gap, No Step
100% Rotor Speed, 92% Span, 105% Chord
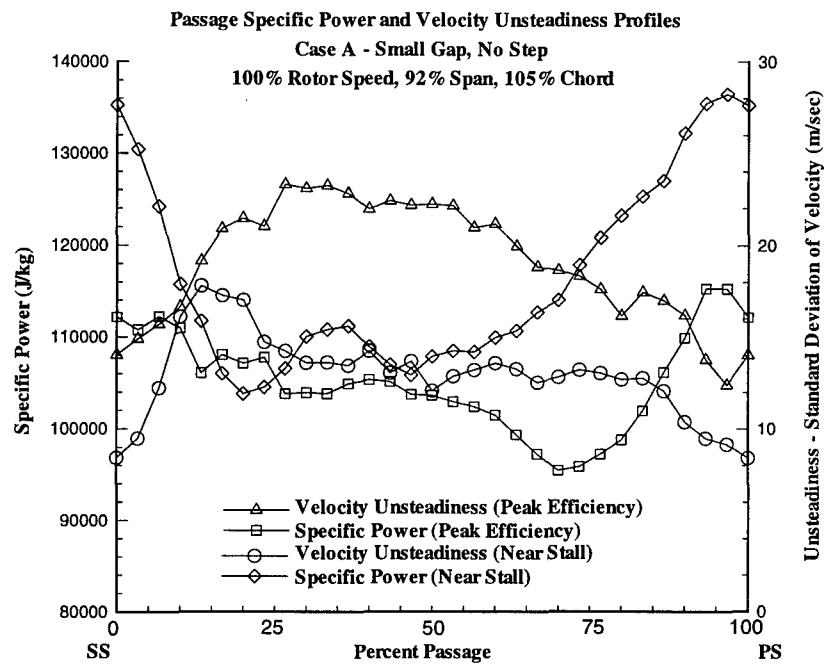
Figure 59. Power and Velocity Unsteadiness at Rotor Exit (Case A, 100% Design Rotor Speed)

100

Passage Velocity Profile
Case B - Small Gap, Aft Step
100% Rotor Speed, 92% Span, 105% Chord

- —□— Relative Velocity (Peak Efficiency)
- —△— Relative Flow Angle (Peak Efficiency)
- —◇— Relative Velocity (Near Stall)
- —○— Relative Flow Angle (Near Stall)
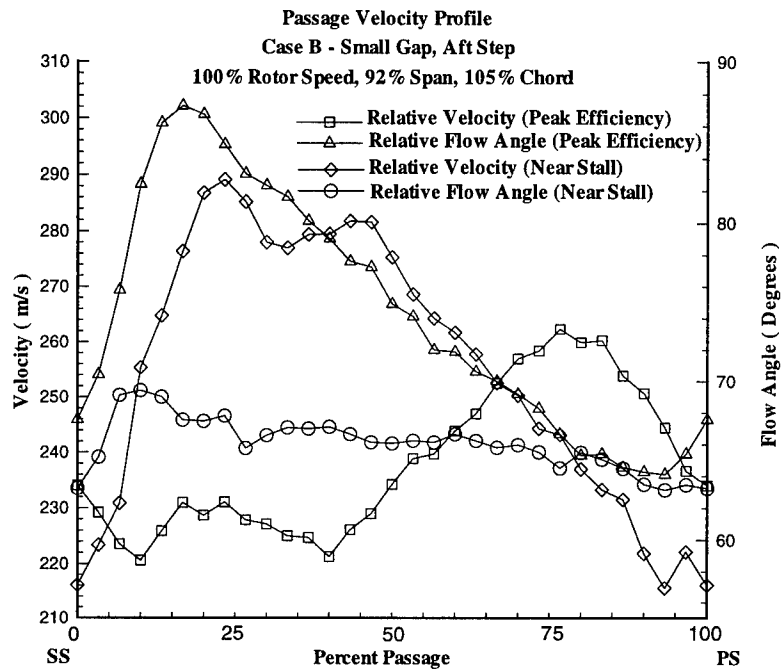
Figure 60. Measured Relative Velocity at Rotor Exit (Case B, 100% Design Rotor Speed)

Passage Specific Power and Velocity Unsteadiness Profiles
Case B - Small Gap, Aft Step
100% Rotor Speed, 92% Span, 105% Chord

- —△— Velocity Unsteadiness (Peak Efficiency)
- —□— Specific Power (Peak Efficiency)
- —○— Velocity Unsteadiness (Near Stall)
- —◇— Specific Power (Near Stall)
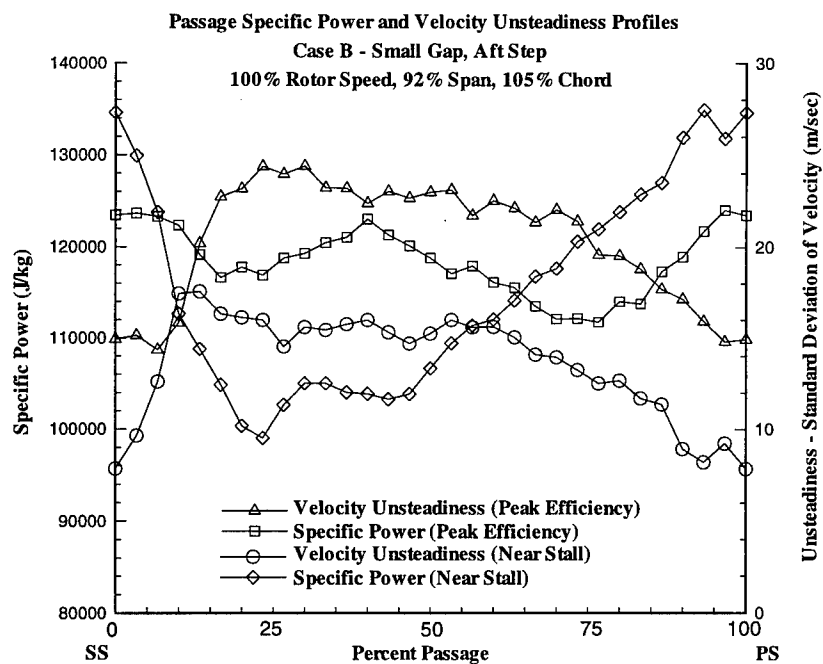
Figure 61. Power and Velocity Unsteadiness at Rotor Exit (Case B, 100% Design Rotor Speed)

101

Passage Velocity Profile
Case C - Small Gap, Forward Step
100 % Rotor Speed, 92 % Span, 105 % Chord

Legend:
- □— Relative Velocity (Peak Efficiency)
- △— Relative Flow Angle (Peak Efficiency)
- ◇— Relative Velocity (Near Stall)
- ⊖— Relative Flow Angle (Near Stall)
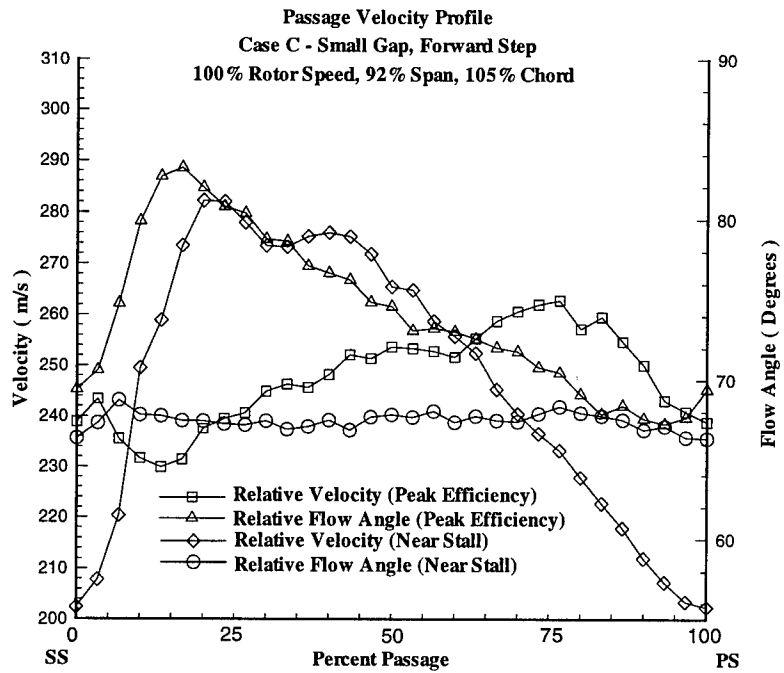
Figure 62. Measured Relative Velocity at Rotor Exit (Case C, 100% Design Rotor Speed)

Passage Specific Power and Velocity Unsteadiness Profiles
Case C - Small Gap, Forward Step
100 % Rotor Speed, 92 % Span, 105 % Chord

Legend:
- △— Velocity Unsteadiness (Peak Efficiency)
- □— Specific Power (Peak Efficiency)
- ⊖— Velocity Unsteadiness (Near Stall)
- ◇— Specific Power (Near Stall)
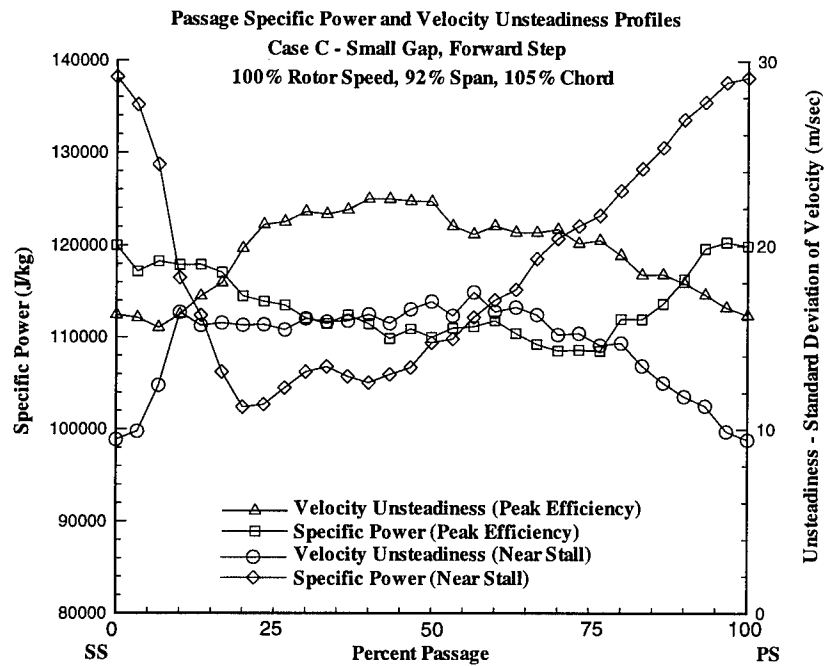
Figure 63. Power and Velocity Unsteadiness at Rotor Exit (Case C, 100% Design Rotor Speed)

102

Passage Velocity Profile
Case D - Medium Gap, No Step
100% Rotor Speed, 92% Span, 105% Chord

Relative Velocity (Peak Efficiency)
Relative Flow Angle (Peak Efficiency)
Relative Velocity (Near Stall)
Relative Flow Angle (Near Stall)
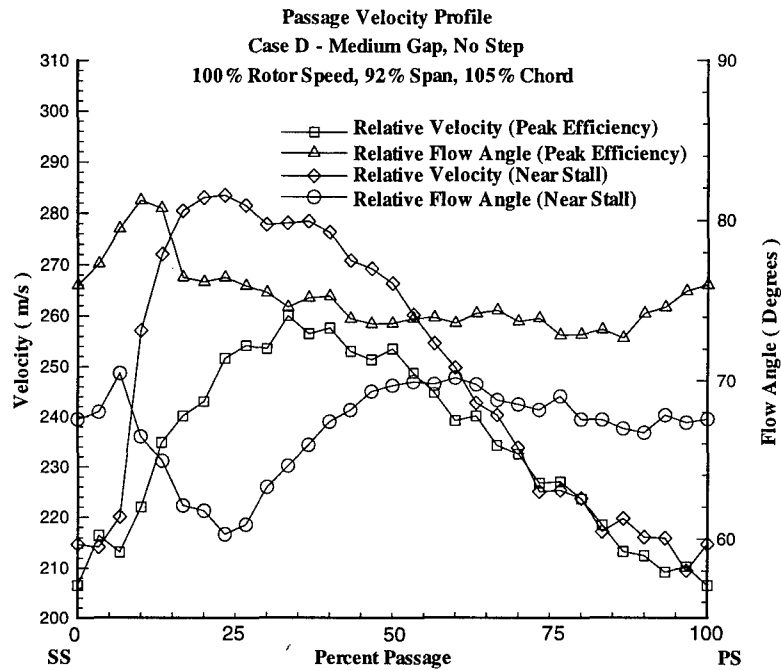
Figure 64. Measured Relative Velocity at Rotor Exit (Case D, 100% Design Rotor Speed)

Passage Specific Power and Velocity Unsteadiness Profiles
Case D - Medium Gap, No Step
100% Rotor Speed, 92% Span, 105% Chord

Velocity Unsteadiness (Peak Efficiency)
Specific Power (Peak Efficiency)
Velocity Unsteadiness (Near Stall)
Specific Power (Near Stall)
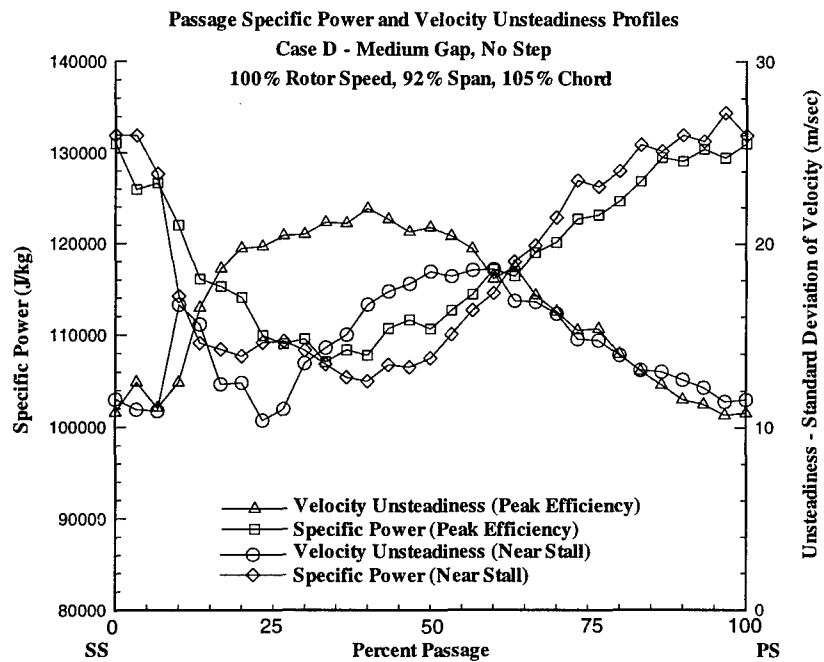
Figure 65. Power and Velocity Unsteadiness at Rotor Exit (Case D, 100% Design Rotor Speed)

103
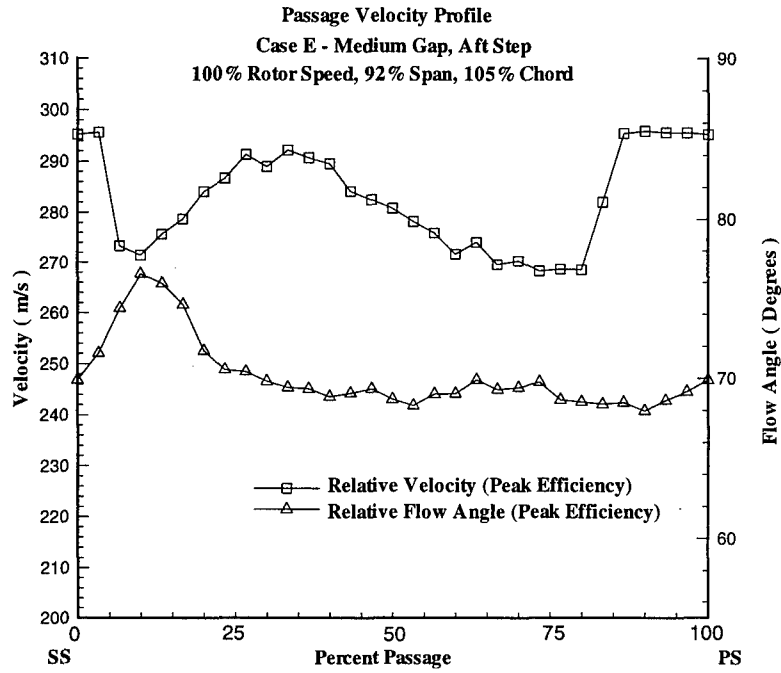
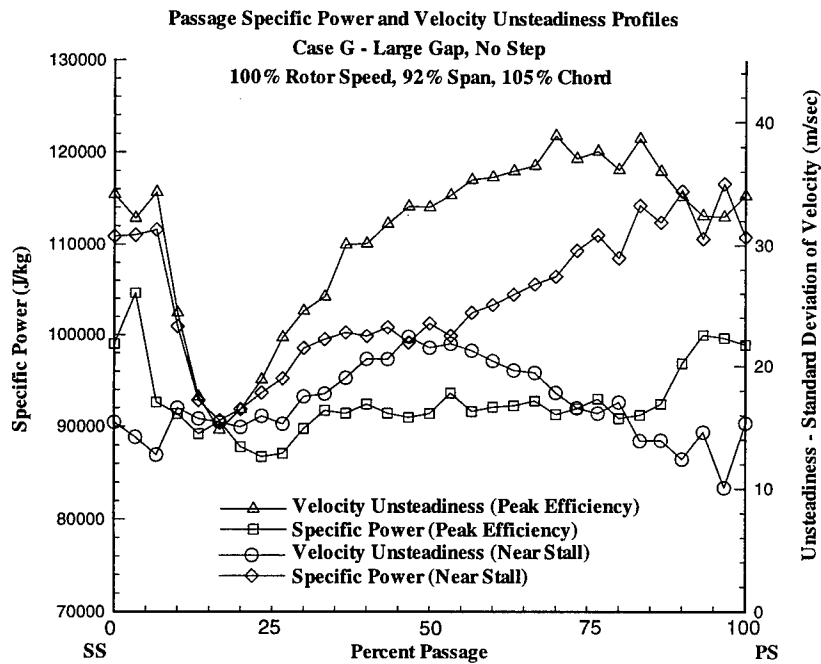Figure 66. Measured Relative Velocity at Rotor Exit (Case E, 100% Design Rotor Speed)
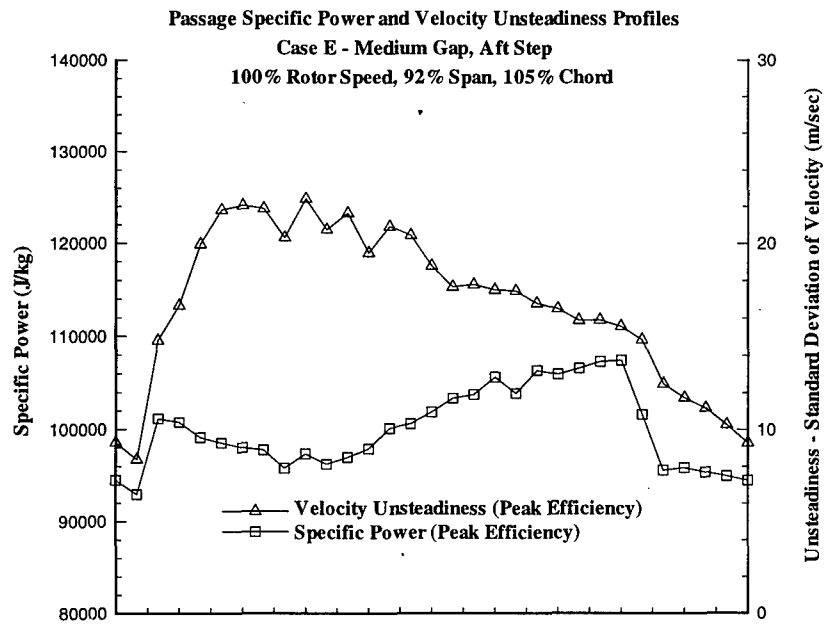
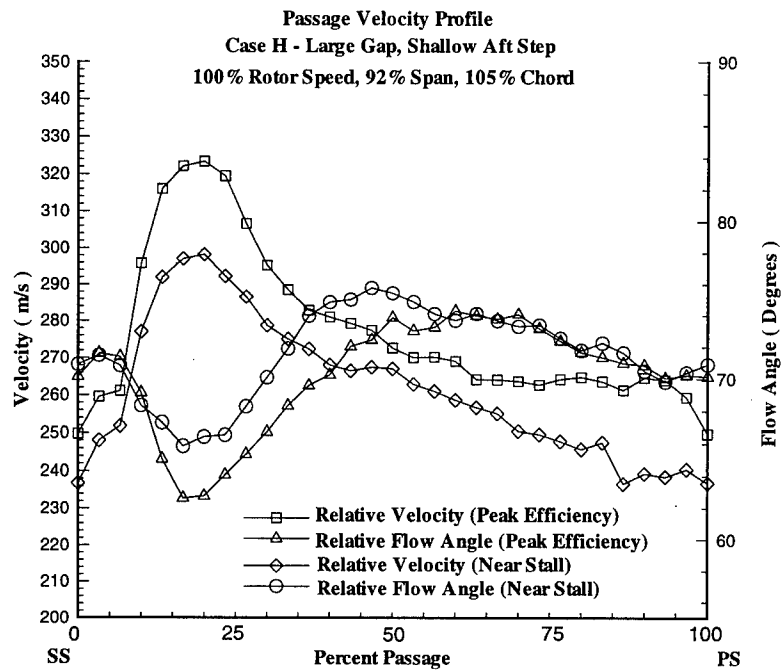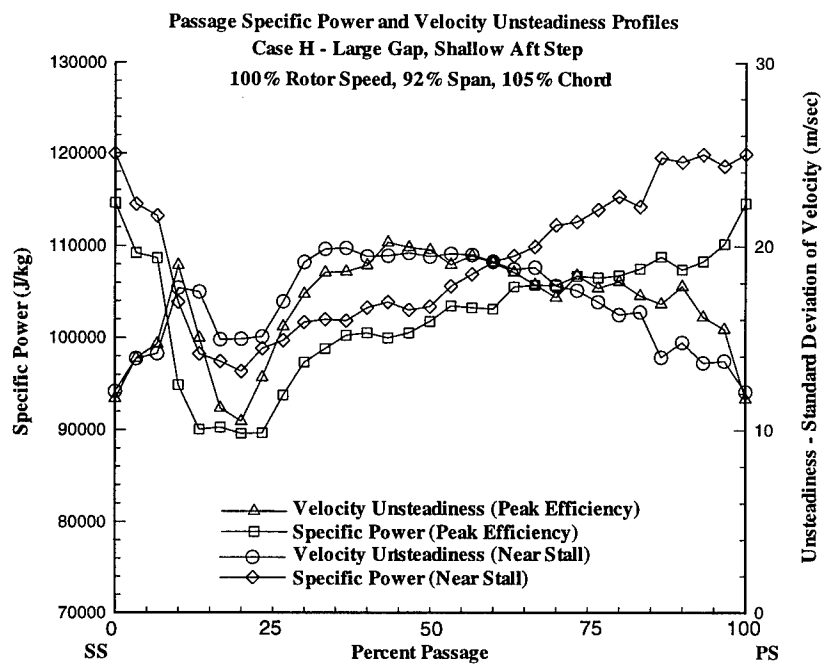Figure 67. Power and Velocity Unsteadiness at Rotor Exit (Case E, 100% Design Rotor Speed)
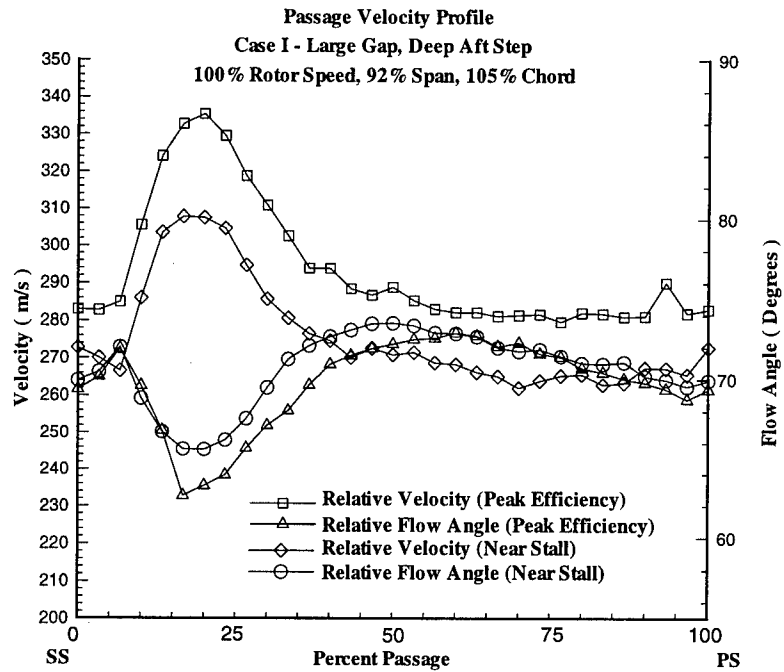
104
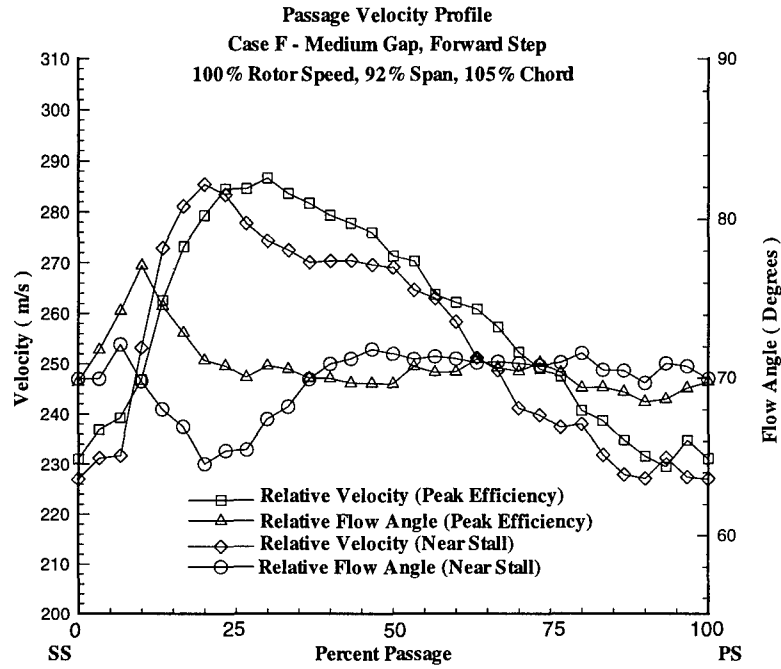
Figure 68. Measured Relative Velocity at Rotor Exit (Case F, 100% Design Rotor Speed)
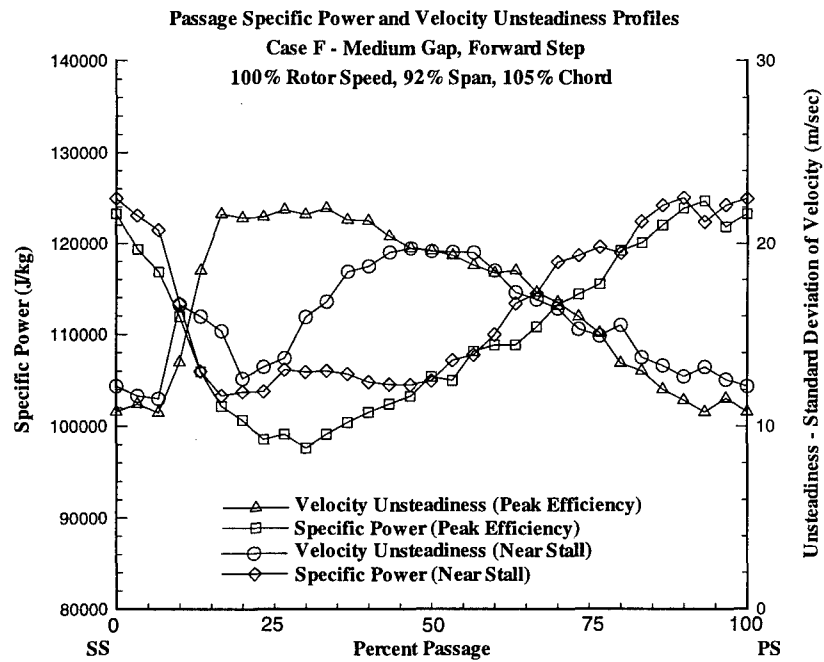
Figure 69. Power and Velocity Unsteadiness at Rotor Exit (Case F, 100% Design Rotor Speed)

105
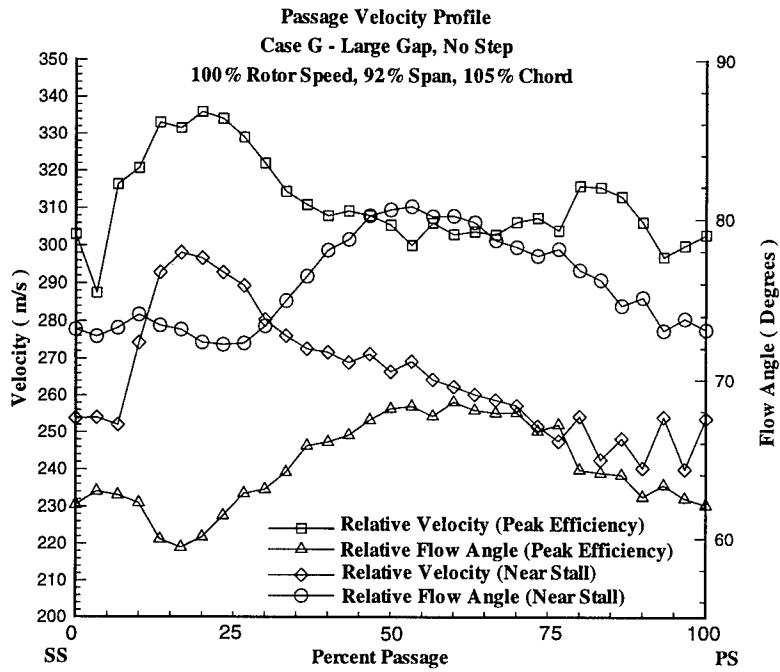
Figure 70. Measured Relative Velocity at Rotor Exit (Case G, 100% Design Rotor Speed)
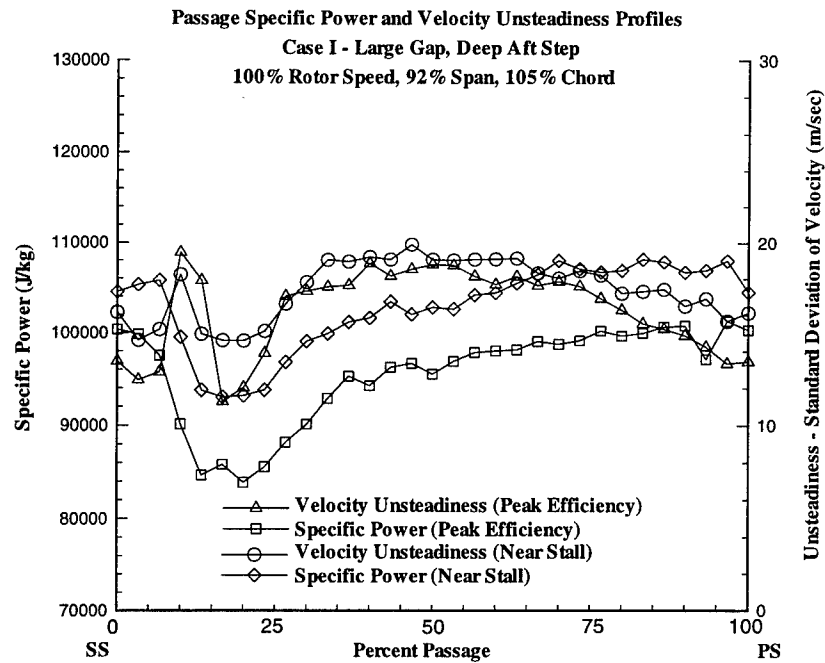

Figure 71. Power and Velocity Unsteadiness at Rotor Exit (Case G, 100% Design Rotor Speed)

106

Passage Velocity Profile
Case H - Large Gap, Shallow Aft Step
100% Rotor Speed, 92% Span, 105% Chord

Figure 72. Measured Relative Velocity at Rotor Exit (Case H, 100% Design Rotor Speed)

Passage Specific Power and Velocity Unsteadiness Profiles
Case H - Large Gap, Shallow Aft Step
100% Rotor Speed, 92% Span, 105% Chord

Figure 73. Power and Velocity Unsteadiness at Rotor Exit (Case H, 100% Design Rotor Speed)

107

Figure 74. Measured Relative Velocity at Rotor Exit (Case I, 100% Design Rotor Speed)

Figure 75. Power and Velocity Unsteadiness at Rotor Exit (Case I, 100% Design Rotor Speed)

108

7.3 Comparisons with Computational Fluid Dynamics

Computational Fluid Dynamic solutions were obtained for five casing configurations with operating conditions of 100% rotor speed and mass flow for peak efficiency; these solutions corresponded to Cases A, D, E, F, and G of Figure 23. For each CFD solution, the total pressure ratio, efficiency, tip region static pressures, and rotor wake velocity profiles were compared to those from experimental testing. Details of these comparisons are shown in the following sections.

7.3.1 Pressure Ratio and Efficiency

The performance trends obtained from CFD were not ideally consistent with experimental measurement. Overall performance data were obtained through area-averaged integration of each CFD solution over the inlet and exit surfaces. As seen in Table 7, peak efficiency for the CFD solution occurred at a lesser mass flow than for experiment, and the pressure ratio and efficiency associated with these mass flows were generally higher than the measured values. Interestingly, the CFD results indicated an unstepped intermediate tip clearance (Case D) to be the optimum based on pressure ratio and efficiency. More importantly, the CFD solutions predicted higher losses in pressure ratio and efficiency when stepped tip gaps were introduced. The CFD predictions were sufficiently accurate to quantify the general performance of the ADLARF rotor within an 8.5% maximum error from experiment (see Table 7). However, due to this error, CFD could not be used with certainty to discriminate performance trends associated with varying casing treatments; the variation of casing treatments during experiment produced less than 3% variation of pressure ratio and efficiency from Case A (small gap, no step) as shown in Figures 32 through 35. Also, it should be noted that the maximum uncertainty of the experimental data was approximately 0.08% for pressure ratio and 1.0% for efficiency (see Table 5). Despite these differences, CFD can provide insight into flow elements and their interactions.

109

Table 7. Comparison of Total Pressure Ratio and Efficiency between CFD and Experiment

	Case A Small Gap No Step	Case D Medium Gap No Step	Case E Medium Gap Aft Step	Case F Medium Gap Forward Step	Case G Large Gap No Step
Mass Flow Rate (kg/sec)					
CFD	70.5	69.5	70.8	71.1	70.3
Experiment	71.6	71.6	72.4	72.1	71.5
CFD Error[1] (percent)	-1.5	-2.9	-2.2	-1.4	-1.7
Total Pressure Ratio					
CFD	2.64	2.69	2.51	2.55	2.52
Experiment	2.53	2.48	2.5	2.49	2.42
CFD Error[1] (percent)	+4.3	+8.5	+0.4	+2.4	+4.1
Isentropic Efficiency					
CFD	0.876	0.882	0.845	0.846	0.846
Experiment	0.850	0.858	0.858	0.854	0.834
CFD Error[1] (percent)	+3.0	+2.9	-1.5	-0.9	+1.4

Note 1: CFD Error is the ratio of the difference between the CFD and experimental value
to the experimental value

7.3.2 Tip Region Mach Number, Static Pressure, and Momentum

Cascade plots of relative Mach number, normalized pressure, and axial momentum calculated for each CFD solution are seen in Figures 76, 77, 78, 79, and 80. These figures are derived from CFD solutions using the theory described in Chapter 5; these figures characterize the tip region flowfield of the ADLARF rotor for Cases A, D, E, F, and G of Figure 23. In each pressure cascade plot, the static pressure is normalized by the stagnation pressure at the rotor inlet.

The leading edge shock and tip leakage vortex plotted in each normalized pressure cascade were similar to those measured by experiment (Section 7.1). For example, as seen in the pressure plot for Case D (Figure 77), the obliquity and curvature of the shock from CFD were similar to the shock geometry from experiment (Figure 46). However, the measured pressures typically indicated more distortion (concavity[4] near the blade suction surface) of the leading edge shock due to interaction with the tip leakage vortex (evidenced by the trough of low pressure near the blade suction surface) than did the CFD. Also, for cases incorporating stepped tip gaps (Cases E and F), the obliquity of the leading edge shock was more swept for the CFD solution (Figures 77 and 78, respectively) than for experiment (Figures 48 and 50, respectively). The tip leakage vortex was clearly evident in the CFD cascade plots of Figures 76, 77, 78, 79, and 80; it is identified by the strong gradient of relative Mach number and axial momentum emanating from the blade leading edge and axially and circumferentially transiting the passage. In the pressure plot of these figures, the path of the tip leakage vortex also was identified by the concavity of the pressure gradient. The tip leakage vortex calculated by CFD transited the passage to the pressure side of the adjacent blade at approximately the same rate as identified by experiment. For example, in the experimentally measured static pressure plot for Case D at peak efficiency mass flow (Figure 46), the tip leakage vortex transited the

---

[4]The center of concavity in the leading edge shock indicates where the center of the tip leakage vortex impacts the leading edge shock.

passage and impinged upon the pressure surface of the adjacent blade at approximately 90% axial

chord. For the CFD solution (Figure 77), the tip leakage vortex followed the same path. Thus, the

general shape of the shock-vortex interaction and the pressure distribution within each passage were
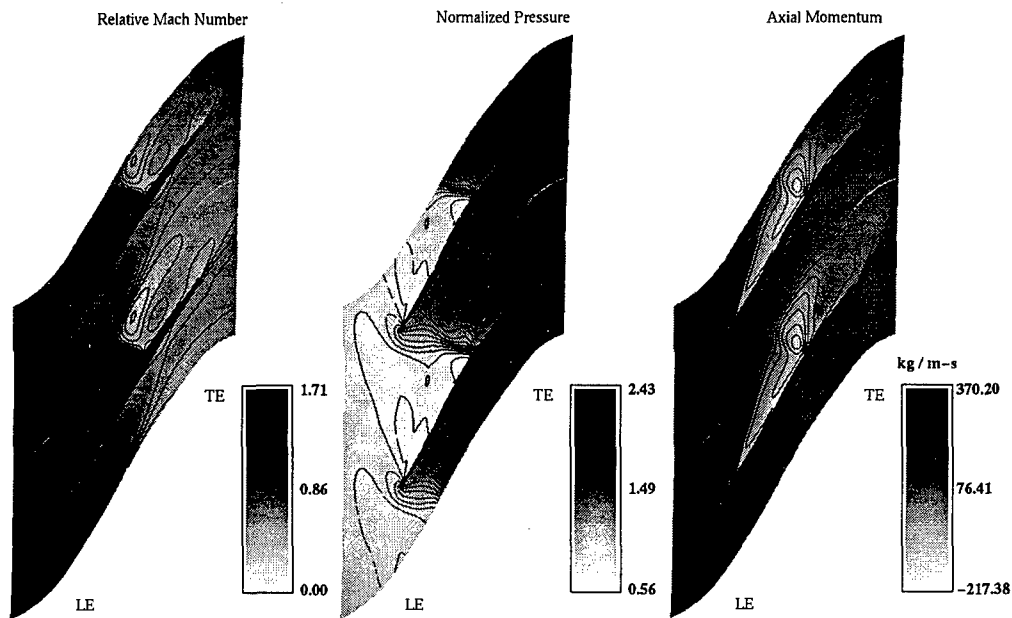
similar.

Figure 76. Theoretical Tip Region Flowfield for Case A (100% Design Rotor Speed, Peak Efficiency)
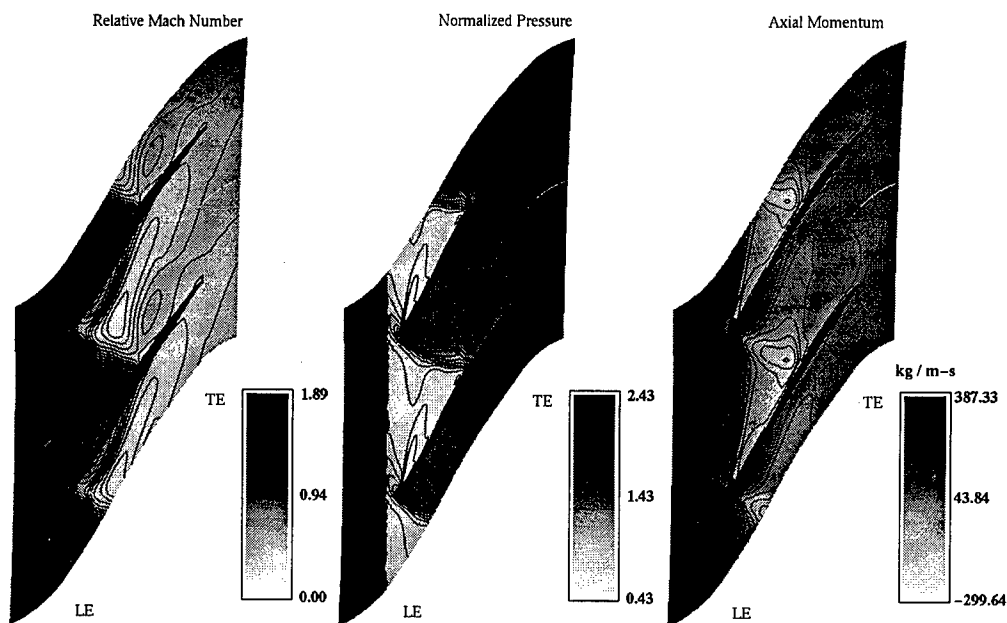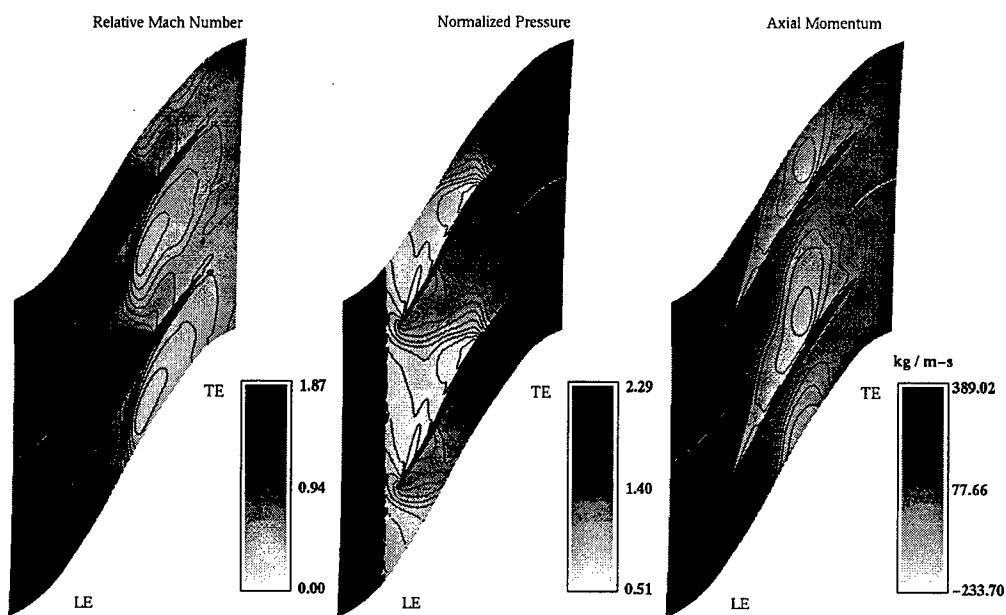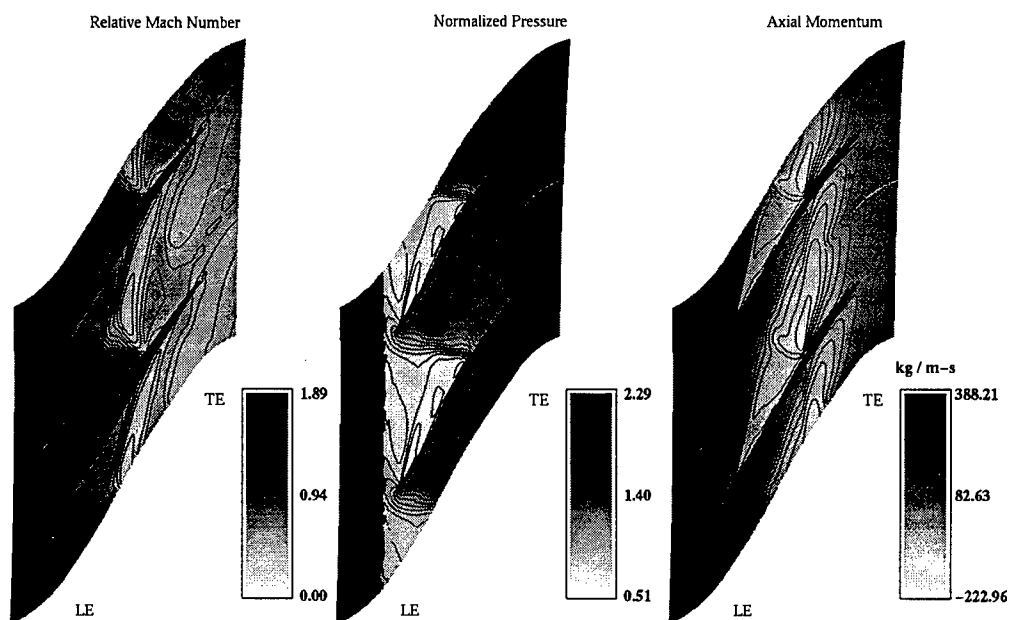
Figure 77. Theoretical Tip Region Flowfield for Case D (100% Design Rotor Speed, Peak Efficiency)

Figure 78. Theoretical Tip Region Flowfield for Case E (100% Design Rotor Speed, Peak Efficiency)

Figure 79. Theoretical Tip Region Flowfield for Case F (100% Design Rotor Speed, Peak Efficiency)
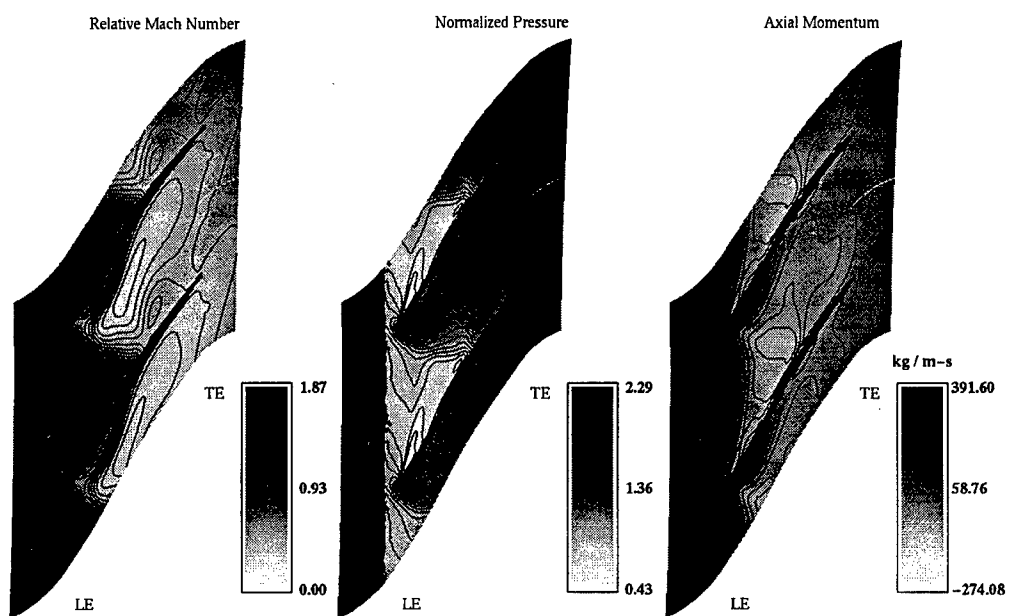
Figure 80. Theoretical Tip Region Flowfield for Case G (100% Design Rotor Speed, Peak Efficiency)

114

7.3.3 Rotor Exit Velocity

Velocity and flow angle profiles near the rotor exit (92% span, 105% axial chord) for each CFD solution are seen in Figures 81, 83, 85, 87, and 89. Also, the specific power profiles at 92% span and 105% chord for each CFD solution are seen in Figures 82, 84, 86, 88, and 90.

Differences existed between measured and calculated relative velocity near the rotor exit (92% span, 105% axial chord) for peak efficiency operation. The measured relative velocity for Cases A, D, E, F, and G (Figures 58, 64, 66, 68, and 70, respectively) was consistently greater than the relative velocity calculated from CFD (Figures 81, 83, 85, 87, and 89, respectively). Except for Case G (large gap, no step), the mean velocity from CFD was typically 20 to 85 m/sec slower than the mean velocity from experiment as seen in Table 8. For Case G, the mean velocity from CFD was 133 m/sec slower than the experimental velocity. Further, except for Case G, the measured relative flow angle at the rotor trailing edge (Figures 58, 64, 66, and 68) was larger than the angle calculated from CFD (Figures 81, 83, 85, and 87).

Table 8. Comparison of Rotor Exit Flow Velocities between CFD and Experiment

Case	Experimental Relative Velocity (m/sec)			CFD Relative Velocity (m/sec)		
	Maximum	Minimum	Mean	Maximum	Minimum	Mean
A	284	245	261	268	204	240
D	260	205	234	210	172	182
E	295	268	282	230	184	197
F	285	230	249	224	172	189
G	335	295	311	232	160	178

Despite these differences, in most cases, except Case A, the calculated velocity relative to the rotor generally followed the same profile (i.e., approximate location within the passage of the maximum and minimum values and the general slope of the curve) as the measured velocity. For Case A, the velocity profile from CFD (Figure 81) was shifted toward the pressure side of the blade by approximately 25% of the passage pitch compared to the measured velocity profile (Figure 58).

Also, for both measured and CFD results for all cases, the location within the passage of the peak relative velocity was not coincident with the location of the peak relative flow angle. Therefore, the specific power, which combines the relative velocity with the relative flow angle via Equation 2, was useful in determining the work imparted to the fluid by the rotor as a function of passage location. For Cases A[5], D, E, F, and G, the specific power profile (neglecting magnitude scale) calculated from CFD (Figures 82, 84, 86, 88, and 90, respectively) generally agreed with the specific power profile derived from measured velocity (Figures 59, 65, 67, 69, and 71, respectively). Therefore, although the magnitudes of velocity differed between CFD and experiment, the similarity of velocity and specific power profiles from CFD and experiment suggested that CFD could be used to provide insight into the location of blockage within a rotor passage.

Also, the average specific power for the passage at 92% span was calculated for each experimental and computational data set, and the results are shown in Figure 91. The average specific power calculated from CFD was consistently greater than the power derived from experiment. To achieve a greater specific power, the absolute tangential velocity at the rotor trailing edge ($C_{\theta 2}$ in Figure 1) must be greater for the same rotor speed. A greater absolute tangential velocity for each CFD solution would result from a tip leakage vortex that has not dissipated to the same extent as that from experiment. For example, as seen in the rotor wake (105% chord) passage cross-section of relative Mach number (CFD solution) for Case D (Figure 92), at 92% span, the tangential velocity was affected by the tip leakage vortex, the displaced flow around the vortex, and the blade velocity. The vortex directly imparted a tangential velocity to the fluid near the pressure surface of the blade,

---

[5] A passage profile shift of 25% pitch toward the pressure surface for the CFD prediction is again noted as previously mentioned.
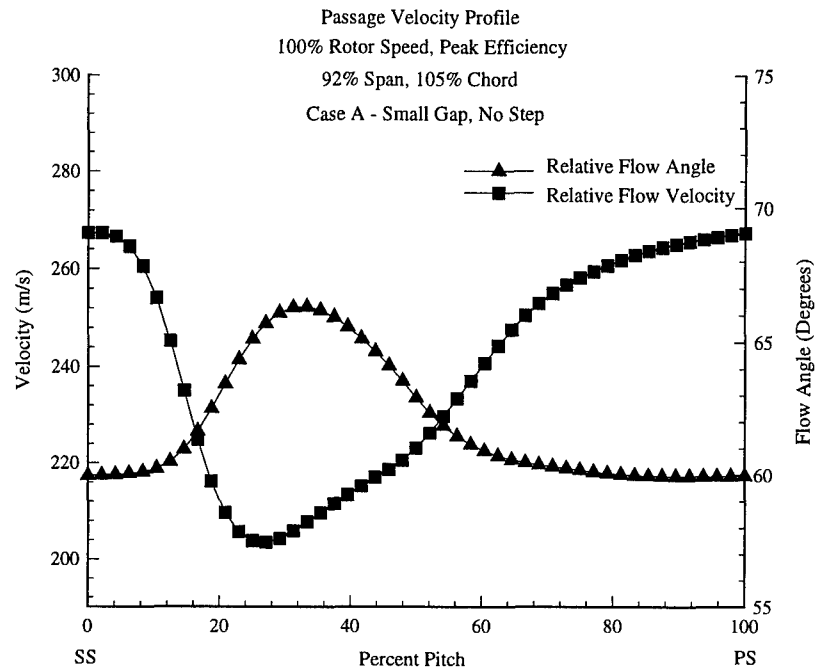
Figure 81. Theoretical Relative Velocity at Rotor Exit (Case A, 100% Design Rotor Speed)
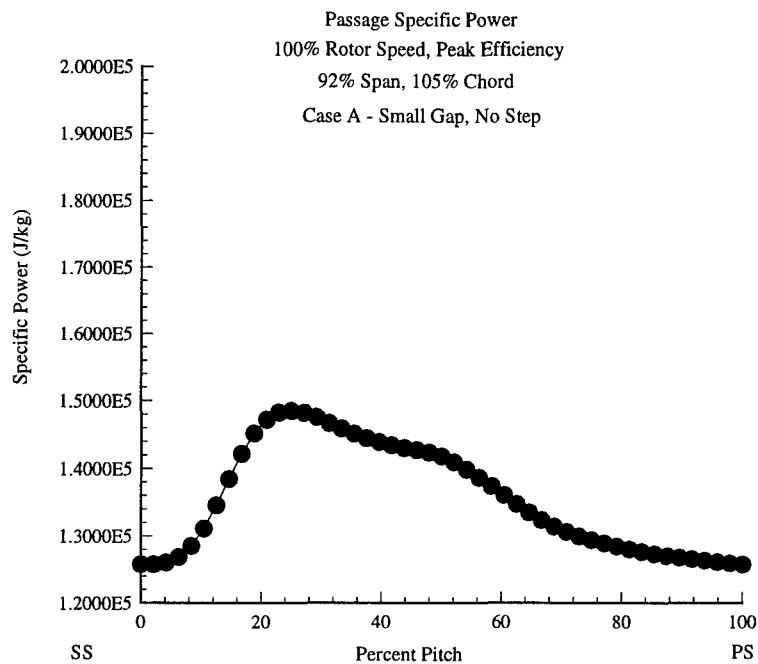
Figure 82. Theoretical Specific Power Profile at Rotor Exit (Case A, 100% Design Rotor Speed)

117
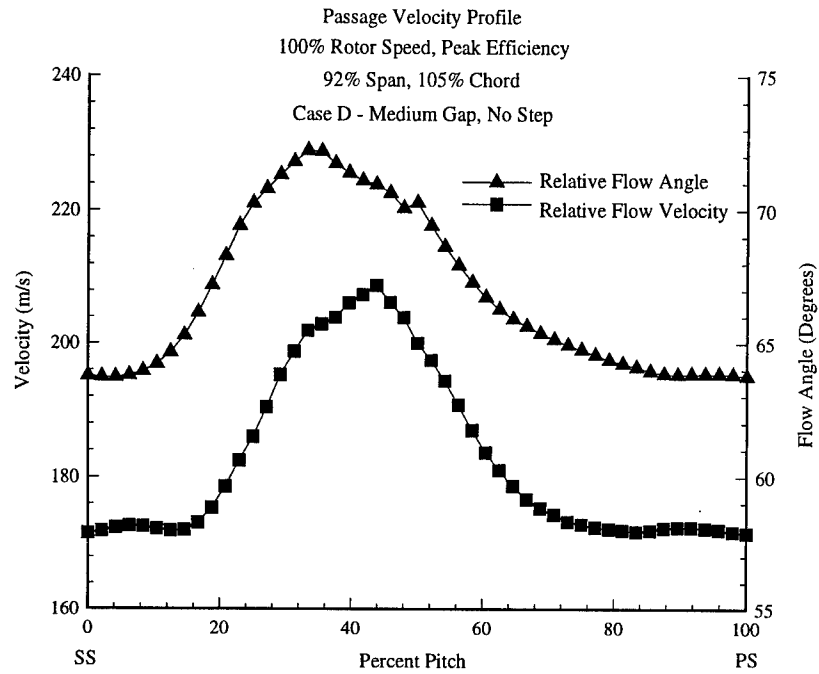
Figure 83. Theoretical Relative Velocity at Rotor Exit (Case D, 100% Design Rotor Speed)
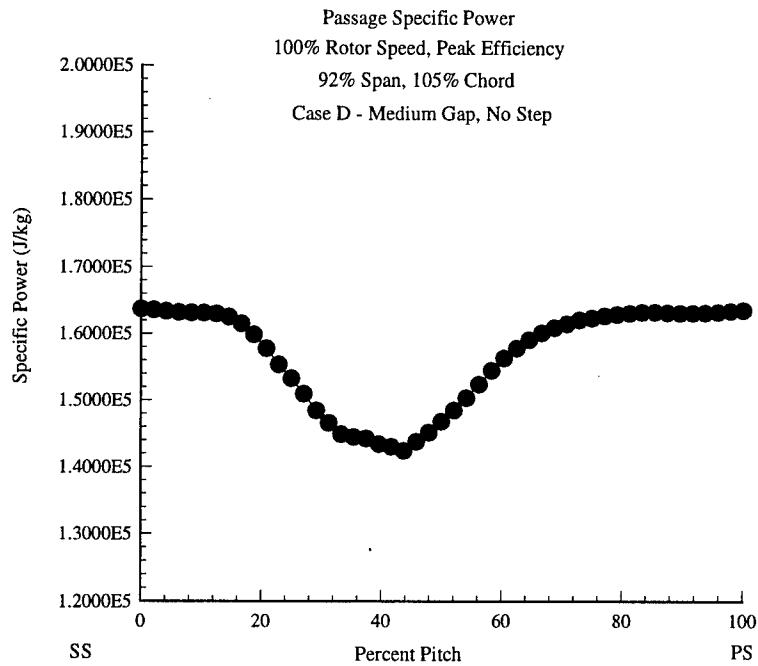

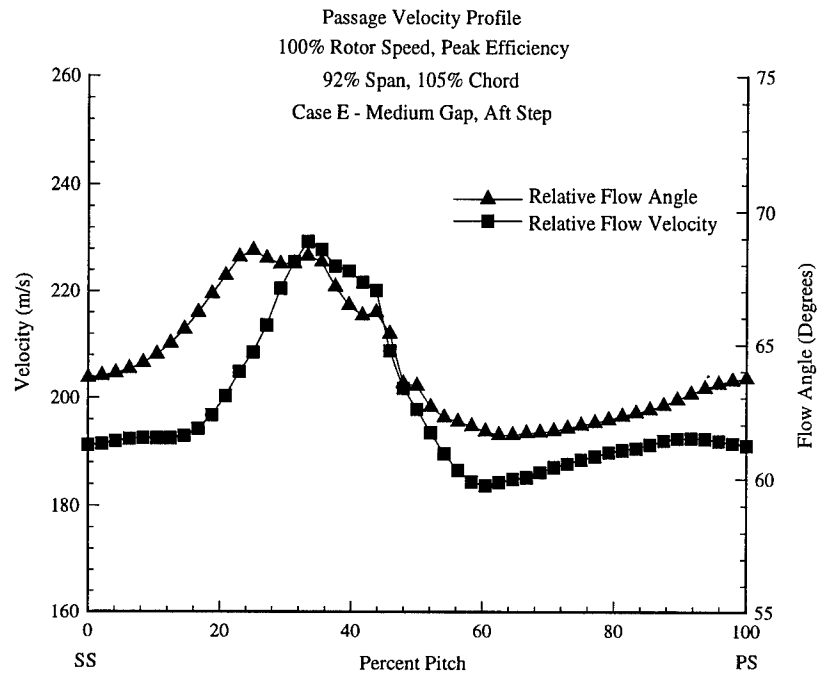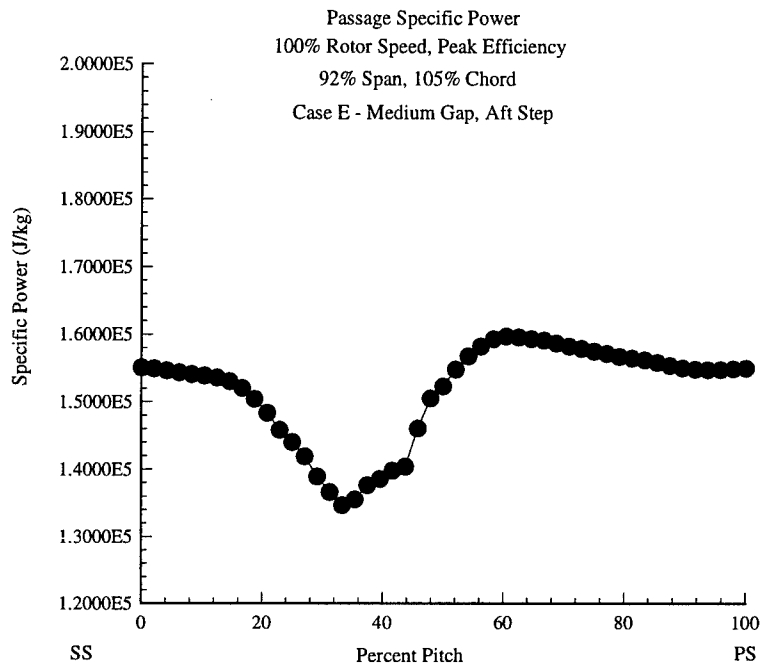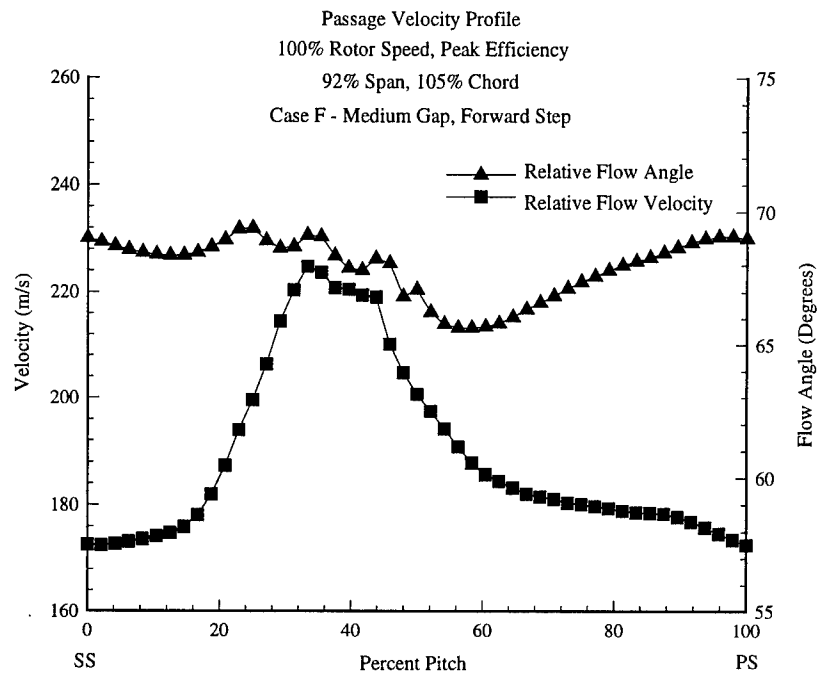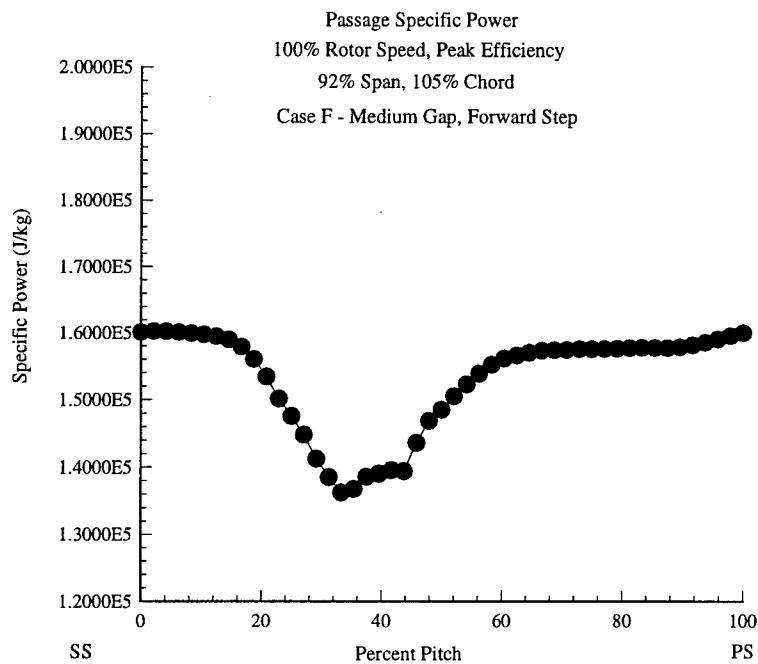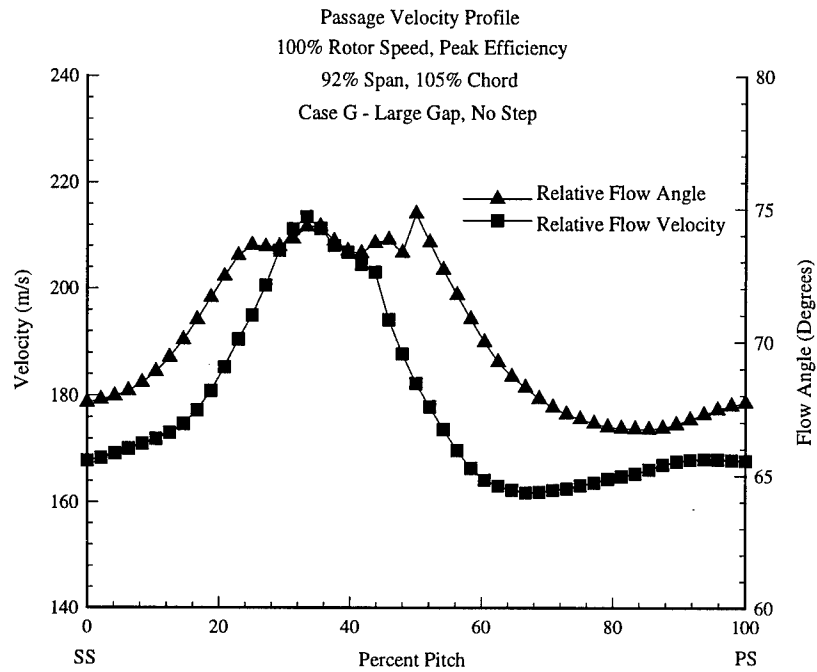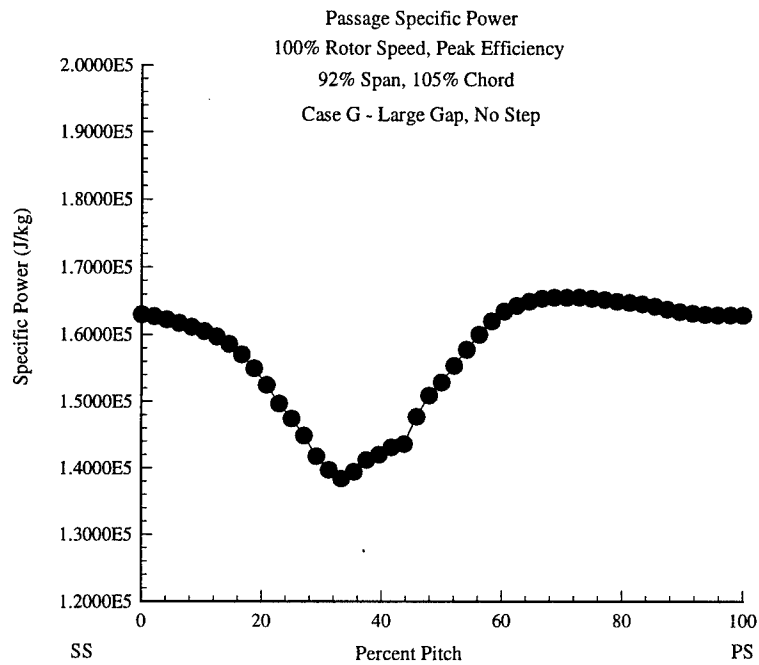Figure 84. Theoretical Specific Power Profile at Rotor Exit (Case D, 100% Design Rotor Speed)

118

Passage Velocity Profile
100% Rotor Speed, Peak Efficiency
92% Span, 105% Chord
Case E - Medium Gap, Aft Step

Figure 85. Theoretical Relative Velocity at Rotor Exit (Case E, 100% Design Rotor Speed)

Passage Specific Power
100% Rotor Speed, Peak Efficiency
92% Span, 105% Chord
Case E - Medium Gap, Aft Step

Figure 86. Theoretical Specific Power Profile at Rotor Exit (Case E, 100% Design Rotor Speed)

119

Passage Velocity Profile
100% Rotor Speed, Peak Efficiency
92% Span, 105% Chord
Case F - Medium Gap, Forward Step

Figure 87. Theoretical Relative Velocity at Rotor Exit (Case F, 100% Design Rotor Speed)

Passage Specific Power
100% Rotor Speed, Peak Efficiency
92% Span, 105% Chord
Case F - Medium Gap, Forward Step

Figure 88. Theoretical Specific Power Profile at Rotor Exit (Case F, 100% Design Rotor Speed)

120

Passage Velocity Profile
100% Rotor Speed, Peak Efficiency
92% Span, 105% Chord
Case G - Large Gap, No Step

Figure 89. Theoretical Relative Velocity at Rotor Exit (Case G, 100% Design Rotor Speed)

Passage Specific Power
100% Rotor Speed, Peak Efficiency
92% Span, 105% Chord
Case G - Large Gap, No Step

Figure 90. Theoretical Specific Power Profile at Rotor Exit (Case G, 100% design Rotor Speed)

121

and the blockage created by the vortex altered the flow to impart a tangential velocity near the suction surface of the blade. Therefore, a larger and stronger tip leakage vortex produced a larger tangential velocity for the CFD solutions than for experiment; a larger specific power was the result. Further, the model for energy dissipation used in the CFD was the most likely cause for its larger tip leakage vortex.
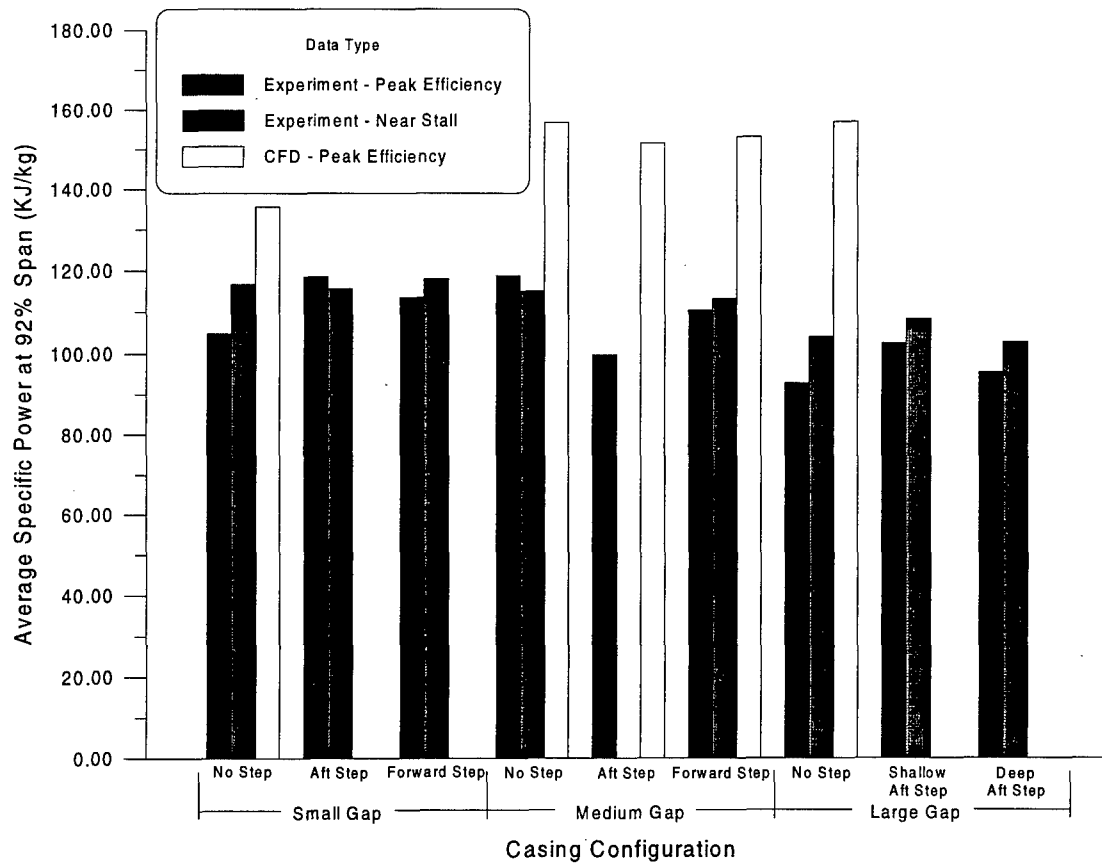
Figure 91. Average Specific Power Near Rotor Exit (92% Span, 105% Chord)

Relative Mach Number
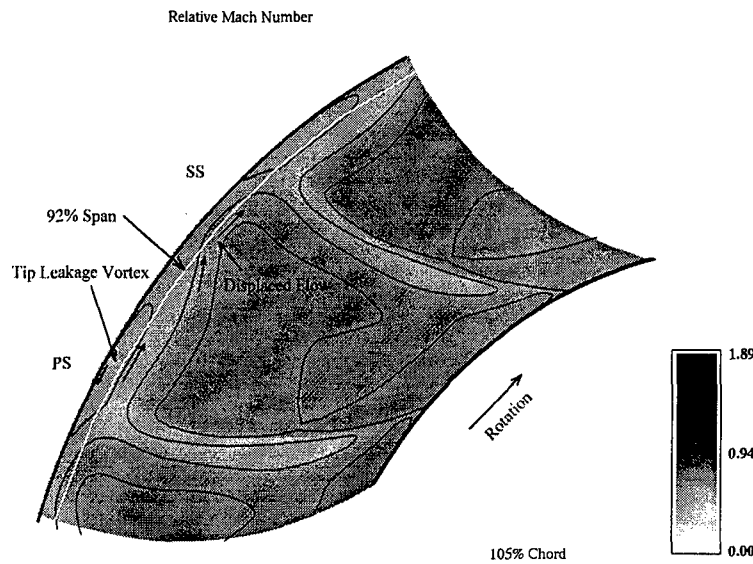
Figure 92. Influence of Tip Leakage Vortex on Tangential Velocity (Case D, 100% Design Speed)

7.3.4 Explanation of Differences between CFD and Experiment

Noting the differences above, the CFD solutions were considered sufficiently valid to provide

insight into the flow where experimental measurements were not possible. The differences that

existed between measured and CFD characteristics were attributed to the following:

1. No attempt was made to optimize the closure coefficients in the semi-empirical $K-\varepsilon$ turbulence model, and this turbulence model influenced all aspects of the flow. As mentioned previously in Section 7.3.2, the CFD solution did not appear to predict a shock-vortex interaction as strong as was identified by experiment. Consequently, the tip leakage vortex did not dissipate as rapidly for the CFD model as it did for experiment (see Section 7.3.3). Also, the turbulence model used was an adaptation of Chien's [16] model which was developed for low Reynold's number flows; tip leakage vortices are high Reynold's number flows (see Sections 2.2.1 and 2.2.2).

2. The air flowing through the CFD control volume was assumed to behave as a calorically and thermally perfect gas. Real gas and relative humidity effects were not modeled.

3. The coefficient of viscosity in the CFD model was assumed to be a known function of static temperature according to Sutherland's equation. This equation introduces errors of up to 2% in the temperature range from 170 to 1900K (White [98]). Also, the bulk viscosity of the fluid in the CFD model was assumed negligible; this assumption prevented truly accurate modeling of

123

shock waves (see Anderson et al. [6]).

4. The Boussinesq approximation was made to simplify turbulence modeling, and the laminar and turbulent Prandtl numbers were assumed constant.

5. Round-off and truncation errors were inherent in the computational process.

6. Laser velocimetry did not accurately measure the velocities in the near-wall regions where viscous forces dominated. The seed particles did not sufficiently penetrate the viscous boundary layers of the rotor blades and endwall region nor the low-velocity core of the tip leakage vortex. Additionally, the acquisition software often rejected velocity measurement of the few particles that penetrated these regions based on Chauvenet's criteria. Consequently, velocity measurement in these slower regions was difficult and possibly erroneous.

7.4 Effect of Tip Clearance on Rotor Flowfield

7.4.1 Effect of Tip Clearance on Tip Region Static Pressure

The principal effect of increased clearance on the tip region flowfield was the associated increase in the size and strength of the tip leakage vortex. With increased clearance, the tip leakage vortex, evidenced by a low pressure trough on the suction side of the blade in the tip region static pressure plots for Cases A, D, and G (Figures 40, 46, and 52, respectively), also had greater influence in the distortion of the leading edge shock and creation of larger zones of low-velocity fluid downstream of the shock-vortex interaction zone. Also, the unsteadiness of the flow, as shown in Figures 41, 47, and 53 for Cases A, D, and G, respectively, was found to increase with increased tip clearance, particularly in the shock-vortex interaction zone and the area of vortex impingement on the adjacent blade.

Although not confirmed by the experimental data, the CFD solutions indicated that the path of the vortex became more normal to the flow (moved farther upstream) with increased clearance. This effect was clearly identified in the Relative Mach Number and Axial Momentum cascade plots of Figures 76, 77, and 80.

7.4.2 Effect of Tip Clearance on Rotor Exit Velocity

The influence of the tip leakage vortex on the measured relative velocity profile at 105% chord and 92% span was evident in Figures 58, 64, and 70, corresponding respectively to Cases A, D, and G. Regions of increased velocity were due to flow acceleration around the blockage associated with the tip leakage vortex and the wake of the blade boundary layer. For the small clearance with no steps (Case A) at peak efficiency mass flow, the peak relative velocity was located at approximately 75% of passage from the blade suction surface (Figure 58). With increased tip clearance, the location of peak velocity migrated toward the suction surface of the blade as shown in Figures 64 and 70; the peak velocity for the large clearance with no steps (Case G) was located at approximately 20% of circumferential passage. Likewise, for near-stall operation, the location of peak velocity migrated from approximately 25% of passage from the blade suction surface for Case A (Figure 58) to approximately 20% passage for Case G (Figure 70). This migration indicated that the blockage near the blade pressure surface increased with increased clearance; this increased blockage was due to a larger tip leakage vortex impinging upon the pressure surface of the adjacent blade.

7.4.3 Effect of Tip Clearance on Throughflow Area

Increased tip clearance yielded a smaller flow area for the high-energy air of the interior passage. The CFD solutions provided insight into the effects of increased clearance on the flow blockage. In Figures 93 through 96, planar views of the relative Mach number at 50%, 70%, 90%, and 105% chord are shown for Case A (small gap, no step); these figures depict the axial progression of passage blockage for Case A. For this case, the tip leakage vortex, identified by the elliptical shape of low-velocity fluid near the rotor case, grew radially and circumferentially as it progressed downstream and merged with the low-energy fluid on the suction surface of the blade. The vortex engulfed less than 50% of the circumferential passage near the outer casing, thereby not provid-

ing sufficient blockage to seal the tip region. It also consumed less than 8% of the passage area. A much larger tip leakage vortex was seen for Case D (medium gap, no step) at all axial positions (Figures 97 through 100); this vortex grew in radial and circumferential extent as it migrated to the pressure surface of the adjacent blade with increased axial position. It was noted that the vortex for this case engulfed greater than 75% of the circumferential passage near the annulus casing; this blockage provided greater sealing of the tip region as it consumed a maximum of 15% of the passage area. Casing configuration G (large gap, no step) effected the largest tip leakage vortex (Figures 101 through 104). The blockage for this case engulfed approximately 80% of the circumferential passage near the rotor tip, but it also consumed up to 20% of the passage area. Therefore, increased tip clearance created a larger source of low-energy blockage affecting the passage throughflow area.
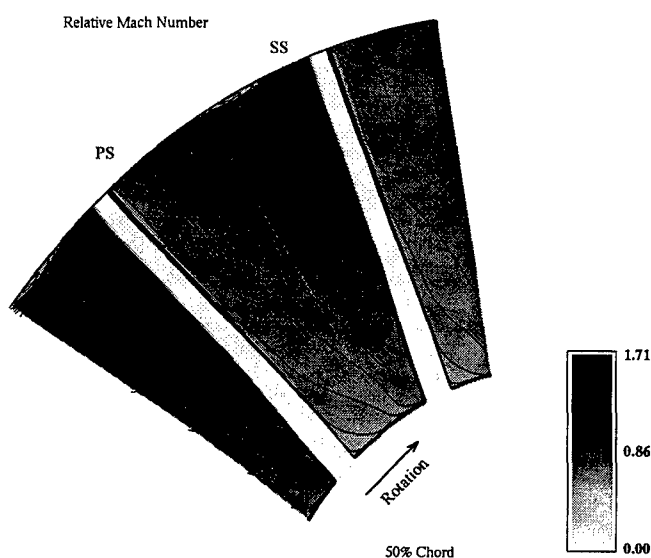
Figure 93. Passage Relative Mach Number for Case A (50% Chord)
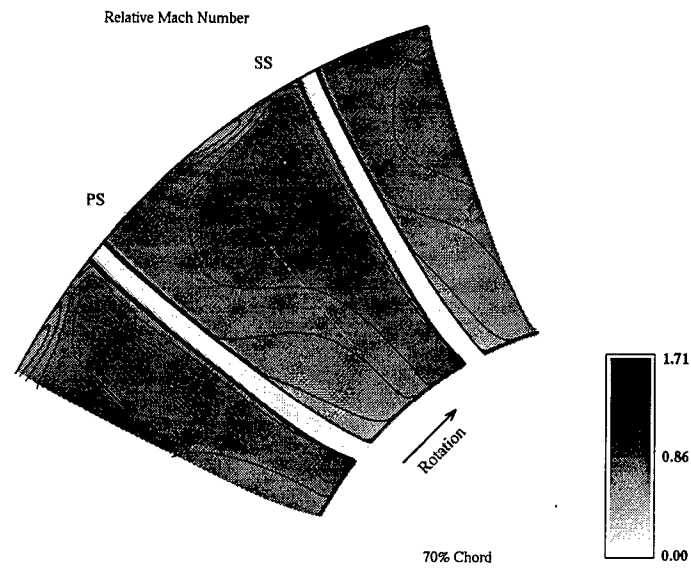
Figure 94. Passage Relative Mach Number for Case A (70% Chord)
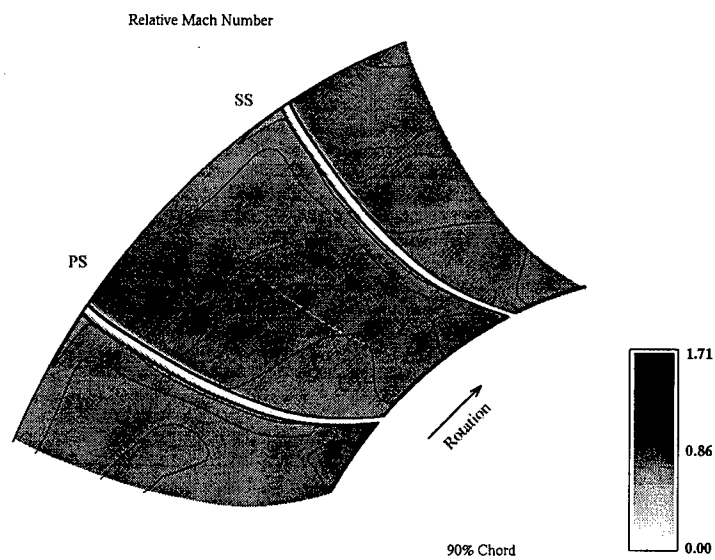
Figure 95. Passage Relative Mach Number for Case A (90% Chord)

127

Relative Mach Number

SS

PS

Rotation

1.71

0.86

105% Chord

0.00
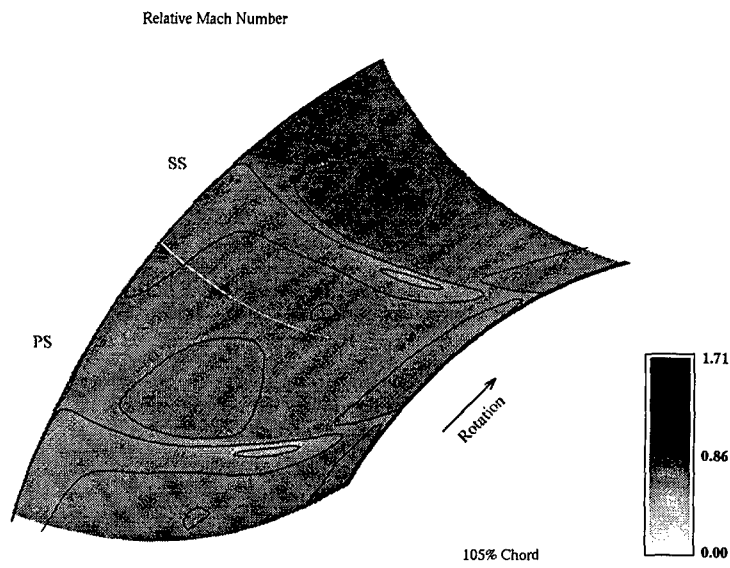
Figure 96. Passage Relative Mach Number for Case A (105% Chord)

Relative Mach Number

SS

PS

Rotation

1.89

0.94

50% Chord

0.00
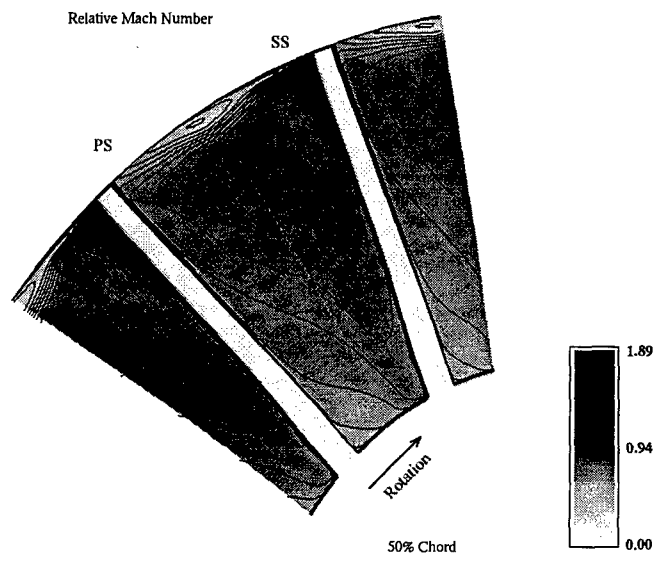
Figure 97. Passage Relative Mach Number for Case D (50% Chord)

128
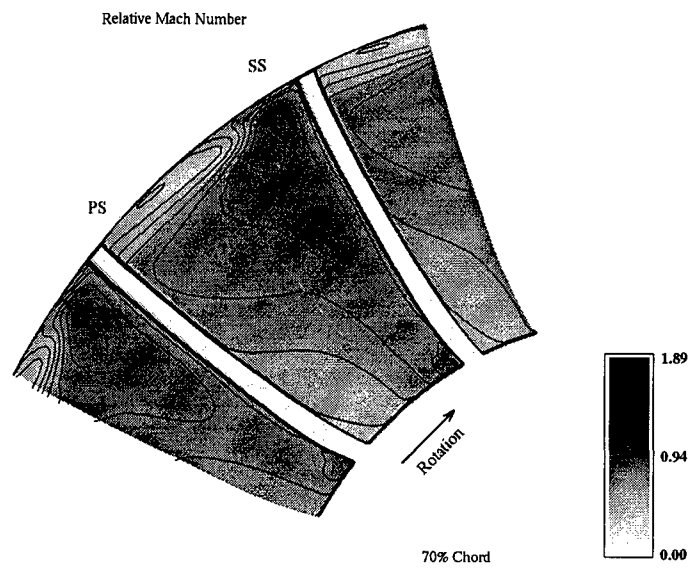
Figure 98. Passage Relative Mach Number for Case D (70% Chord)
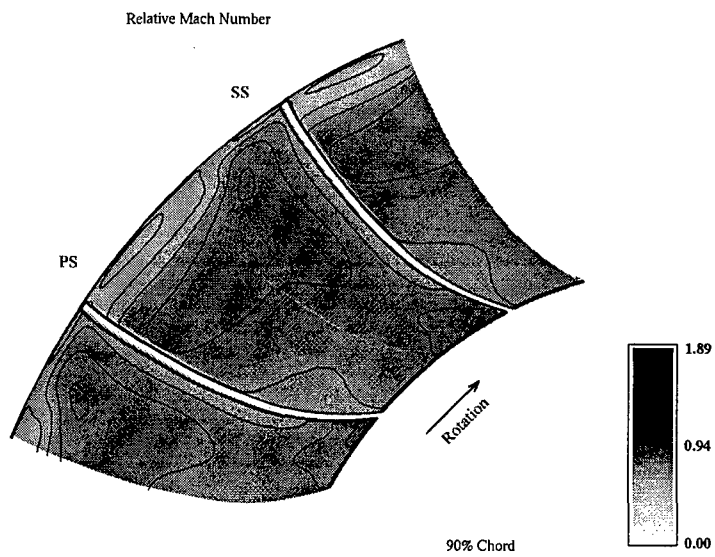
Figure 99. Passage Relative Mach Number for Case D (90% Chord)

129
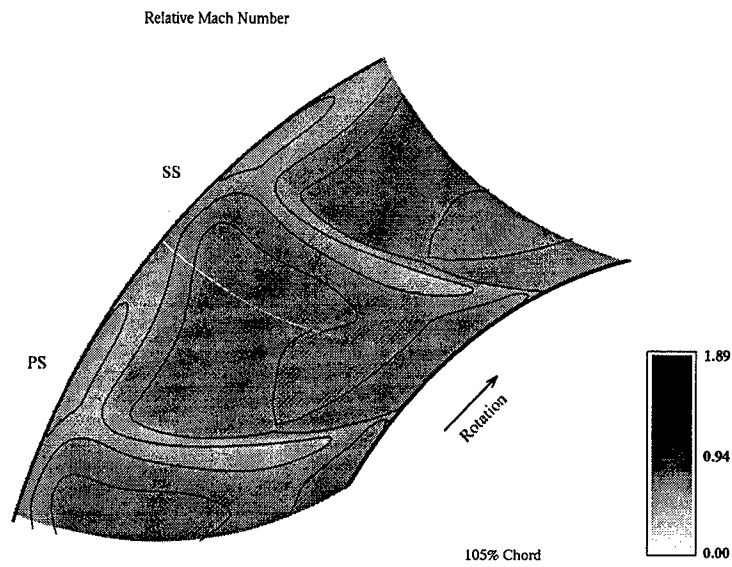
Figure 100. Passage Relative Mach Number for Case D (105% Chord)
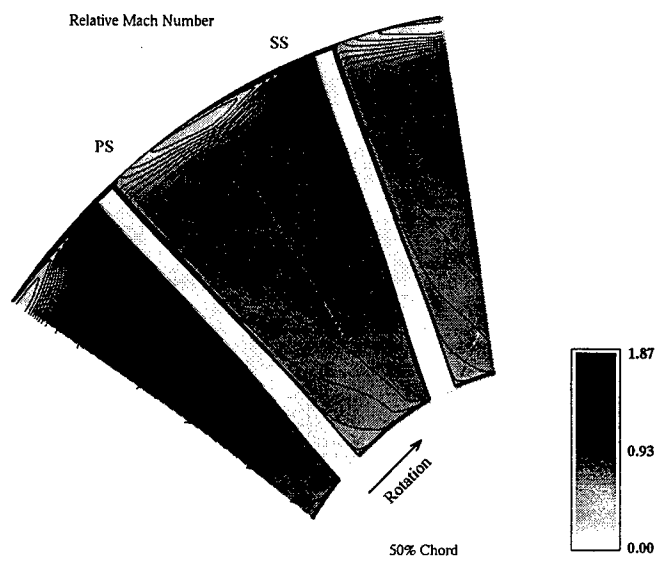
Figure 101. Passage Relative Mach Number for Case G (50% Chord)

130
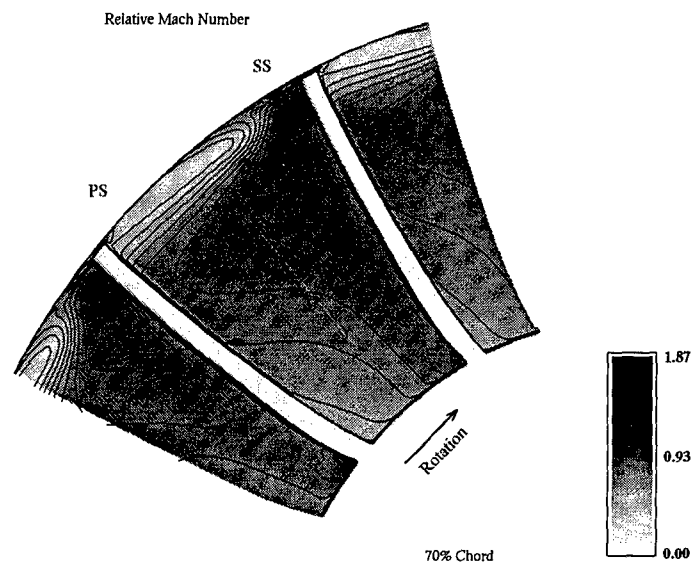
Figure 102. Passage Relative Mach Number for Case G (70% Chord)
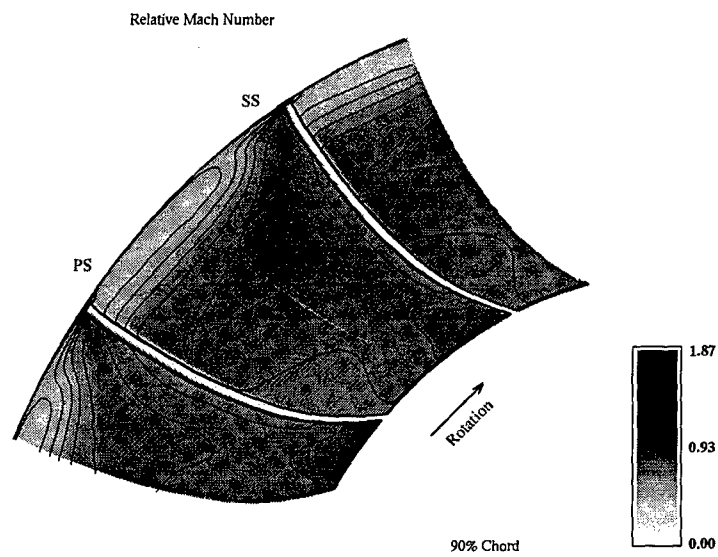
Figure 103. Passage Relative Mach Number for Case G (90% Chord)

131
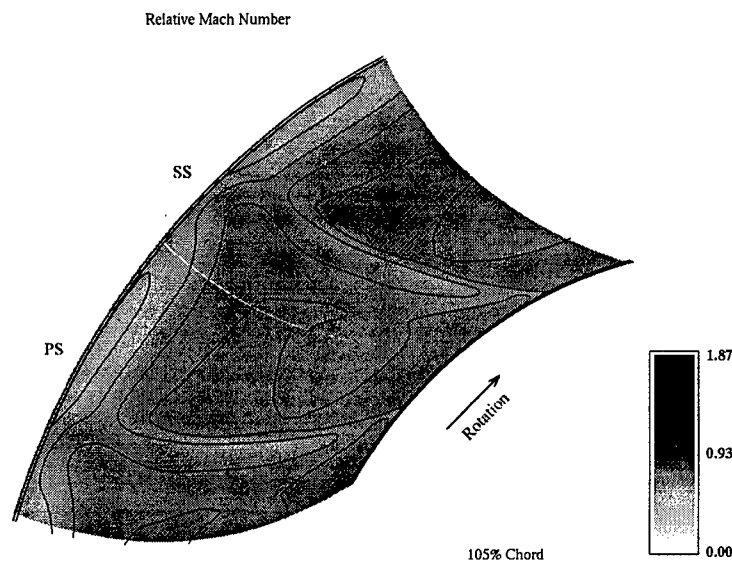
Figure 104. Passage Relative Mach Number for Case G (105% Chord)

7.5 Effect of Stepped Tip Gap on Rotor Flowfield

7.5.1 Effect of Stepped Tip Gap on Tip Region Static Pressure

Stepped tip gaps manipulated the tip region flow to entrain the low-velocity blockage into the increased clearance; however, significant effects of stepped tip gap on the tip region flowfield were not clearly evident in the cascade plots of measured pressure in the tip region. The normalized pressure distribution for the medium clearance with no step (Figure 46) was similar to those for the same medium clearance but with steps at 86% axial tip chord (Figure 48) and 58% axial tip chord (Figure 50). Therefore, masking techniques, explained in the following paragraph, and plots of the CFD solution were used to extract the prominent effects of stepped tip gap on the tip region flowfield.

132

Attempts were made to visualize the effects of stepped tip gap on the tip region flow structure by masking the experimental flowfield data of Case E (medium gap, aft step) with those of Case A (small gap, no steps) and Case D (medium gap, no step). Figure 105 was produced by subtracting the pressure distribution of Case A from that of Case E; the change in unsteadiness of the flow (Figure 106) for these two cases was produced in similar manner. The pressure and unsteadiness of Case E masked by Case D are seen, respectively, in Figures 107 and 108.
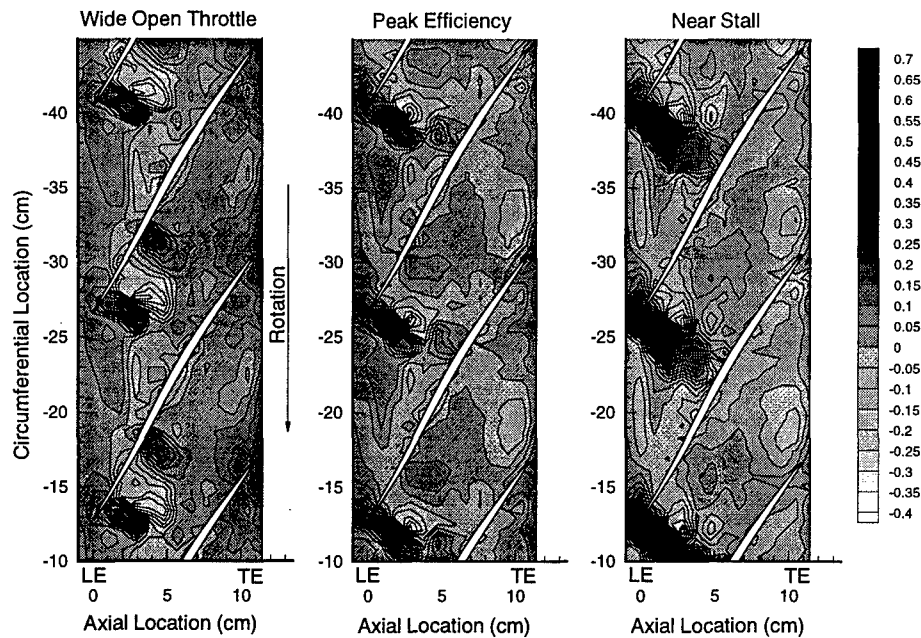
Figure 105. Normalized Pressure of Case E Masked by Case A (100% Design Rotor Speed)
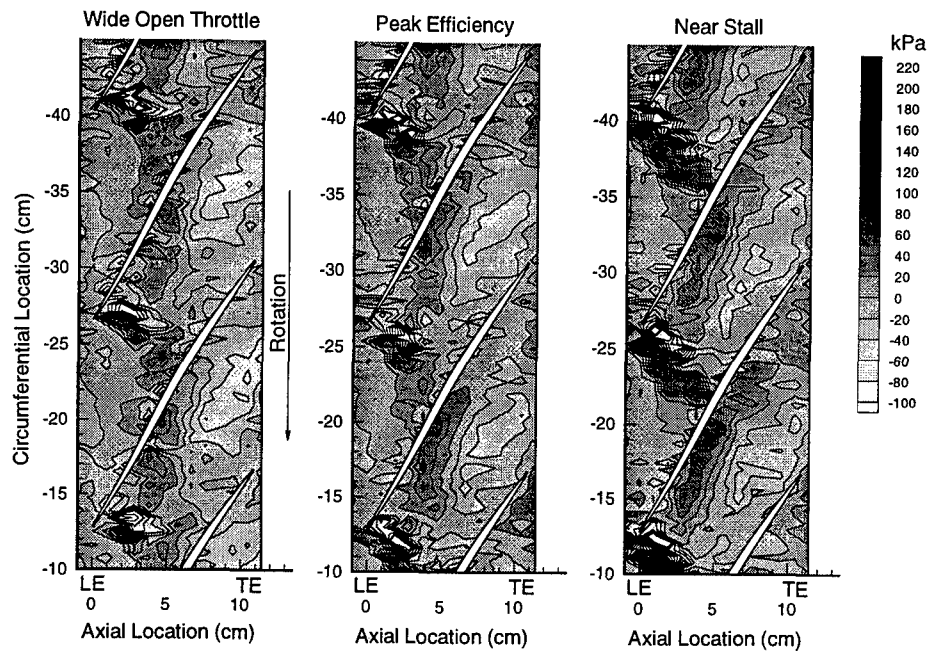
Figure 106. Pressure Unsteadiness of Case E Masked by Case A (100% Design Rotor Speed)
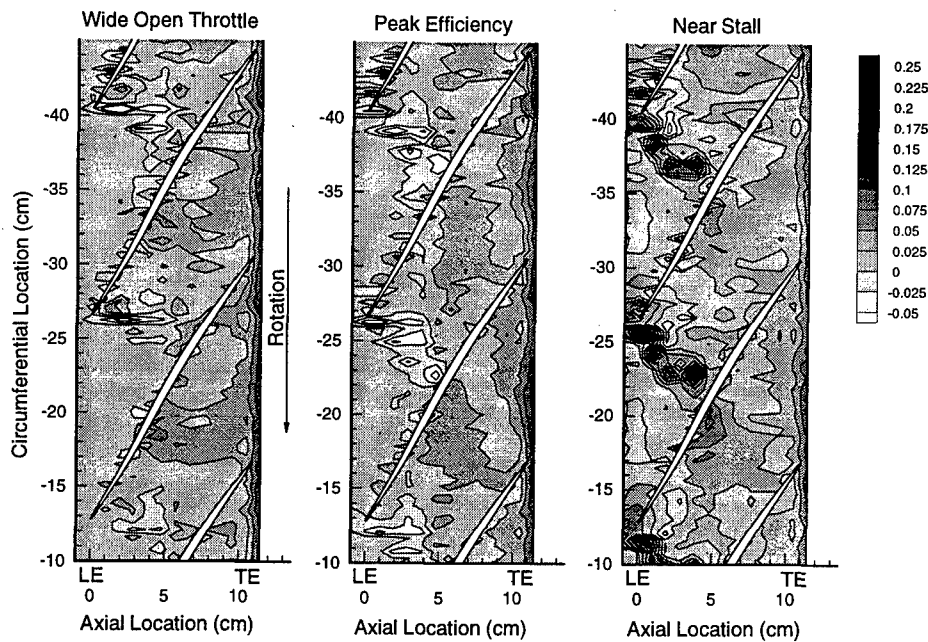
Figure 107. Normalized Pressure of Case E Masked by Case D (100% Design Rotor Speed)
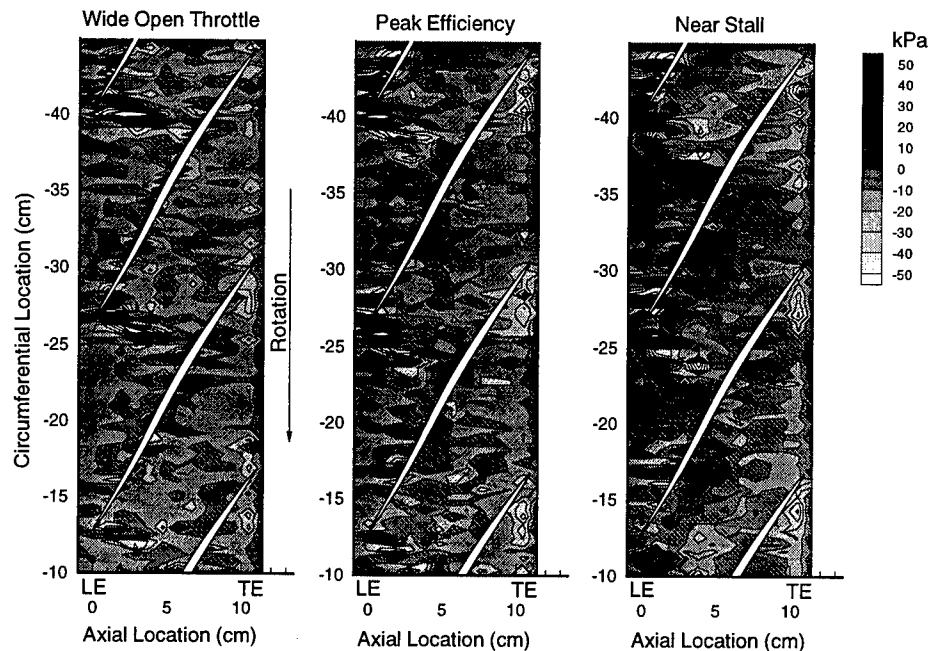
Figure 108. Pressure Unsteadiness of Case E Masked by Case D (100% Design Rotor Speed)

Figure 105 depicts the effects of increased clearance and stepped tip gap at 86% axial chord on the cascade pressure distribution. As shown in this figure, a large oval-shaped zone of decreased pressure was produced near the trailing edge of the rotor; for the wide open throttle condition, this zone was near mid passage, but it moved closer to the suction surface as the flow was throttled to near stall. This zone of reduced pressure was evidence of increased flow velocity through the gap created by the increased clearance at 86% axial chord. A zone of greater pressure located at approximately 30% axial chord on the pressure surface of the blade diffused with decreased mass flow; this zone is likely a secondary shock formed by increased throughflow resulting from the stepped tip gap. A significant decrease in the unsteadiness of the downstream passage is seen in Figure 106 as noted by a lighter colored zone centered in the passage from 50% to 105% axial chord.

The effects of stepped tip gap (without a clearance increase) on the tip region static pressure and unsteadiness are shown, respectively, in Figures 107 and 108; in these figures, the values asso-

135

ciated with Case D are subtracted from the values associated with Case E. A stepped tip gap yielded a uniform increase of pressure at the rotor trailing edge (Figure 107) near the outer casing. The unsteadiness or turbulence of the flowfield also was reduced at the rotor trailing edge with the use of a stepped tip gap (Figure 108). These characteristics suggest that stepped tip gaps effect a downstream flowfield with improved steadiness and uniformity over the unstepped case.

The Relative Mach Number and Axial Momentum cascade plots derived from CFD for Cases D, E, and F (Figures 77, 78, and 79, respectively) provided more detailed insight into the effect of stepped tip gap on the flow structures of the tip region. The cascade flowfield for the unstepped medium clearance (Case D) is seen in Figure 77. With the introduction of a stepped tip gap at 86% axial tip chord (Case E), the blockage, identified by the area of low Mach number and low axial momentum associated with the shock-vortex interaction zone in Figure 77, was elongated and diffused as it was drawn into the increased clearance (Figure 78). For the stepped tip gap at 58% axial tip chord (Figure 79), the low-energy zone was elongated circumferentially across the passage as it was drawn into the increased clearance, but it was not diffused to the same extent as that of the step at 86% axial tip chord. Thus, stepped tip gaps manipulated the tip region blockage as postulated in Chapter 3.

7.5.2 Effect of Stepped Tip Gap on Rotor Exit Velocity

The effect of stepped tip gap on relative velocity at the rotor exit (105% chord and 92% span) is seen in Figures 58 through 75. For all tip clearances, the location within the passage of the peak velocity was unaffected with the use of a step. For example, the relative velocity profiles of Cases A, B, and C (i.e., small tip clearance), shown respectively in Figures 58, 60, and 62, indicated that the peak velocity for all three cases was located at approximately 75% of passage from the blade suction surface for peak efficiency operation. For near-stall operation, the location of the peak velocity was

at approximately 25% of passage. These results indicated that stepped tip gaps had no apparent effect on the circumferential extent of the blockage at 92% span and 105% chord. Also, from the specific power profiles for each case (Figures 59, 61, 63, 65, 67, 69, 71, 73, and 75), stepped tip gap provided no apparent effect on the work distribution within the passage at 92% span and 105% chord. However, velocity distributions at a single span and chord location did not provide sufficient information to draw valid conclusions regarding the effects of stepped tip gaps on the overall rotor flowfield.

7.5.3 Effect of Stepped Tip Gap on Throughflow Area

Stepped tip gaps induced a larger passage throughflow area by attenuating the tip leakage vortex along the rotor casing. The CFD solutions provided insight into this effect. Planar views of the relative Mach number at 50%, 70%, 90%, and 105% chord were generated for Cases D, E, and F. The axial progression of passage blockage for Case D (medium gap, no step) was earlier seen in Figures 97 through 100 and was discussed in Section 7.4.3. As seen in Figures 109 through 112 depicting the axial progression of blockage for Case E (medium gap, aft step), the introduction of a stepped tip gap at 86% axial tip chord caused the tip leakage vortex to be circumferentially elongated as it was drawn into the increased clearance. The blockage for this case engulfed approximately 90% of the circumferential passage near the rotor tip, and it consumed less than 10% of the passage area. Casing configuration F (medium gap, forward step at 58% axial chord), with blockage progression shown in Figures 113 through 116, effected similar results. For this case, the blockage encompassed approximately 90% of the circumferential passage near the rotor tip, and it consumed up to 15% of the passage area. Thus, based on the amount of throughflow area consumed, the stepped tip gap at 58% axial chord was not as effective in reducing the blockage for the medium clearance as was the stepped gap at 86% axial chord.
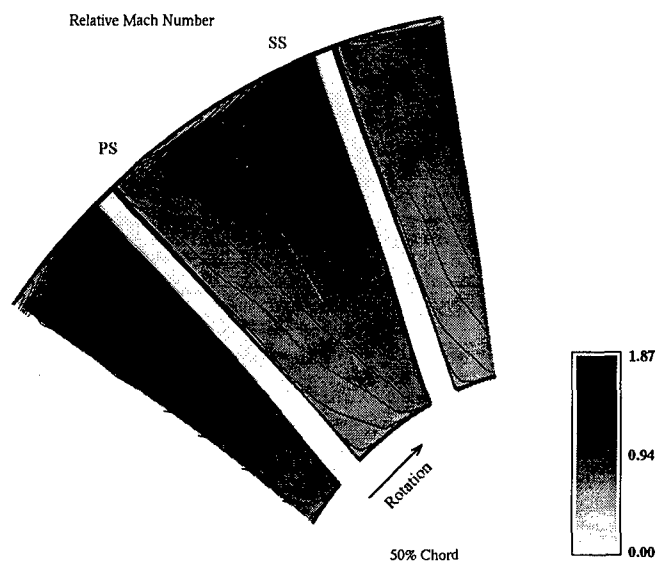
Figure 109. Passage Relative Mach Number for Case E (50% Chord)
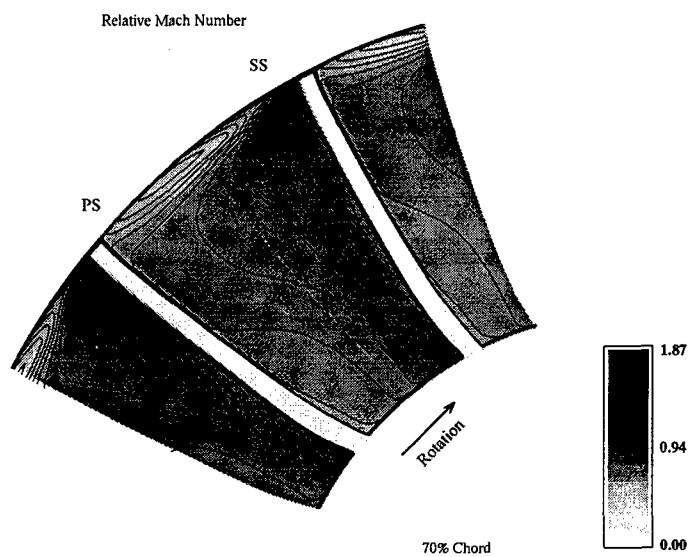
Figure 110. Passage Relative Mach Number for Case E (70% Chord)

138
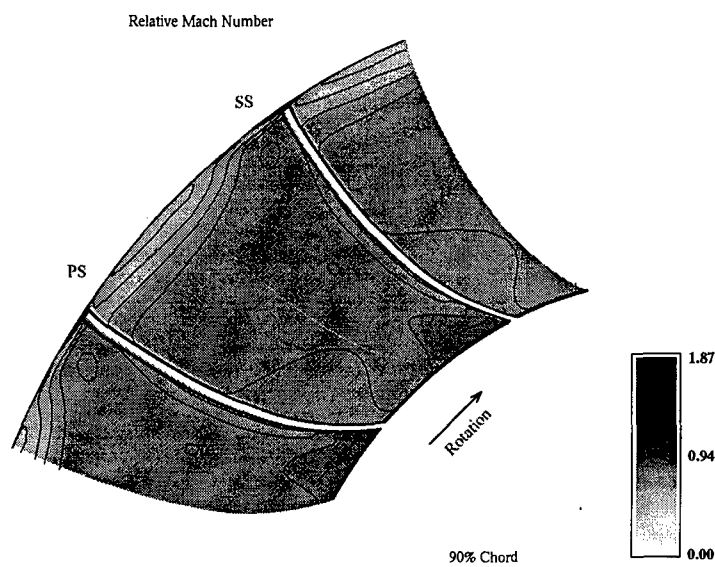
Figure 111. Passage Relative Mach Number for Case E (90% Chord)
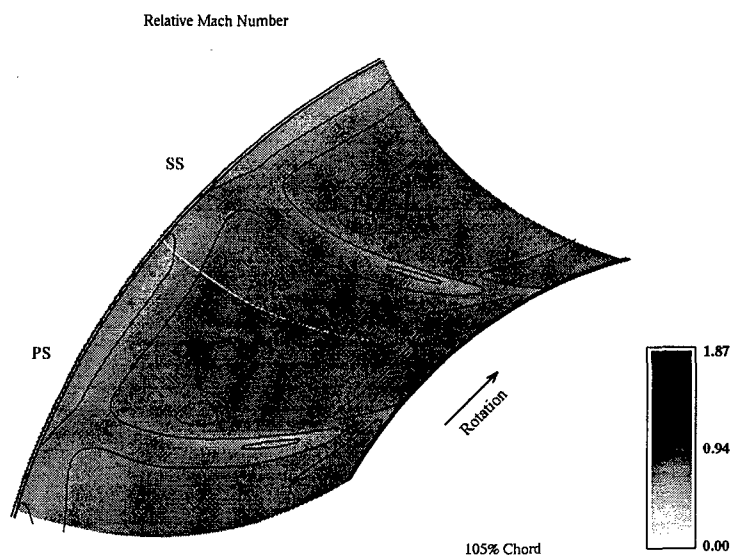
Figure 112. Passage Relative Mach Number for Case E (105% Chord)

139
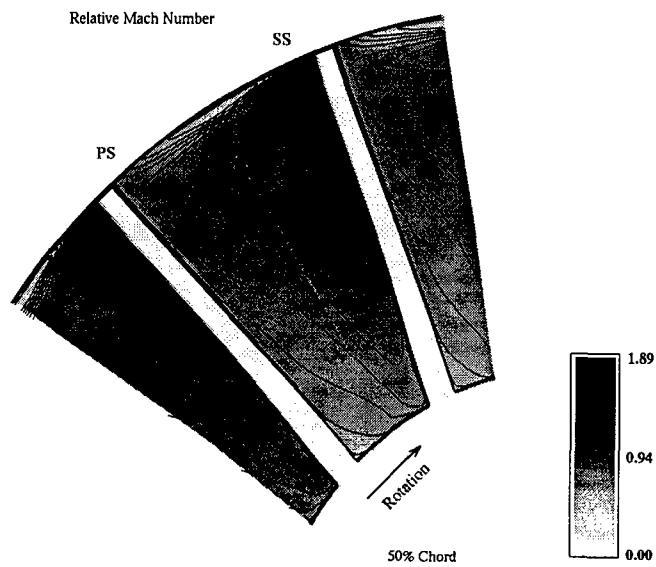
Figure 113. Passage Relative Mach Number for Case F (50% Chord)
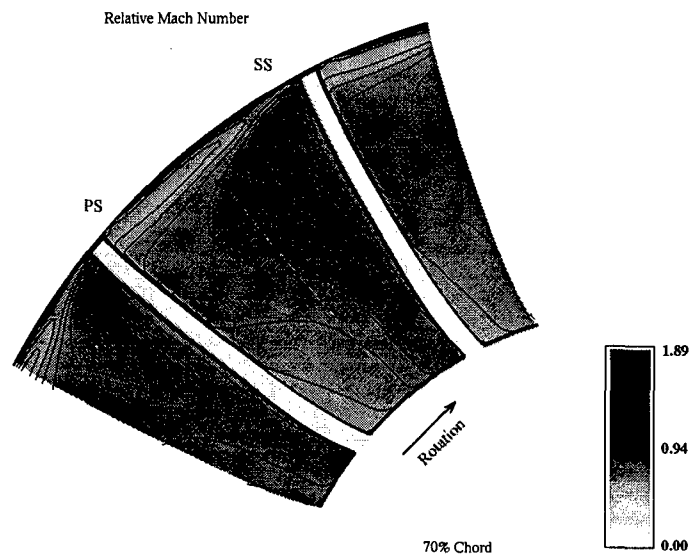
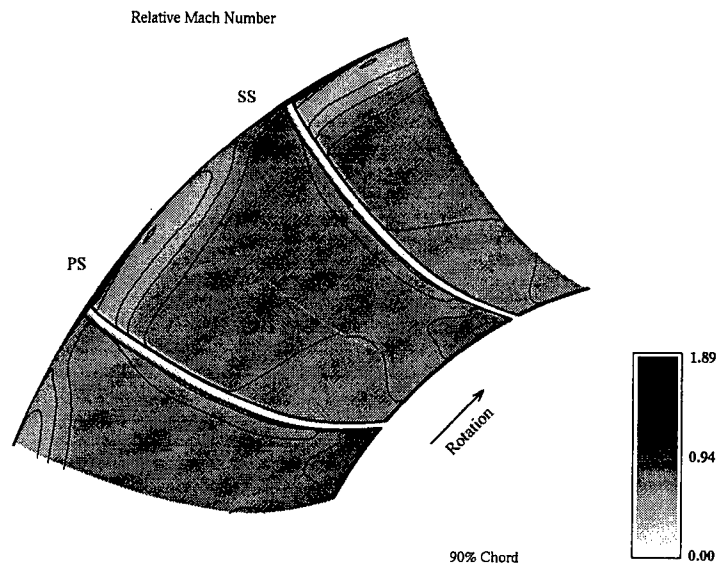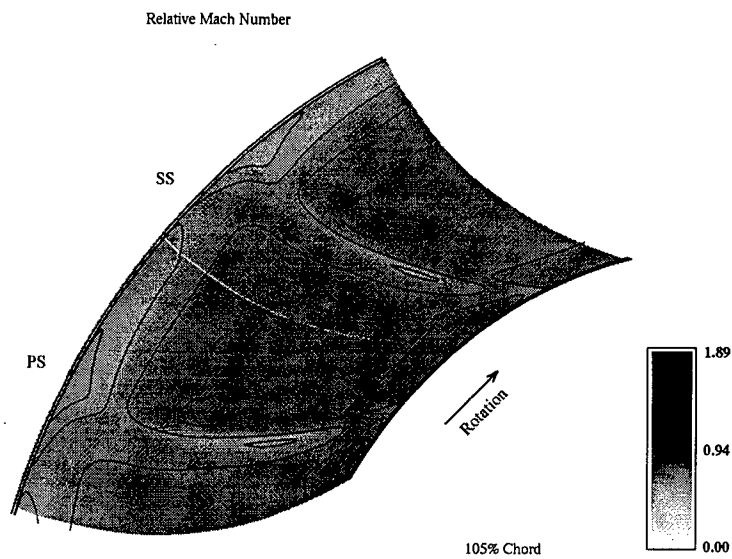Figure 114. Passage Relative Mach Number for Case F (70% Chord)

140

Figure 115. Passage Relative Mach Number for Case F (90% Chord)

Figure 116. Passage Relative Mach Number for Case F (105% Chord)

141

7.6 Summary

The results presented in this chapter confirmed the principle of beneficial flowfield manipulation using stepped tip gaps. Using a combination of experimental and computational data, the flowfield associated with the ADLARF rotor was characterized at various operating conditions. Increased tip clearance was confirmed to increase the size and strength of the tip leakage vortex which leads to greater blockage of the passage throughflow area. Stepped tip gaps were shown to alter the extent of the blockage to increase the passage throughflow area, an effect which yielded the performance improvements previously detailed in Chapter 6. In the next chapter, the effects of tip gap geometry on the stall characteristics of the ADLARF rotor will be addressed.

Chapter 8 - Stall Characteristics

The effects of clearance geometry on the stall characteristics of the ADLARF rotor were investigated. Stall was achieved by maintaining a constant rotor speed while reducing the mass flow below the stability limit, as described in Section 1.4. The discharge valve throttling the mass flow was closed at a constant rate of one degree per second during each stall test. For each casing configuration, stall data were collected (see Sections 4.3.4 and 4.4.4) at each of 85%, 90%, 95%, and 100% corrected rotor speeds. Stall data were analyzed using the algorithm described in Appendix E. Stall characteristics were found to be primarily a function of the rotor and its operating conditions; the size of the tip clearance was found to have limited effect on stall and surge, and stepped tip gaps in the aft portion of the rotor were determined to have no significant effects on compressor stall or surge characteristics.

In the following sections, comparisons are made of the effects of varying casing geometry on specific stall characteristics, whereas, plots of the stall and surge signals for each casing configuration and operating condition are seen in Appendix E. For example, Figure 117 (extracted from Appendix E for Case A) illustrates the time history of rotating stall and surge waves as functions of rotor revolutions during the onset and development of rotating stall. Additionally, Figure 118 illustrates the frequency spectrum associated with stall and surge. Significant attributes extracted from the figures in Appendix E are summarized in Table 9.

Differenced AC Signals of Sensor #1 and Sensor #5

Added AC Signals of Sensor #1 and Sensor #5
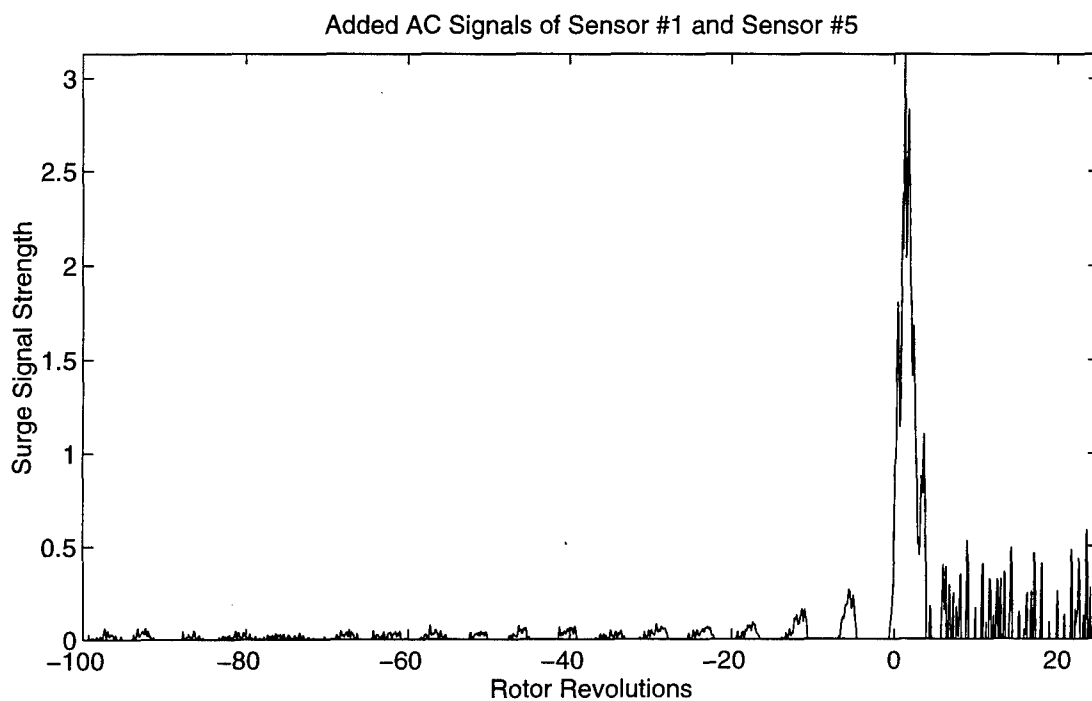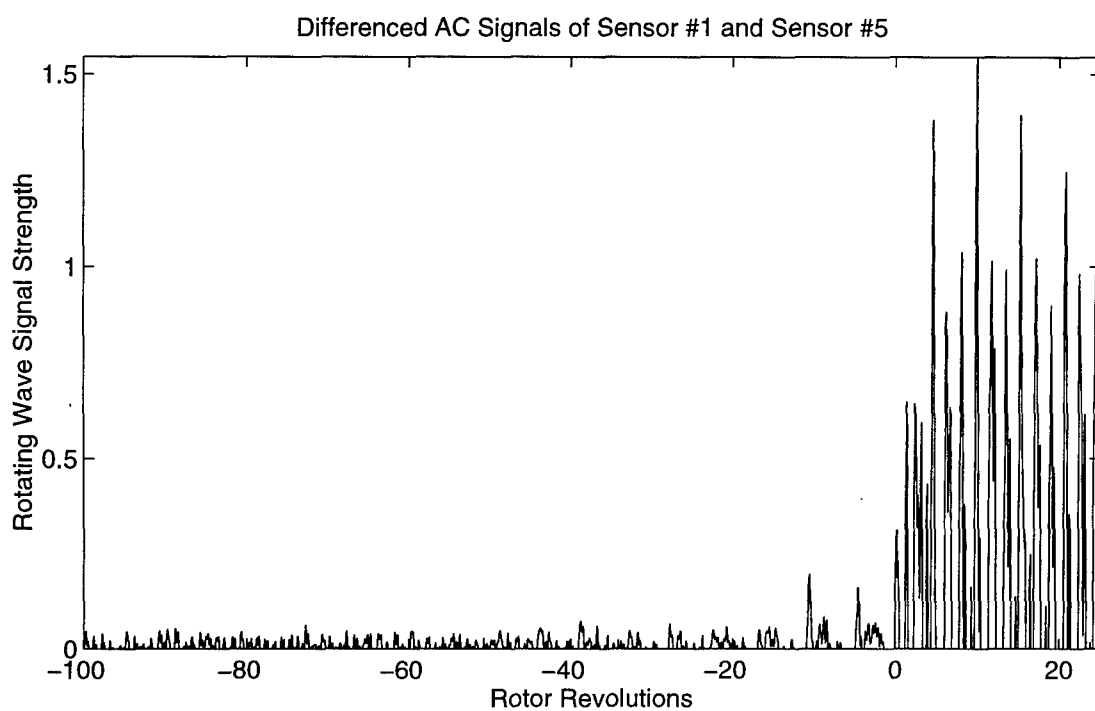
Figure 117. Onset of Rotating Stall and Surge (Case A, 100% Rotor Speed, 218.729 revs/sec)

144
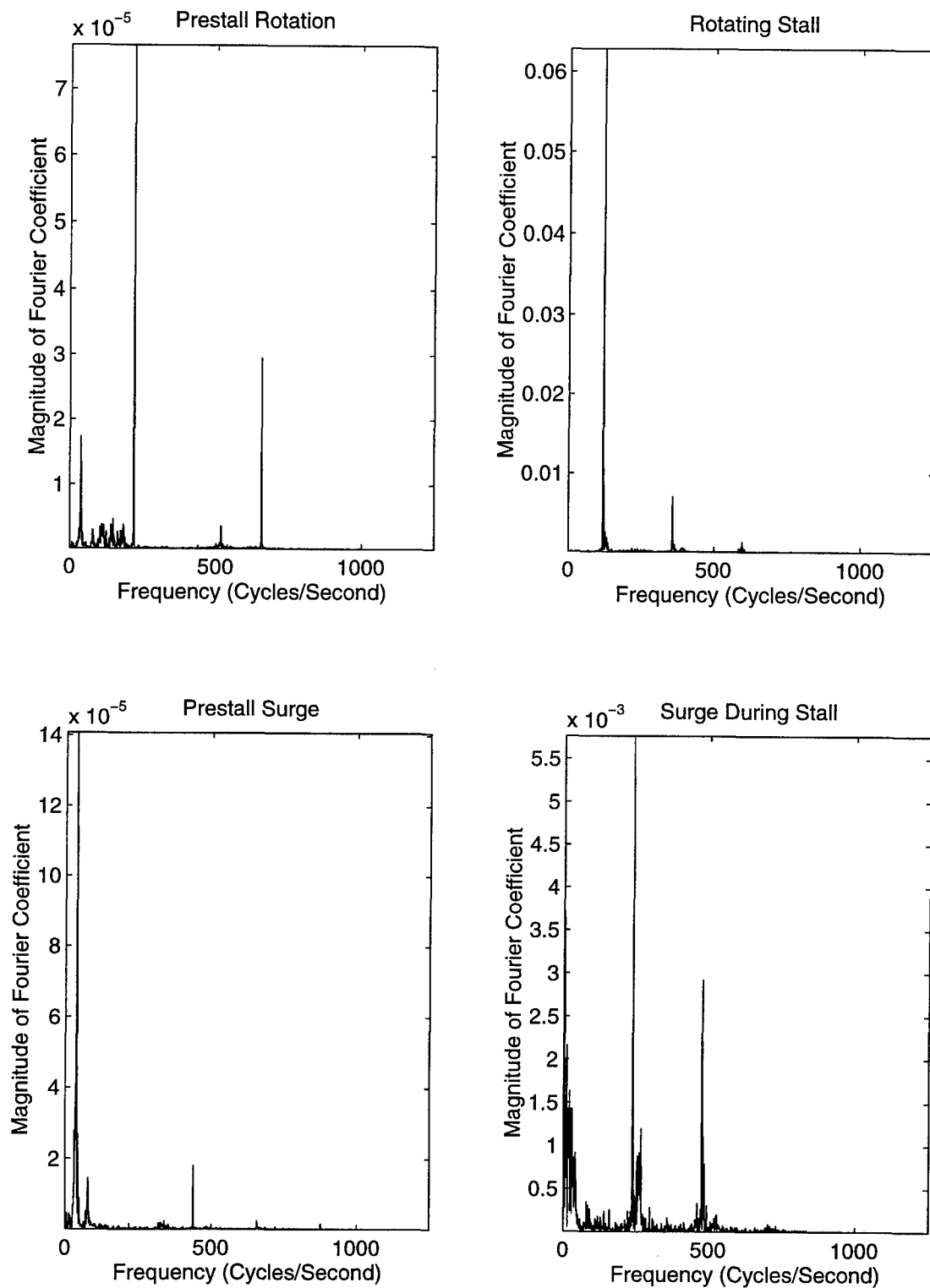
Figure 118. Frequency of Rotating Stall and Surge (Case A, 100% Rotor Speed, 218.729 revs/sec)

In Table 9, the following definitions apply:

1. Critical Stall Cell Formation is the reference time (or revolutions) at which a stall cell forms (denoted as zero rotor revolutions in Figure 117) and rapidly progresses into fully developed rotating stall.

2. Prestall Rotation Frequency (Figure 118) is the frequency of rotating disturbances (possibly transient) during the period prior to critical stall cell formation.

3. Rotating Stall Frequency (Figure 118) is the frequency of rotating stall during the period following critical stall cell formation. Fully developed rotating stall is evidenced by large amplitude steady-state rotating wave signals (see Figure 117).

4. Prestall Surge Frequency (Figure 118) is the frequency of planar surge waves moving axially during the period prior to critical stall cell formation.

5. In-Stall Surge Frequency ("Surge During Stall" in Figure 118) is the frequency of planar surge waves moving axially during the period following critical stall cell formation.

6. Modal Waves are low-frequency fluctuations (less than rotor frequency) prior to critical stall cell formation. They are clearly evident as clumps of amplitude magnification in Figure 117.

7. Stall Onset is the period (in rotor revolutions) from critical stall cell formation until the occurrence of fully developed rotating stall.

8.1 Effect of Tip Clearance on Compressor Instability

8.1.1 Effect of Tip Clearance on Rotating Stall Inception

Increased clearance (Cases D through I) caused a more abrupt stall as measured by the period (i.e., the number of revolutions) for stall onset to occur (Table 9). The stall onset tended to be less abrupt with decreased rotor speed. In all cases of unstepped tip gap, the progression from stall cell initiation to fully developed rotating stall occurred in less than seven rotor revolutions, with the onset period being less than two rotor revolutions for the large clearance. For the small and medium clearances, prestall modal waves, identified by frequencies less than the rotor frequency in the frequency plots and/or periodic clumps of amplitude magnification in the time plots, were evident for 95% and 100% design rotor speeds. Modal waves were not distinctly evident for the large clearance (Cases G to I); only for 100% design rotor speed were small amplitude modal waves distinguishable from apparent random noise. For the case of the medium clearance at 85% design

146

Table 9. Effect of Clearance Geometry on Compressor Stability

Casing	Nominal Rotor Speed percent	Rotor Frequency cycles/sec	Normalized[1] Prestall Rotation Frequency percent	Normalized[2] Rotating Stall Frequency percent	Normalized[3] Prestall Surge Frequency percent	Normalized[4] In-stall Surge Frequency percent	Modal Waves	Stall Onset Period revs	Maximum Surge Magnitude
A	100	218.729	17.3	54.7	17.3	1.1	yes	5	3.20
	95	207.676	20.6	55.3	19.4	8.8	yes	1	3.20
	90	197.030	99.2	55.8	23.6	1.2	no	7	2.66
	85	185.965	99.2	56.5	23.6	1.3	no	4	1.58
B	100	220.130	16.6	54.4	17.2	7.2	yes	2	2.45
	95	209.208	20.4	55.5	20.4	8.8	yes	1	2.70
	90	198.413	99.1	55.4	22.2	11.1	no	6	2.07
	85	187.150	99.2	56.1	23.5	1.3	no	13	1.50
C	100	223.759	56.2	54.6	16.9	8.7	yes	0	2.26
	95	212.748	20.1	55.1	18.9	1.1	yes	3	3.35
	90	201.676	21.8	55.1	21.8	1.2	yes	5	2.30
	85	190.375	99.4	56.5	23.7	1.3	no	3	1.58
D	100	219.296	56.2	54.6	15.6	8.9	yes	0	2.79
	95	208.382	19.3	55.1	19.3	1.2	yes	2	3.60
	90	197.708	99.5	55.6	22.2	1.2	no	4	2.44
	85	186.184	97.7	57.1	23.6	9.8	no	4	1.64
E	100	218.201	56.0	54.3	17.9	1.1	yes	2	2.63
	95	207.391	57.7	55.4	18.8	9.4	yes	1	2.62
	90	196.308	98.3	55.4	22.4	10.0	no	3	1.76
	85	185.507	99.4	56.0	23.7	9.2	no	3	1.76
F	100	217.676	54.4	54.4	2.8	6.7	yes	0	2.53
	95	206.743	99.2	54.9	19.5	9.5	yes	2	2.21
	90	195.966	99.1	56.1	23.7	9.3	no	3	1.79
	85	185.009	99.0	56.8	23.8	5.9	no	5	1.66
G	100	220.300	54.3	53.8	0.0	8.3	yes	0	2.20
	95	209.253	99.2	54.9	8.2	9.3	no	2	2.14
	90	198.133	56.1	54.9	23.4	8.6	no	2	1.49
	85	187.355	99.1	56.7	23.5	8.5	no	2	1.46
H	100	223.569	51.9	54.1	0.0	4.4	yes	2	1.83
	95	212.555	63.8	54.6	28.2	8.6	no	2	2.03
	90	201.204	61.9	55.8	23.7	1.2	no	3	1.64
	85	190.102	98.9	56.5	23.8	18.6	no	4	1.23
I	100	221.280	56.3	54.1	0.0	8.8	yes	2	1.95
	95	209.918	99.5	54.7	28.5	8.7	no	2	1.62
	90	199.264	80.3	55.2	23.9	9.2	no	3	1.46
	85	187.603	99.0	57.3	23.4	8.5	no	3	1.25

Notes: 1. Prestall rotation frequency as a percentage of the rotor frequency
2. Rotating (fully developed) stall frequency as a percentage of the rotor frequency
3. Prestall surge frequency as a percentage of the rotor frequency
4. In-stall surge frequency as a percentage of the rotor frequency

147

rotor speed (Figure 119), an instability occurred approximately 60 revolutions prior to the actual stall, but the instability dissipated without intervention in less than seven rotor revolutions.

8.1.2 Effect of Tip Clearance on Fully Developed Rotating Stall

Tip clearance had minimal effect on the rotation rate of the fully developed stall cell. In all cases, the cell rotated at approximately 55% of rotor speed, with the ratio decreasing with increased rotor speed. For the small and medium clearances, the fully developed stall was immediately alleviated by rapidly opening the downstream throttling valve. Opening this valve for the large clearance did not clear the stall condition; a reduction of rotor speed to less than 50% design speed was also required to clear the stall.

8.1.3 Effect of Tip Clearance on Prestall Surge

For the small and medium clearances, consistent prestall surge frequencies of 15% to 25% of rotor frequency (35 to 45 cycles per second) were identified for all rotor operating speeds. This prestall surge was not consistent for the large clearance; for 85% and 90% design rotor speed, the surge frequency remained consistent at approximately 25% of rotor speed (45 cycles per second), but the surge frequency was significantly slower for 95% rotor speed and nonexistent for 100% rotor speed (see Table 9).

8.1.4 Effect of Tip Clearance on In-Stall Surge

A larger tip clearance generally lessened the magnitude of the maximum surge wave at each rotor speed, with the greatest decrease occurring for 95% and 100% rotor speed (Table 9). The magnitude of the surge tended to be stronger with increased rotor speed for all cases. Also, the dominant surge frequency tended to increase with increased clearance (Table 9). The dominant surge frequency for the small clearance was approximately 1% of rotor speed (2.5 cycles per second) while the surge frequency for the large clearance was in the range from 8% to 9% of rotor speed (15 to 20

148
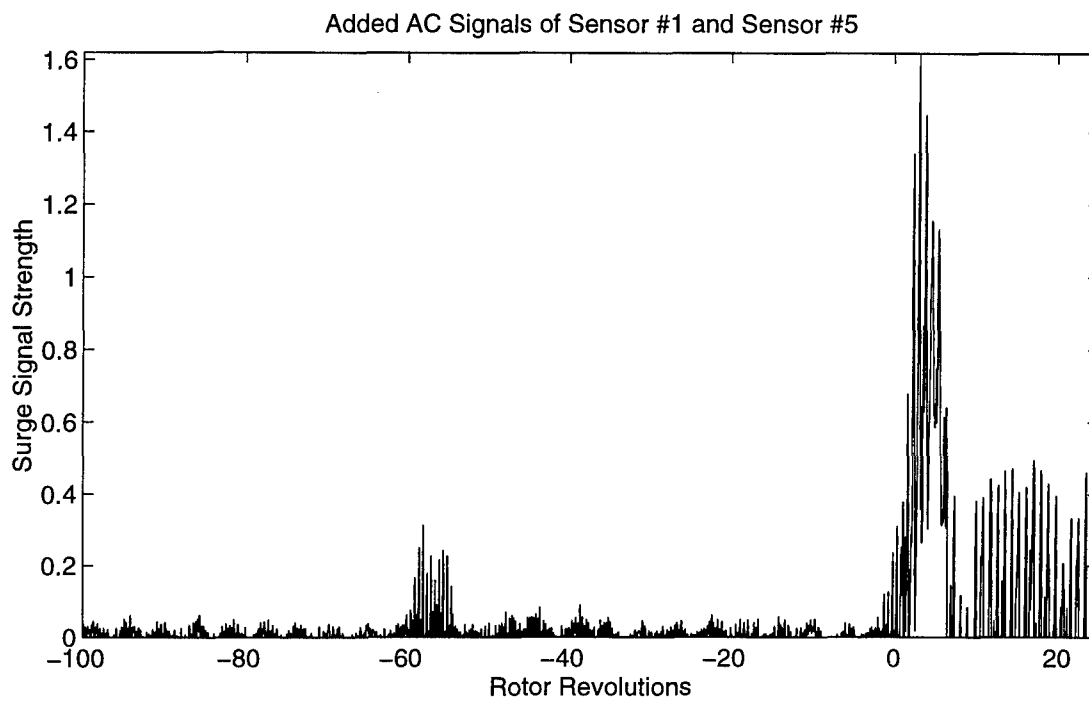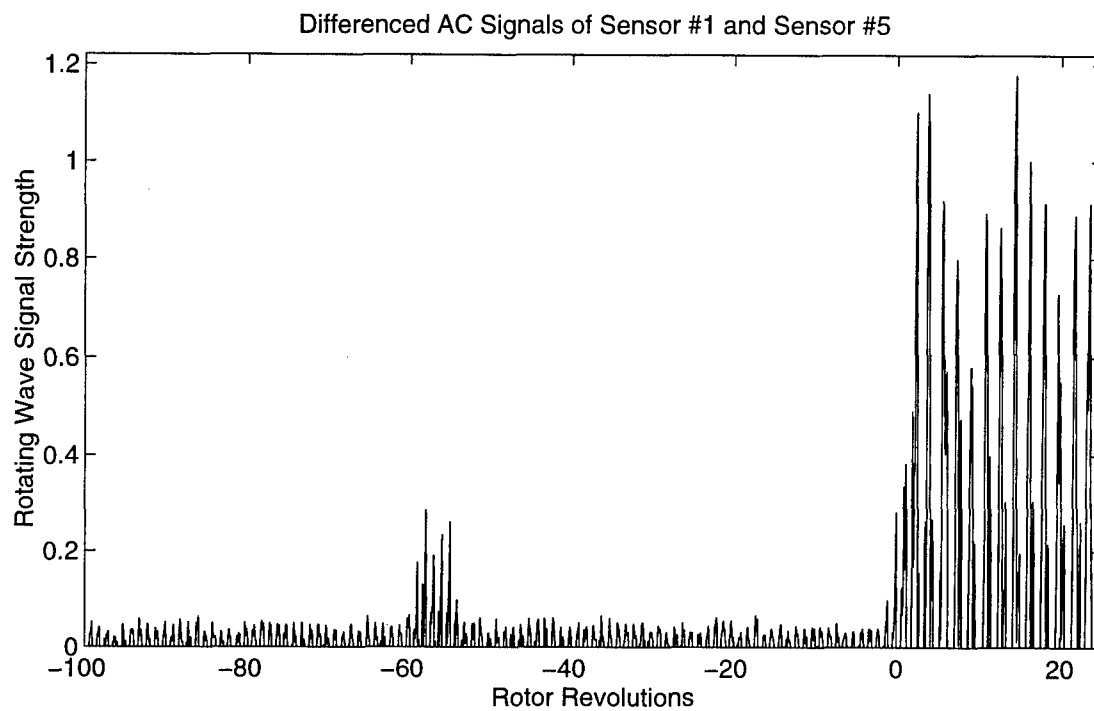
Figure 119. Stall Transient (Case D, 85% Rotor Speed, 186.184 revs/sec)

149

cycles per second). The surge frequency for the medium clearance was mixed between these two extremes. The highest frequency for the in-stall surge was generally less than half of the prestall surge frequency. Also, the wide variety of prestall and in-stall surge frequencies suggest that factors other than tip clearance (i.e., discharge valve dynamics, volume of the compressor cavity, etc.) have significant influence on the surge characteristics; surge is a dynamic of a compression system and not simply that of the rotor and its tip clearance.

8.2 Effect of Stepped Tip Gap on Compressor Instability

As seen in Table 9, stepped tip gaps (increased tip clearance over the aft portion of the rotor blade) had no significant affects on the stall and surge characteristics of the rotor. For each rotor operating speed, stall and surge frequencies for the stepped cases were similar to the unstepped cases. These results suggest that the tip clearance over the forward portion of the blade determined the stall characteristics of the rotor; this result confirmed the numerical predictions of Adamczyk et al. [5] described in Section 2.3.2.

8.3 Summary

In this chapter, the effects of tip clearance and stepped tip gaps on the stall and surge characteristics of the ADLARF rotor were presented. Increased tip clearance was found to produce a more abrupt stall and a weaker surge wave. Increased clearance had minimal effect on the rotation rate of a fully developed rotating stall cell; the stall cell was found to rotate at approximately 55% of rotor speed for all cases. Also, stepped tip gaps were found to have no significant affect on stall or surge characteristics. In the next chapter, the net effects of tip clearance and stepped tip gaps on rotor performance, flowfield, and stall characteristics are discussed and summarized; suggestions for additional research are also presented.

Chapter 9 - CONCLUSIONS AND RECOMMENDATIONS

9.1 Objectives

The primary goal of this dissertation was to relocate the inherent tip region blockage to benefit compressor performance. Supporting this goal, the objectives of this dissertation (see Section 1.5.2) were to expand the database of experimental information available in the open literature for transonic axial-flow rotors while determining the effects of tip geometry on the performance, flowfield, and stall characteristics of the ADLARF rotor. Also, the key geometric bounds to achieve the above objectives were to be identified, and guidance was to be provided for future designs. The objective of expanding the experimental database was a natural consequence of studying tip geometry effects. The effects of tip clearance on the performance, flowfield, and stall characteristics of the ADLARF rotor were addressed in Sections 6.1, 7.4, and 8.1, respectively. Likewise, the effects of stepped tip gaps on the performance, flowfield, and stall characteristics of the ADLARF rotor were presented in Sections 6.2, 7.5, and 8.2, respectively. In the following section, the effects of tip geometry on rotor performance, flowfield, and stall characteristics are addressed in relation to the primary goal of blockage relocation for improved performance. From this analysis, key geometric bounds are identified for future study, and guidance is provided to rotor designers.

9.2 Discussion and Conclusions

Trade-offs exist when optimizing performance measures based purely on clearance level. The tip gap that yields the greatest pressure ratio and efficiency is not necessarily the gap giving the largest flow range, mass flow capability, and stall margin. As a result, one performance measure is optimized at the expense of others, or a compromise is made of all measures to achieve a best all-around performance. These results suggest one cannot claim an overall optimum tip gap exists based on one performance measure alone, and any optimum gap may change with operating conditions.

151

The results of this series of tests indicate that the tip region flowfield of a transonic axial-flow rotor can be controlled with judicious choice of clearance level and a stepped tip gap. Moreover, changes to this flowfield can improve rotor performance in many instances. Although increased tip clearance alone typically harms performance by introducing more blockage, an increased tip clearance uniquely paired with a stepped gap can improve performance by offsetting the undesirable effects of increased clearance. In essence, the blockage created by the increased clearance is used to minimize tip region losses and maximize core passage performance--the author chooses to call this process an "aerodynamic seal" of the tip region, a process that was described in Chapter 3. This seal can be created by entraining the blockage produced by the upstream flow interaction into the tip gap of an adjacent blade; a stepped tip gap in the aft portion of the blade chord will accomplish this action. This flowfield manipulation was confirmed with experimental testing and numerical simulation (see Chapter 7). The range of clearance levels for which the aerodynamic sealing process is achievable lies between 0.318% and 1.002% tip chord. Furthermore, the results shown in Figures 32 through 35 indicate that for any clearance within this range, a unique axial location of stepped tip gap exists to achieve improved performance. The optimum stepped tip gap size and location will depend on the specific compressor rotor, its application, and operating conditions. The best depth of the stepped tip gap requires further study as does the effects of the sharpness of the step cut into the casing wall. Also, any practical applications must include the effects of material erosion occurring in normal operation.

A summary of specific conclusions relating to the objectives of this research follows:

1. The optimum tip gap depends on the performance measure optimized. To maximize efficiency and pressure ratio, an unstepped tip gap should be the narrowest possible; pressure ratio and efficiency decrease with increased clearance. However, the optimum tip clearance to maximize mass flow range and stall margin falls between 0.318% and 1.002% tip chord. Thus, the designer

must choose the best compromise to optimize overall rotor performance. However, when stepped tip gaps are employed, further performance increases are possible.

2. Stepped tip gaps benefit some or all measures of rotor performance. For tip clearances less than 1.002% tip chord, stepped tip gaps yield improved pressure ratio, efficiency, and flow range over the straight casing profile for many operating conditions. A small clearance level (0.318% tip chord) with forward (58% axial chord) stepped tip gap, Case C in Figure 23, and a medium clearance level (0.574% tip chord) with aft (86% axial chord) stepped tip gap, Case E in Figure 23, yielded the best improvement of performance measures of the configurations tested.

3. The optimum axial location of the stepped tip gap moves aft as clearance level increases, with the largest clearance level (1.002% tip chord) not needing a step; additional study is needed to determine a functional pairing. Studies should focus on clearance levels between 0.318% and 1.002% tip chord.

4. An optimum paired combination of clearance level and stepped tip gap may exist. If mass flow range and maximum mass flow capability are important to the designer, the best candidate is an intermediate clearance level with a stepped tip gap located toward the rotor trailing edge. If efficiency and pressure ratio are most important, the small gap with forward step is the best candidate.

5. The stall and surge characteristics of a transonic rotor are primarily determined by the rotor and its operating condition, with the tip clearance providing limited effect on the stability of the rotor. For transonic rotors, stall initiation is abrupt and accompanied by a strong surge wave; increased tip clearance causes a more abrupt stall and a higher prestall surge frequency. Also, increased clearance has little effect on the rotation rate of the fully-developed rotating stall. Stepped tip gaps have no significant effect on the stall or surge characteristics of the rotor; the stability characteristics

153

attributable to tip geometry are determined by the clearance over the forward portion of the rotor blade.

9.3 Recommendations

The results of this thesis apply to the first-stage rotor of a transonic compressor. Since the stepped gap was located downstream of the leading edge shock where it affected the subsonic flow-field, there is reason to believe that stepped tip gaps will have similar beneficial effects on subsonic compressors and downstream stages of a transonic compressor. Experimental research will be required to confirm this speculation. Also, as mentioned previously, an optimization study should be accomplished to determine the best tip geometry for a particular operating condition as well as a range of operating conditions; it may be possible to engineer a mechanism that varies tip geometry with operating condition to maximize the performance parameter important to the designer.

Great progress been made in computational fluid dynamics during recent years; however, the computational solutions do not ideally reflect the characteristics obtained from experiment. In future studies, various turbulence models should be tried to determine the best turbulence closure coefficients. Also, the incorporation of real gas effects (including viscosity, humidity, specific heat, thermal conductivity, and state relations) instead of the assumption of a thermally and calorically perfect gas may help to eliminate the differences between CFD and experiment. Finally, the experimental data collected in this study should be used as a validity check for future CFD models of transonic flows.

In closing, stepped tip gaps improve compressor performance by cleaning up the blockage within the rotor passage. Using stepped tip gaps in future designs will aid the IHPTET program in accomplishing its goal of doubling thrust-to-weight ratio of turbojet engines.

BIBLIOGRAPHY

[1] "Compressor Research Facility," 1995.

[2] Abdalla, H. A. and S. Soundranayagam. "Flow in Compressor Interstage Ducts." In *International Symposium on Airbreathing Engines, 9th, Proceedings, Vol. I*, pages 207–215, Sept 3–8, 1989, Athens, Greece. ISABE 89-7020.

[3] Abernethy, R. B. and J. W. Thompson. *Handbook, Uncertainty Analysis in Gas Turbine Measurements*. Technical Report, Arnold Engineering Development Center, TN, 1973. AD 755 356.

[4] Aboulafia, R. "Engines Face Slow Times (Outlook/Specifications — Gas Turbine Engines)," *Aviation Week and Space Technology*, pages 95–109 (Jan 8, 1996).

[5] Adamczyk, J. J., M. L. Celestina and E. M. Greitzer. "The Role of Tip Clearance in High-Speed Fan Stall," *Transactions of the ASME: Journal of Turbomachinery*, 115(1):29–39 (Jan 1993). ASME Paper 91-GT-83.

[6] Anderson, Dale A., John C. Tannehill and Richard H. Pletcher. *Computational Fluid Mechanics and Heat Transfer*. Computational Methods in Mechanics and Thermal Sciences, Taylor and Francis, Bristol, PA, 1984.

[7] Anderson, John D. *Modern Compressible Flow with Historical Perspective* (Second Edition). McGraw-Hill, 1990.

[8] Anderson, John D. Jr. *Fundamentals of Aerodynamics* (Second Edition). McGraw-Hill, 1991.

[9] Aris, Rutherford. *Vectors, Tensors, and the Basic Equations of Fluid Mechanics*. Dover, 1962.

[10] Ashley, S. "Thrust Vectoring: A New Angle to Air Superiority," *Mechanical Engineering*, 117(1):58–64 (Jan 1995).

[11] Basson, A. and B. Lakshminarayana. "Numerical Simulation of Tip Clearance Effects in Turbomachinery," *Transactions of the ASME: Journal of Turbomachinery*, 117(3):348–359 (July 1995). ASME Paper 93-GT-316.

[12] Bettner, J. L. and C. Elrod. "The Influence of Tip Clearance, Stage Loading, and Wall Roughness on Compressor Casing Boundary Layer Development," *Transactions of the ASME: Journal of Enginering for Power*, 105(2):281–287 (April 1983). ASME Paper 82-GT-153.

[13] Boyer, K. M., P. I. King and W. W. Copenhaver. "Stall Inception in Single Stage, High-Speed Compressors With Straight and Swept Leading Edges." In *AIAA/ASME/SAE/ASEE Joint Propulsion Conference and Exhibit, 29th*, June 28–30, 1993, Monterey, CA. AIAA Paper 93-1870.

[14] Brines, G. L. "The Turbofan of Tomorrow," *Mechanical Engineering*, 112(8):65–67 (August 1990).

[15] Chen, G. T., E. M. Greitzer, C. S. Tan and F. E. Marble. "Similarity Analysis of Compressor Tip Clearance Flow Structure," *Transactions of the ASME: Journal of Turbomachinery*, 113(2):260–271 (April 1991). ASME Paper 90-GT-153.

[16] Chien, Kuei-Yuan. "Predictions of Channel and Boundary-Layer Flows with a Low-Reynolds-Number Turbulence Model," *AIAA Journal*, *20* (1):33–38 (Jan 1982). AIAA Paper 80-0134R.

[17] Cohen, H., G. F. C. Rogers and H. I. H. Saravanamuto. *Gas Turbine Theory* (Third Edition). Longman Scientific and Technical, Essex, England, 1987.

[18] Copenhaver, W. W., C. Hah and S. L. Puterbaugh. "Three-Dimensional Flow Phenomena in a Transonic, High-Throughflow, Axial-Flow Compressor Stage," *Transactions of the ASME: Journal of Turbomachinery*, *115* (2):240–248 (April 1993). ASME Paper 92-GT-169.

[19] Copenhaver, W. W., E. R. Mayhew and C. Hah. "The Effect of Tip Clearance on a Swept Transonic Compressor Rotor." In *ASME International Gas Turbine and Aeroengine Congress and Exposition*, June 13–16, 1994, The Hague, Netherlands. ASME Paper 94-GT-363.

[20] Copenhaver, W. W. and T. H. Okiishi. "Rotating Stall Performance and Recoverability of a High-Speed 10-Stage Axial Flow Compressor," *AIAA Journal of Propulsion and Power*, *9* (2):281–292 (Mar–Apr 1993). AIAA Paper 89-2684.

[21] Crook, A. J., E. M. Greitzer, C. S. Tan and J. J. Adamczyk. "Numerical Simulation of Compressor Endwall Casing Treatment Flow Phenomena," *Transactions of the ASME: Journal of Turbomachinery*, *115* (3):501–512 (July 1993). ASME Paper 92-GT-300.

[22] Cumpsty, N. A. *Compressor Aerodynamics*. Longman Scientific and Technical, Essex, England, 1989.

[23] Cumpsty, N. A. and E. M. Greitzer. "A Simple Model for Compressor Stall Cell Propagation," *Transactions of the ASME: Journal of Engineering for Power*, *104* (1):170–176 (Jan 1982). ASME Paper 81-GT-73.

[24] Cybyk, B. Z., D. C. Rabe, P. M. Russler and C. Hah. "Characterization of the First Stage Rotor in a Two-stage Transonic Compressor." In *AIAA/ASME/SAE/ASEE Joint Propulsion Conference and Exhibit, 31st*, July 10–12, 1995, San Diego, CA. AIAA Paper 95-2460.

[25] Day, I. J. "Stall Inception in Axial Flow Compressors," *Transactions of the ASME: Journal of Turbomachinery*, *115* (1):1–9 (Jan 1993). ASME Paper 91-GT-86.

[26] Day, I. J. and N. A. Cumpsty. "The Measurement and Interpretation of Flow Within Rotating Stall Cells in Axial Compressors," *Proceedings of IMechE: Journal of Mechanical Engineering Science*, *20* (2):101–114 (1978).

[27] Day, I. J. and C. Freeman. "The Unstable Behavior of Low and High-Speed Compressors," *Transactions of the ASME: Journal of Turbomachinery*, *116* (2):194–201 (April 1994). ASME Paper 93-GT-26.

[28] Dring, R. P. and H. D. Joslyn. "Through-Flow Modelling of Axial Turbomachinery," *Transactions of the ASME: Journal of Engineering for Gas Turbines and Power*, *108* (1):246–253 (Jan 1986). ASME Paper 85-IGT-42.

[29] Dring, R. P. and H. D. Joslyn. "Throughflow Analysis of a Multistage Compressor Operating at Near-Stall Conditions," *Transactions of the ASME: Journal of Turbomachinery*, *109* (4):483–491 (Oct 1987). ASME Paper 87-GT-51.

[30] Emmons, H. W., C. E. Pearson and H. P. Grant. "Compressor Surge and Stall Propagation," *Transactions of the ASME*, 27:455–469 (May 1955). ASME Paper 53-A-65.

[31] Epstein, A. H., J. L. Kerrebrock and W. T. Thompkins Jr. "Shock Structure in Transonic Compressor Rotors," *AIAA Journal*, 17(4):375–379 (April 1979). AIAA Paper 79-4043.

[32] Freeman, C. "Effect of Tip Clearance on Compressor Stability and Engine Performance." In *Von Karman Institute Lecture Series on Tip Clearance Effects in Axial Turbomachines*, April 15–19, 1985.

[33] Gorrell, S. E. and P. M. Russler. "Stall Inception in a High-Speed Low Aspect Ratio Fan Including the Effects of Casing Treatments." In *ASME International Gas Turbine and Aeroengine Congress and Exposition*, June 13–16, 1994, The Hague, Netherlands. ASME Paper 94-GT-322.

[34] Grier, Peter. "At the Aeronautical Frontier," *Air Force Magazine*, 78(1):22–28 (Jan 1995).

[35] Hah, C. "A Numerical Modeling of Endwall and Tip Clearance Flow of an Isolated Compressor Rotor," *Transactions of the ASME: Journal of Engineering for Gas Turbines and Power*, 108(1):15–21 (Jan 1986). ASME Paper 85-GT-116.

[36] Hah, C. "Calculation of Three-Dimensional Viscous Flows in Turbomachinery with an Implicit Relaxation Method," *AIAA Journal of Propulsion and Power*, 3(5):415–422 (Sept–Oct 1987). AIAA Paper 86-0555.

[37] Hah, C. and A. J. Wennerstrom. "Three-Dimensional Flowfields Inside a Transonic Compressor with Swept Blades." In *ASME International Gas Turbine and Aeroengine Congress and Exposition, Proceedings, 35th*, June 11–14 1990, Brussels, Belgium. ASME Paper 90-GT-359.

[38] Hah, Chunill. "Generation and Decay of Secondary Flows and their Impact on Aerodynamic Performance of Modern Turbomachinery Components." In *AGARD Conference Proceedings on Secondary Flows in Turbomachines*, pages 16–1 – 16–11, 1989. AGARD-CP-469.

[39] Hah, Chunill, Douglas C. Rabe, Thomas J. Sullivan and Aspi R. Wadia. "Effects of Inlet Distortion on the Flowfield in a Transonic Compressor Rotor." In *ASME International Gas Turbine and Aeroengine Congress and Exposition, Proceedings, 41st*, June 10–13 1996. ASME Paper 96-GT-547.

[40] Hall, E. J., A. J. Crook and R. A. Delaney. "Aerodynamic Analysis of Compressor Casing Treatment with a 3-D Navier-Stokes Solver." In *AIAA/ASME/SAE/ASEE Joint Propulsion Conference and Exhibit, 30th*, June 27–29, 1994, Indianapolis, IN. AIAA Paper 94-2796.

[41] Hawthorne, W. R. "Some Notes on Frank Whittle's Contribution to the Turbo-Jet," *IGTI Global Gas Turbine News*, 36(3):5–6 (1996).

[42] Heiser, W. H. and D. T. Pratt. *Hypersonic Airbreathing Propulsion* (First Edition). AIAA Education Series, Washington, DC, American Institute of Aeronautics and Astronautics, 1994.

[43] Hill, P. P. and C. R. Peterson. *Mechanics and Thermodynamics of Propulsion* (Second Edition). Addison-Wesley, 1992.

[44] Holmon, J. P. *Experimental Methods for Engineers* (Third Edition). McGraw-Hill, 1978.

[45] Hoying, D. A. "Stall Inception in a Multistage High-Speed Axial Compressor," *AIAA Journal of Propulsion and Power*, *11* (5):915–922 (Sept–Oct 1995). AIAA Paper 93-2386.

[46] Incropera, F. P. and D. P. DeWitt. *Fundamentals of Heat and Mass Transfer* (Third Edition). John Wiley & Sons, New York, 1990.

[47] Inoue, M. and M. Kuroumara. "Three-Dimensional Structure and Decay of Vortices Behind an Axial Flow Rotating Blade Row," *Transactions of the ASME: Journal of Engineering for Gas Turbines and Power*, *106* (3):561–569 (July 1984). ASME Paper 83-GTJ-21.

[48] Inoue, M., M. Kuroumara, T. Iwamoto and Y. Ando. "Detection of a Rotating Stall Precursor in Isolated Axial Flow Compressor Rotors," *Transactions of the ASME: Journal of Turbomachinery*, *113* (2):281–289 (April 1991). ASME Paper 90-GT-157.

[49] Inoue, M. and M. Kuroumaru. "Structure of Tip Clearance Flow in an Isolated Axial Compressor Rotor," *Transactions of the ASME: Journal of Turbomachinery*, *111* (3) (July 1989). ASME Paper 88-GT-251.

[50] Jackson, A. D. "Stall Cell Development in an Axial Compressor," *Transactions of the ASME: Journal of Turbomachinery*, *109* (4):492–498 (Oct 1987). ASME Paper 86-GT-249.

[51] Kang, S. and C. Hirsch. "Experimental Study on the Three-Dimensional Flow Within a Compressor Cascade With Tip Clearance: Part II — The Tip Leakage Vortex," *Transactions of the ASME: Journal of Turbomachinery*, *115* (3):444–452 (July 1993). ASME Paper 92-GT-432.

[52] Kerrebrock, J. L. "Flow in Transonic Compressors," *AIAA Journal*, *19* (1):4–19 (January 1981). AIAA Paper 80-0124R.

[53] Kunz, R. F., B. Lakshminarayana and A. H. Basson. "Investigation of Tip Clearance Phenomena in an Axial Compressor Cascade Using Euler and Navier-Stokes Procedures," *Transactions of the ASME: Journal of Turbomachinery*, *115* (3):453–467 (July 1993). ASME Paper 92-GT-299.

[54] Lakshminarayana, B. "Experimental Investigation of Tip Flows in Axial Compressors." In *Von Karman Institute Lecture Series on Tip Clearance Effects in Axial Turbomachines*, April 15–19, 1985.

[55] Lakshminarayana, B. "Experimental Investigation on the Effects of Tip Clearance in Turbomachinery." In *Von Karman Institute Lecture Series on Tip Clearance Effects in Axial Turbomachines*, April 15–19, 1985.

[56] Lakshminarayana, B. and P. Popovski. "Three-Dimensional Boundary Layer on a Compressor Rotor Blade at Peak Pressure Rise Coefficient," *Transactions of the ASME: Journal of Turbomachinery*, *109* (1):91–98 (Jan 1987). ASME Paper 86-GT-186.

[57] Lakshminarayana, B., M. Zaccaria and B. Marathe. "The Structure of Tip Clearance Flow in Axial Flow Compressors," *Transactions of the ASME: Journal of Turbomachinery*, *117* (3):336–347 (July 1995).

[58] Lakshminarayana, B., J. Zhang and K. N. S. Murthy. "An Experimental Study of the Effects of Tip Clearance on Flow Field and Losses in an Axial Flow Compressor Rotor." In *International Symposium on Airbreathing Engines, 8th, Proceedings, Vol. 1*, pages 273–290, June 14–19, 1987, Cincinnati, OH. ISABE 87-7045.

[59] Law, C. H., R. D. DeRose, D. J. Gurecki and E. C. Strain. *Investigation of a High-Through-Flow, Single-Stage Axial-Flow Compressor with Tip Clearance Increased 0.010 Inch (Configuration 2)*. Technical Report, Air Force Wright Aeronautical Laboratories, Wright-Patterson AFB, OH, April 1981. AFWAL-TR-80-2079, ADB059621.

[60] Law, C. H., R. D. DeRose, D. J. Gurecki and E. C. Strain. *Investigation of a High-Through-Flow, Single-Stage Axial-Flow Compressor with Tip Clearance Increased 0.020 Inch (Configuration 3)*. Technical Report, Air Force Wright Aeronautical Laboratories, Wright-Patterson AFB, OH, April 1981. AFWAL-TR-81-2029, ADB059618.

[61] Law, C. H. and A. R. Wadia. "Low Aspect Ratio Transonic Rotors: Part 1 — Baseline Design and Performance," *Transactions of the ASME: Journal of Turbomachinery*, *115* (2):218–225 (April 1993). ASME Paper 92-GT-185.

[62] Longley, J. P. "A Review of Nonsteady Flow Models for Compressor Stability," *Transactions of the ASME: Journal of Turbomachinery*, *116* (2):202–215 (April 1994). ASME Paper 93-GT-17.

[63] Longley, J. P. and T. P. Hynes. "Stability of Flow Through Multi-Stage Axial Compressors," *Transactions of the ASME: Journal of Turbomachinery*, *112* (1):126–132 (Jan 1990). ASME Paper 89-GT-311.

[64] Mattingly, J. D., W. H. Heiser and D. H. Daley. *Aircraft Engine Design* (First Edition). AIAA Education Series, Washington, DC, 1987.

[65] McDougall, N. M., N. A. Cumpsty and T. P. Hynes. "Stall Inception in Axial Compressors," *Transactions of the ASME: Journal of Turbomachinery*, *112* (1):116–125 (Jan 1990). ASME Paper 89-GT-63.

[66] Moore, R. D. *Rotor Tip Clearance Effects on Overall and Blade-Element Performance of Axial-Flow Transonic Fan Stage*. Technical Report, NASA, 1982. NASA TP-2049.

[67] Moyle, Ian N. *An Experimental and Analytical Study of Tip Clearance Effects in Axial Flow Compressors*. PhD dissertation, Naval Postgraduate School, Monterey, CA, December 1991. AD-A256 434.

[68] Newland, D. E. *An Introduction to Random Vibrations, Spectral and Wavelet Analysis* (Third Edition). Longman Scientific and Technical, Essex, England, 1993.

[69] Peacock, R. E. "Turbomachinery Tip Gap Aerodynamics — A Review." In *International Symposium on Airbreathing Engines, 9th, Proceedings, Vol. 1*, pages 549–559, Sept 3–8, 1989, Athens, Greece. ISABE 89-7056.

[70] Peter, L. J. and P. I. King. "Moving Endwall Effects on Passage Losses in Compressor Cascade." In *AIAA/ASME/SAE/ASEE Joint Propulsion Conference and Exhibit, 32d*, July 1–3 1996, Lake Buena Vista, FL. AIAA Paper 96-2653.

[71] Puterbaugh, S. L. *Tip Clearance Flow-Shock Interaction in an Advanced, Transonic, Axial-Flow Compressor Rotor*. PhD dissertation, University of Dayton, Dayton, OH, December 1994.

[72] Puterbaugh, S. L. and M. Brendel. "Tip Clearance Flow-Shock Interaction in a Transonic Compressor Rotor." In *AIAA/ASME/SAE/ASEE Joint Propulsion Conference and Exhibit, 31st*, July 10–12, 1995, San Diego, CA. AIAA Paper 95-2459.

[73] Puterbaugh, S. L. and W. W. Copenhaver. "Flow Field Unsteadiness in the Tip Region of a Transonic Compressor Rotor." Wright Laboratories Compressor Aero Research Lab, Wright-Patterson AFB, OH.

[74] Rabe, D. C. and K. Sabroske. "Laskin Particle Generator for Laser Anemometry." In *31st Aerospace Sciences Meeting and Exhibit*, 1993, Reno, NV. AIAA Paper 93-0044.

[75] Rabe, D. C., A. J. Wennerstrom and W. F. O'Brien. "Characterization of Shock Wave-Endwall Boundary Layer Interactions in a Transonic Compressor Rotor," *Transactions of the ASME: Journal of Turbomachinery*, 110 (3):386–392 (July 1988). ASME Paper 87-GT-166.

[76] Reitz, M. D. "CRF Database User's Guide." Wright Laboratories Compressor Research Facility, Wright-Patterson AFB, OH.

[77] Reynolds, William C. *Thermodynamics* (Second Edition). McGraw-Hill, 1968.

[78] Russler, P. M. *Acquisition and Reduction of Rotor Tip Static Pressure Transducer Data From a Low Aspect Ratio Transonic Fan*. Technical Report, Battelle Memorial Institute, Dayton, OH, 1995. Wright Laboratory Technical Report WL-TR-95-2022.

[79] Russler, P. M., D. C. Rabe, B. Z. Cybyk and C. Hah. *Tip Flow Fields in a Low Aspect Ratio Transonic Compressor*. Technical Report, Battelle Memorial Institute, Dayton, OH, 1995. ASME Paper 95-GT-89.

[80] Scott, P. "Birth of the Jet Engine," *Mechanical Engineering*, 117 (1):66–71 (Jan 1995).

[81] Sellin, M. D., S. L. Puterbaugh and W. W. Copenhaver. "Tip Shock Structures in Transonic Compressor Rotors." In *AIAA/ASME/SAE/ASEE Joint Propulsion Conference and Exhibit, 29th*, June 28–30, 1993, San Diego, CA. AIAA Paper 93-1869.

[82] Smith, G. D. J. "Radial Boundary Layer Flow on an Axial Compressor Rotor Blade." In *International Symposium on Airbreathing Engines, 9th, Proceedings, Vol. 1*, pages 560–565, Sept 3–8, 1989, Athens, Greece. ISABE 89-7057.

[83] Stauter, R. C. "Measurement of the Three-Dimensional Tip Region Flowfield in an Axial Compressor," *Transactions of the ASME: Journal of Turbomachinery*, 115 (3):468–476 (July 1993). ASME Paper 92-GT-211.

[84] Storer, J. A. and N. A. Cumpsty. "Tip Leakage Flow in Axial Compressors," *Transactions of the ASME: Journal of Turbomachinery*, 113 (2):252–259 (April 1991). ASME Paper 90-GT-127.

[85] Strazisar, A. J., J. R. Wood, M. D. Hathaway and K. L. Suder. *Laser Anemometer Measurements in a Transonic Axial-Flow Fan Rotor*. Technical Report, NASA, 1989. NASA TP 2879.

[86] Suder, K. L. and M. L. Celestina. "Experimental and Computational Investigation of the Tip Clearance Flow in a Transonic Axial Compressor Rotor." In *ASME International Gas Turbine and Aeroengine Congress and Exposition*, June 13–16, 1994, The Hague, Netherlands. ASME Paper 94-GT-365.

[87] Valenti, M. "Upgrading Jet Turbine Technology," *Mechanical Engineering*, 117 (12):56–60 (Dec 1995).

[88] Van Wylen, Gordon J. and Richard E. Sonntag. *Fundamentals of Classical Thermodynamics* (Second Edition). John Wiley and Sons, 1978.

[89] Wadia, A. R. and C. H. Law. "Low Aspect Ratio Transonic Rotors: Part 2 — Influence of Location of Maximum Thickness on Transonic Compressor Performance," *Transactions of the ASME: Journal of Turbomachinery*, 115 (2):226–239 (April 1993). ASME Paper 92-GT-186.

[90] Wagner, J. H., R. P. Dring and H. D. Joslyn. "Inlet Boundary Layer Effects in an Axial Compressor Rotor: Part I — Blade-to-Blade Effects," *Transactions of the ASME: Journal of Engineering for Gas Turbines and Power*, 107 (2):374–380 (April 1985). ASME Paper 84-GT-84.

[91] Wagner, J. H., R. P. Dring and H. D. Joslyn. "Inlet Boundary Layer Effects in an Axial Compressor Rotor: Part II — Throughflow Effects," *Transactions of the ASME: Journal of Engineering for Gas Turbines and Power*, 107 (2):381–386 (April 1985). ASME Paper 84-GT-85.

[92] Walatka, Pamela P., Jean Clucas, R. Kevin McCabe, Todd Plessell and Rick Potter. *Flow Analysis Software Toolkit (FAST) User's Guide* (Version 1.1a Edition), 1994.

[93] Wennerstrom, A. J. "Experimental Study of a High Through-Flow Transonic Axial Compressor Stage," *Transactions of the ASME: Journal of Engineering for Gas Turbines and Power*, 106 (3):552–560 (July 1984).

[94] Wennerstrom, A. J. "Highly Loaded Axial Flow Compressors: History and Current Developments," *Transactions of the ASME: Journal of Turbomachinery*, 112 (4):567–578 (Oct 1990).

[95] Wennerstrom, A. J., C. H. Law, W. A. Buzzell and R. D. DeRose. *Investigation of a 1500 ft/sec, Transonic, High-Through-Flow, Single-Stage Axial-Flow Compressor with Low Hub/Tip Ratio*. Technical Report, Air Force Aeropropulsion Laboratory, Wright-Patterson AFB, OH, Oct 1976. AFAPL-TR-76-92, ADB016506.

[96] Wennerstrom, A. J. and S. L. Puterbaugh. "A Three-Dimensional Model for the Prediction of Shock Losses in Compressor Blade Rows," *Transactions of the ASME: Journal of Engineering for Gas Turbines and Power*, 106 (2):295–299 (April 1984). ASME Paper 83-GT-216.

[97] White, Frank M. *Fluid Mechanics*. McGraw-Hill, 1979.

[98] White, Frank M. *Viscous Fluid Flow* (Second Edition). McGraw-Hill, 1991.

[99] Wilcox, David C. *Turbulence Modeling for CFD*. DCW Industries, Inc., La Canada, CA, 1993.

[100] Wilson, A. G. and C. Freeman. "Stall Inception and Development in an Axial Flow Aeroengine," *Transactions of the ASME: Journal of Turbomachinery*, 116 (2):216–225 (April 1994). ASME Paper 93-GT-2.

[101] Yaras, M. I. and S. A. Sjolander. "Effects of Simulated Rotation on Tip Leakage in a Planar Cascade of Turbine Blades: Part I — Tip Gap Flow," *Transactions of the ASME: Journal of Turbomachinery*, 114 (3):652–659 (July 1992). ASME Paper 91-GT-127.

[102] Yaras, M. I. and S. A. Sjolander. "Effects of Simulated Rotation on Tip Leakage in a Planar Cascade of Turbine Blades: Part II — Downstream Flow Field and Blade Loading," *Transactions of the ASME: Journal of Turbomachinery*, *114* (3):660–667 (July 1992). ASME Paper 91-GT-128.

[103] Zhang, J. and B. Lakshminarayana. "Computation of Three Dimensional Turbulent Boundary Layers in Internal Flows, Including Turbomachinery Rotor Blades." In *International Symposium on Airbreathing Engines, 9th, Proceedings, Vol. I*, pages 529–538, Sept 3–8, 1989, Athens, Greece. ISABE 89-7054.

APPENDICES

APPENDIX A - Performance Data Analysis and Curve-Fits

A.1 Performance Calculations

The following methods are used by the Compressor Research Facility data analysis software to calculate compressor performance.

A.1.1 Mass Flow Rate

Using the definition of mass flow parameter (Mattingly et al. [64]),

$$MFP \equiv \frac{\dot{m}\sqrt{T_0}}{AP_0} = \frac{M\sqrt{\frac{\gamma g_c}{R}}}{\left[1 + \frac{\gamma-1}{2}M^2\right]^{\frac{\gamma+1}{2(\gamma-1)}}} \tag{29}$$

which can be rewritten in terms of static pressure,

$$MFP \equiv \frac{\dot{m}\sqrt{T_0}}{AP} = M\sqrt{\frac{\gamma g_c}{R}}\left[1 + \frac{\gamma-1}{2}M^2\right]^{\frac{1}{2}} \tag{30}$$

the mass flow rate can be expressed as:

$$\dot{m} = \frac{APM\sqrt{\frac{\gamma g_c}{R}}}{\sqrt{T_0}}\left[1 + \frac{\gamma-1}{2}M^2\right]^{\frac{1}{2}} \tag{31}$$

Using the isentropic relation for total to static pressure ratio (Anderson [8]),

$$\frac{P_o}{P} = \left[1 + \frac{\gamma-1}{2}M^2\right]^{\frac{\gamma}{\gamma-1}} \tag{32}$$

Equation 31 becomes the form used by the CRF software to calculate mass flow rate:

$$\dot{m} = \frac{APM\sqrt{\frac{\gamma g_c}{R}}}{\sqrt{T_0}}\left[\left(\frac{P_o}{P}\right)^{\frac{\gamma-1}{\gamma}}\right]^{\frac{1}{2}} \tag{33}$$

where the Mach number in Equation 33 is calculated by inverting Equation 32 to give:

$$M = \left\{\frac{2}{\gamma-1}\left[\left(\frac{P_o}{P}\right)^{\frac{\gamma-1}{\gamma}} - 1\right]\right\}^{\frac{1}{2}} \tag{34}$$

Thus, the mass flow through the compressor is calculated using Equation 33 and Equation 34 with measured input flow parameters of static pressure (P), total pressure (P_0), and total temperature (T_0). These parameters are measured in the inlet duct to the rotor, and the area of the duct (A) is known to be 0.3902 m^2. The ratio of specific heats (γ) and the specific gas constant (R) could be assumed constant, but the CRF software adjusts these quantities based on the temperature and rela-

164

tive humidity of the air; these adjustments are omitted for simplicity of presentation. The correction factor (g_c) is not required when using SI units.

A.1.2 Total Pressure Ratio

The total pressure ratio is simply the ratio of the averaged total pressures measured at the rotor inlet and exit planes.

$$PR = \frac{P_{02}}{P_{01}} \tag{35}$$

A.1.3 Efficiency

The efficiency of the rotor is calculated in the traditional sense based on the work required by an isentropic compression process as a ratio of the actual work done by the rotor on the fluid (Cohen et al. [17] ; Van Wylen and Sonntag [88]):

$$\eta = \frac{\text{ideal work}}{\text{actual work}} = \frac{h_{02s} - h_{01}}{h_{02} - h_{01}} = \frac{C_{p2s}T_{02s} - C_{p1}T_{01}}{C_{p2}T_{02} - C_{p1}T_{01}} \tag{36}$$

where the ideal total temperature at the rotor exit is found by the isentropic relation:

$$T_{02s} = \left(\frac{P_{02}}{P_{01}}\right)^{\frac{\gamma-1}{\gamma}} \tag{37}$$

So, the rotor efficiency is calculated from averaged measured parameters of total pressure and total temperature at the rotor inlet and exit. The specific heat at constant pressure (C_p) and ratio of specific heats (γ) are adjusted for temperature and humidity by the CRF software.

A.1.4 Corrections for Nonstandard Conditions

It is customary to correct the mass flow rate and rotor speed for operating conditions other than sea-level standard atmosphere. This adjustment to the inlet freestream, described by Hill and Peterson [43] and Mattingly et al. [64] , uses the dimensionless pressure and temperature ratios of:

$$\delta = \frac{P_{01}}{P_{SL}} \tag{38}$$

165

and

$$\theta = \frac{T_{01}}{T_{SL}} \qquad (39)$$

A.1.4.1 Corrected Mass Flow

The mass flow calculated using Equation 33 is adjusted using the definition of corrected mass flow:

$$\dot{m}_c \equiv \frac{\dot{m}\sqrt{\theta}}{\delta} \qquad (40)$$

A.1.4.2 Corrected Rotor Speed

The rotor speed is adjusted using the definition of corrected rotor speed:

$$N_c \equiv \frac{N}{\sqrt{\theta}} \qquad (41)$$

A.2 Rotor Map Curve-Fits

Curve-fits of the superimposed steady-state and transient performance data for each casing config-uration and rotor operating speed are seen in the following figures. Steady-state data points are identified by diamonds, whereas, transient data points are represented by small cross-hair symbols. A spline fit with a tension factor of two was determined to provide the best fit of the experimental data for each case and operating condition. These spline fits are used in the rotor maps presented in Chapter 6 and Appendix C.

166
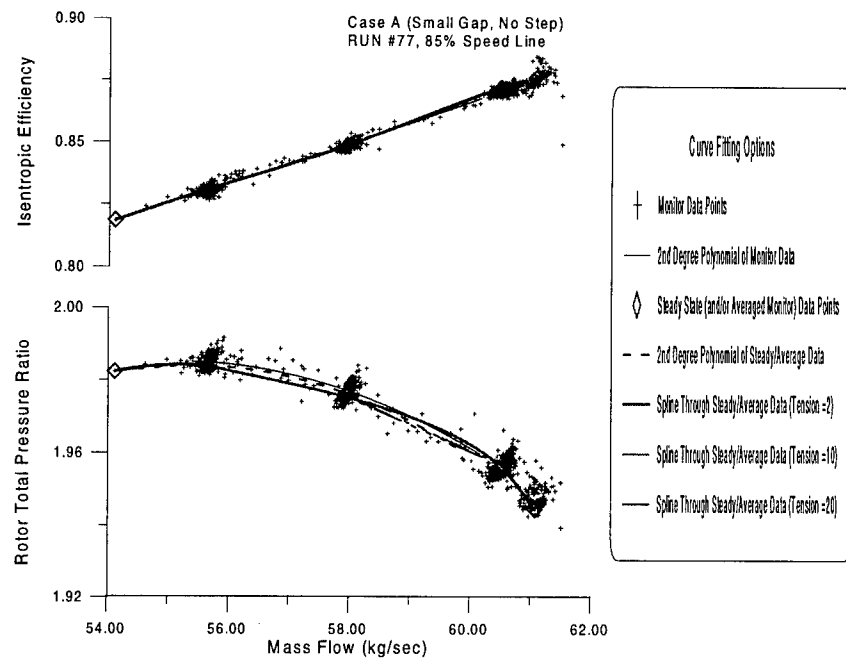
Figure 120. Performance Curve-Fit for Casing Configuration A (85% Design Rotor Speed)
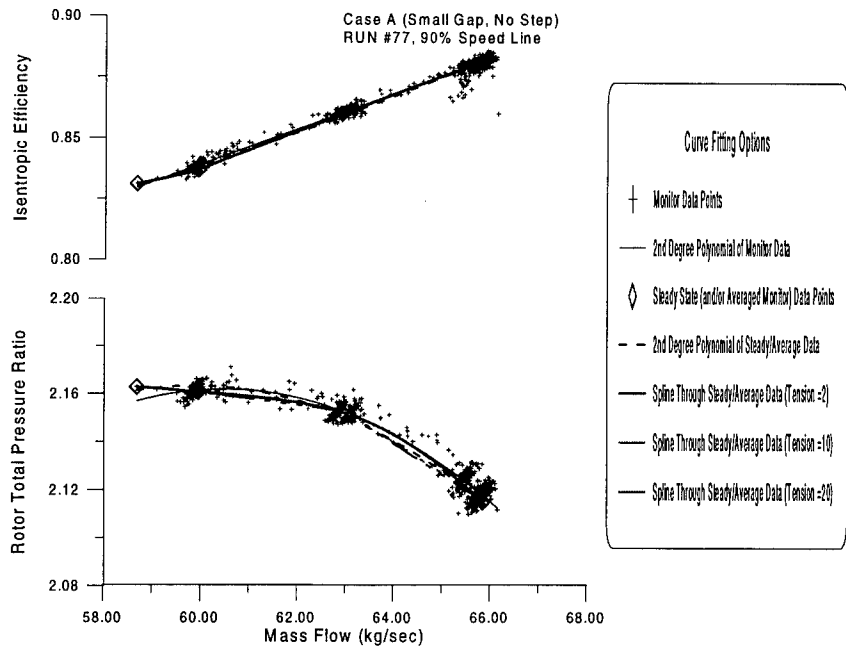
Figure 121. Performance Curve-Fit for Casing Configuration A (90% Design Rotor Speed)

167
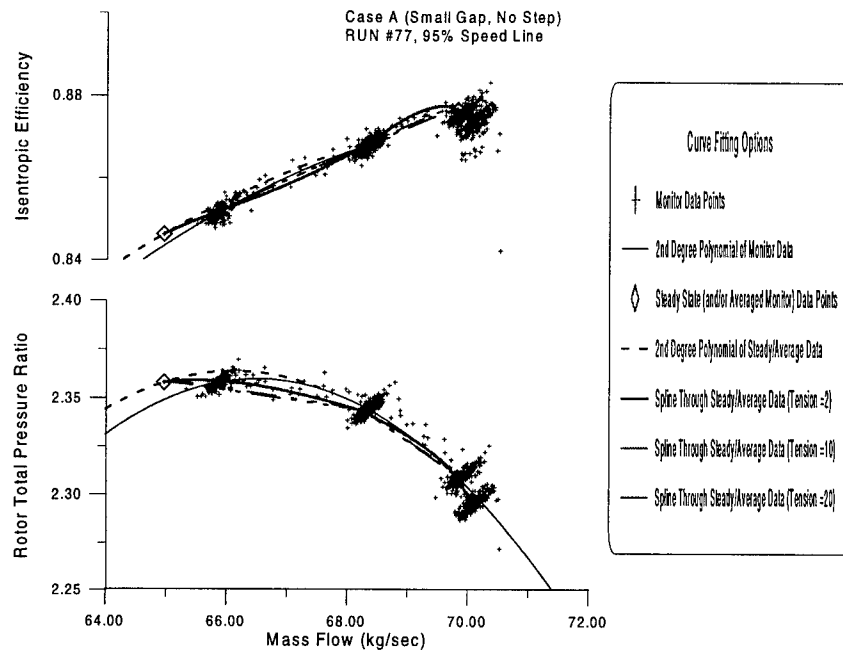
Figure 122. Performance Curve-Fit for Casing Configuration A (95% Design Rotor Speed)
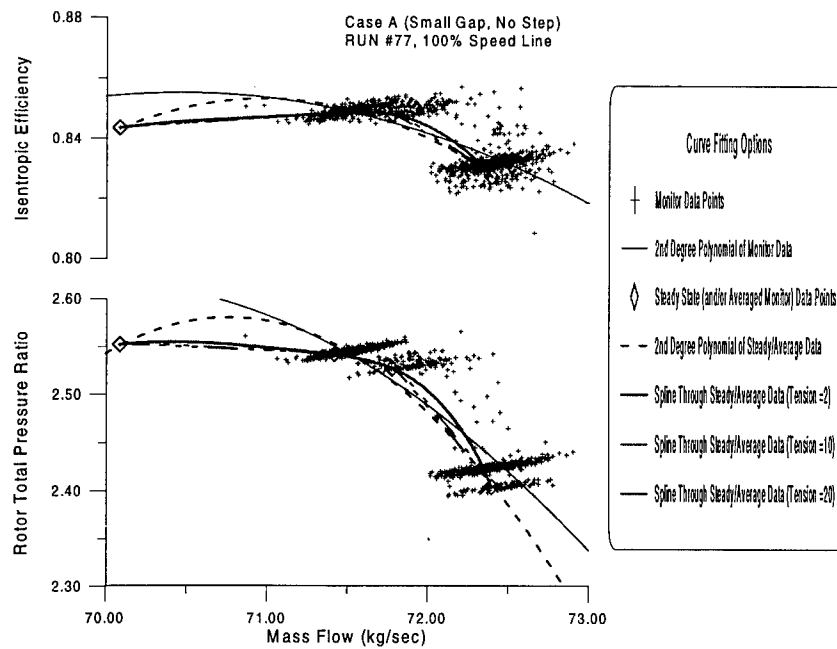
Figure 123. Performance Curve-Fit for Casing Configuration A (100% Design Rotor Speed)

168
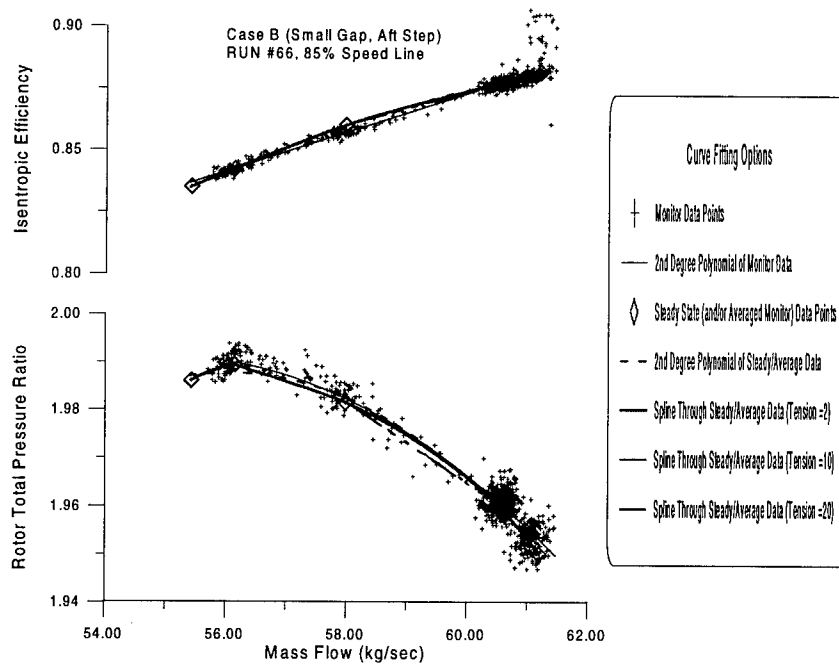
Figure 124. Performance Curve-Fit for Casing Configuration B (85% Design Rotor Speed)
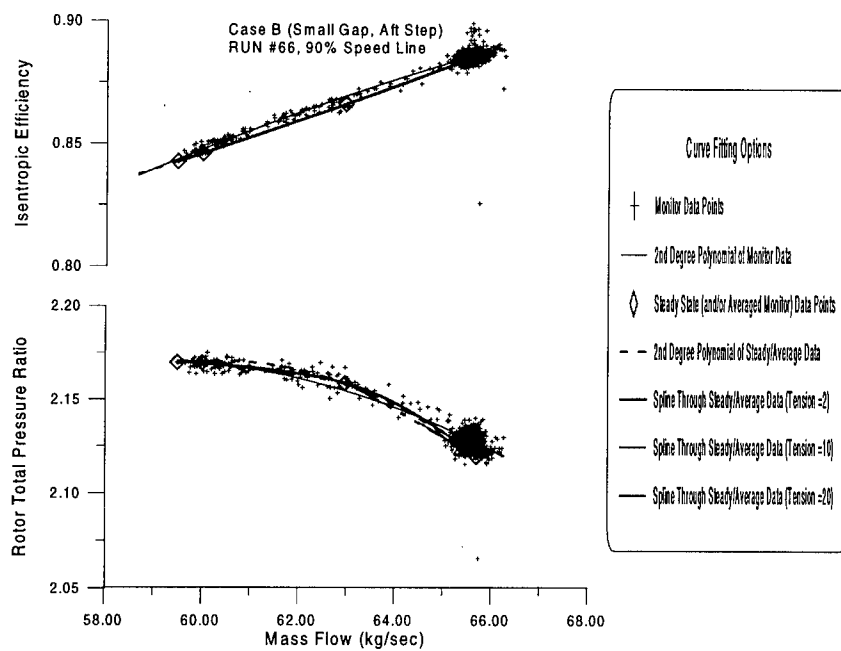
Figure 125. Performance Curve-Fit for Casing Configuration B (90% Design Rotor Speed)
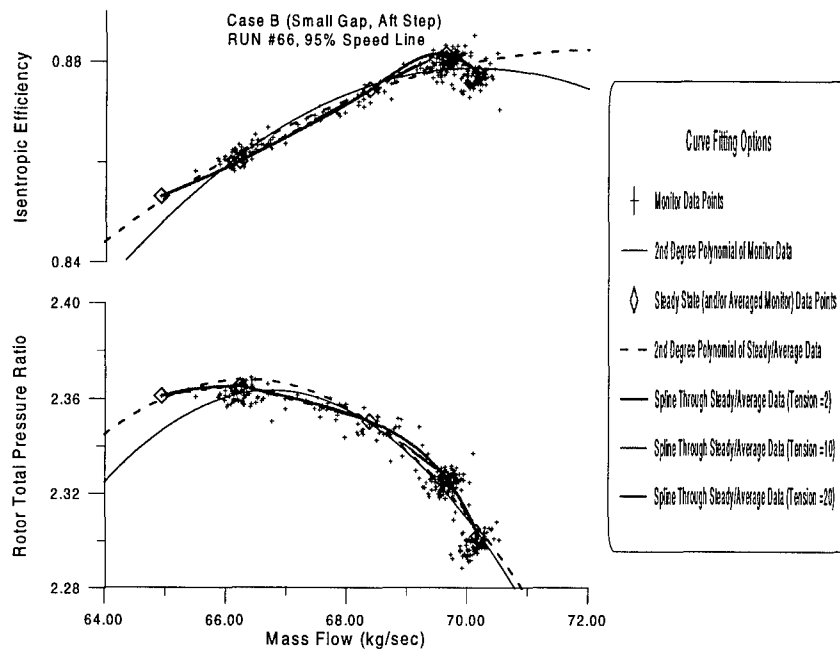
Figure 126. Performance Curve-Fit for Casing Configuration B (95% Design Rotor Speed)
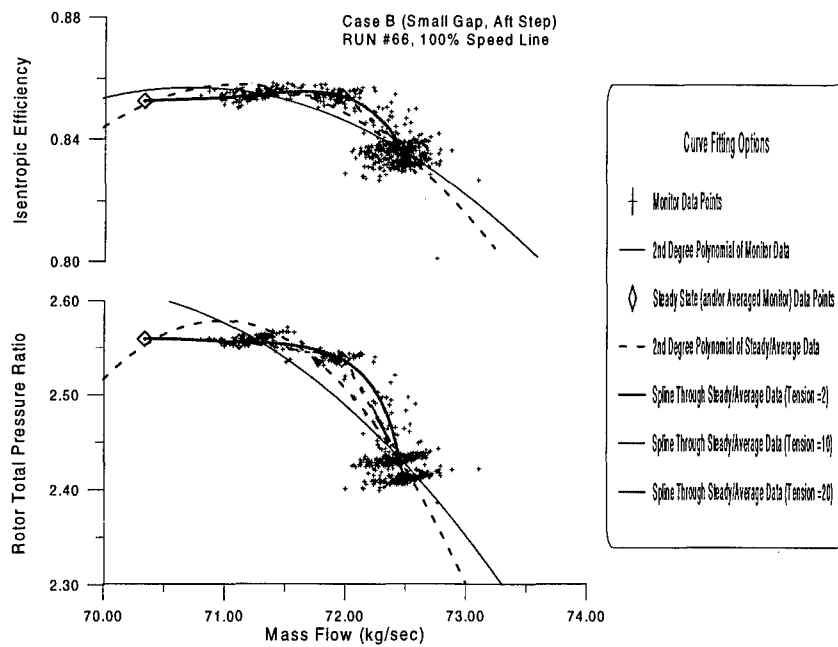
Figure 127. Performance Curve-Fit for Casing Configuration B (100% Design Rotor Speed)

170
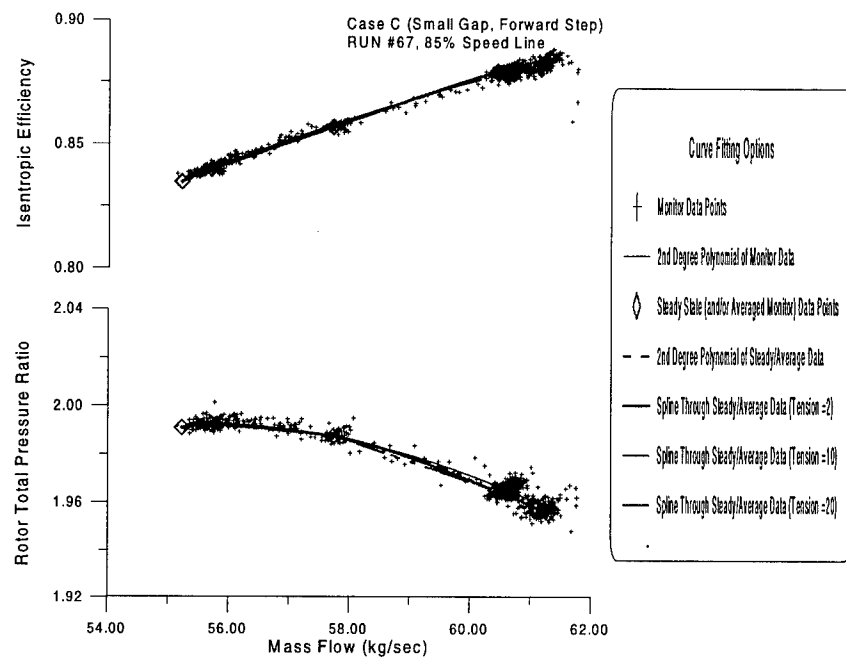
Figure 128. Performance Curve-Fit for Casing Configuration C (85% Design Rotor Speed)
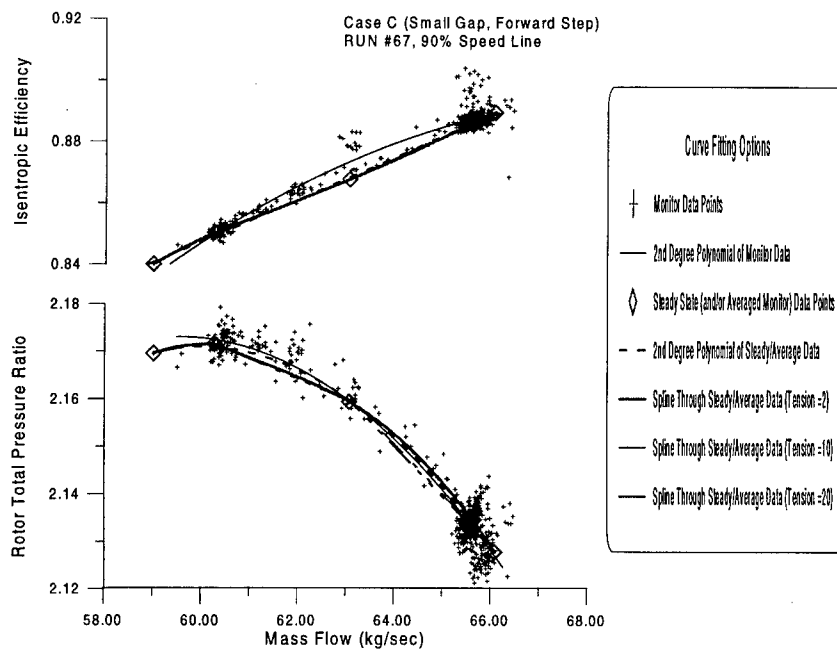
Figure 129. Performance Curve-Fit for Casing Configuration C (90% Design Rotor Speed)

171
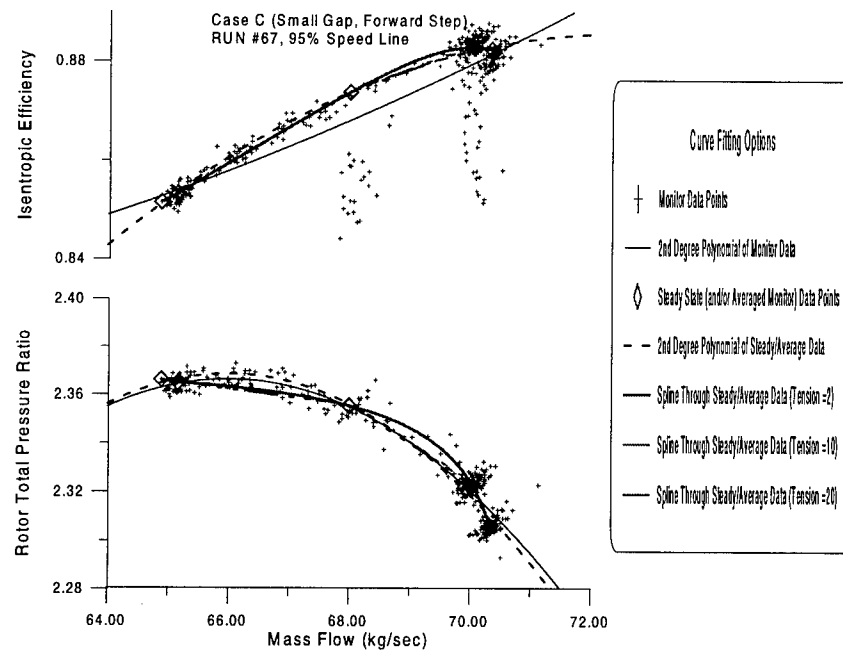
Figure 130. Performance Curve-Fit for Casing Configuration C (95% Design Rotor Speed)
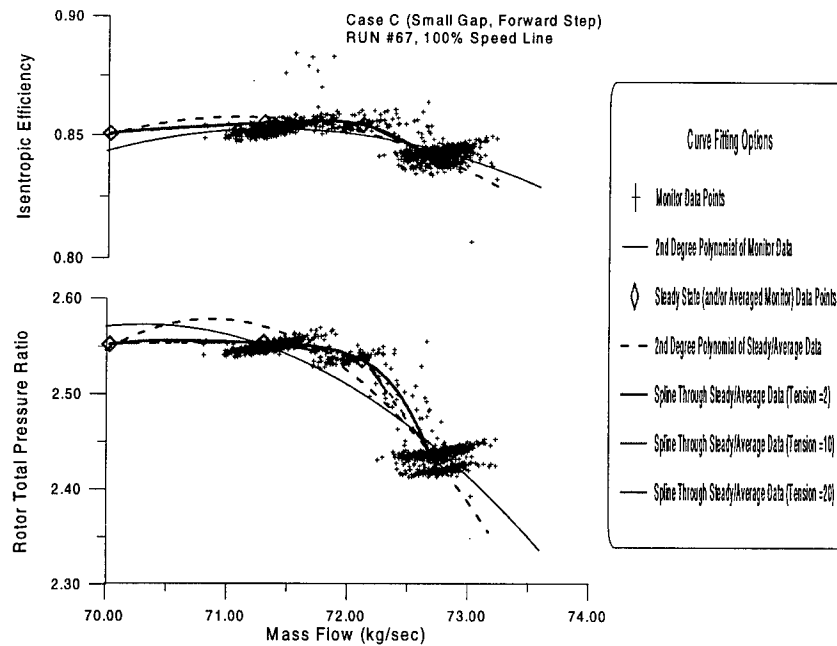
Figure 131. Performance Curve-Fit for Casing Configuration C (100% Design Rotor Speed)

172
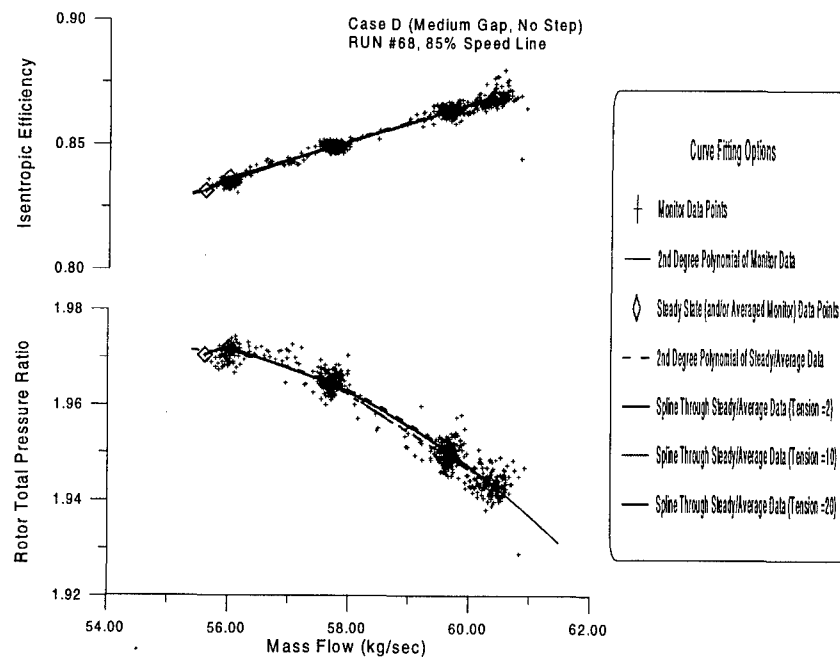
Figure 132. Performance Curve-Fit for Casing Configuration D (85% Design Rotor Speed)
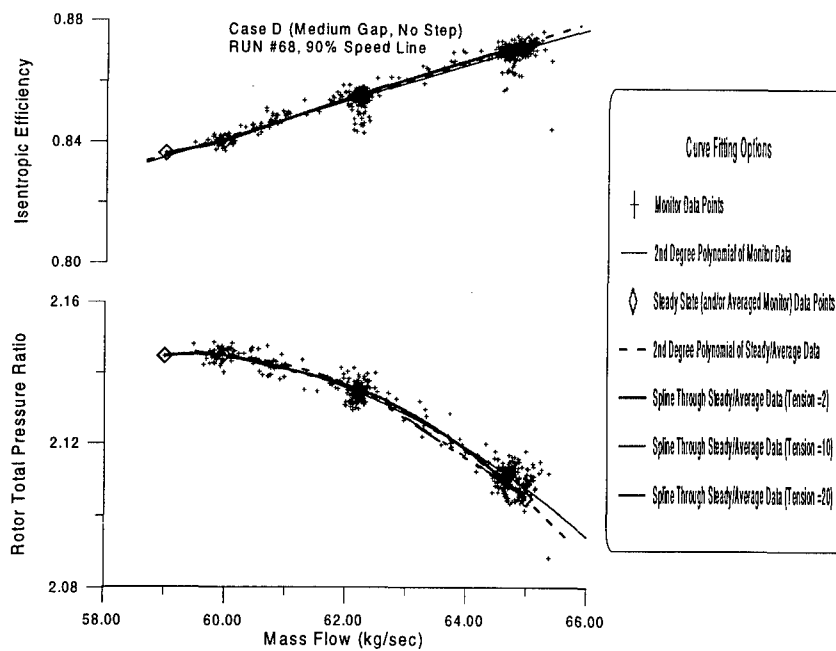
Figure 133. Performance Curve-Fit for Casing Configuration D (90% Design Rotor Speed)

173
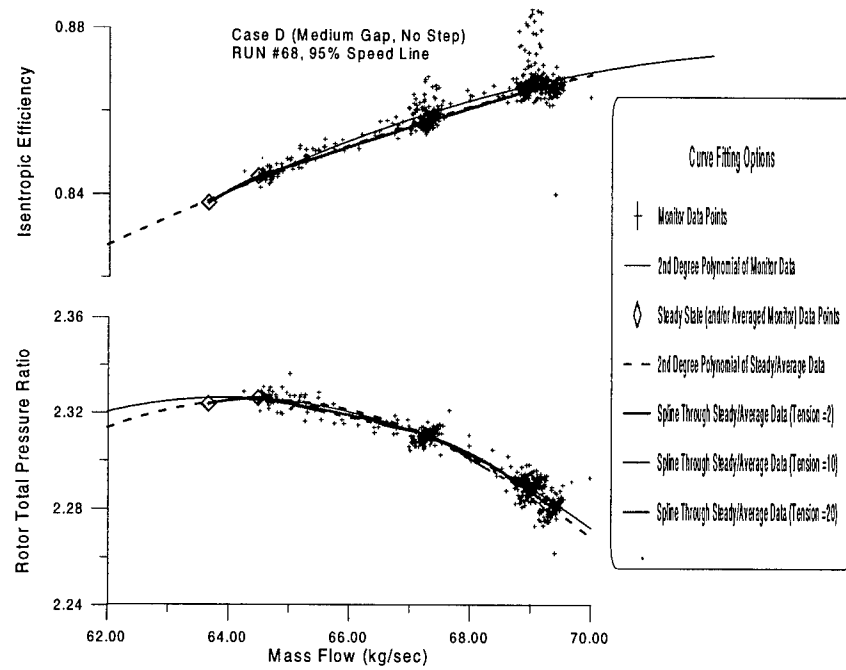
Figure 134. Performance Curve-Fit for Casing Configuration D (95% Design Rotor Speed)
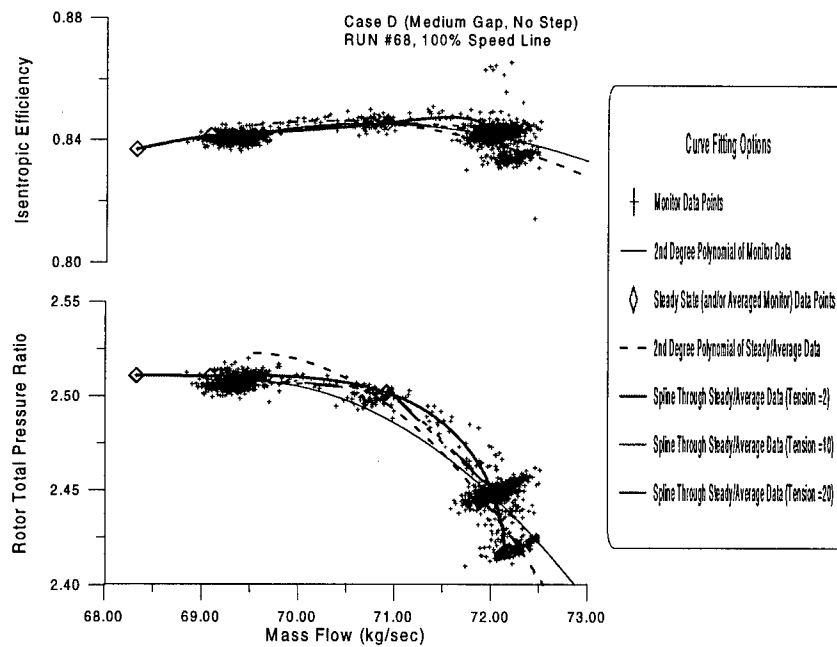
Figure 135. Performance Curve-Fit for Casing Configuration D (100% Design Rotor Speed)

174
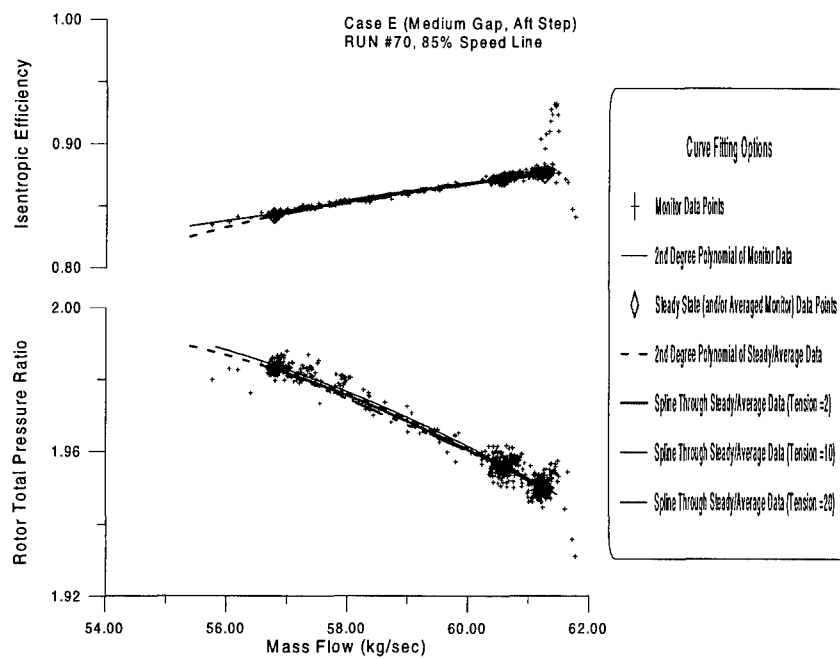
Figure 136. Performance Curve-Fit for Casing Configuration E (85% Design Rotor Speed)
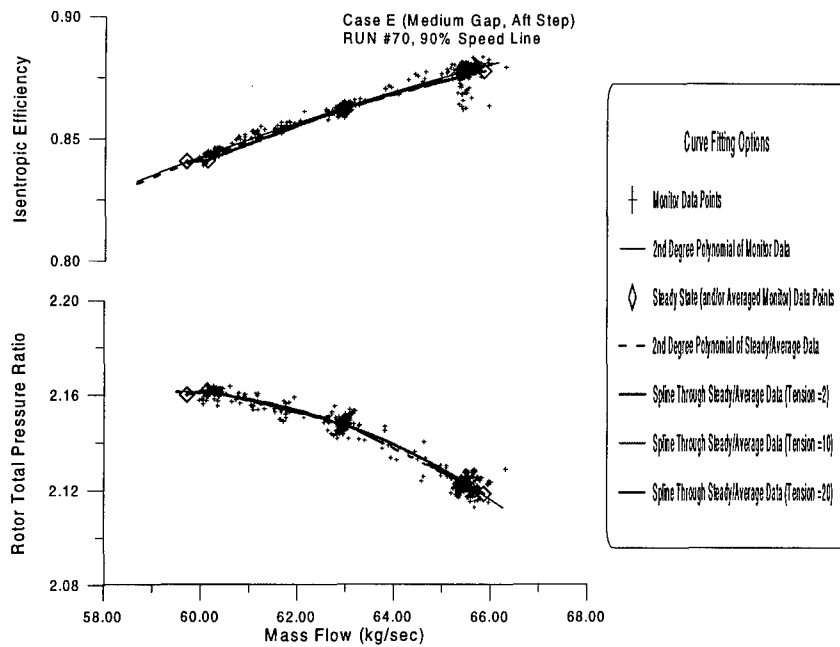
Figure 137. Performance Curve-Fit for Casing Configuration E (90% Design Rotor Speed)

175
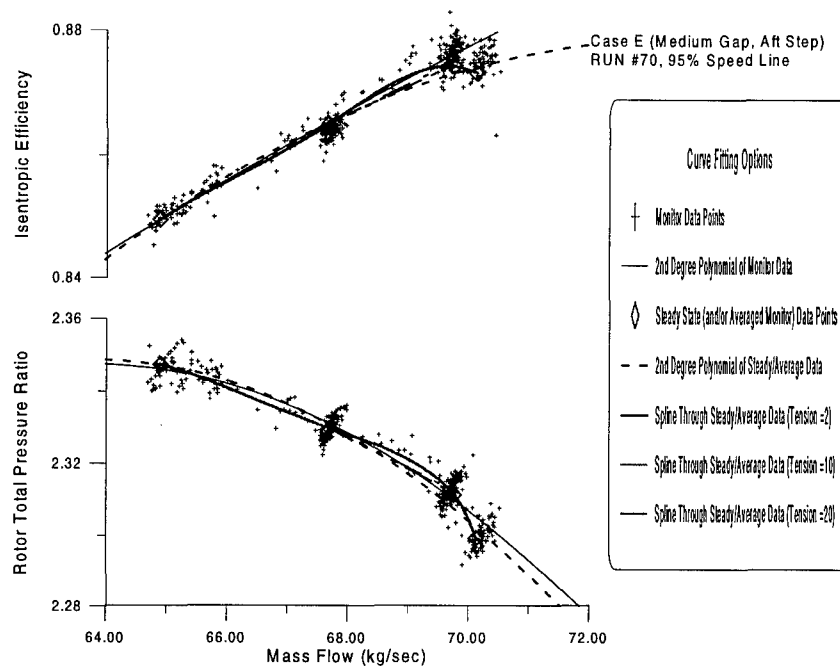
Figure 138. Performance Curve-Fit for Casing Configuration E (95% Design Rotor Speed)
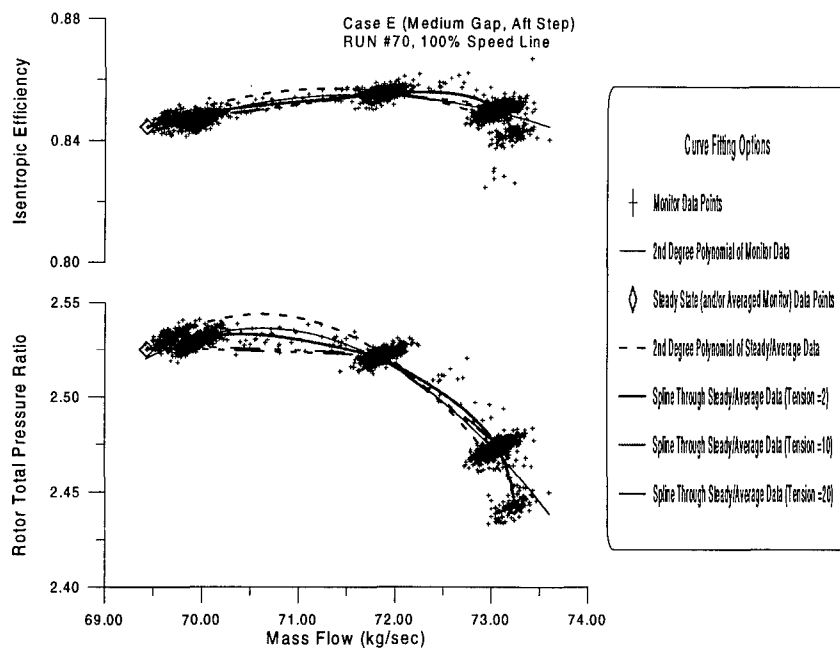
Figure 139. Performance Curve-Fit for Casing Configuration E (100% Design Rotor Speed)

176
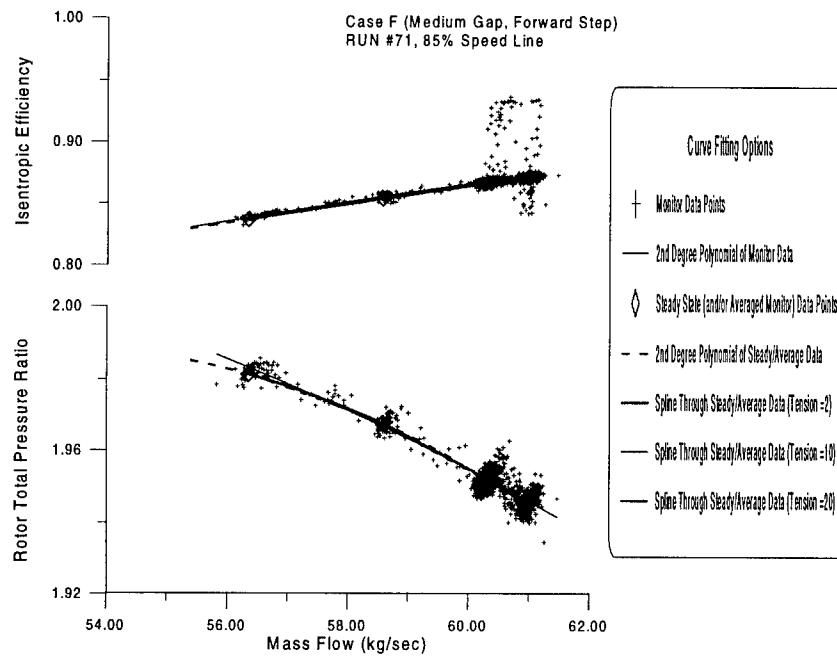
Figure 140. Performance Curve-Fit for Casing Configuration F (85% Design Rotor Speed)
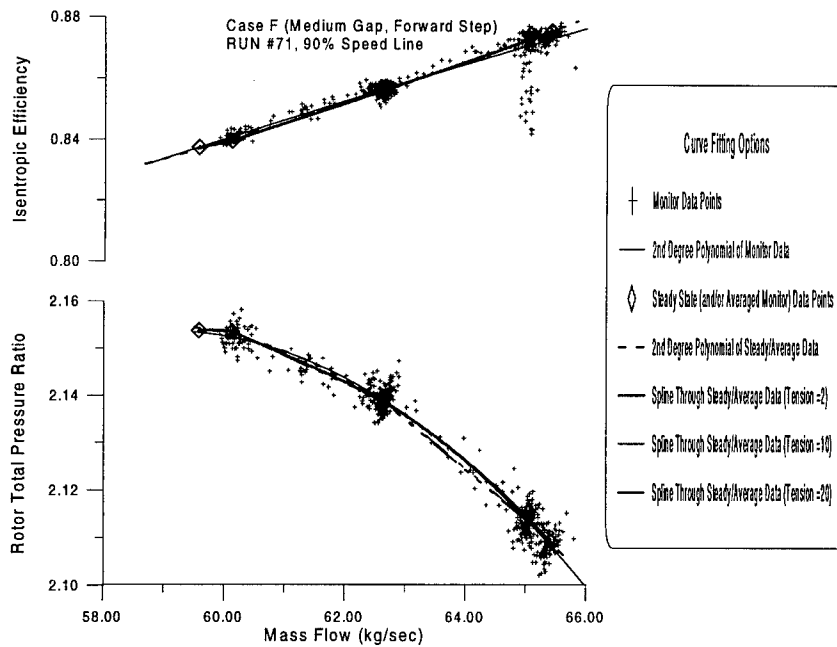
Figure 141. Performance Curve-Fit for Casing Configuration F (90% Design Rotor Speed)
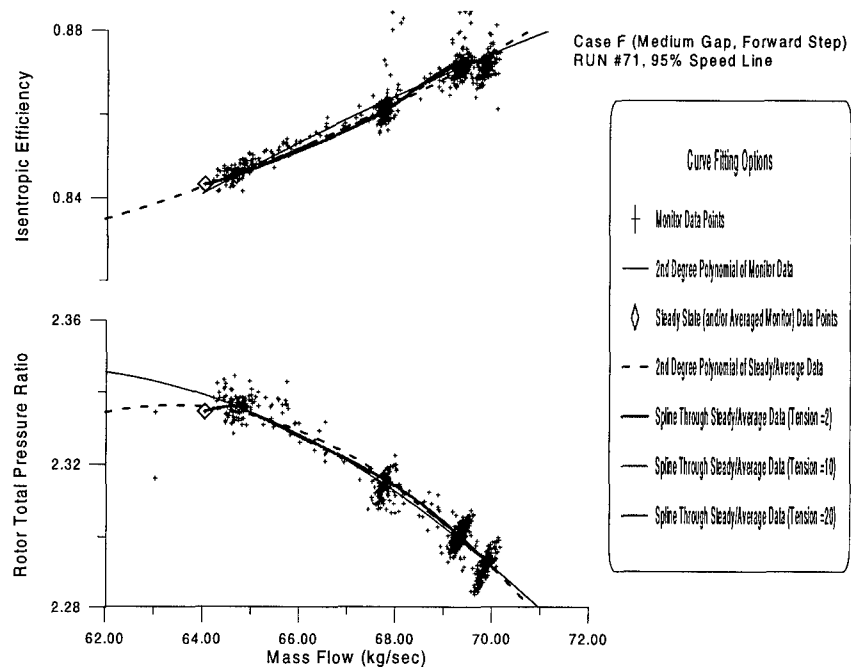
Figure 142. Performance Curve-Fit for Casing Configuration F (95% Design Rotor Speed)
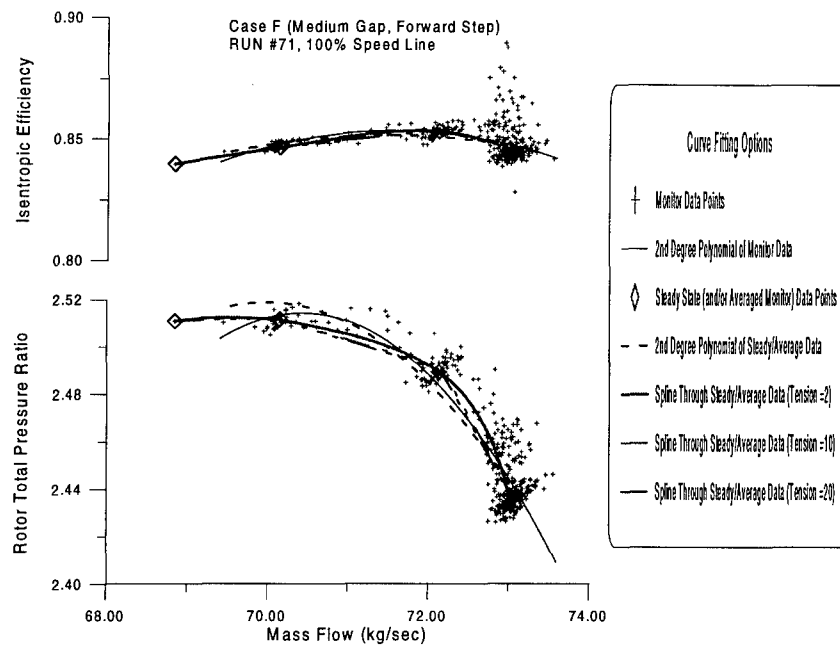
Figure 143. Performance Curve-Fit for Casing Configuration F (100% Design Rotor Speed)

178
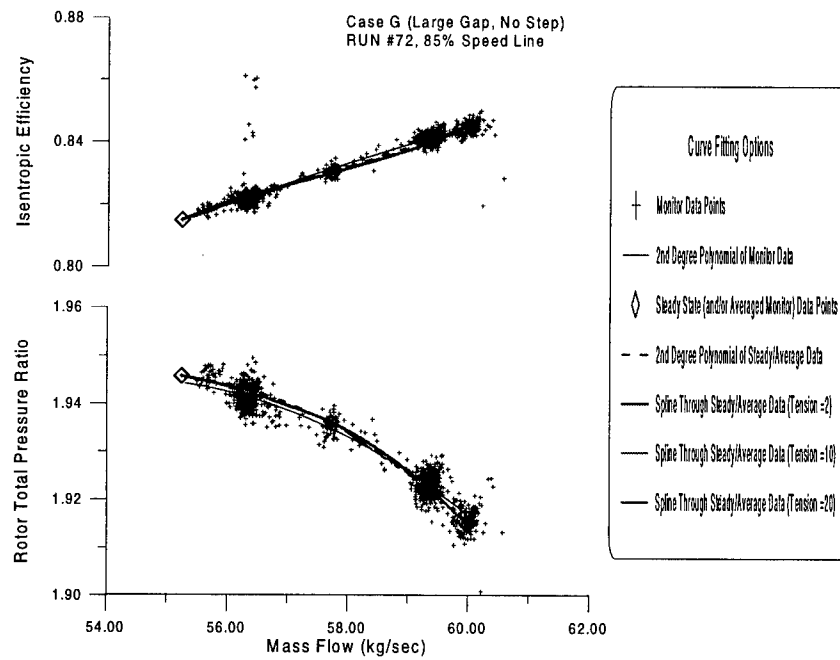
Figure 144. Performance Curve-Fit for Casing Configuration G (85% Design Rotor Speed)
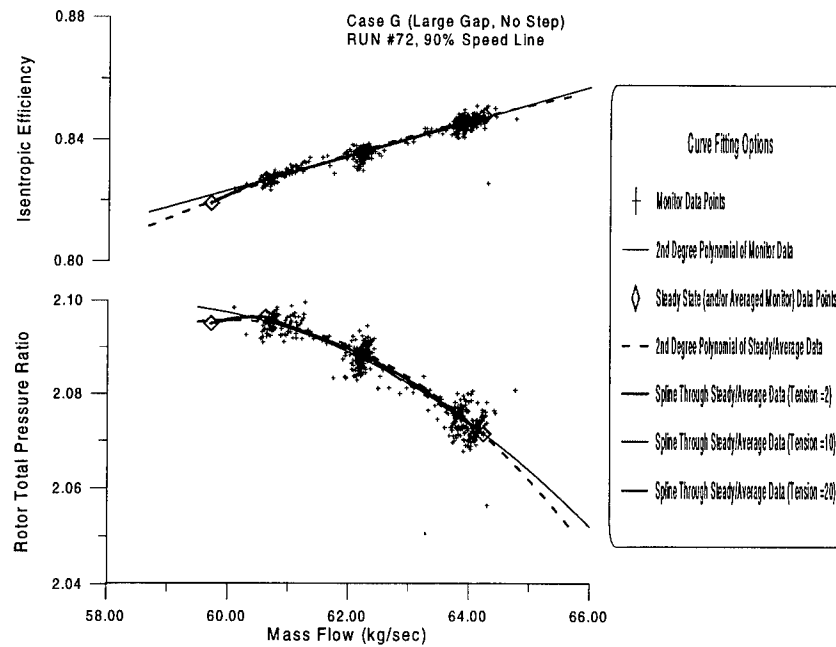
Figure 145. Performance Curve-Fit for Casing Configuration G (90% Design Rotor Speed)

179
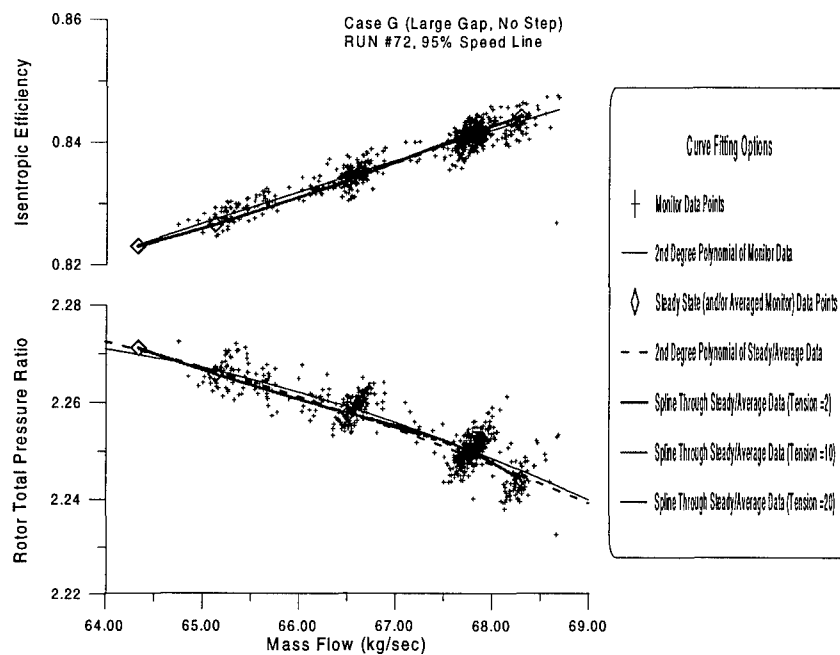
Figure 146. Performance Curve-Fit for Casing Configuration G (95% Design Rotor Speed)
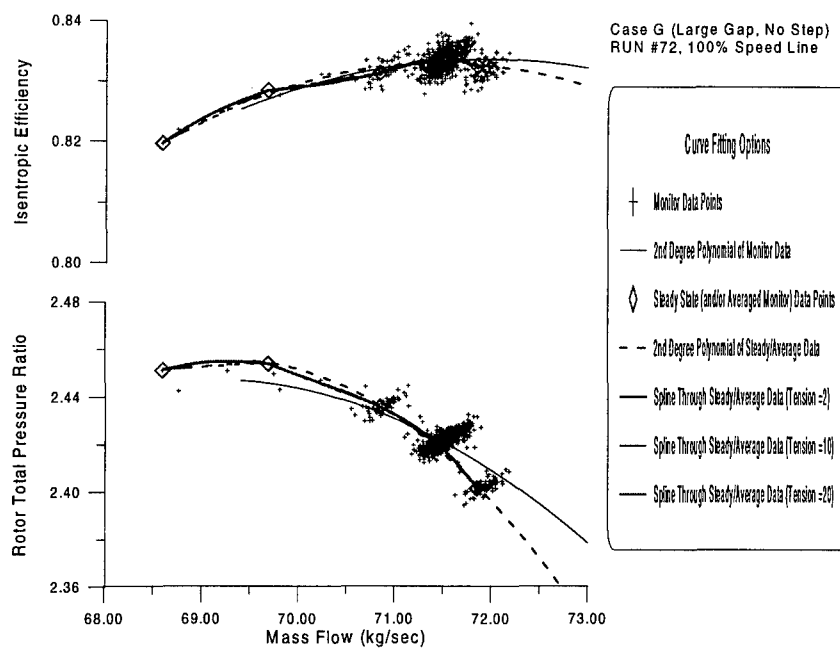
Figure 147. Performance Curve-Fit for Casing Configuration G (100% Design Rotor Speed)

180
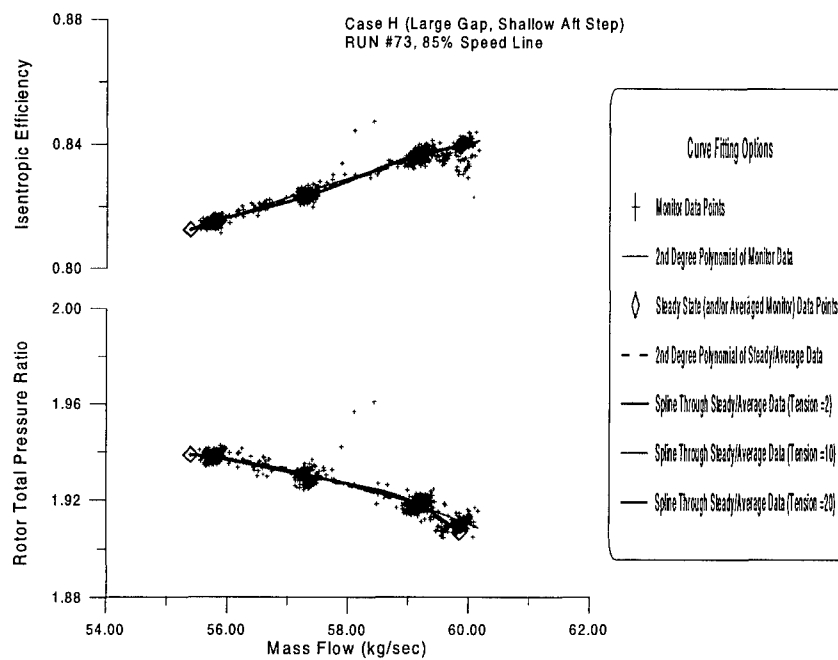
Figure 148. Performance Curve-Fit for Casing Configuration H (85% Design Rotor Speed)
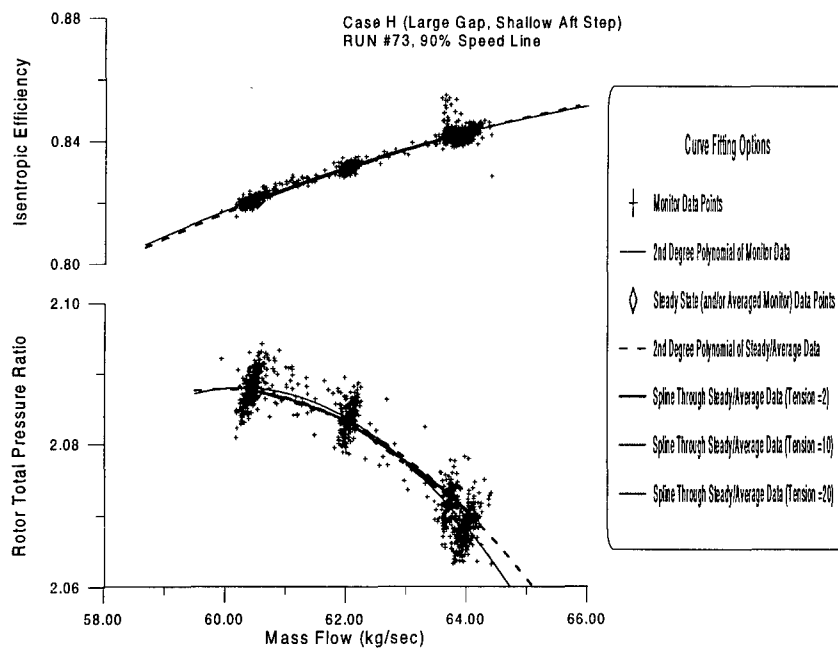
Figure 149. Performance Curve-Fit for Casing Configuration H (90% Design Rotor Speed)

181
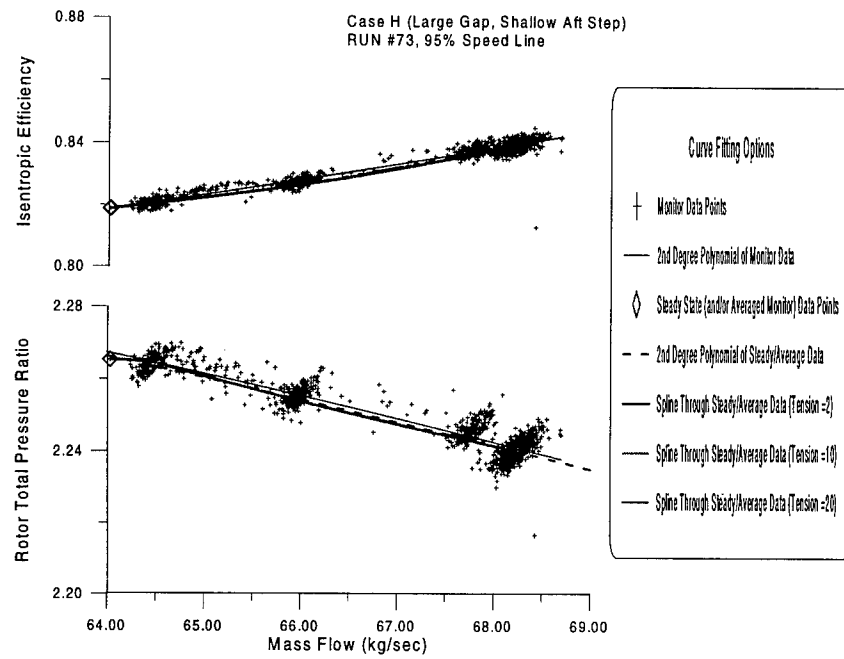
Figure 150. Performance Curve-Fit for Casing Configuration H (95% Design Rotor Speed)
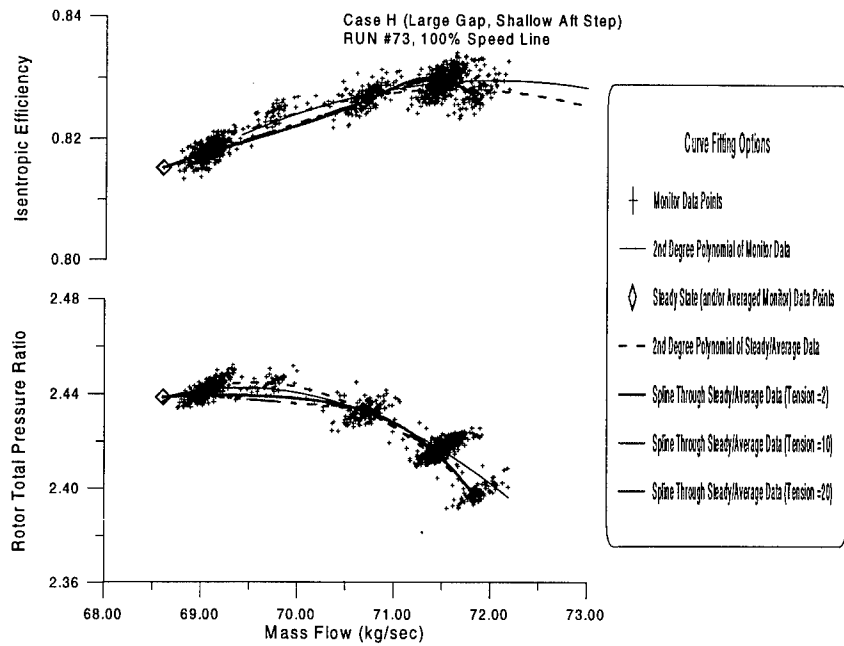
Figure 151. Performance Curve-Fit for Casing Configuration H (100% Design Rotor Speed)

182
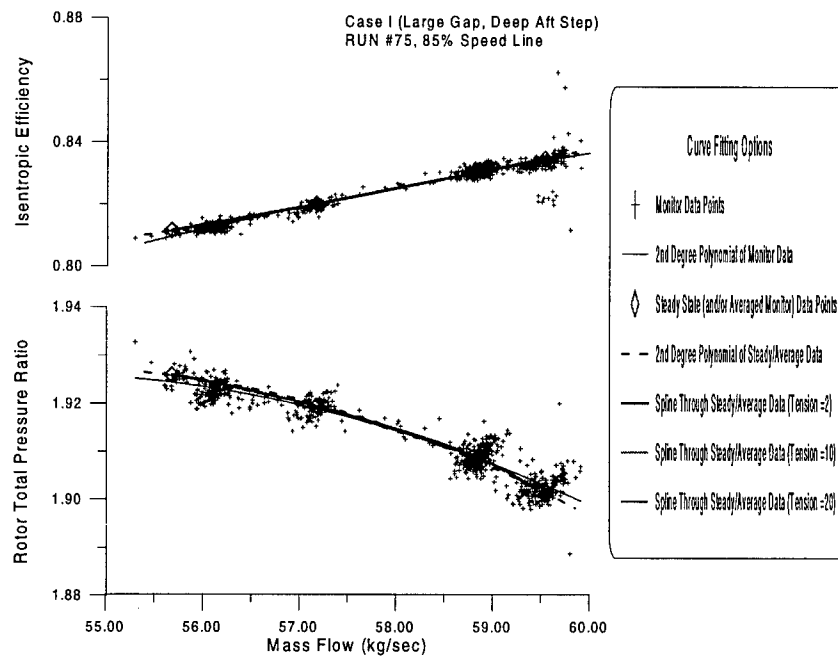
Figure 152. Performance Curve-Fit for casing Configuration I (85% Design Rotor Speed)
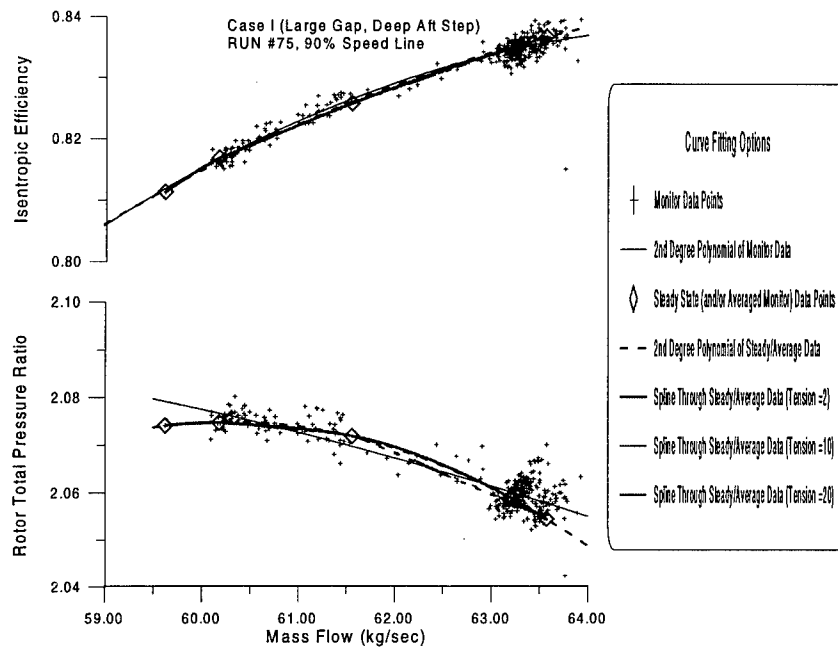
Figure 153. Performance Curve-Fit for Casing Configuration I (90% Design Rotor Speed)
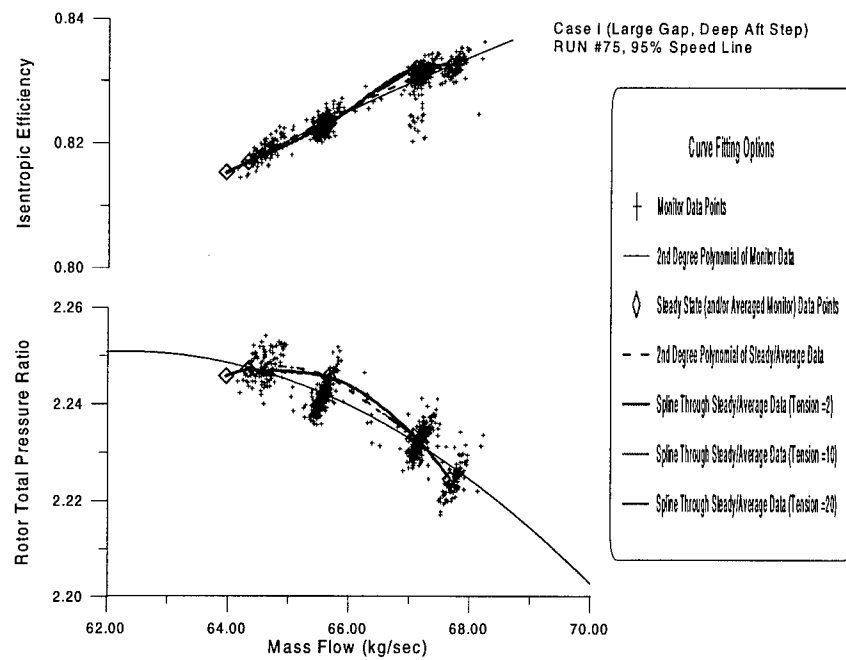
Figure 154. Performance Curve-Fit for Casing Configuration I (95% Design Rotor Speed)
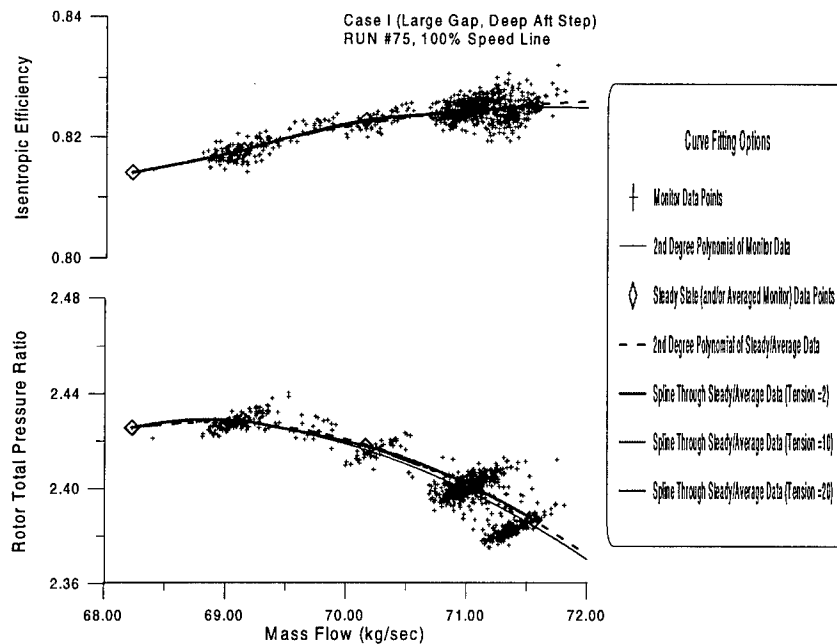
Figure 155. Performance Curve-Fit for Casing Configuration I (100% Design Rotor Speed)

184

APPENDIX B - Uncertainty Analysis

B.1 Errors of Data Acquisition

Every attempt was made to minimize uncertainties associated with the performance measurement instruments and acquisition process. Prior to the first test in the series of nine tests corresponding to each casing configuration, each pressure transducer channel was calibrated and validated; the calibration constants were determined, and this calibration was used throughout the test series. Likewise, the temperature measurement system was calibrated and maintained. Prior to and immediately after each test, a confidence check of each data channel was conducted. During this check, a precisely controlled pressure was applied to each pressure transducer, and a precisely controlled temperature was applied to each thermocouple junction. Feedback data on each channel was sampled a minimum of thirty times (a steady-state data point is the average of thirty consecutive samples taken in less than a half second). If the time-average of each channel was found to be outside of a predefined tolerance (typically ±35Pa for pressure and ±0.2K for temperature), the channel was flagged by the operator for exclusion from data averaging during the test and post-processing. Additionally, during testing and post-processing, if a channel was found to exceed three standard deviations from the average of all data channels measuring the same parameter, the data acquisition software automatically excluded that channel from data averaging. Also, individual samples used in the calculation of a channel average were subject to outlier rejection using Chauvenet's criterion (Holman [44]). These checks provided a measurement system of high precision and accuracy. The confidence check conducted prior to each test also provided the precision and bias errors of each data channel for that test. The bias error of a channel was determined to be the difference between the mean of the time-averaged samples and the calibration reference applied to the transducer. The precision error of a channel was defined to be the standard deviation of the channel average. The

185

degrees of freedom associated with each channel was specified to be the number of valid (Chauvenet outliers excluded) data samples used to calculate the mean. As a check, the calculated bias and precision errors were compared to the chained system errors calculated from manufacturers' specifications for each piece of hardware; the channel-averaging method described above was determined to be the more conservative and reliable method. Thus, the uncertainty errors of the data acquisition process were determined by the pretest confidence check. The propagation of these errors is presented in the following section.

B.2 Error Propagation - Sample Calculation

Propagation of errors occurs anytime a variable is calculated from component variables. The following sample calculation demonstrates the propagation of errors associated with the calculation of corrected mass flow rate from the uncorrected mass flow rate, referenced temperature ratio, and referenced pressure ratio (see Equation 40 in Appendix A). This process, described in detail by Abernethy and Thompson [3] , was used to calculate the error propagation throughout the CRF's data analysis software.

B.2.1 Basic Equation

$$\dot{m}_c \equiv \frac{\dot{m}\sqrt{\theta}}{\delta} \tag{42}$$

B.2.2 Partial Derivatives

$$\frac{\partial \dot{m}_c}{\partial \dot{m}} = \frac{\sqrt{\theta}}{\delta} = \frac{\dot{m}_c}{\dot{m}} \tag{43}$$

$$\frac{\partial \dot{m}_c}{\partial \theta} = \frac{\dot{m}}{2\delta\sqrt{\theta}} = \frac{\dot{m}_c}{2\theta} \tag{44}$$

$$\frac{\partial \dot{m}_c}{\partial \delta} = \frac{-\dot{m}\sqrt{\theta}}{\delta^2} = -\frac{\dot{m}_c}{\delta} \tag{45}$$

186

B.2.3 Error Equation

The most probable error is simply the root-sum-square of the contributions from the component errors.

$$\omega_{\dot{m}_c} = \left[\left(\frac{\partial \dot{m}_c}{\partial \dot{m}} \omega_{\dot{m}} \right)^2 + \left(\frac{\partial \dot{m}_c}{\partial \theta} \omega_\theta \right)^2 + \left(\frac{\partial \dot{m}_c}{\partial \delta} \omega_\delta \right)^2 \right]^{\frac{1}{2}} \qquad (46)$$

B.2.4 Bias Error

Expressing Equation 46 in terms of component bias error gives:

$$b_{\dot{m}_c} = \left[\left(\frac{\partial \dot{m}_c}{\partial \dot{m}} b_{\dot{m}} \right)^2 + \left(\frac{\partial \dot{m}_c}{\partial \theta} b_\theta \right)^2 + \left(\frac{\partial \dot{m}_c}{\partial \delta} b_\delta \right)^2 \right]^{\frac{1}{2}} \qquad (47)$$

$$= \left[\left(\frac{\dot{m}_c}{\dot{m}} b_{\dot{m}} \right)^2 + \left(\frac{\dot{m}_c}{2\theta} b_\theta \right)^2 + \left(-\frac{\dot{m}_c}{\delta} b_\delta \right)^2 \right]^{\frac{1}{2}} \qquad (48)$$

B.2.5 Precision Error

Expressing Equation 46 in terms of component precision error gives:

$$s_{\dot{m}_c} = \left[\left(\frac{\partial \dot{m}_c}{\partial \dot{m}} s_{\dot{m}} \right)^2 + \left(\frac{\partial \dot{m}_c}{\partial \theta} s_\theta \right)^2 + \left(\frac{\partial \dot{m}_c}{\partial \delta} s_\delta \right)^2 \right]^{\frac{1}{2}} \qquad (49)$$

$$= \left[\left(\frac{\dot{m}_c}{\dot{m}} s_{\dot{m}} \right)^2 + \left(\frac{\dot{m}_c}{2\theta} s_\theta \right)^2 + \left(-\frac{\dot{m}_c}{\delta} s_\delta \right)^2 \right]^{\frac{1}{2}} \qquad (50)$$

B.2.6 Degrees of Freedom

The degrees of freedom of the calculated variable is a function of the calculated variable and its precision error, the component variables and their precision errors, and the component degrees of freedom.

$$df_{\dot{m}_c} = \frac{s_{\dot{m}_c}^4}{\left[\frac{\left(\frac{\dot{m}_c}{\dot{m}} s_{\dot{m}} \right)^4}{df_{\dot{m}}} + \frac{\left(\frac{\dot{m}_c}{2\theta} s_\theta \right)^4}{df_\theta} + \frac{\left(-\frac{\dot{m}_c}{\delta} s_\delta \right)^4}{df_\delta} \right]} \qquad (51)$$

B.2.7 Uncertainty

The uncertainty is the sum of the bias error and the precision error weighted by the probability from the student-t distribution. The student-t probability is a function of the degrees of freedom of the

187

calculated variable and the specified confidence interval; for this study, a 95% confidence interval was specified.

$$U_{\dot{m}_c} = \pm \left[b_{\dot{m}_c} + t_{95} s_{\dot{m}_c} \right] \tag{52}$$

B.3 Performance Data Uncertainty

The uncertainty of the performance data is summarized in Table 5 of Section 4.4.1. Data are presented for only the 100 percent design rotor speed at peak efficiency mass flow for each casing configuration; the uncertainty for slower rotor speeds are less than those shown in Table 5.

APPENDIX C - Rotor Maps

The following figures are performance maps of the ADLARF first-stage rotor for each casing configuration. Each rotor map includes the full mass flow range for each nominal rotor speed.
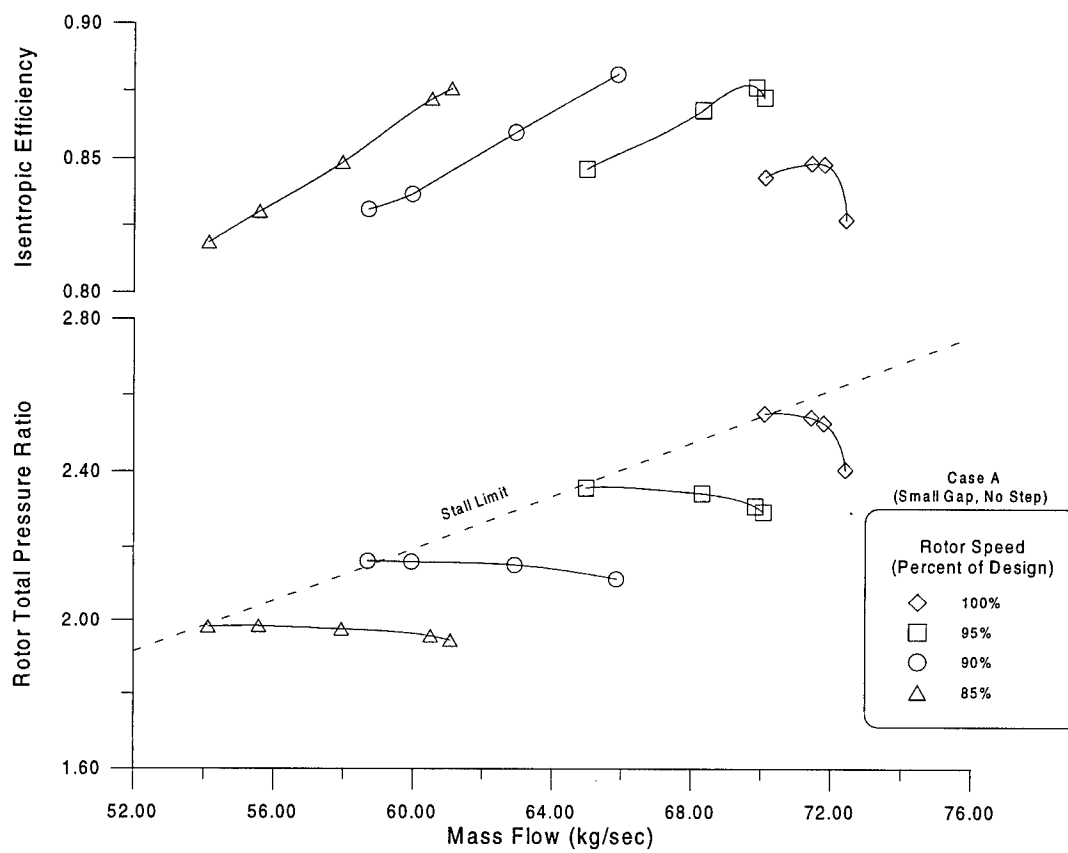
Figure 156. Rotor Map for Configuration A (Small Gap, No Step)
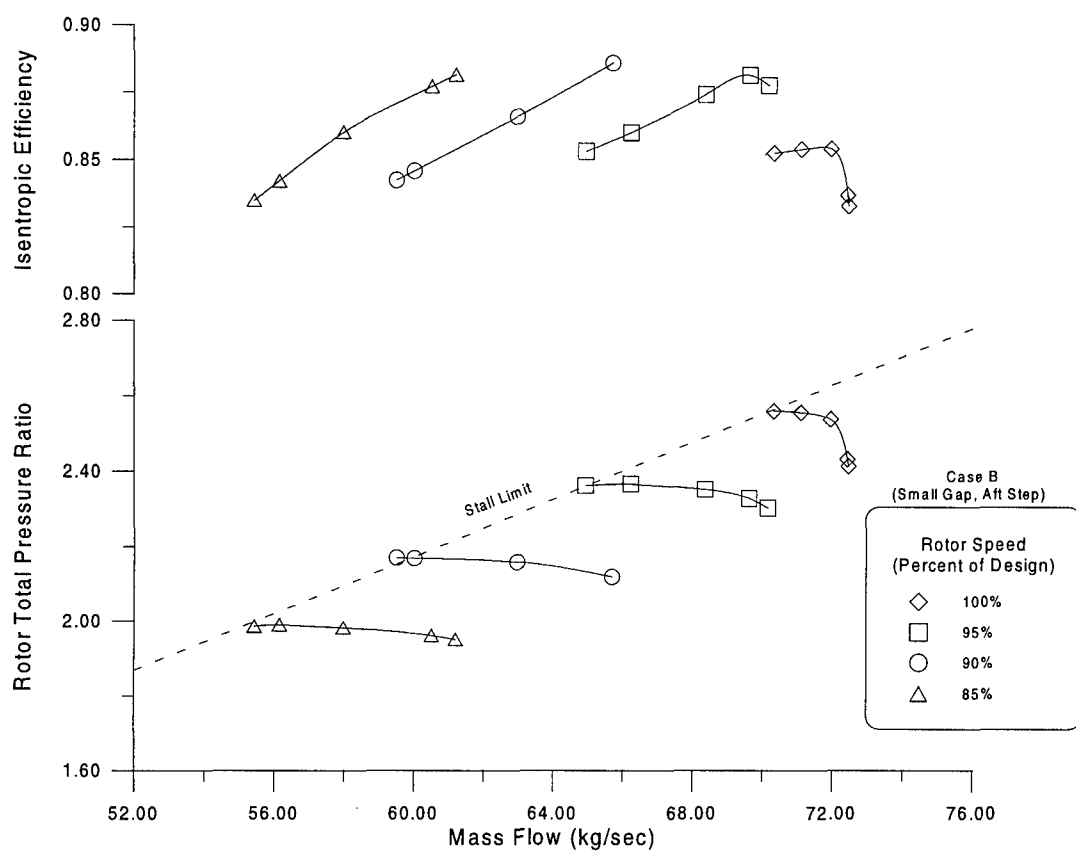
Figure 157. Rotor Map for Configuration B (Small Gap, Aft Step)

191
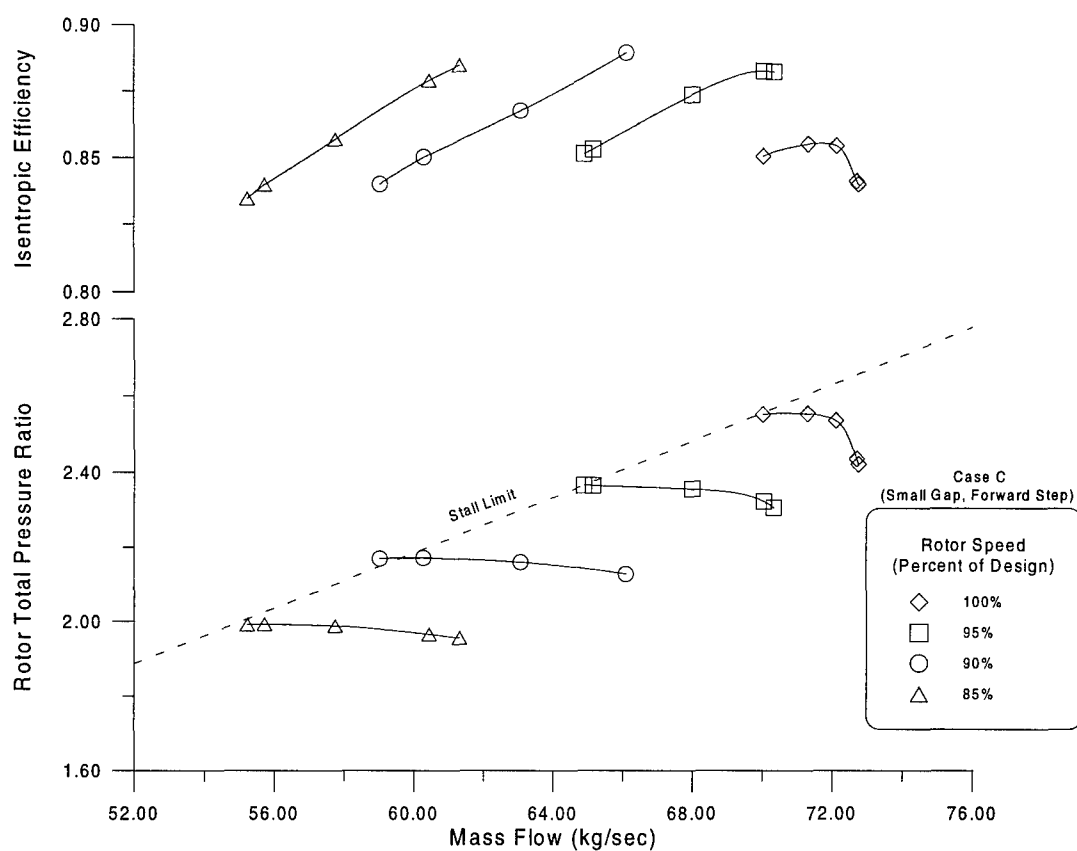
Figure 158. Rotor Map for Configuration C (Small Gap, Forward Step)
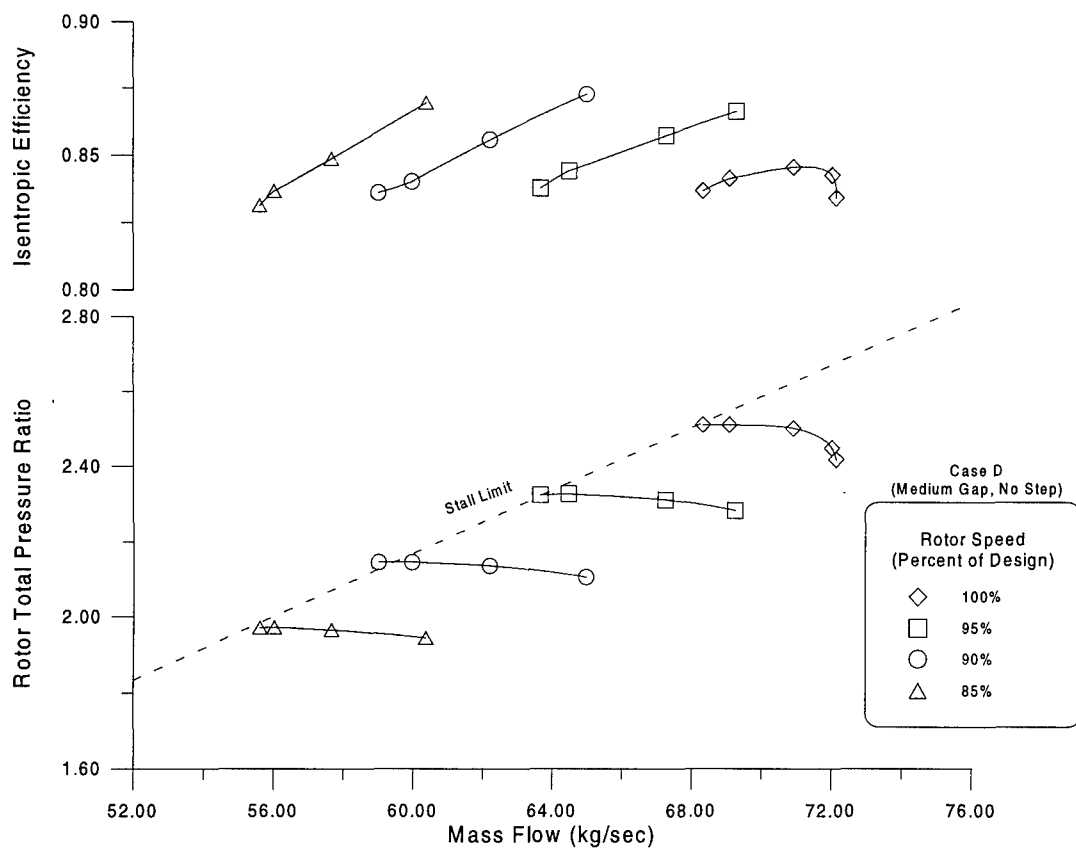
Figure 159. Rotor Map for Configuration D (Medium Gap, No Step)
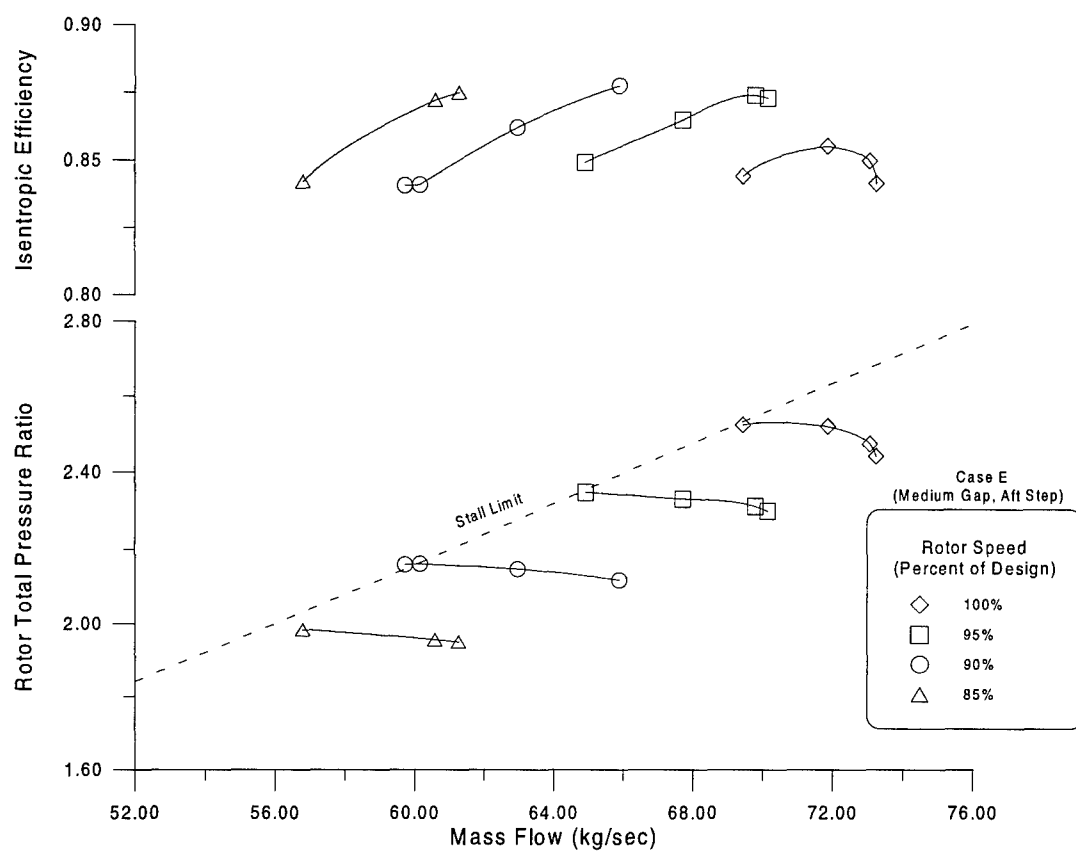
Figure 160. Rotor Map for Configuration E (Medium Gap, Aft Step)
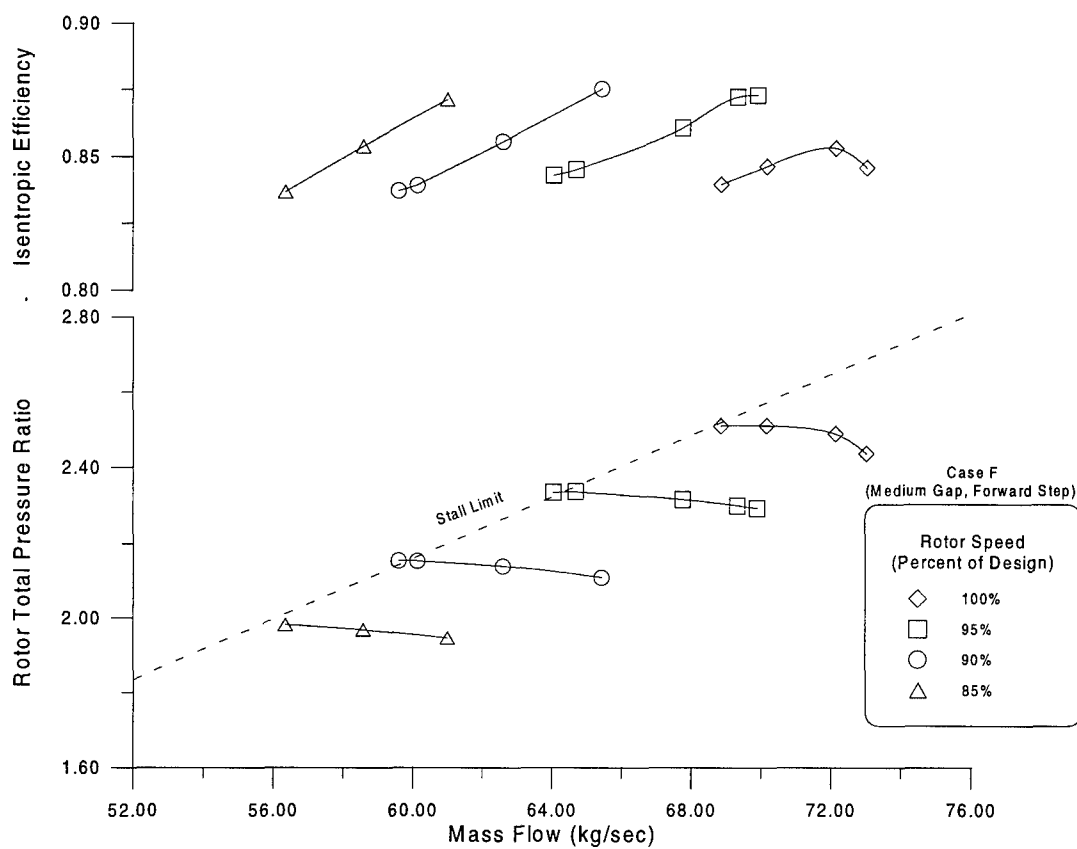
Figure 161. Rotor Map for Configuration F (Medium Gap, Forward Step)
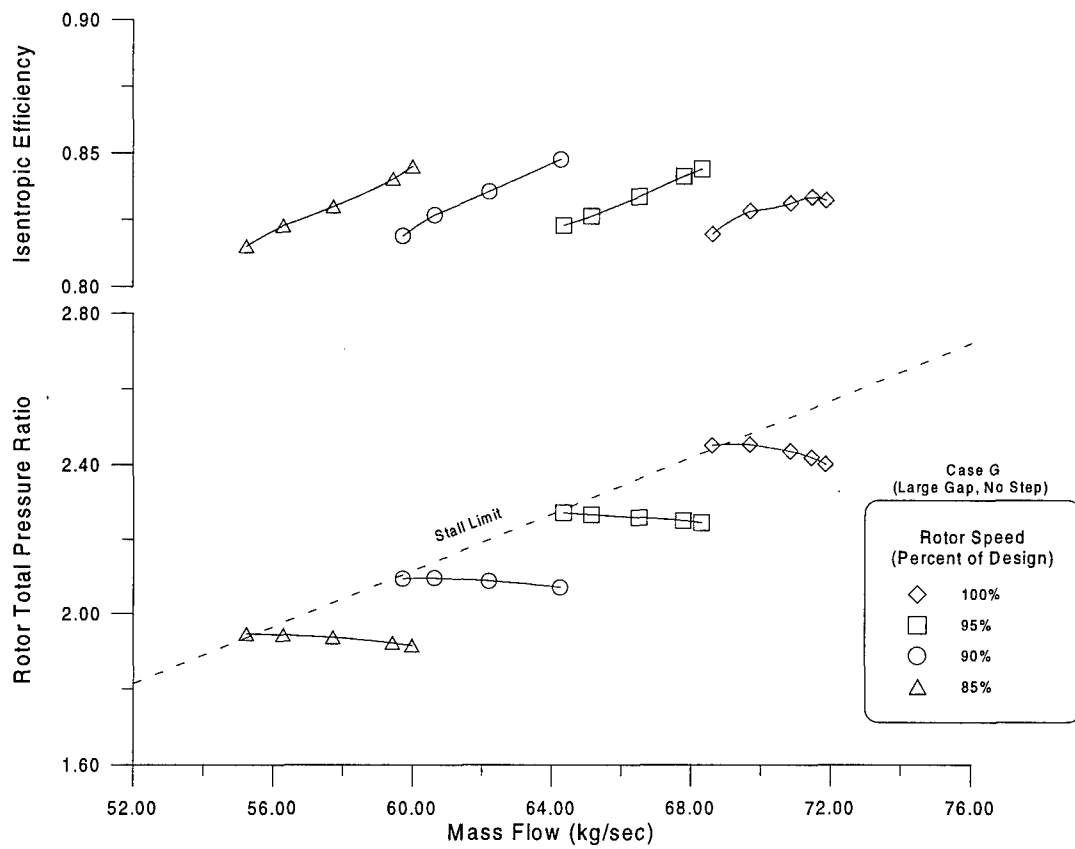
Figure 162. Rotor Map for Configuration G (Large Gap, No Step)
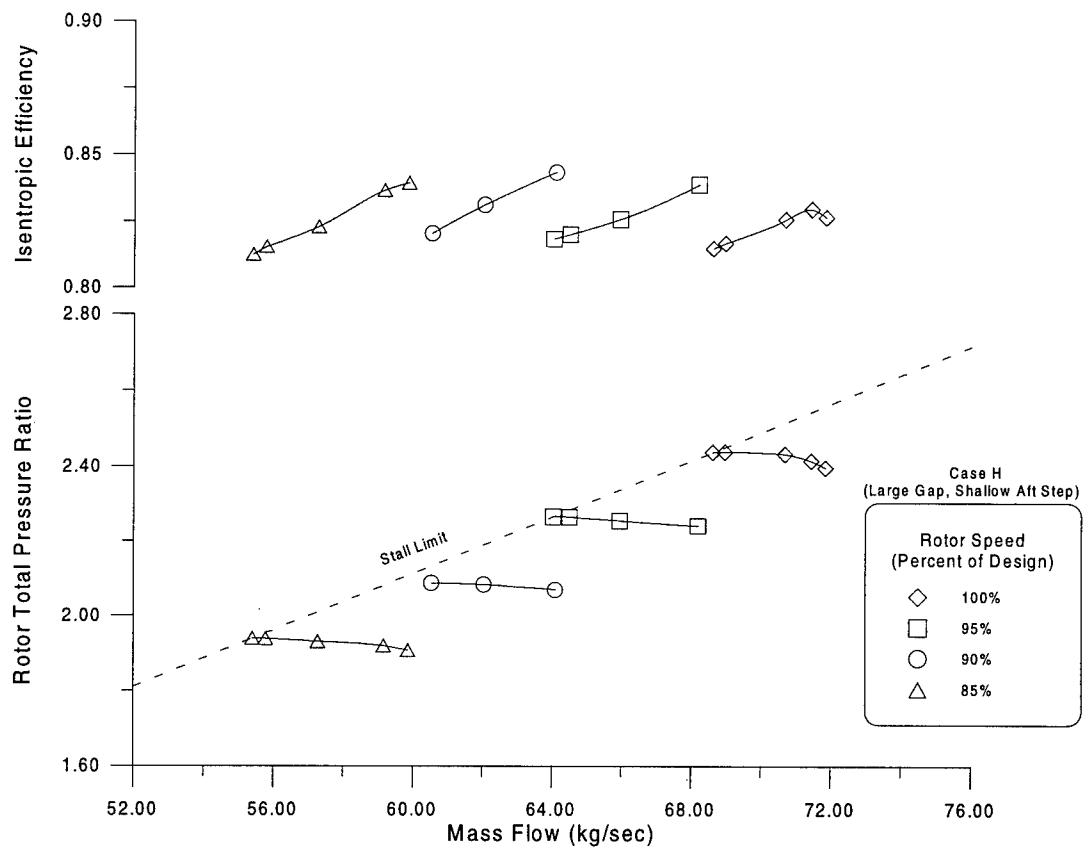
Figure 163. Rotor Map for Configuration H (Large Gap, Shallow Aft Step)
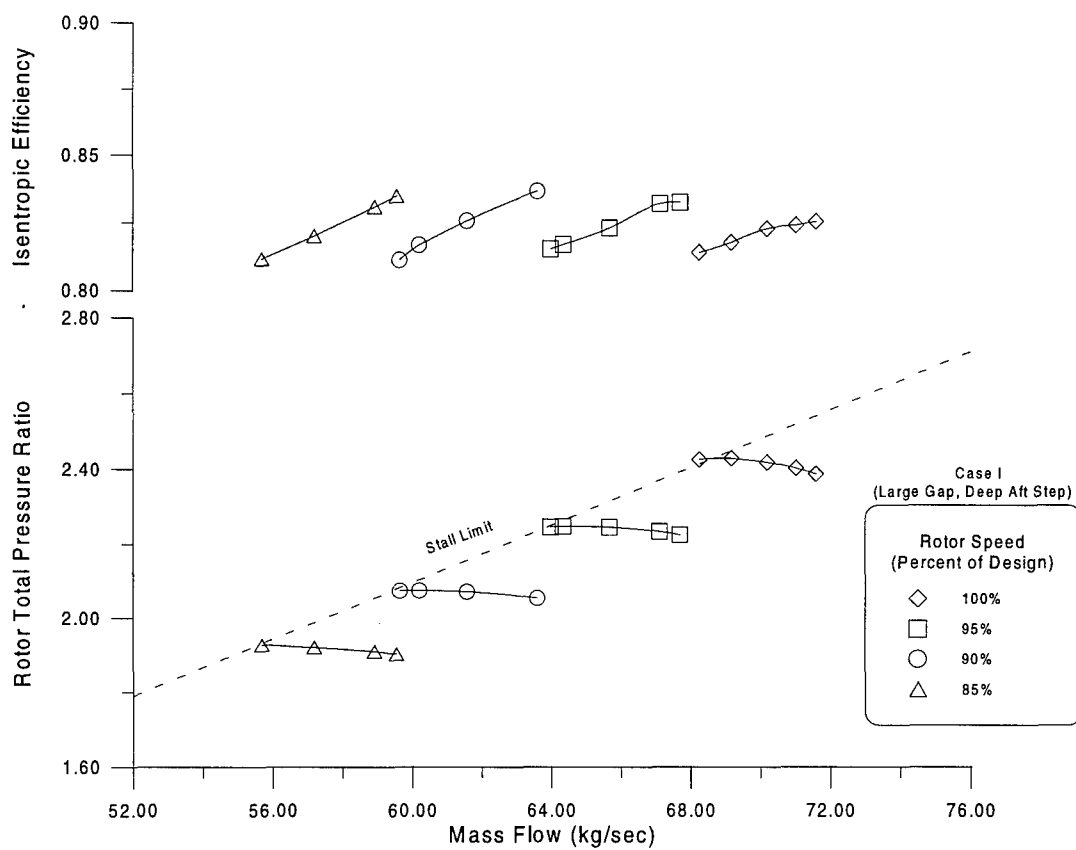
Figure 164. Rotor Map for Configuration I (Large Gap, Deep Aft Step)

APPENDIX D - Mission Performance

Sample mission analyses were performed to evaluate the sensitivity of aircraft mission performance to the changes in the compressor first-stage fan casing configuration. For each analysis, the total fuel burned during a mission was calculated based on the experimentally determined isentropic efficiency and pressure ratio at 100% design rotor speed and design mass flow for a particular casing configuration. A medium (unstepped) tip clearance was found to yield better fuel economy than a small (unstepped) clearance; and stepped tip gaps improved the fuel economy over the unstepped configurations at both the small and medium clearance levels.

D.1 The Mission

A hypothetical mission was devised for a future fighter aircraft based on the anticipated needs of the Air Force and the practical experience of the author in the tactical combat arena. This mission was defined according to the analytical tools and software developed by Mattingly et al. [64] . For this mission, the aircraft was specified to have the following performance criteria:

1. Gross weight at takeoff: $W_{TO} = 32,500$ lbf $(144,567.2N)$

2. Wing Loading: $\frac{W_{TO}}{S} = 64.0$ lbf/ft^2 $(3064.3N/m^2)$

3. Thrust Loading: $\frac{T_{SL}}{W_{TO}} = 1.3$

4. Initial Weight Factor: $\beta_i = \frac{W_i}{W_{TO}} = 1.0$

The mission consisted of the following:

1. Warm-up, takeoff, and accelerate to climb speed
   (pressure altitude = 2000 feet; temperature = $100^\circ F$; takeoff power = maximum afterburner)

2. Climb, accelerate, and level-off in military power
   (final altitude = 43,000 feet; final Mach number = 0.9)

3. Cruise at Best Cruise Mach (BCM) Airspeed to the penetration (push) point
   (BCM = 0.9; 300 nautical mile leg)

4. Penetrate enemy airspace
   - Descend to 30,000 feet altitude and accelerate to Mach 1.6 using maximum afterburner
   - Ingress to the Combat Air Patrol (CAP) zone (100 nautical miles) in military power

5. Engage in air-to-air combat
   - Fire two AMRAAMs
   - Perform two 5g turns at 30,000 feet altitude and 1.6 Mach using maximum afterburner
   - Perform four 5g turns at 30,000 feet altitude and 0.9 Mach using maximum afterburner

6. Egress enemy airspace
   - Accelerate to 1.6 Mach at 30,000 feet altitude using maximum afterburner
   - Cruise to the egress point (100 nautical miles) using military power

7. Climb to Best Cruise Mach altitude using a constant energy (zoom) maneuver
   (Level-off at approximately 50,000 feet altitude at Best Cruise Mach airspeed of 0.9)

8. Cruise at BCM altitude and airspeed to the recovery holding pattern (300 nautical mile leg)

9. Hold for 20 minutes in a recovery holding pattern for landing sequence
   (20,000 feet pressure altitude; best endurance airspeed)

10. Descend and land

D.2 Control Parameters

The fuel used during a mission is a function not only of the mission operating conditions but also of the engine powering the aircraft in those conditions. In these analyses, the mission was held constant for each casing configuration, isolating fuel usage specifically to engine performance. In turn, all performance parameters of the engine (compressor pressure ratio, component efficiencies, etc.) were held constant except for the efficiency and pressure ratio of the first-stage fan. The efficiency and pressure ratio of the fan were linked as pairs according to the experimental performance results obtained for each casing configuration of the ADLARF rotor at design mass flow (71.66 kg/sec); these pairs are shown in nondimensional form (nondimensionalized by the respective performance parameter of Case A) in Table 10. The ONX computer program was used to generate engine off-design parameters for each casing configuration based on a fan pressure ratio and efficiency scaled by the factors shown in Table 10. The off-design cycle parameters were input into the MISS computer program to simulate the mission for each case.

Table 10. First-Stage Rotor Performance Scaling Factors

Casing Configuration	Pressure Ratio Scaling Factor	Efficiency Scaling Factor
A (Small Gap, No Step)	1.0000	1.0000
B (Small Gap, Aft Step)	1.0079	1.0083
C (Small Gap, Forward Step)	1.0079	1.0094
D (Medium Gap, No Step)	0.9802	0.9988
E (Medium Gap, Aft Step)	0.9980	1.0094
F (Medium Gap, Forward Step)	0.9880	1.0059
G (Large Gap, No Step)	0.9526	0.9823
H (Large Gap, Shallow Aft Step)	0.9506	0.9764
I (Large Gap, Deep Aft Step)	0.9407	0.9729

D.3 Sensitivity Results

Mission analyses yielded the sensitivity of fuel economy to casing configuration shown in Table 6

of Chapter 6.

APPENDIX E - Stall Analysis and Plots

E.1 Signal Processing - Conditioning

The filtered and digitized stall data obtained from the eight stall sensors contained stall and surge signals. Before the stall and surge signals could be isolated, signal conditioning of the raw data was required. Signal conditioning involved removing sensory and playback equipment bias from the digitized data and normalizing each of the resulting signals. The bias of each signal was removed by calculating the mean value of the raw data and subtracting this mean from the raw data, resulting in a fluctuation signal. The eight fluctuation signals were normalized by scaling factors according to the ratio of the root-mean-square (RMS) magnitude to the maximum RMS value in the set. Stall and surge data were extracted from the conditioned set of composite signals using the analytical technique described in the following section.

E.2 Signal Processing - Stall and Surge Isolation

Stall and surge signals can be extracted from conditioned signals using the following algorithm. This technique is based on the premise that surge is a planar wave sensed equally and simultaneously by the pressure transducers at equally spaced circumferential locations, whereas the pressure waves from rotating stall are not sensed simultaneously. A rotating pressure wave is comprised of several modal frequencies. The magnitude of a modal wave at any transducer is expressed as a sine wave

$$A_{jm} = \sin\left(\frac{2\pi m j}{N_T}\right) \tag{53}$$

where $m =$ mode of the wave; $N_T =$ the number of transducers; and $j = 1, 2, ...N_T$ is the index representing the transducer. The pressure at any transducer j can be expressed as the sum of the planar surge and the modal rotating wave pressure.

$$P_{jm} = A_0 + A_{jm} \tag{54}$$

202

The result of subtracting one data channel from another is the differenced pressure

$$P_{Djm} = P_{jm} - P_{(j+n)m} = (A_0 + A_{jm}) - (A_0 + A_{(j+n)m}) \tag{55}$$

$$= \sin\left(\frac{2\pi mj}{N_T}\right) - \sin\left(\frac{2\pi m(j+n)}{N_T}\right) \tag{56}$$

where n is the number of $2\pi/N_T$ circumferential increments. Note that the surge has been cancelled by the substraction process. For the case of eight sensors, $N_T = 8$, and using the signals from two diametrically opposite sensors (180 degrees apart), $n = 4$, Equation 55 becomes:

$$P_{Djm} = \sin\left(\frac{2\pi mj}{8}\right) - \sin\left(\frac{2\pi mj}{8} + m\pi\right) \tag{57}$$

The effect of this differencing on any even rotating mode, $m = 0, 2, 4, \ldots$ is:

$$P_{Djeven} = (1 - \cos m\pi)\sin\left(\frac{2\pi mj}{8}\right) - \sin m\pi \cos\left(\frac{2\pi mj}{8}\right) = 0 \tag{58}$$

The effect of this differencing on any odd rotating mode, $m = 1, 3, 5, \ldots$ is

$$P_{Djodd} = 2\sin\left(\frac{2\pi mj}{8}\right) \tag{59}$$

which gives an amplification factor of twice the original signal. So the difference of two opposing signals eliminates the surge mode and all even rotating modes, leaving only odd rotating modes amplified by a factor of two.

If two data signals are added rather than differenced, the result is:

$$P_{Ajm} = P_{jm} + P_{(j+n)m} = (A_0 + A_{jm}) + (A_0 + A_{(j+n)m}) \tag{60}$$

$$= 2A_0 + \sin\left(\frac{2\pi mj}{N_T}\right) + \sin\left(\frac{2\pi m(j+n)}{N_T}\right) \tag{61}$$

Note that the surge, A_0, has been doubled by the addition process. Again, for the case where $N_T = 8$ and $n = 4$, Equation 60 becomes:

$$P_{Ajm} = 2A_0 + \sin\left(\frac{2\pi mj}{8}\right) + \sin\left(\frac{2\pi mj}{8} + m\pi\right) \tag{62}$$

The effect of this addition on any even rotating mode, $m = 0, 2, 4, ...$ is

$$P_{Ajeven} = 2A_0 + (1 + \cos m\pi) \sin\left(\frac{2\pi mj}{8}\right) + \sin m\pi \cos\left(\frac{2\pi mj}{8}\right) = 2A_0 + 2\sin\left(\frac{2\pi mj}{8}\right)$$

(63)

which gives an amplification factor of two for the surge and all even mode rotating waves. The

effect of addition on any odd rotating mode, $m = 1, 3, 5, ...$ is

$$P_{Ajodd} = 2A_0$$

(64)

which eliminates all odd mode rotating waves and gives an amplification factor of two for the planar

surge wave. So the addition of two opposing signals eliminates the odd rotating modes and isolates

the surge and even rotating modes amplified by a factor of two.

The process of adding and subtracting opposite data signals inherently forms spatial signals suited

for Fourier analysis. Therefore, the Discrete Fourier Transform (DFT) (Newland [68]) can be cal-

culated from windowed samples of each added and differenced signal. The DFT algorithm trans-

forms the data from the time domain into the frequency domain, allowing the magnitudes of the

various modal rotating waves to be determined. Thus, the process of adding and subtracting oppo-

site channels provides a simplified means to qualify the rotating stall and surge characteristics of the

rotor using only two data channels, and it contains essentially the same information as more com-

plex and computationally time-consuming Spatial Fourier Transform (SFT) methods (Gorrell and

Russler [33]).

E.3 Stall and Surge Plots

The following figures characterize the onset and fully-developed stages of rotating stall and surge

for each experimental casing configuration and nominal rotor speed. The strength of isolated stall

and surge are expressed in terms of rotor revolutions and also in terms of the frequency of the

pressure variations. Each "Prestall Rotation" frequency subplot depicts the rotor frequency, any

204

odd mode harmonics of the rotor, and rotating disturbances (possibly transient) prior to critical stall cell formation; modal frequencies less than the rotor frequency are also shown in this subplot. A "Rotating Stall" frequency subplot depicts the primary modal frequency of rotating stall (the largest magnitude signal) and any odd mode harmonics of the rotating stall. In a similar manner, a "Prestall Surge" frequency subplot depicts the primary mode of prestall surge (the largest magnitude signal) and any even mode harmonics of the rotor, and a "Surge During Stall" frequency subplot depicts the primary mode of surge during fully-developed rotating stall and any even mode harmonics of rotating stall.

Differenced AC Signals of Sensor #1 and Sensor #5

Added AC Signals of Sensor #1 and Sensor #5
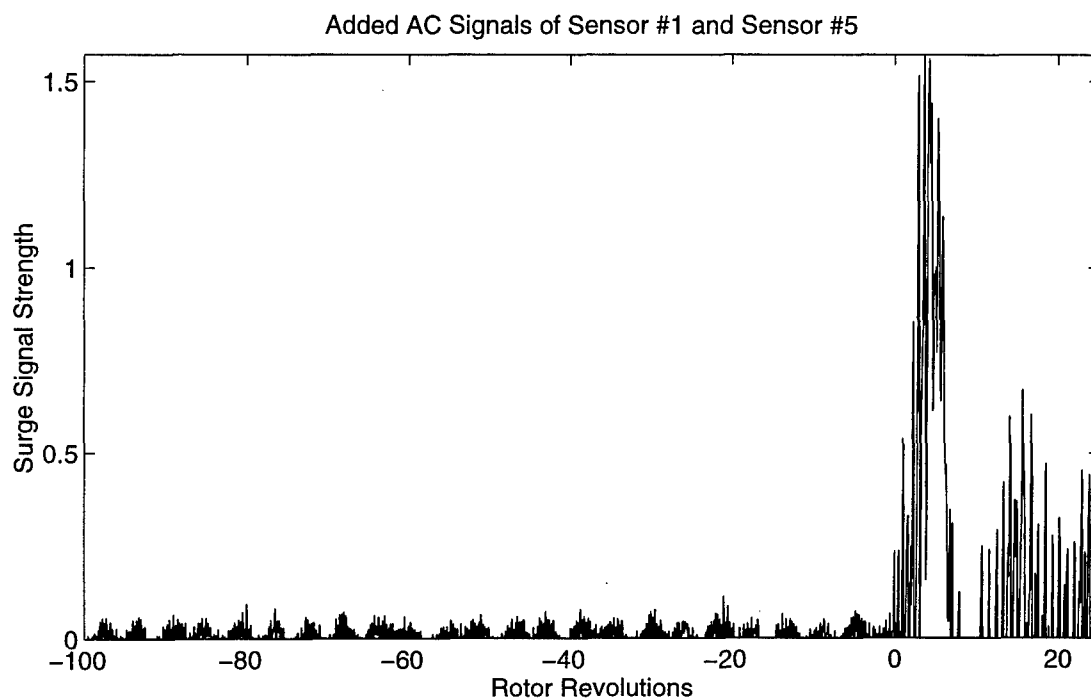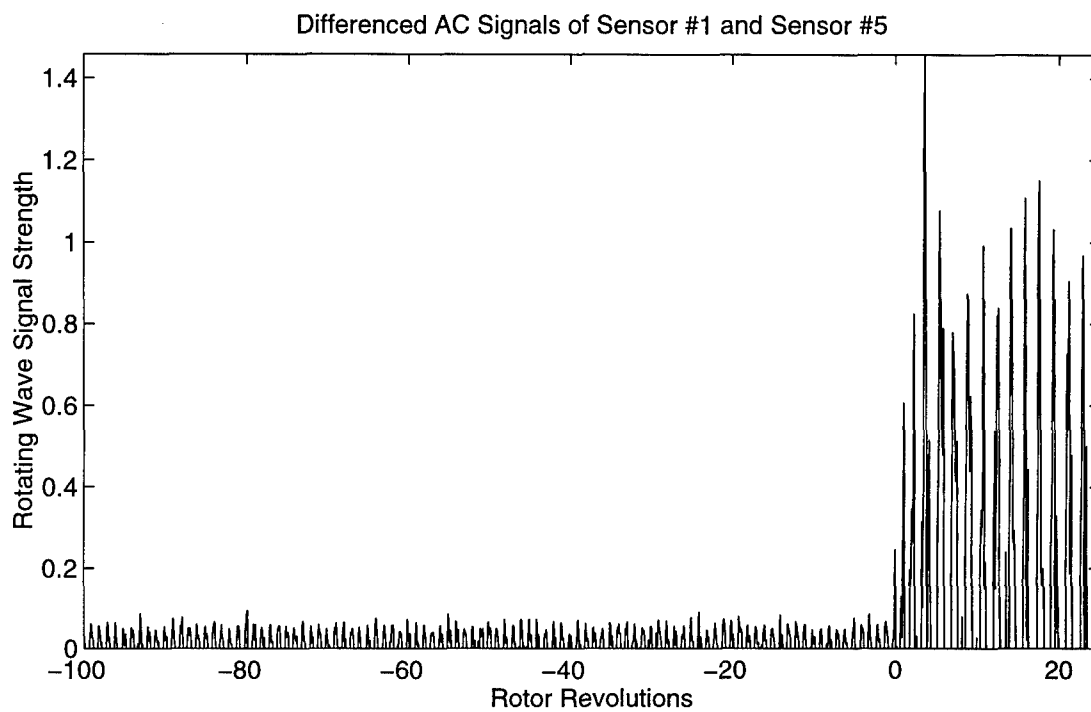
Figure 165. Onset of Rotating Stall and Surge (Case A, 85% Rotor Speed, 185.965 revs/sec)

206
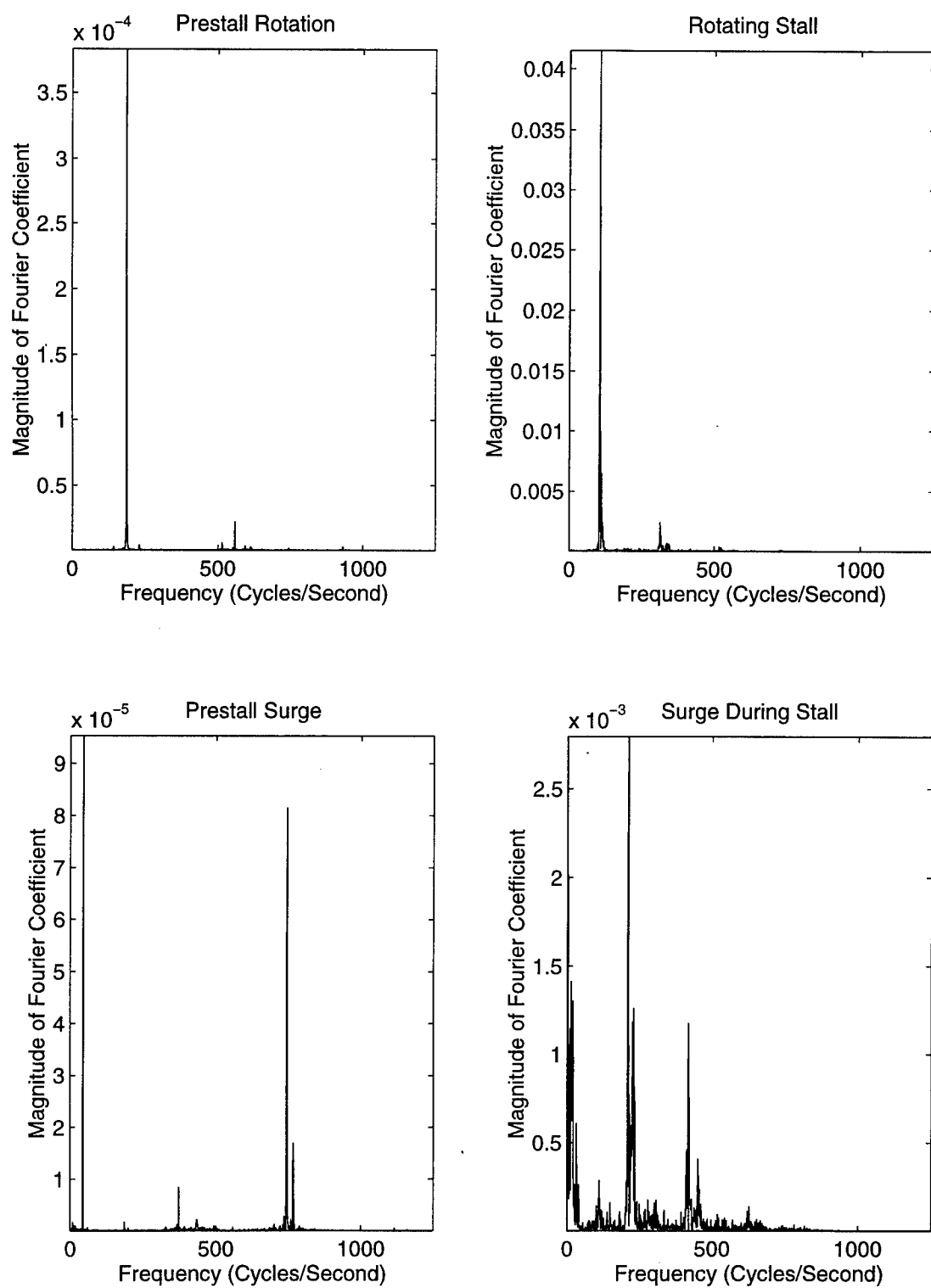
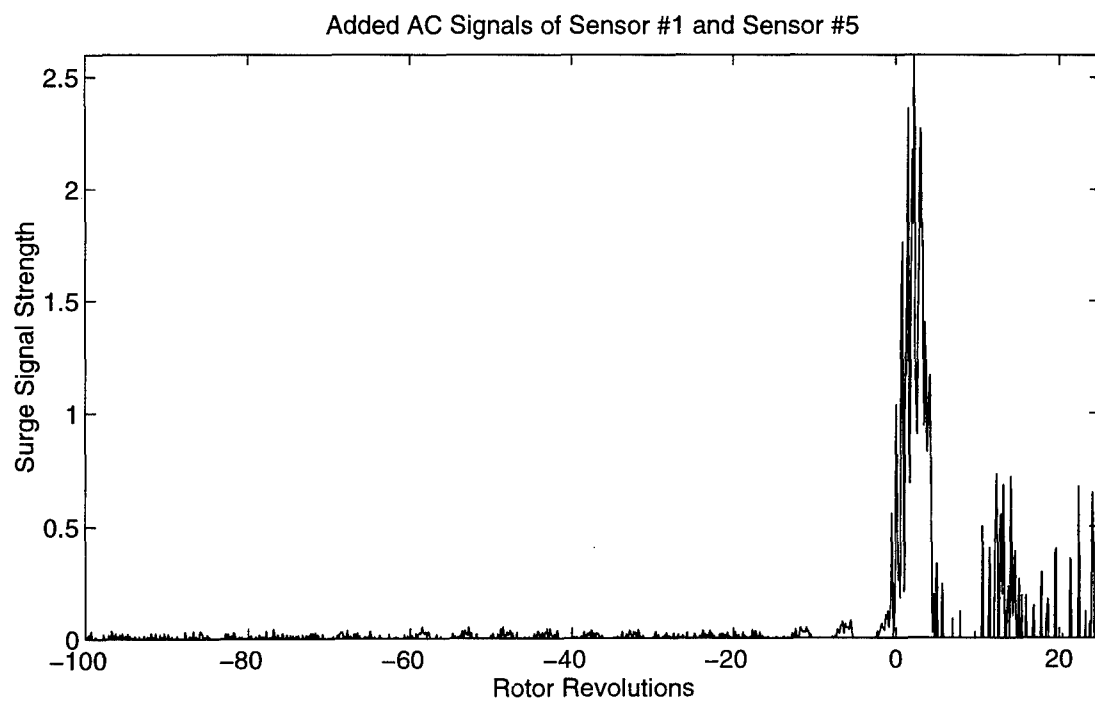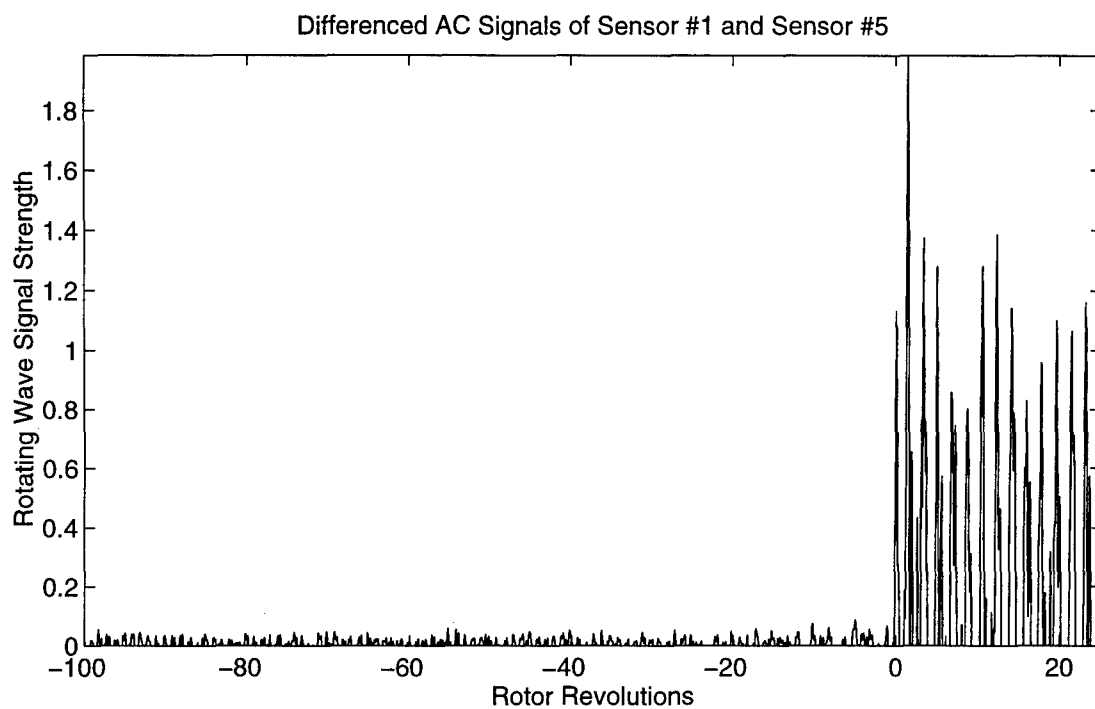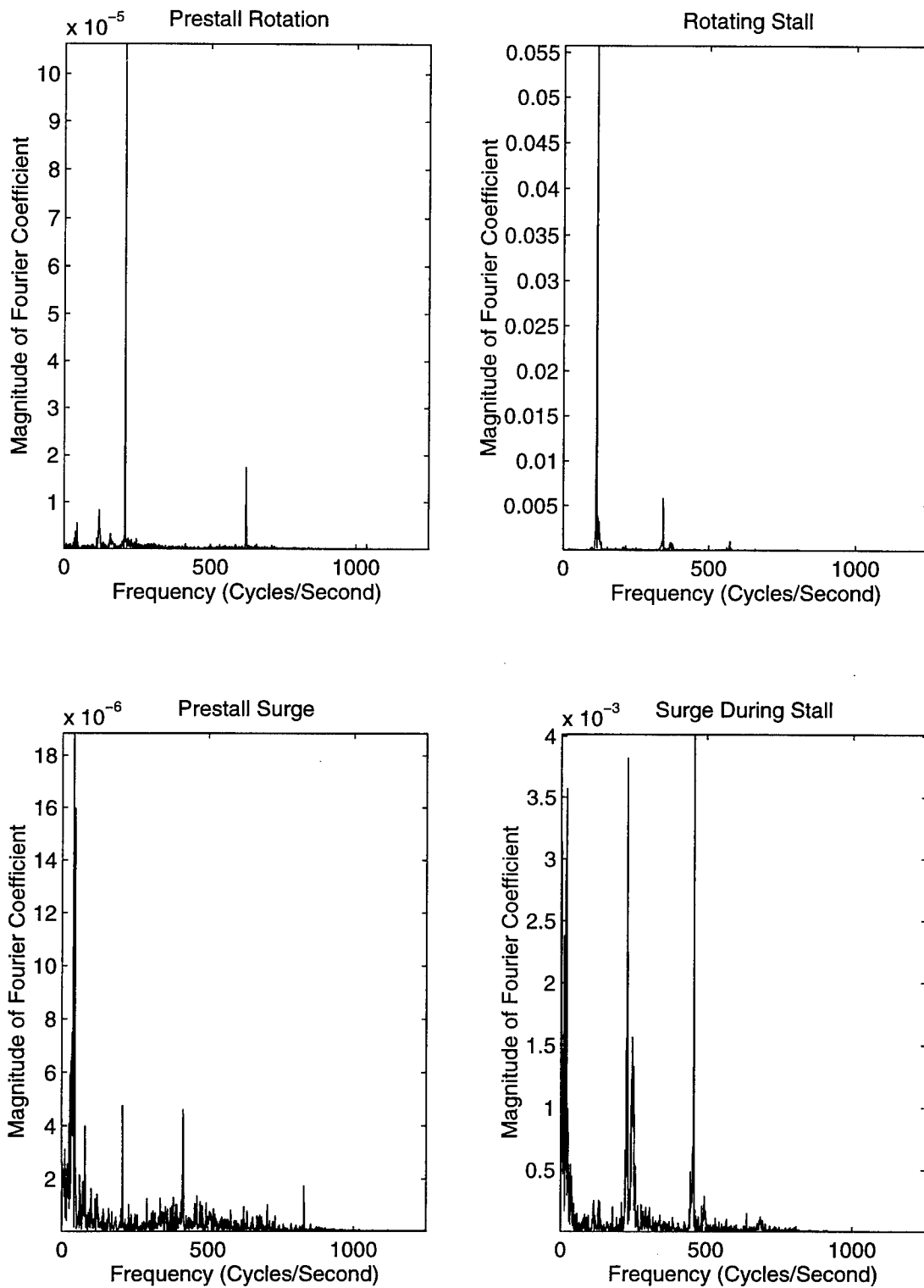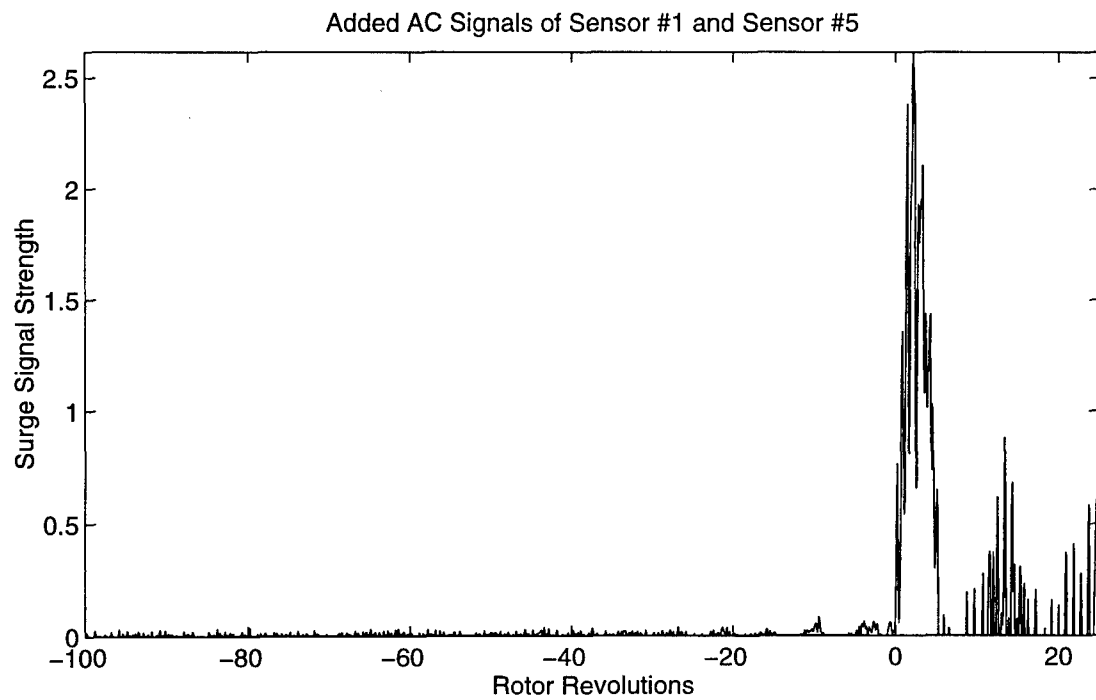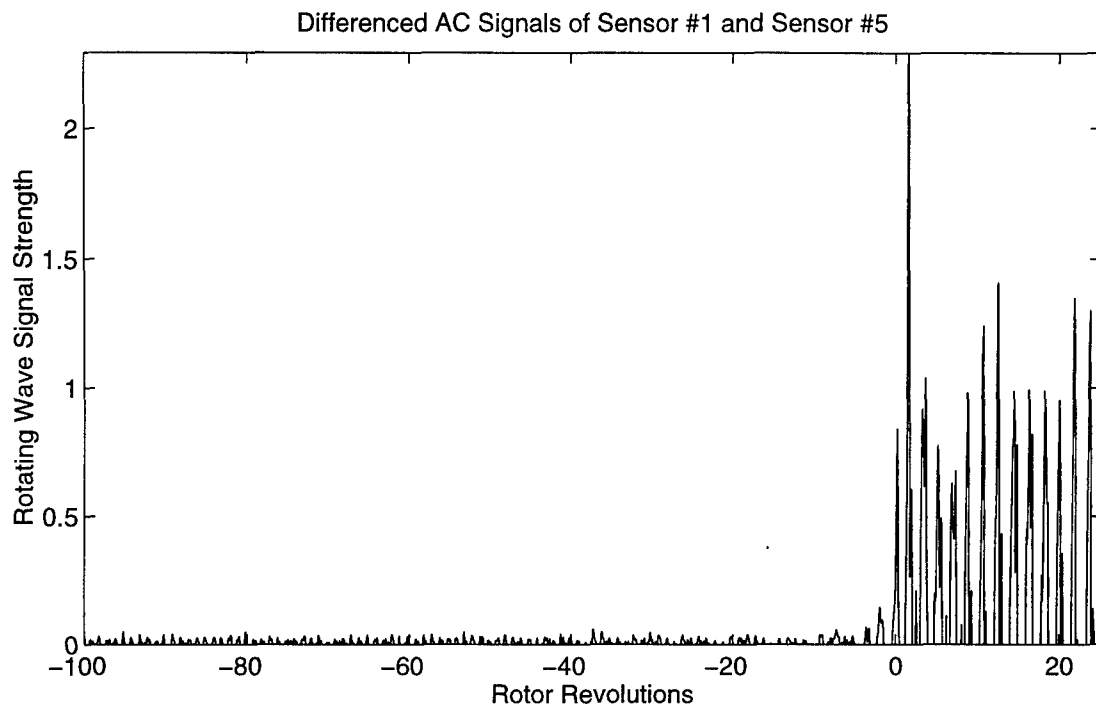Figure 166. Frequency of Rotating Stall and Surge (Case A, 85% Rotor Speed, 185.965 revs/sec)

207
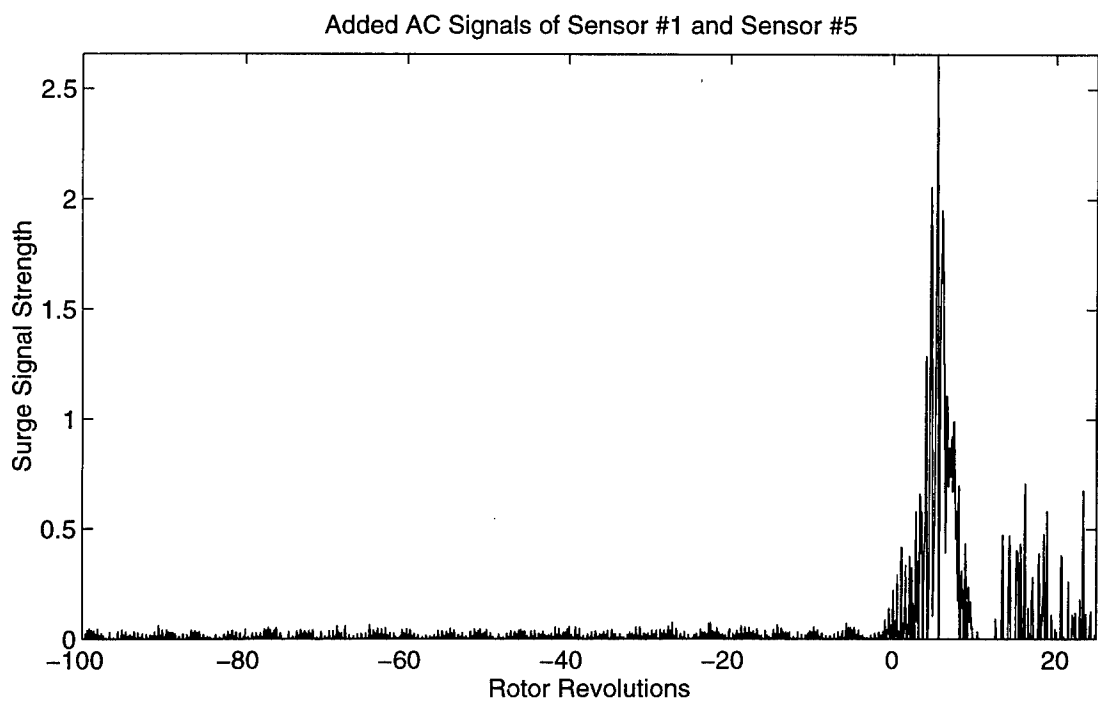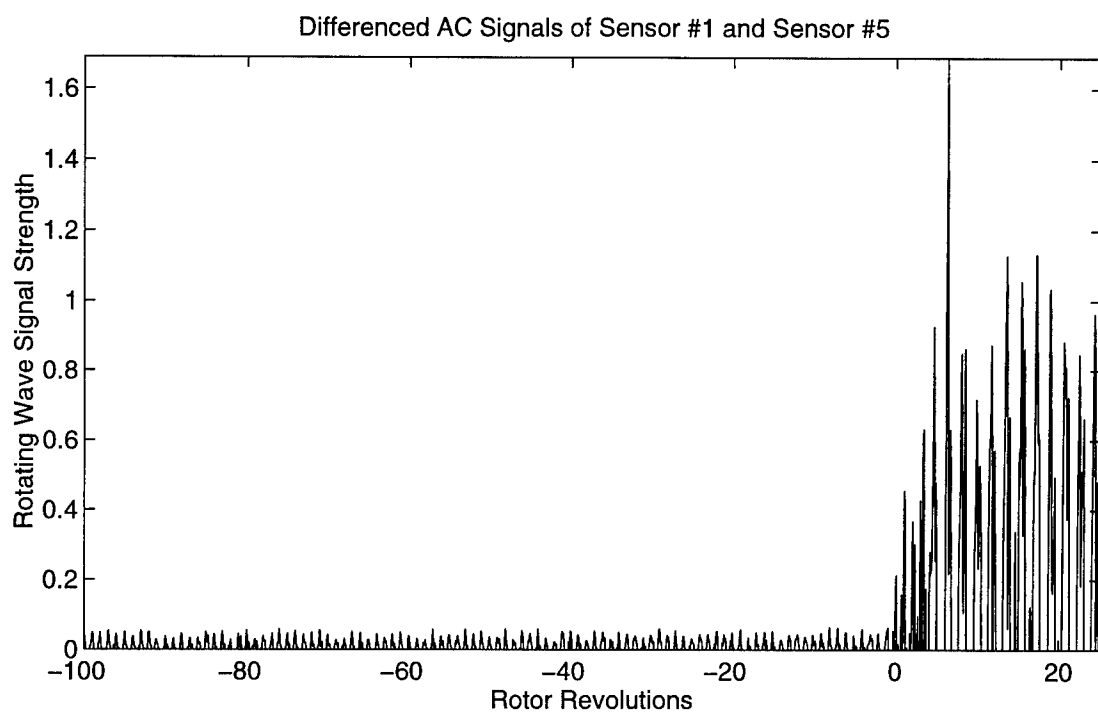
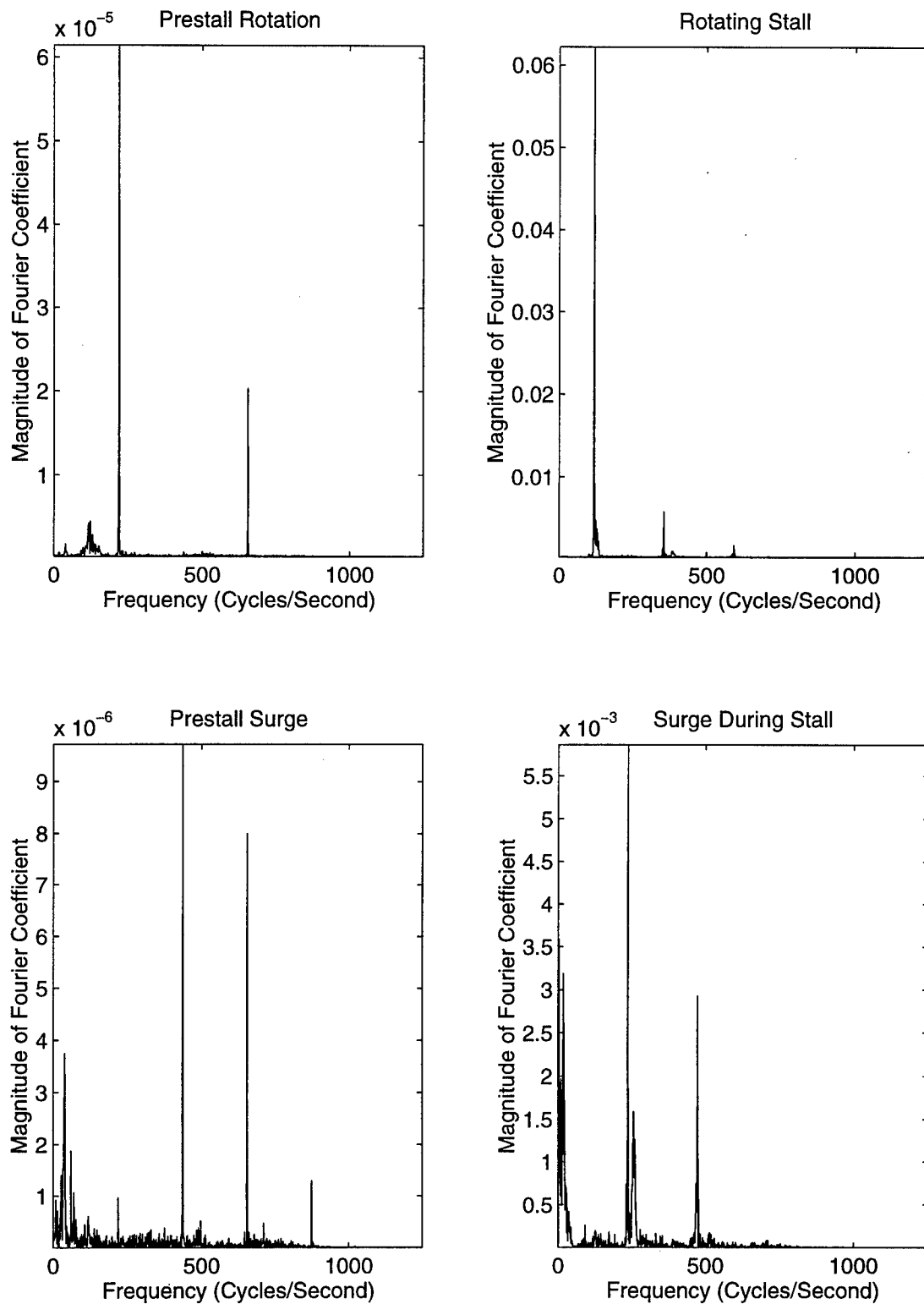Figure 167. Onset of Rotating Stall and Surge (Case A, 90% Rotor Speed, 197.030 revs/sec)
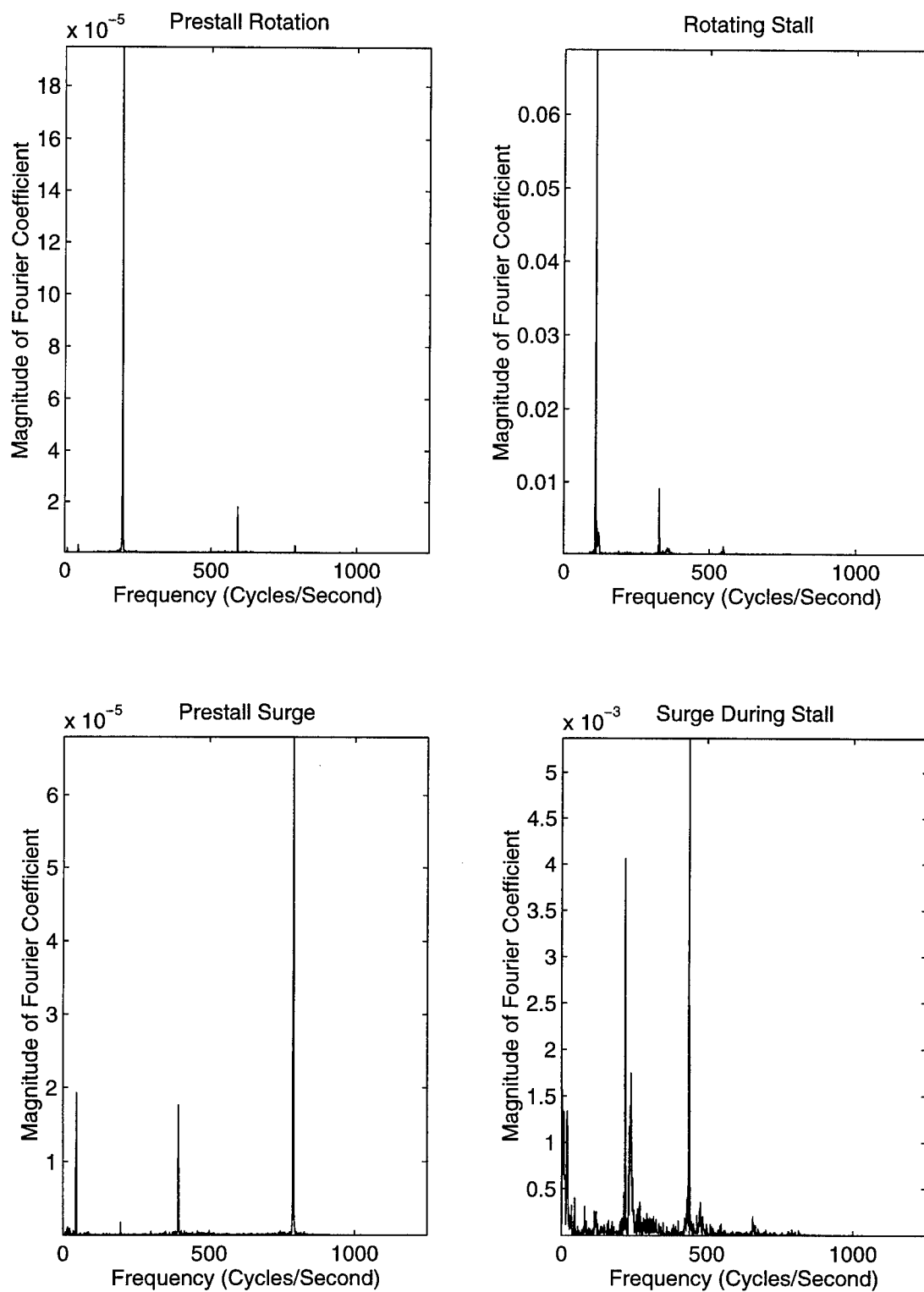
Figure 168. Frequency of Rotating Stall and Surge (Case A, 90% Rotor Speed, 197.030 revs/sec)
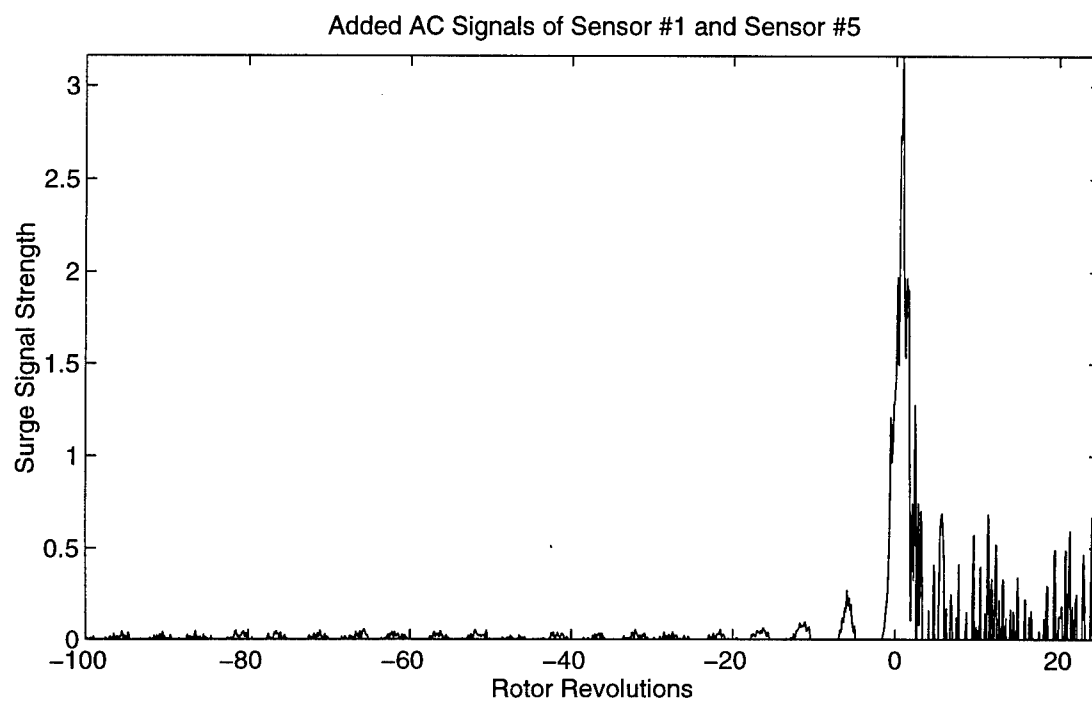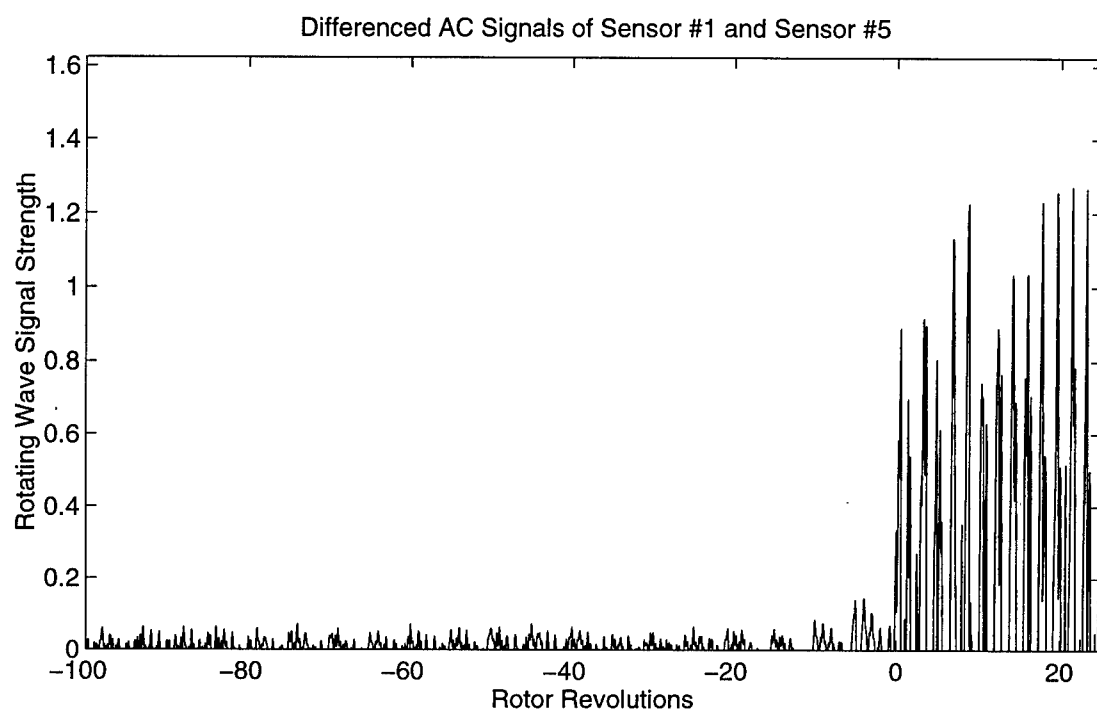
Figure 169. Onset of Rotating Stall and Surge (Case A, 95% Rotor Speed, 207.676 revs/sec)
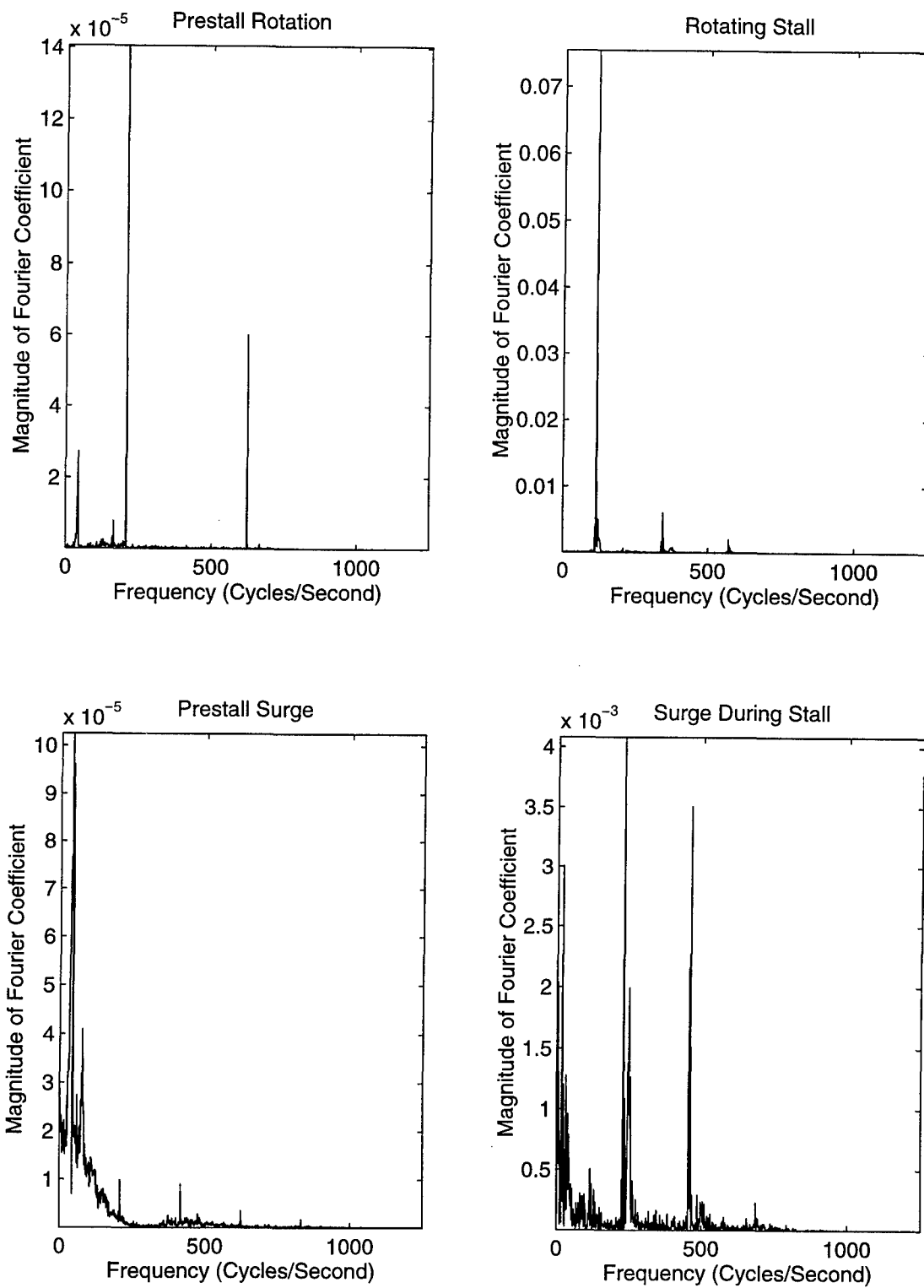
Figure 170. Frequency of Rotating Stall and Surge (Case A, 95% Rotor Speed, 207.676 revs/sec)

211
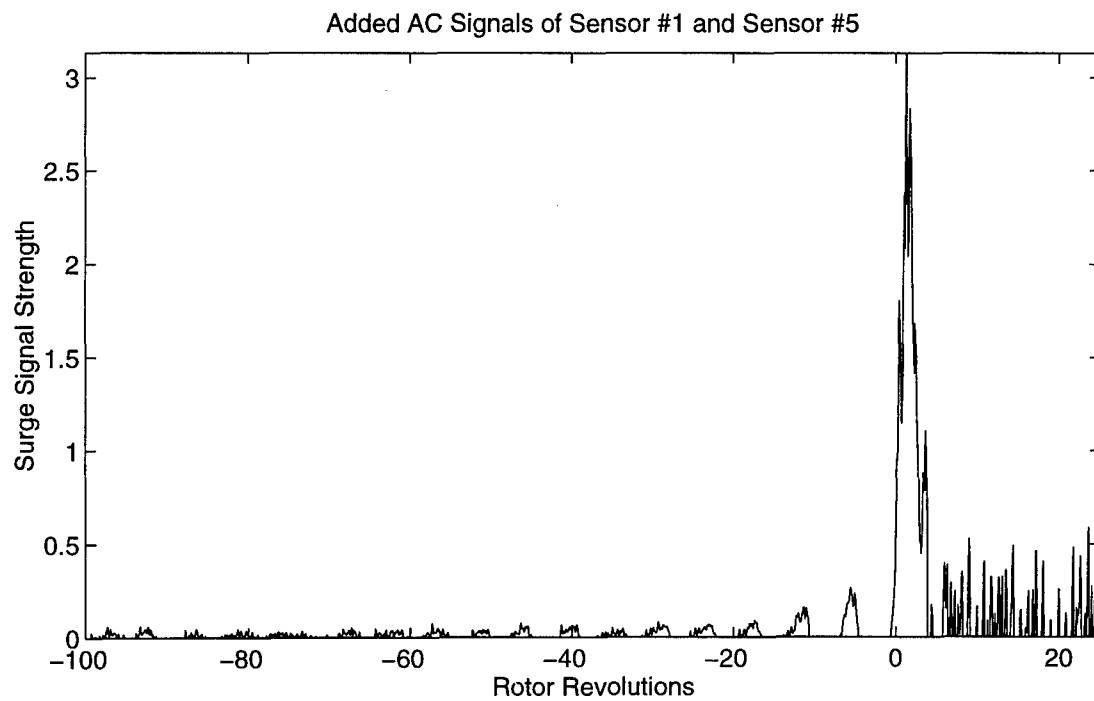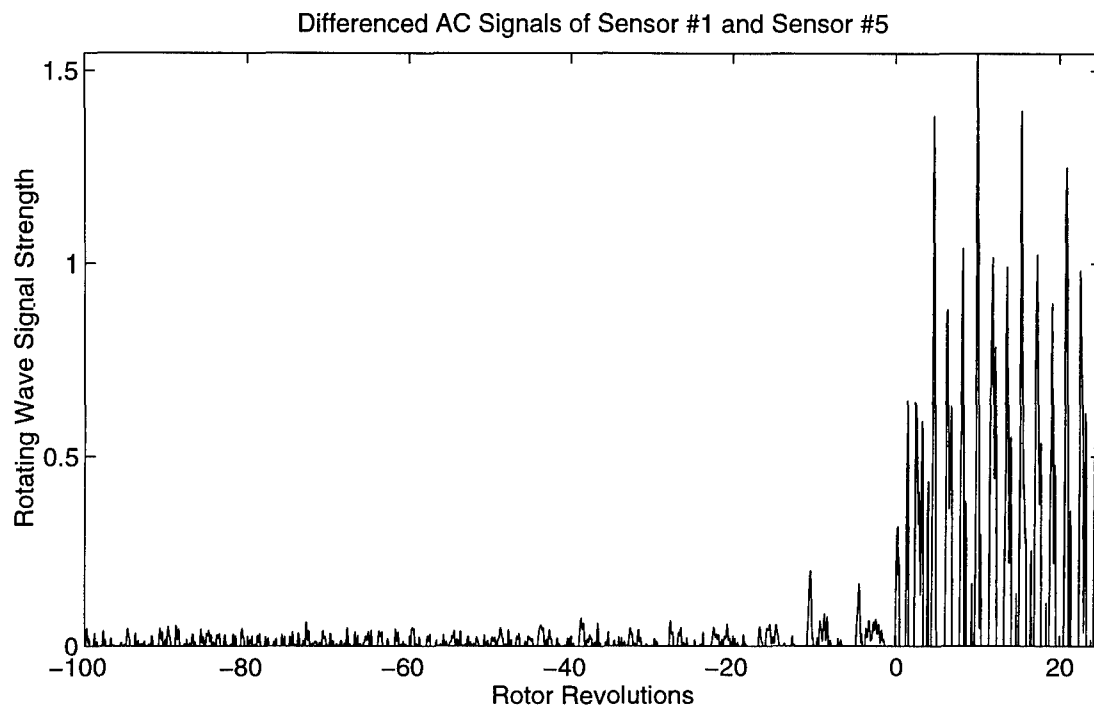
Figure 171. Onset of Rotating Stall and Surge (Case A, 100% Rotor Speed, 218.729 revs/sec)
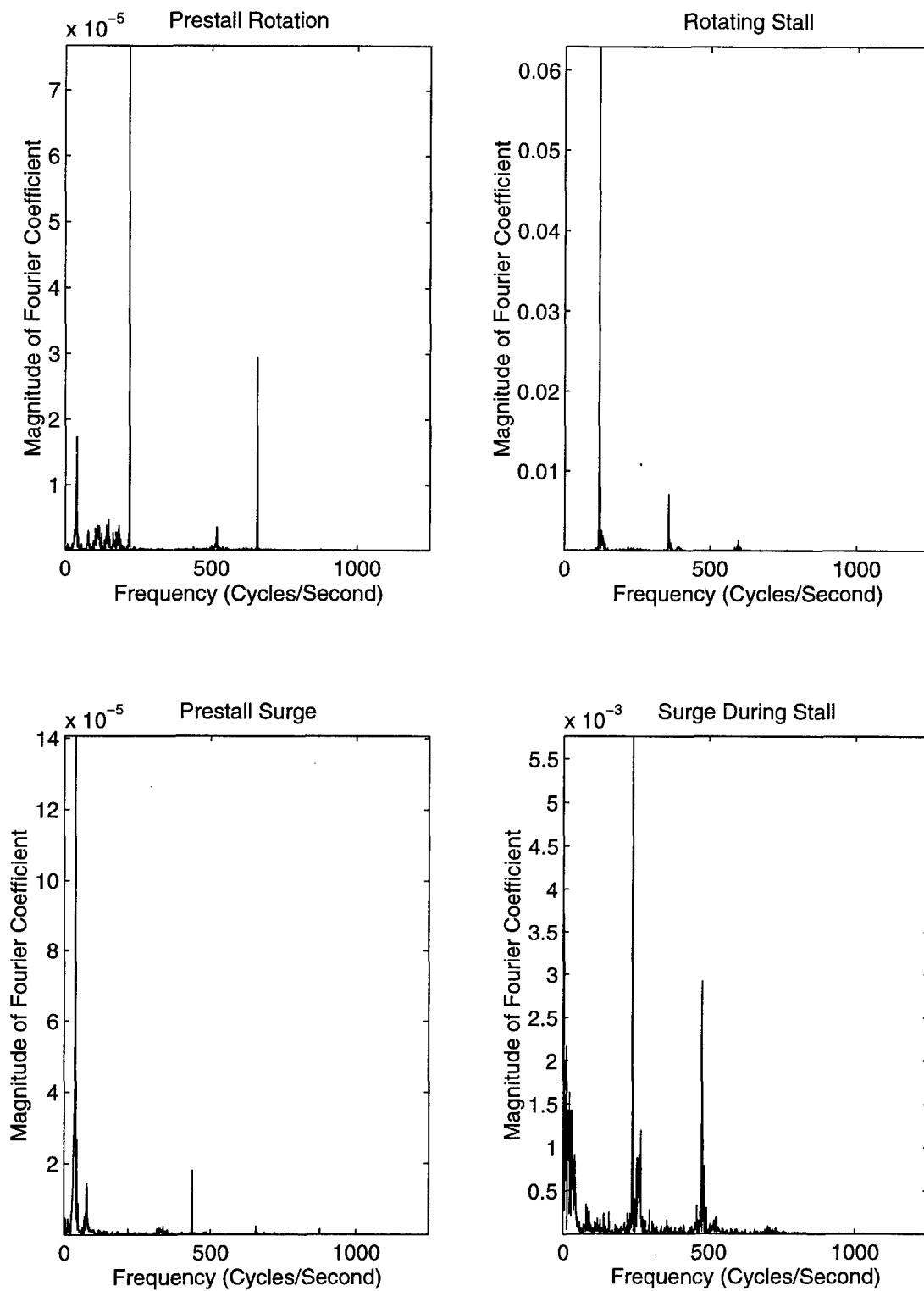
Figure 172. Frequency of Rotating Stall and Surge (Case A, 100% Rotor Speed, 218.729 revs/sec)
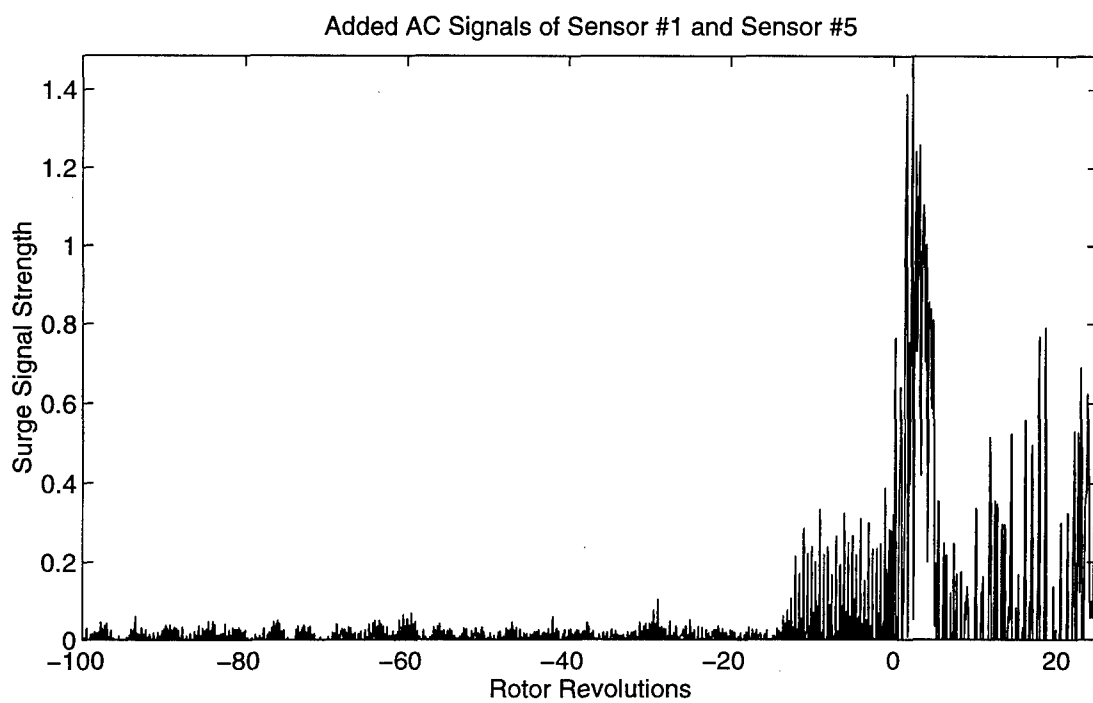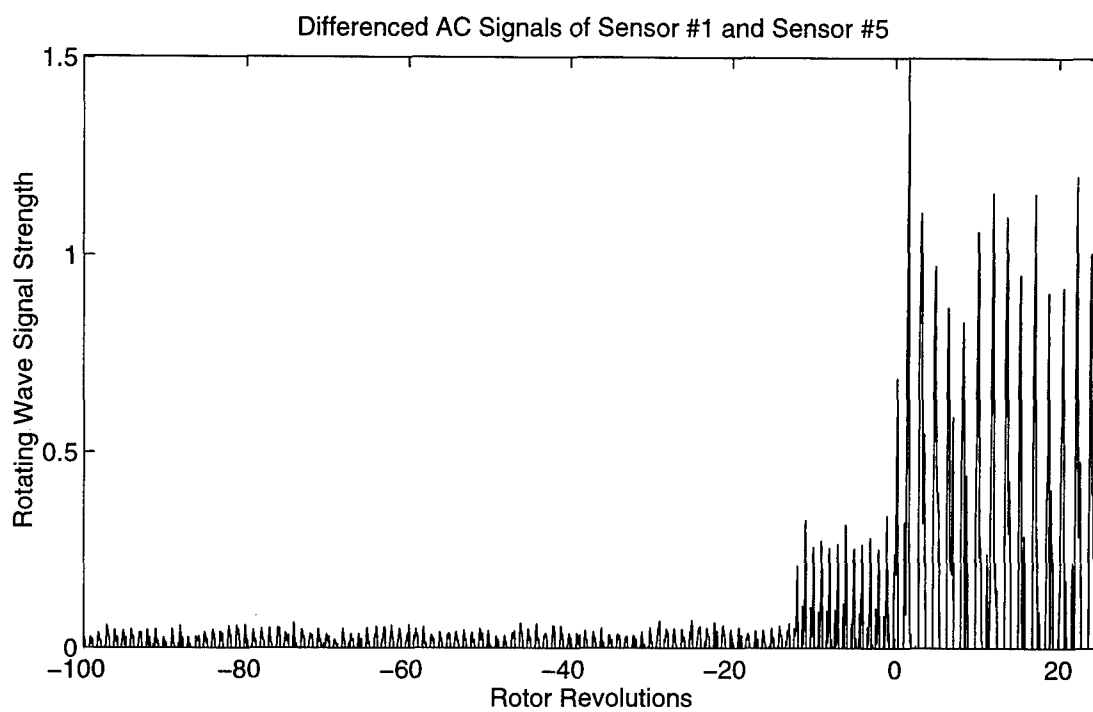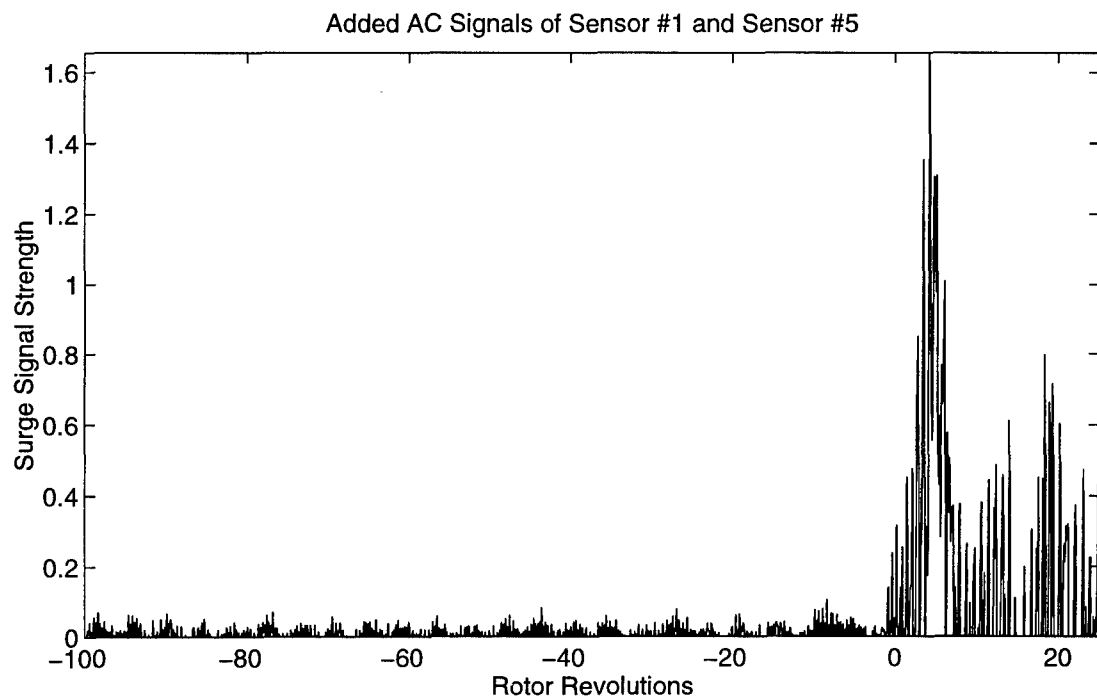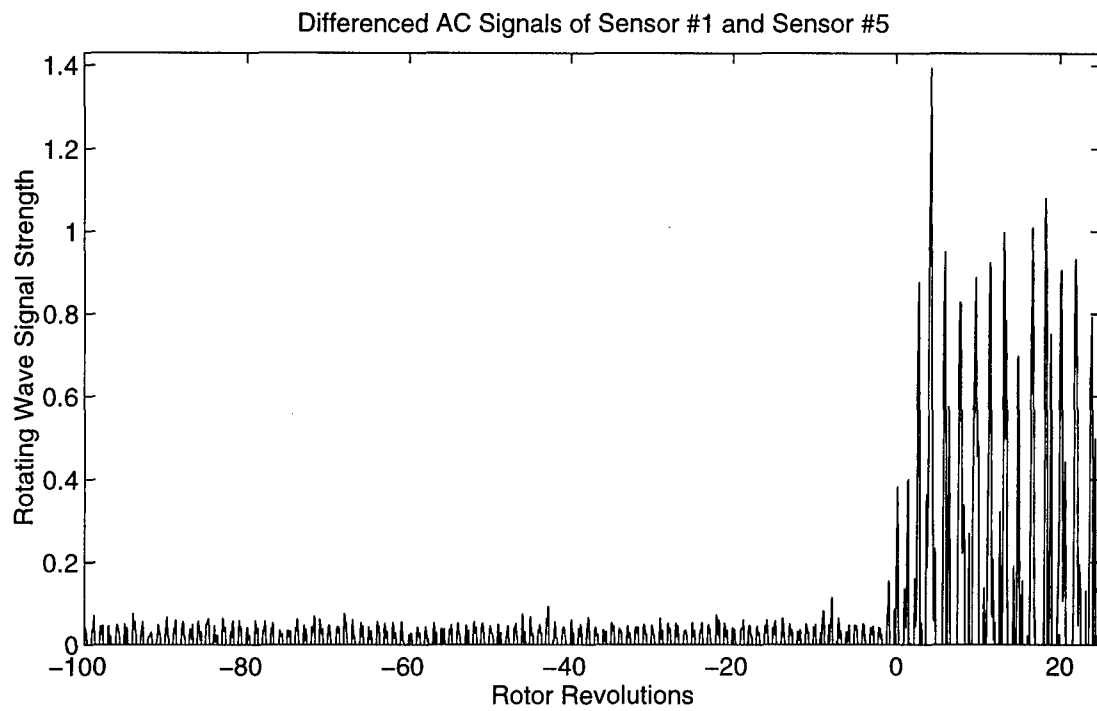
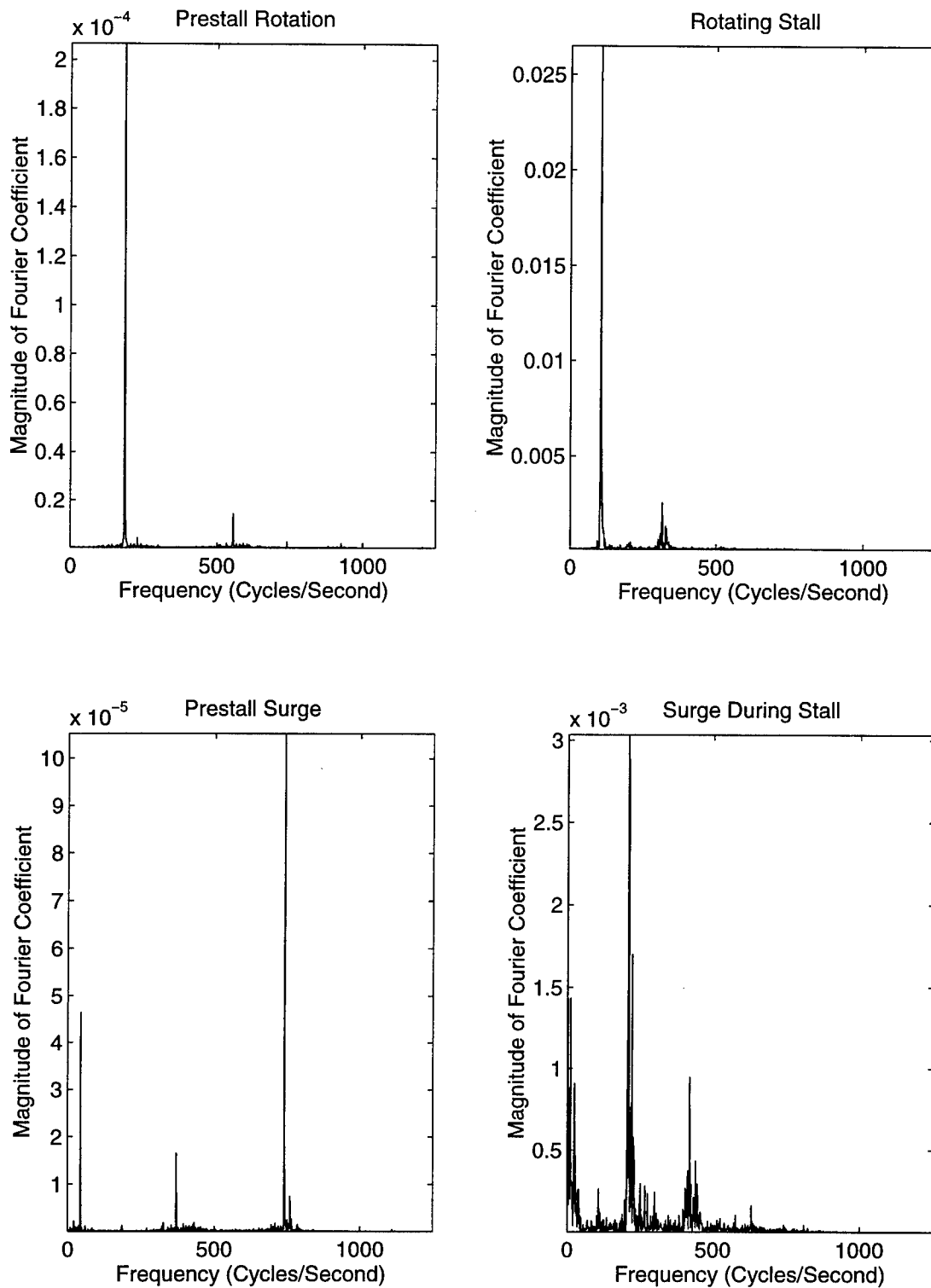Figure 173. Onset of Rotating Stall and Surge (Case B, 85% Rotor Speed, 187.150 revs/sec)
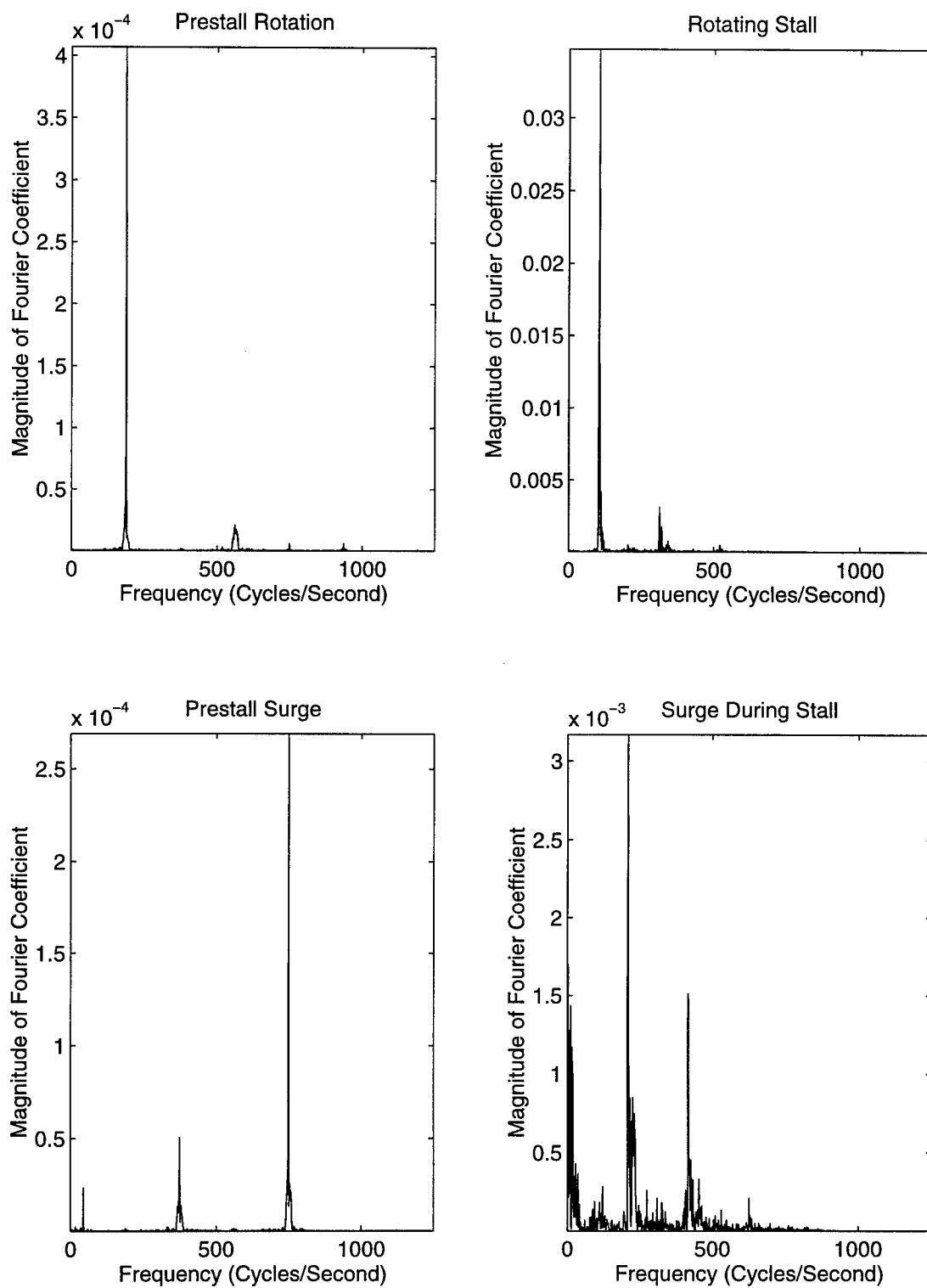
Figure 174. Frequency of Rotating Stall and Surge (Case B, 85% Rotor Speed, 187.150 revs/sec)
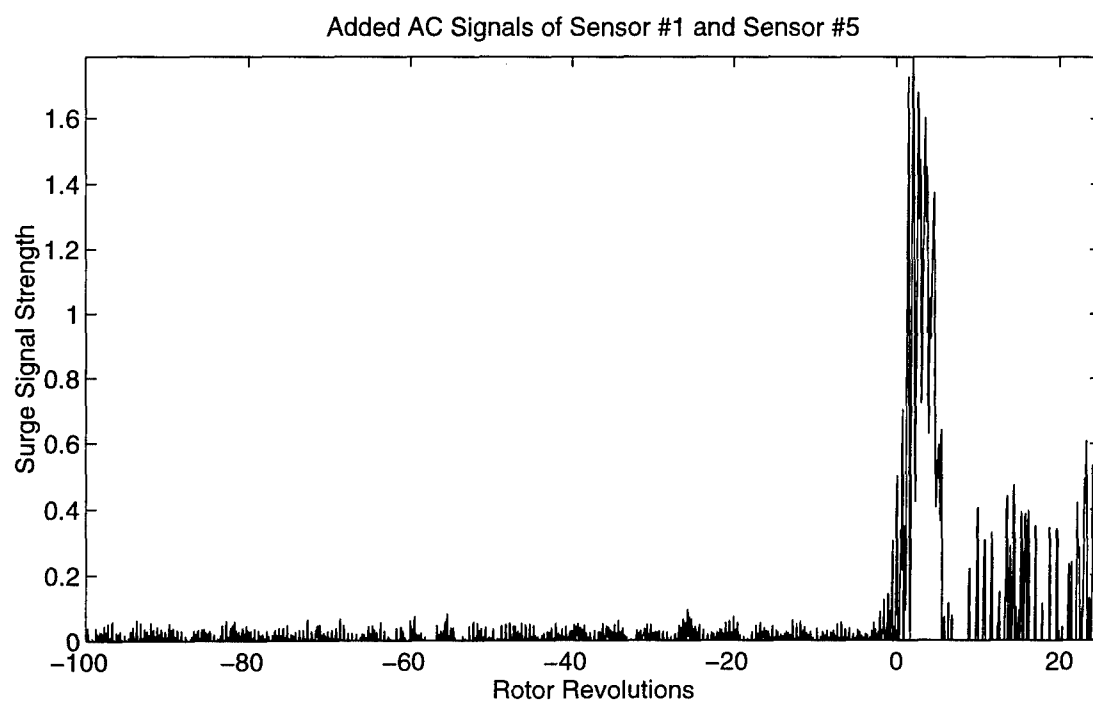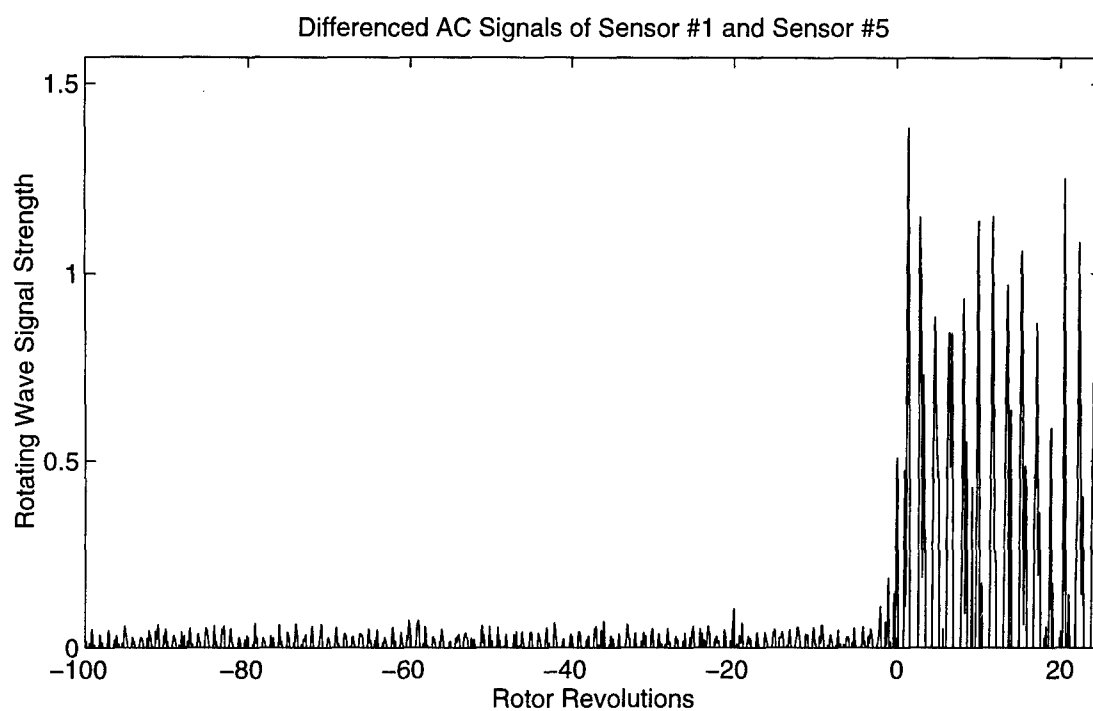
215
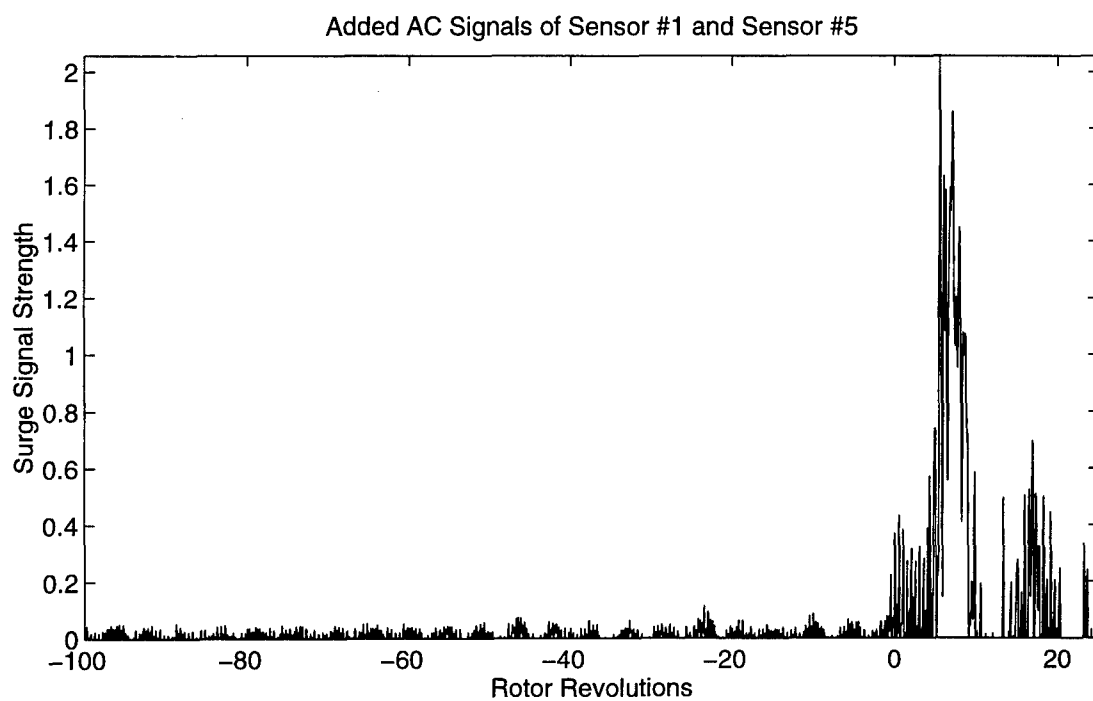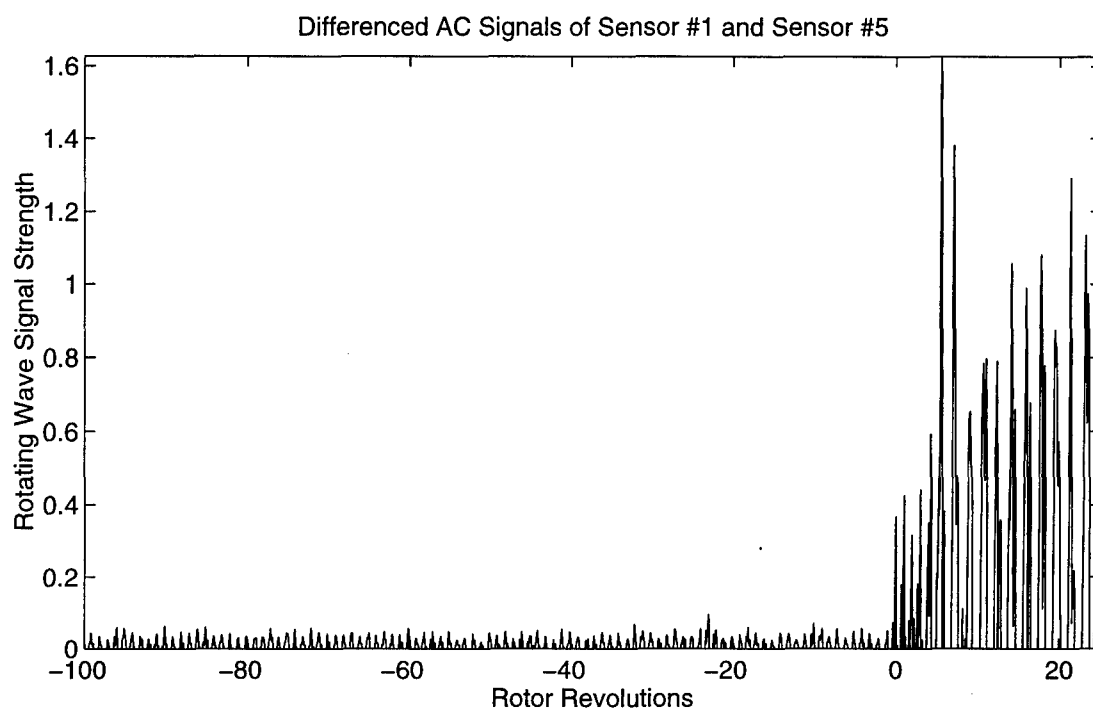
Figure 175. Onset of Rotating Stall and Surge (Case B, 90% Rotor Speed, 198.413 revs/sec)

216
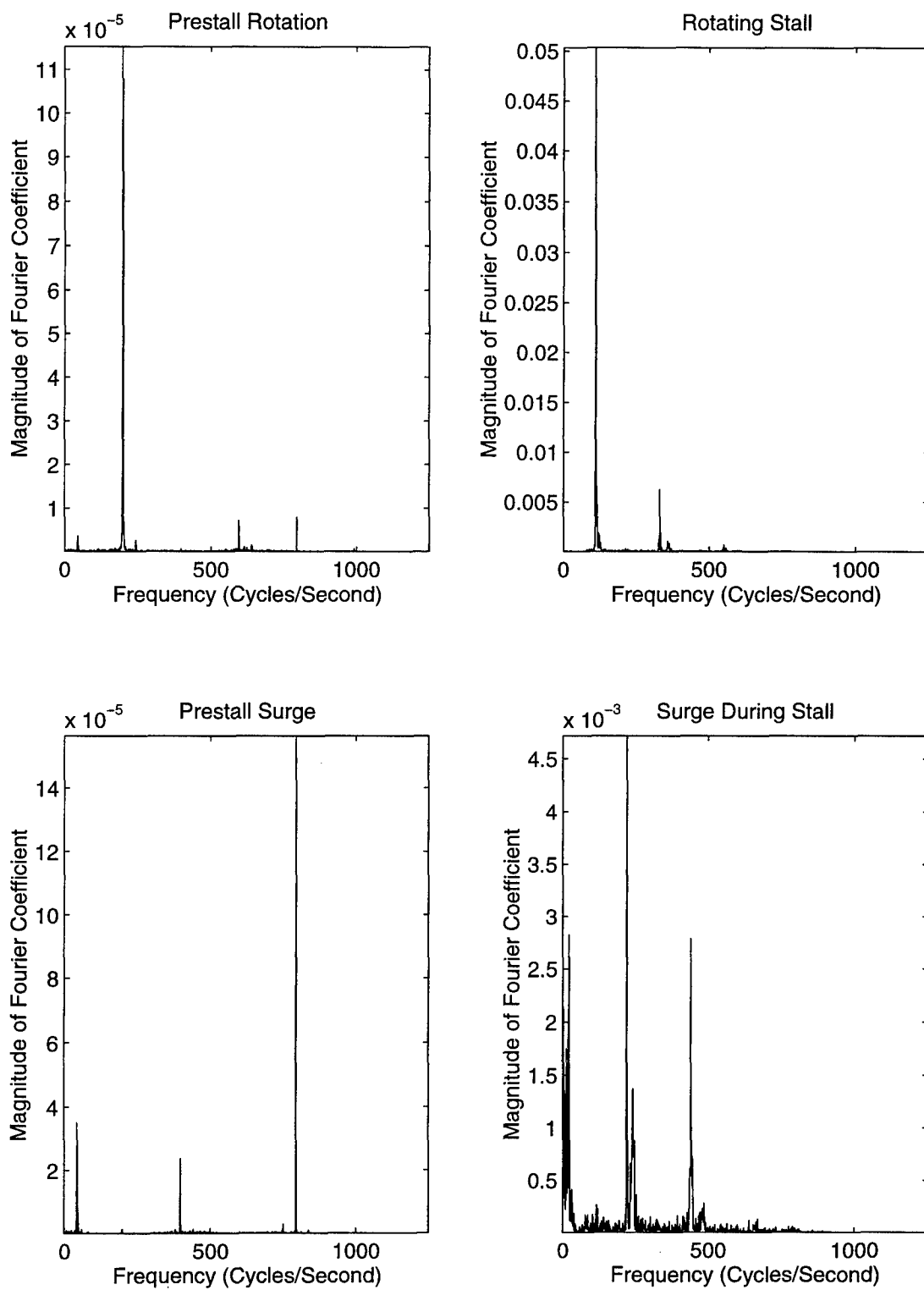
Figure 176. Frequency of Rotating Stall and Surge (Case B, 90% Rotor Speed, 198.413 revs/sec)

217
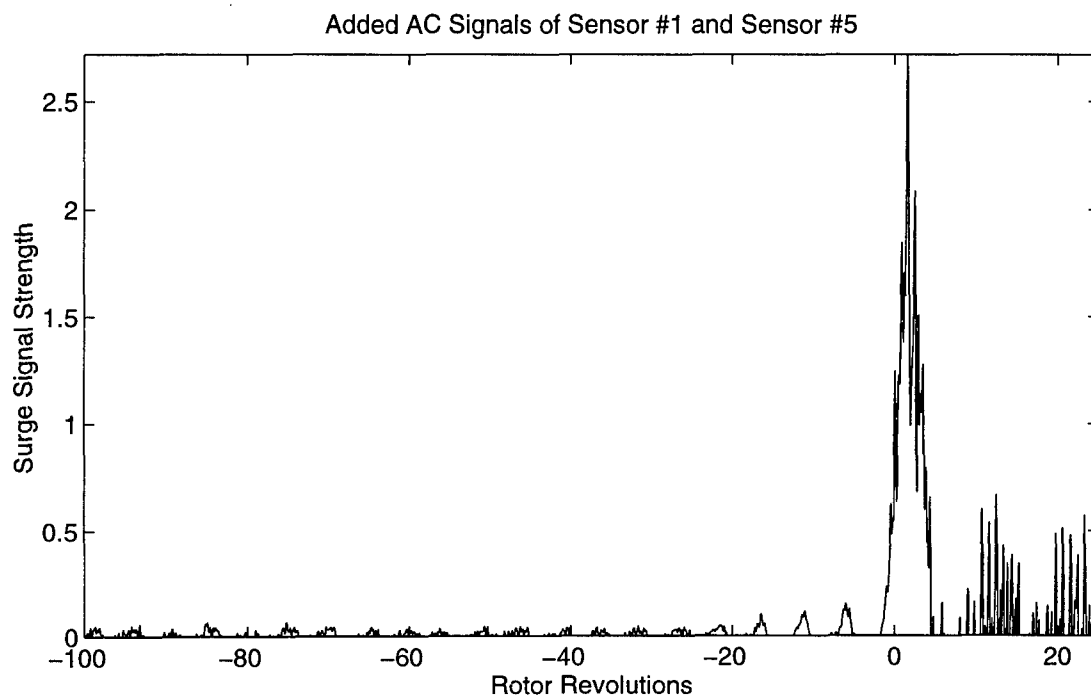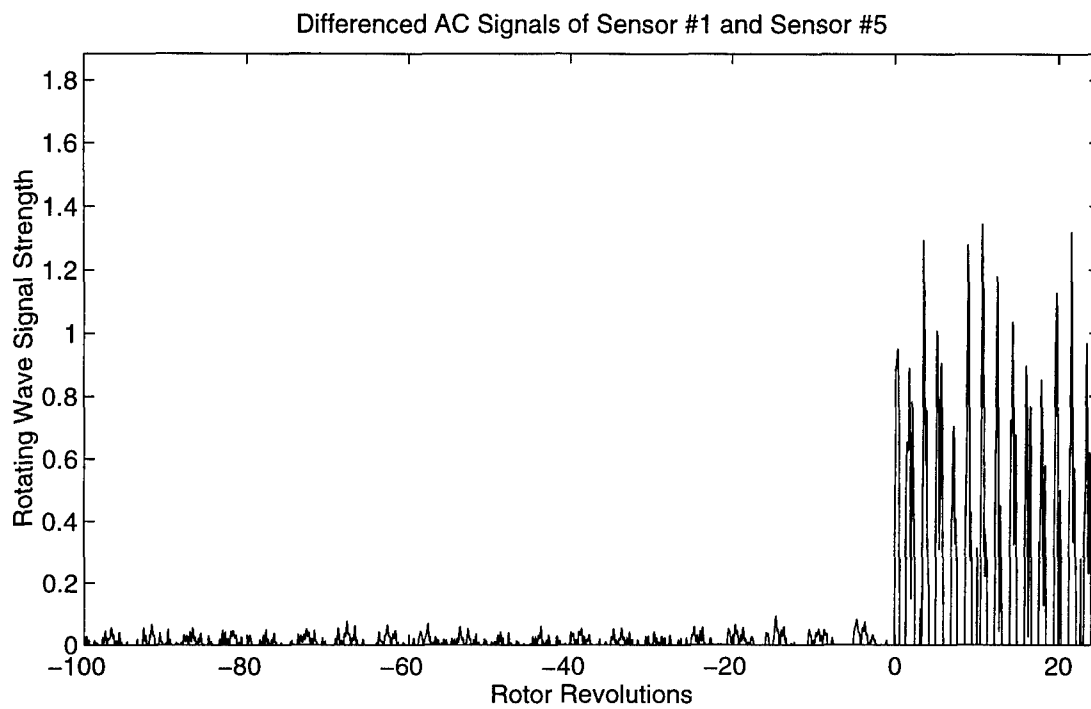
Figure 177. Onset of Rotating Stall and Surge (Case B, 95% Rotor Speed, 209.208 revs/sec)
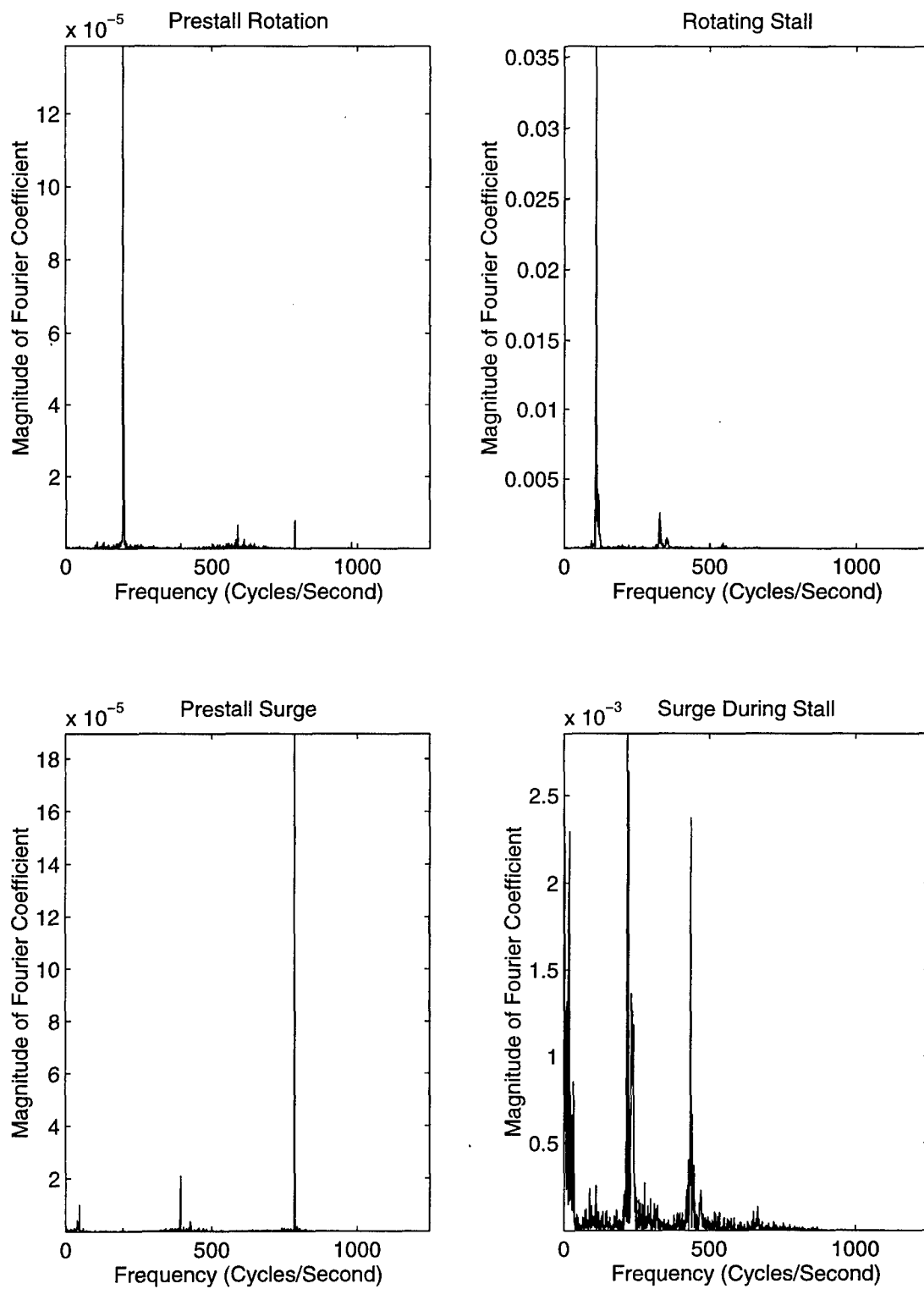
218
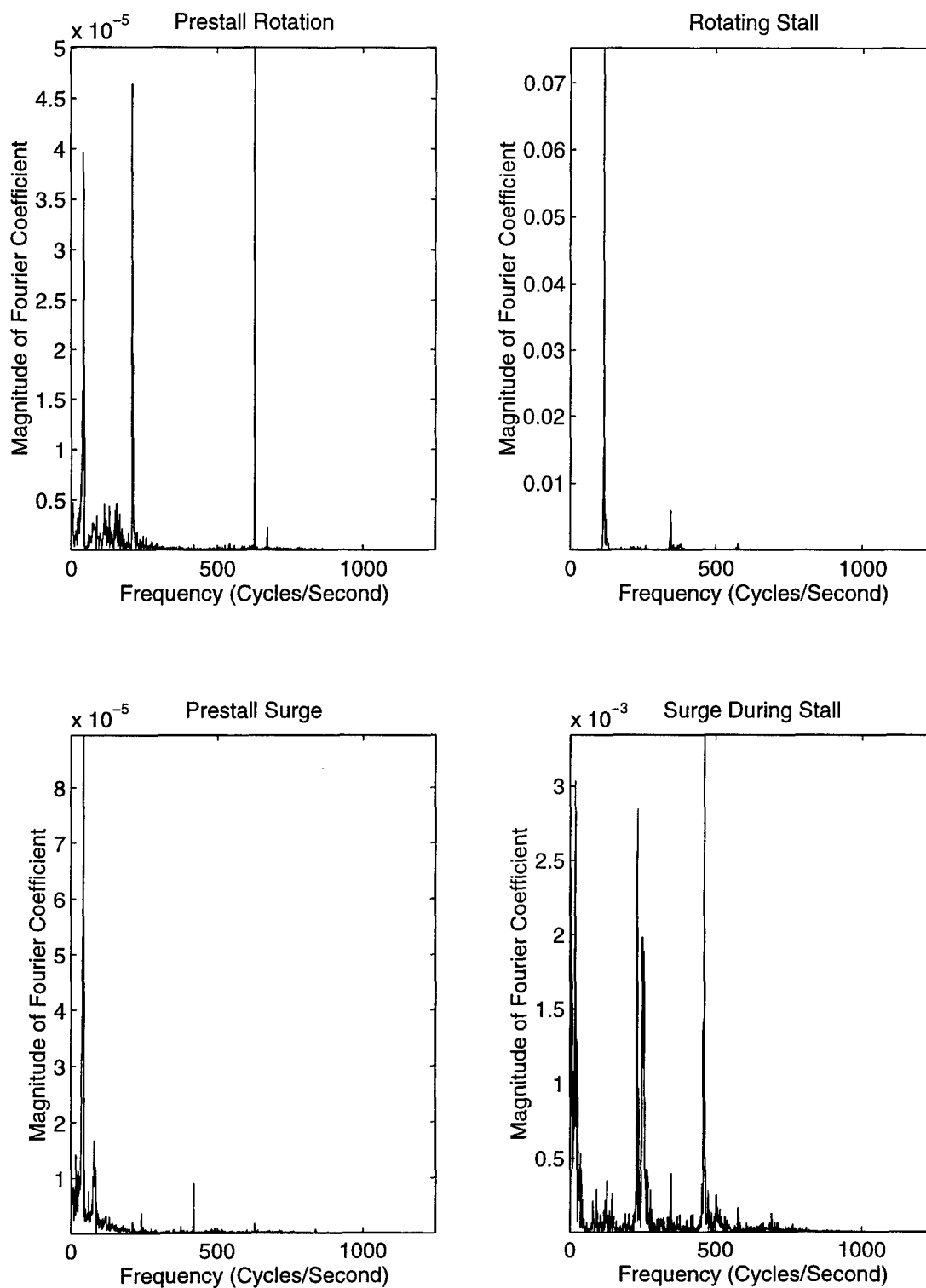
Figure 178. Frequency of Rotating Stall and Surge (Case B, 95% Rotor Speed, 209.208 revs/sec)
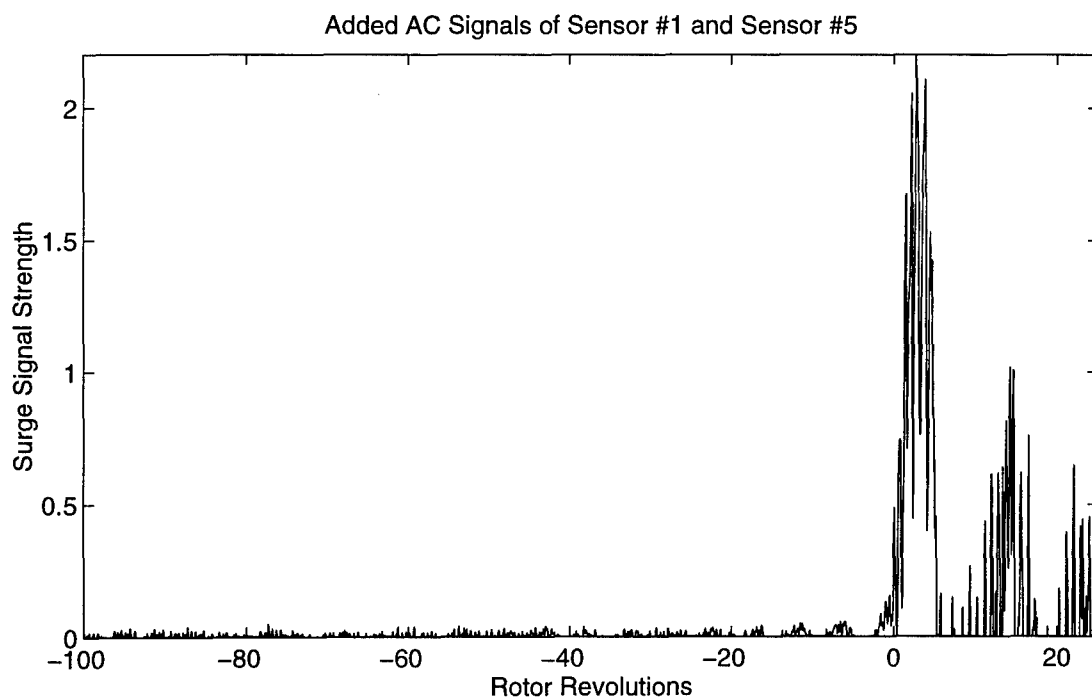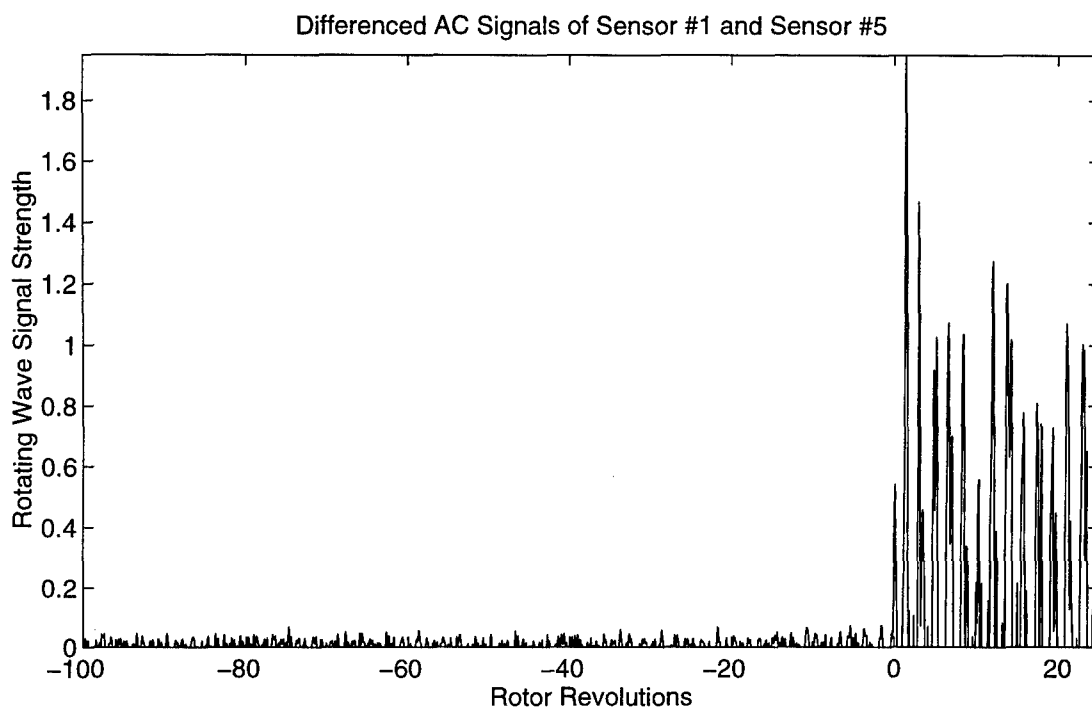
219
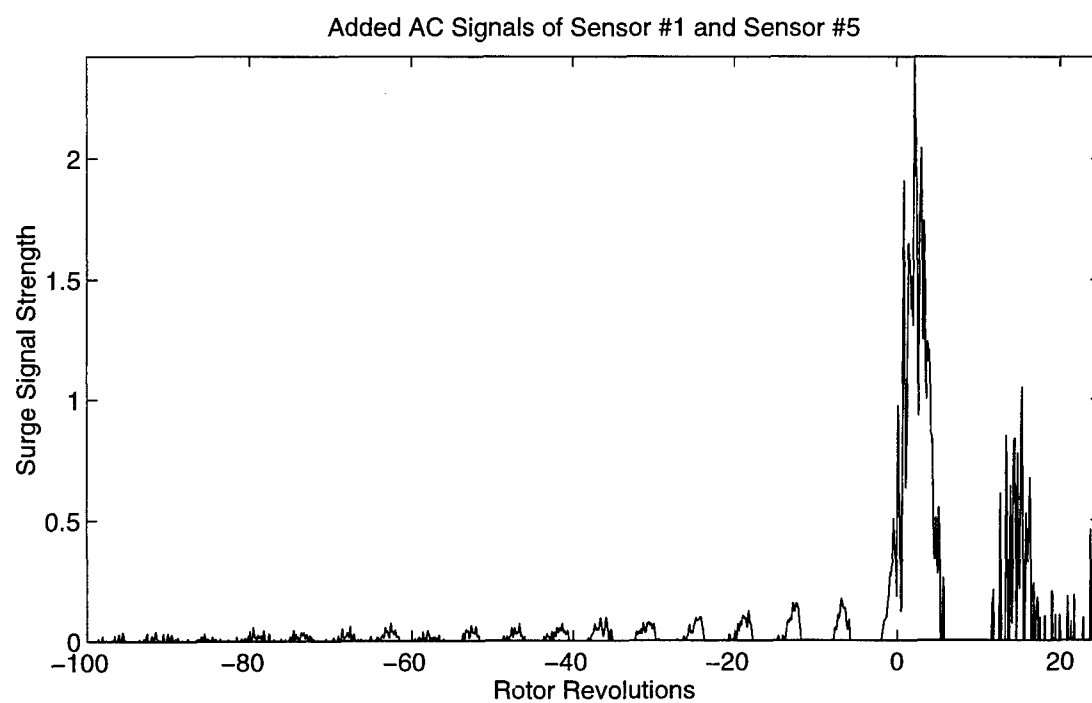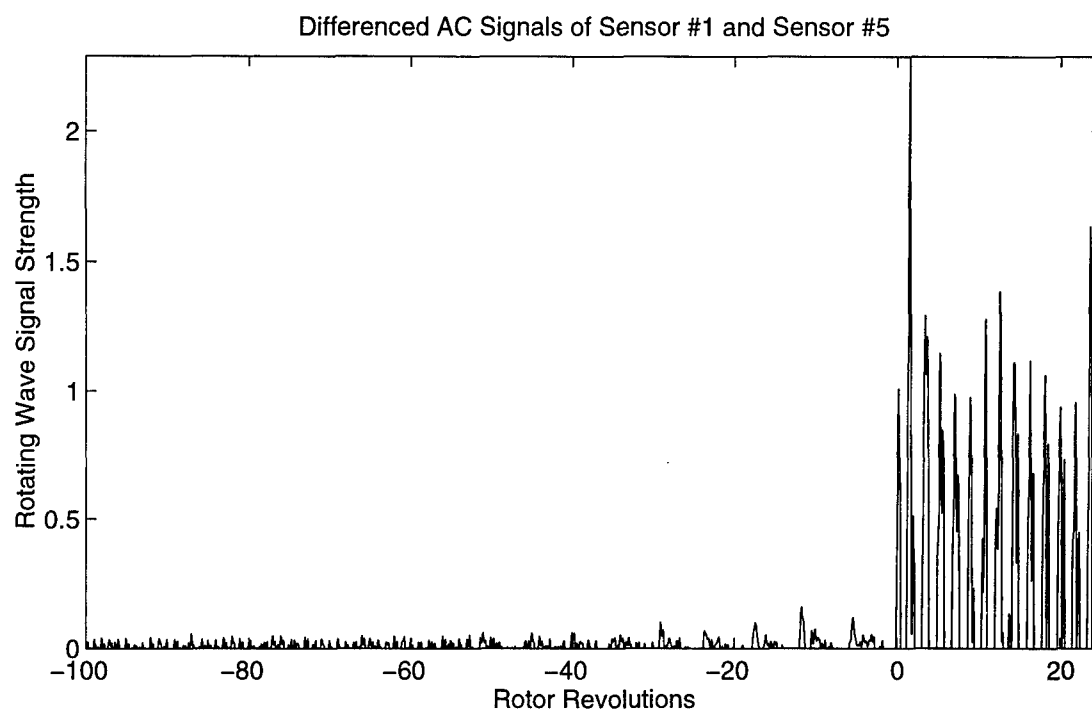
Figure 179. Onset of Rotating Stall and Surge (Case B, 100% Rotor Speed, 220.130 revs/sec)
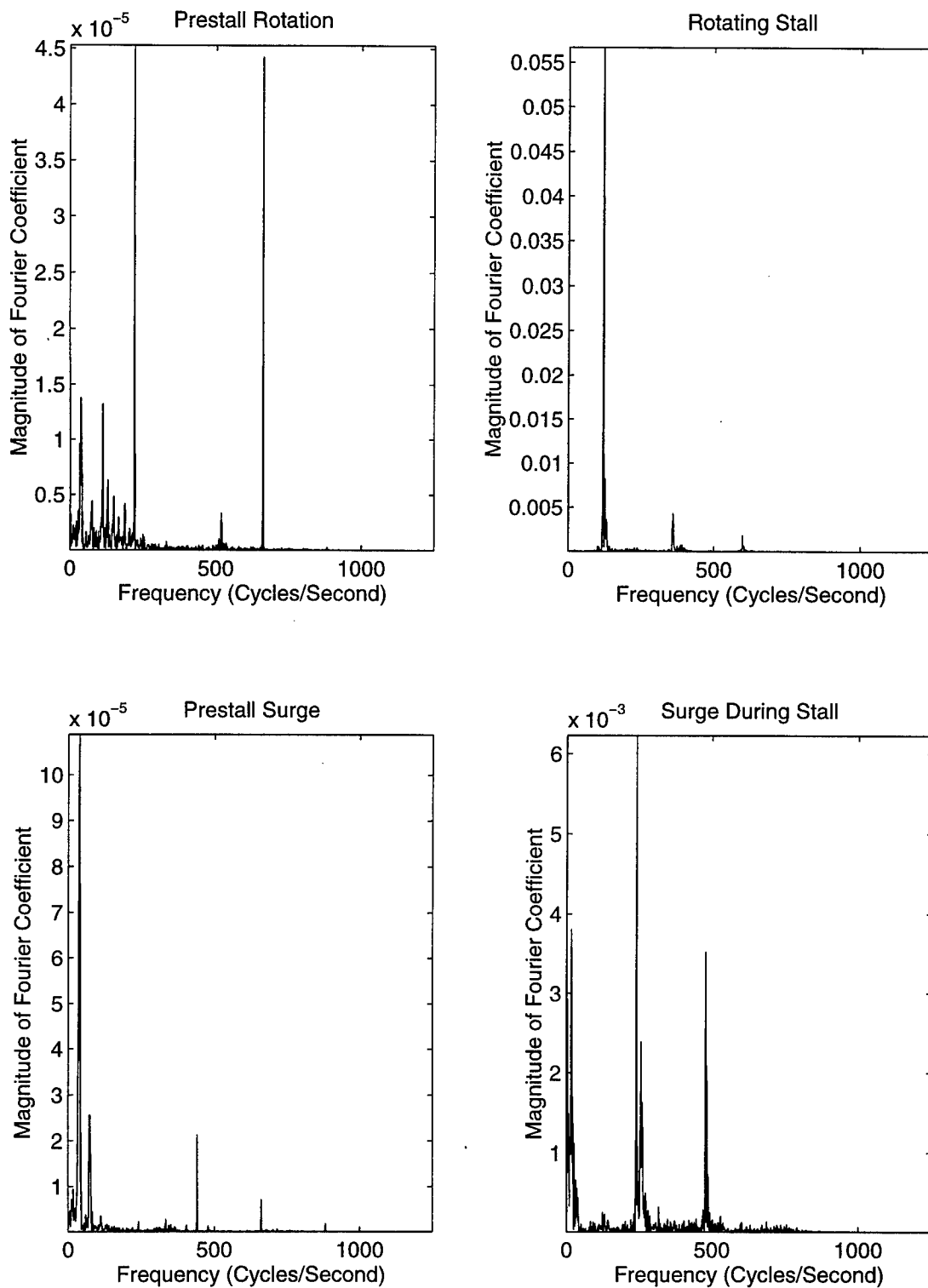
Figure 180. Frequency of Rotating Stall and Surge (Case B, 100% Rotor Speed, 220.130 revs/sec)

Differenced AC Signals of Sensor #1 and Sensor #5

Added AC Signals of Sensor #1 and Sensor #5
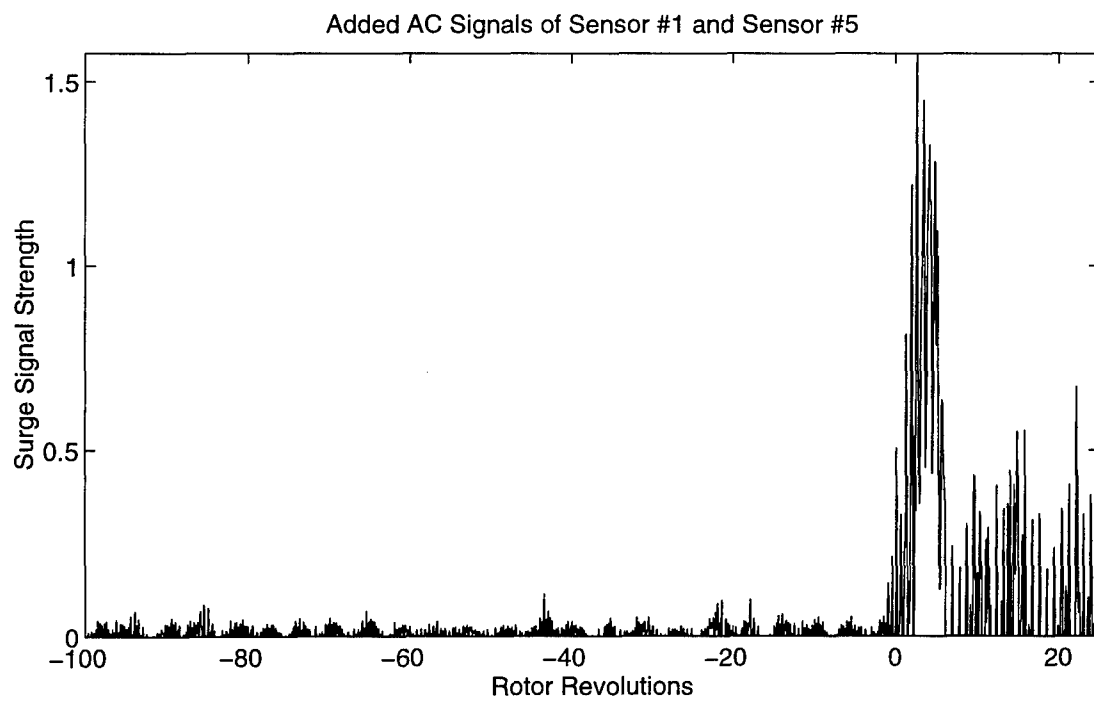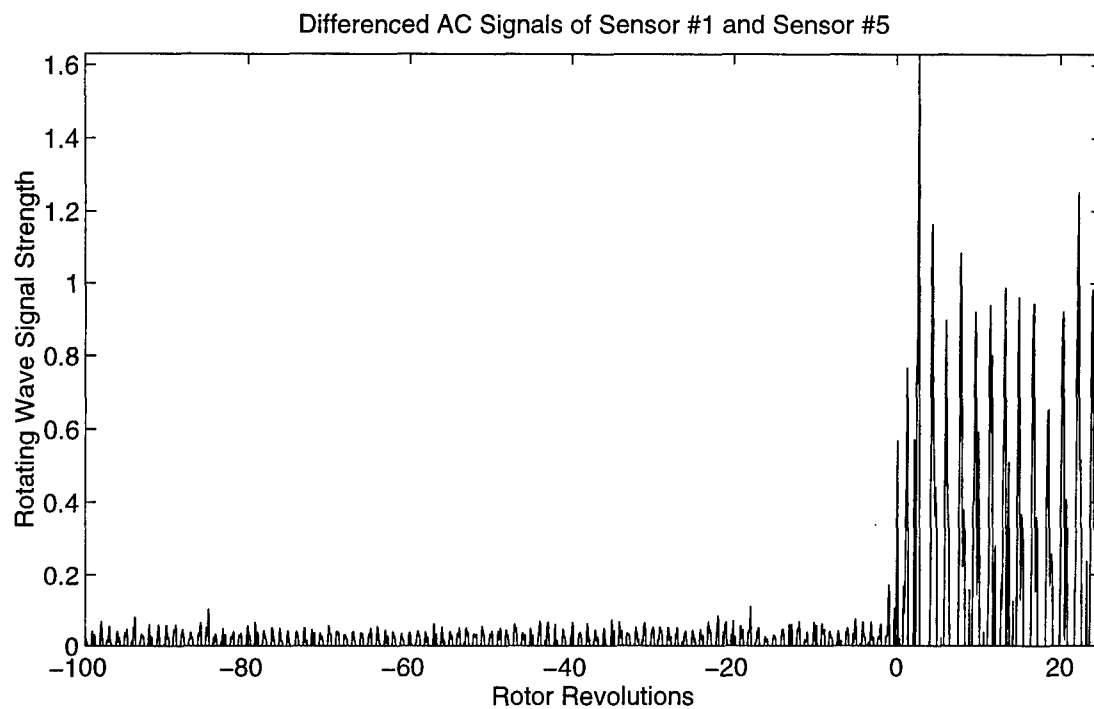
Figure 181. Onset of Rotating Stall and Surge (Case C, 85% Rotor Speed, 190.375 revs/sec)
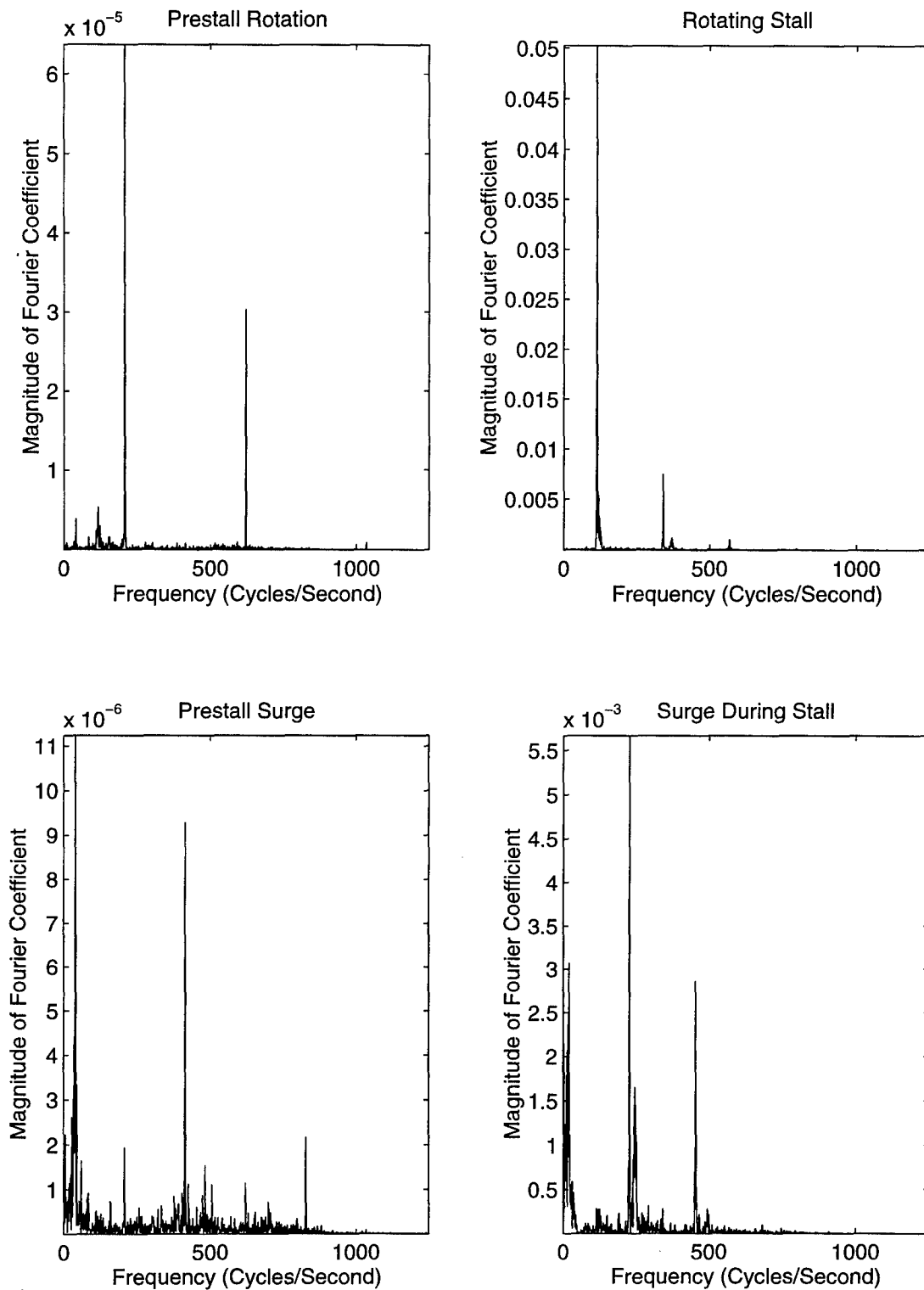
222
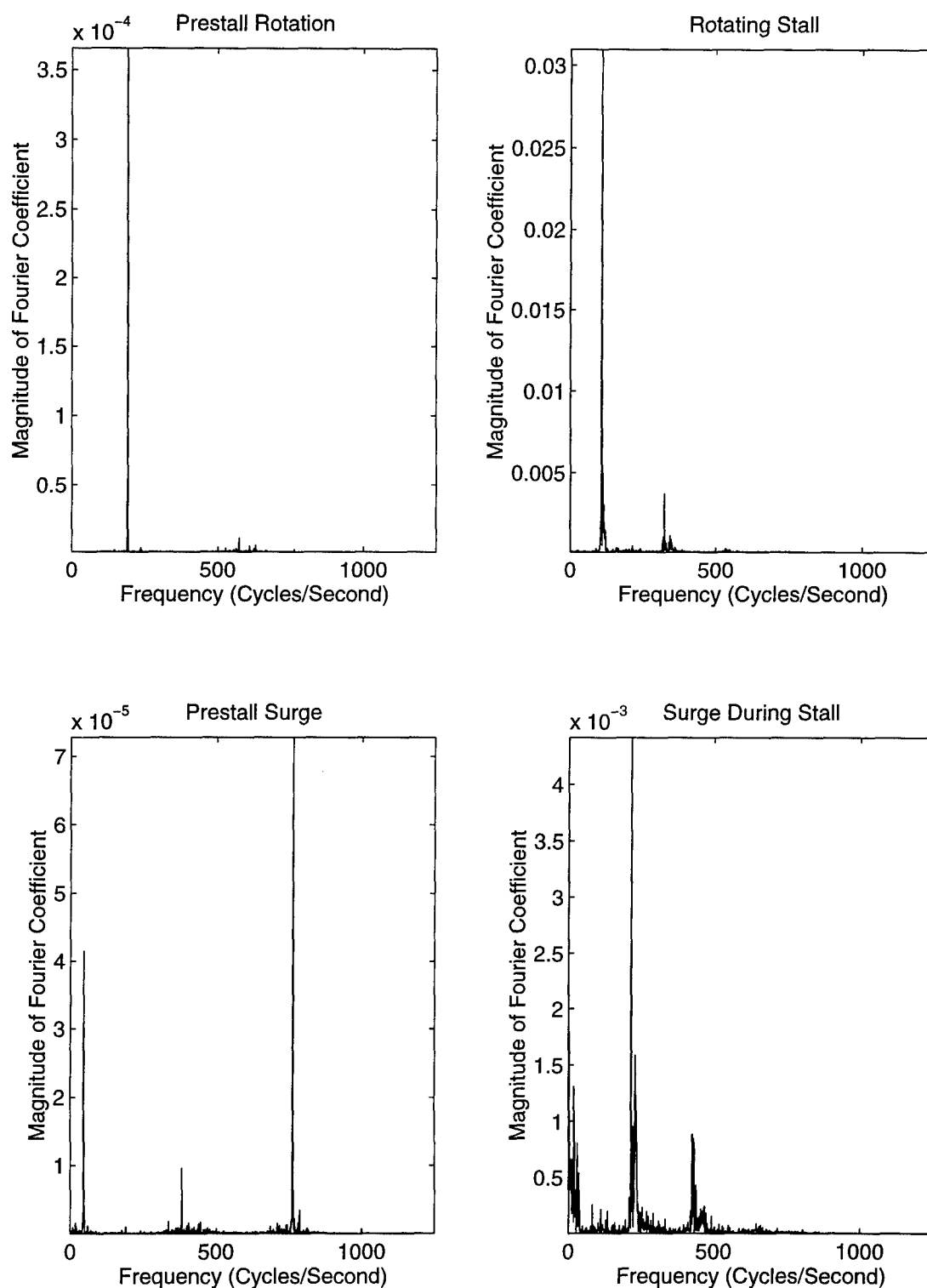
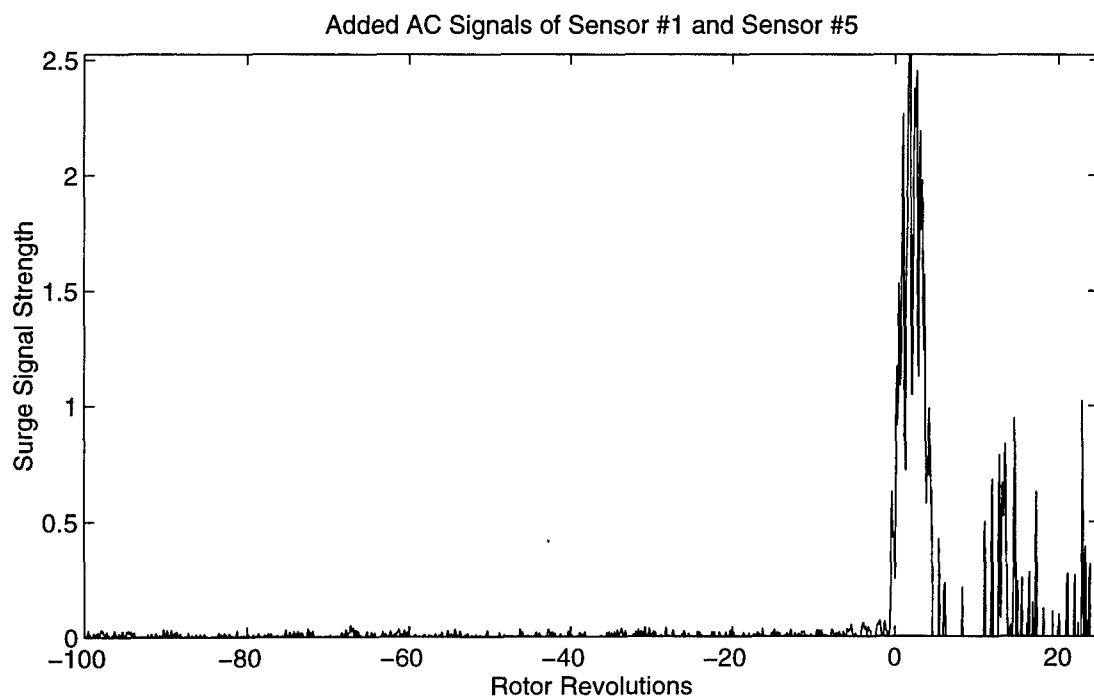Figure 182. Frequency of Rotating Stall and Surge (Case C, 85% Rotor Speed, 190.375 revs/sec)
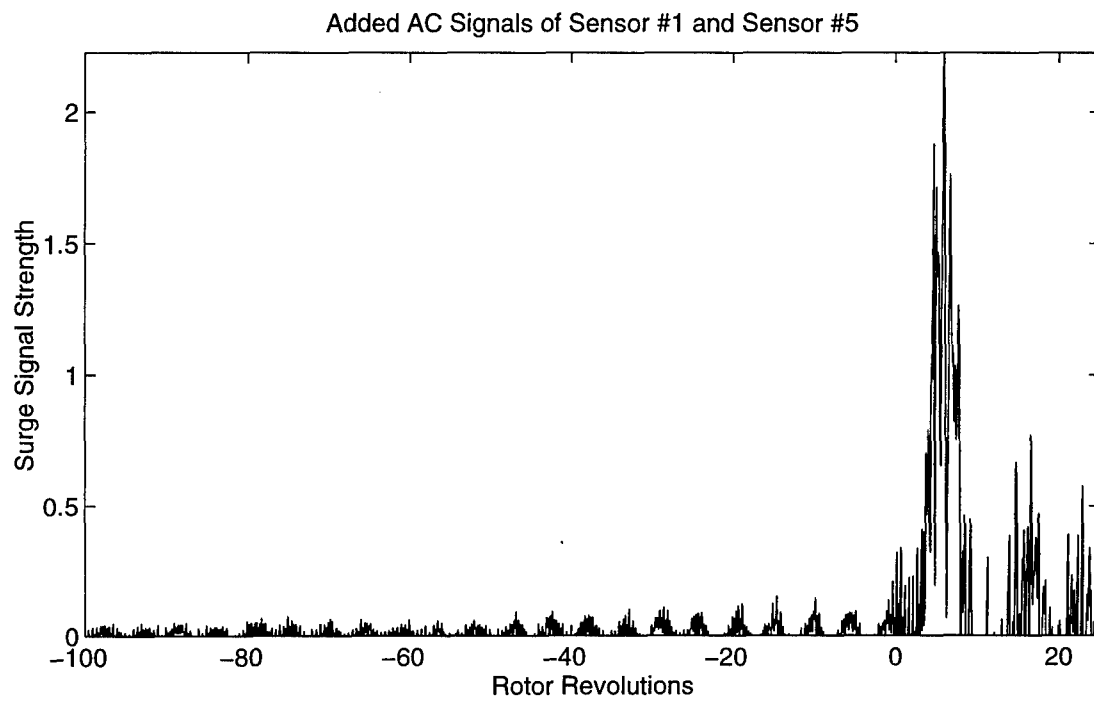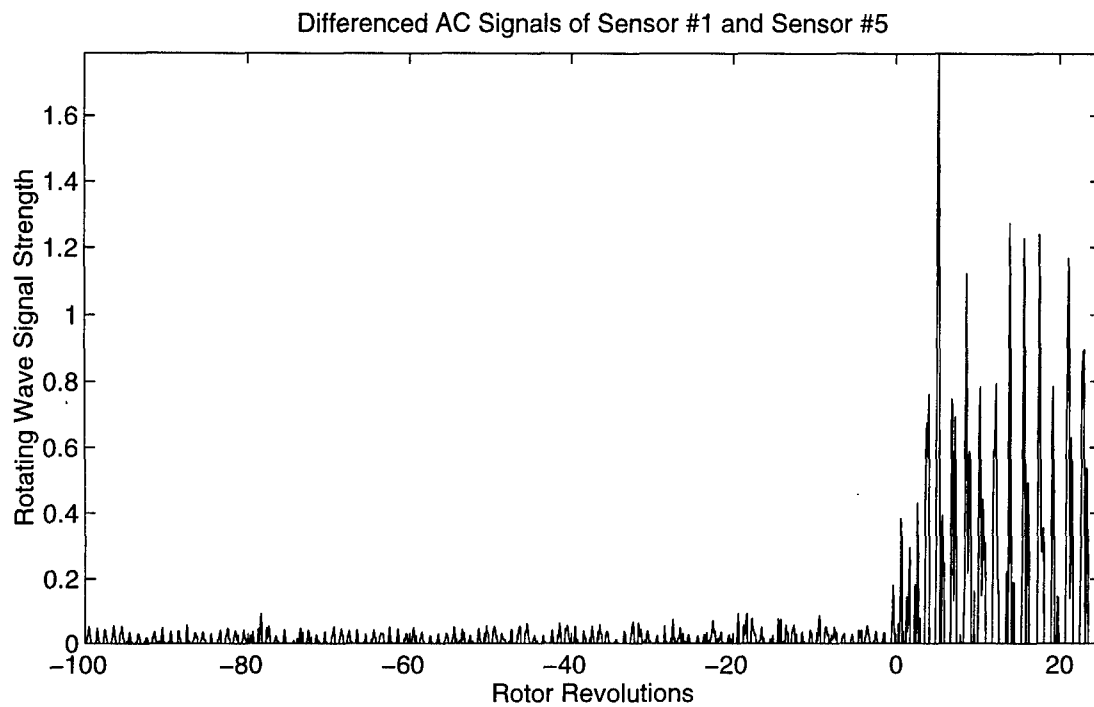
Figure 183. Onset of Rotating Stall and Surge (Case C, 90% Rotor Speed, 201.676 revs/sec)
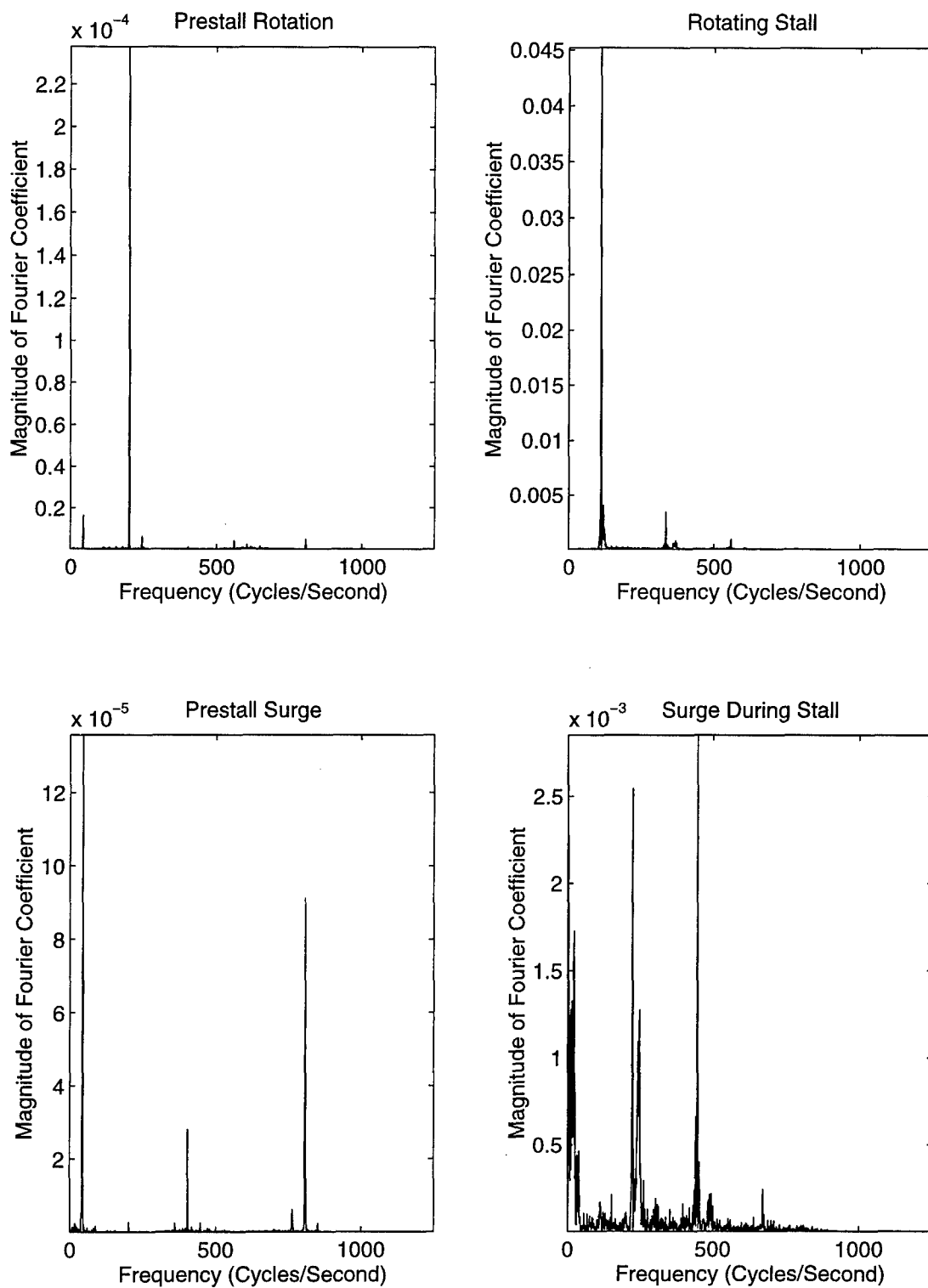
Figure 184. Frequency of Rotating Stall and Surge (Case C, 90% Rotor Speed, 201.676 revs/sec)

225
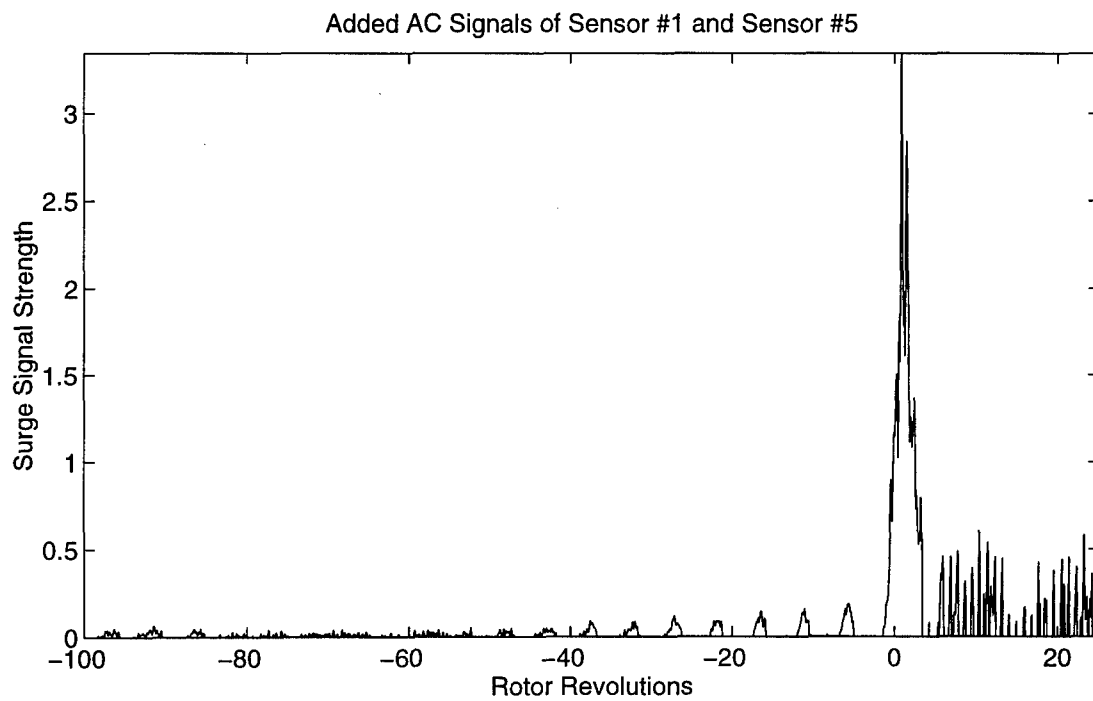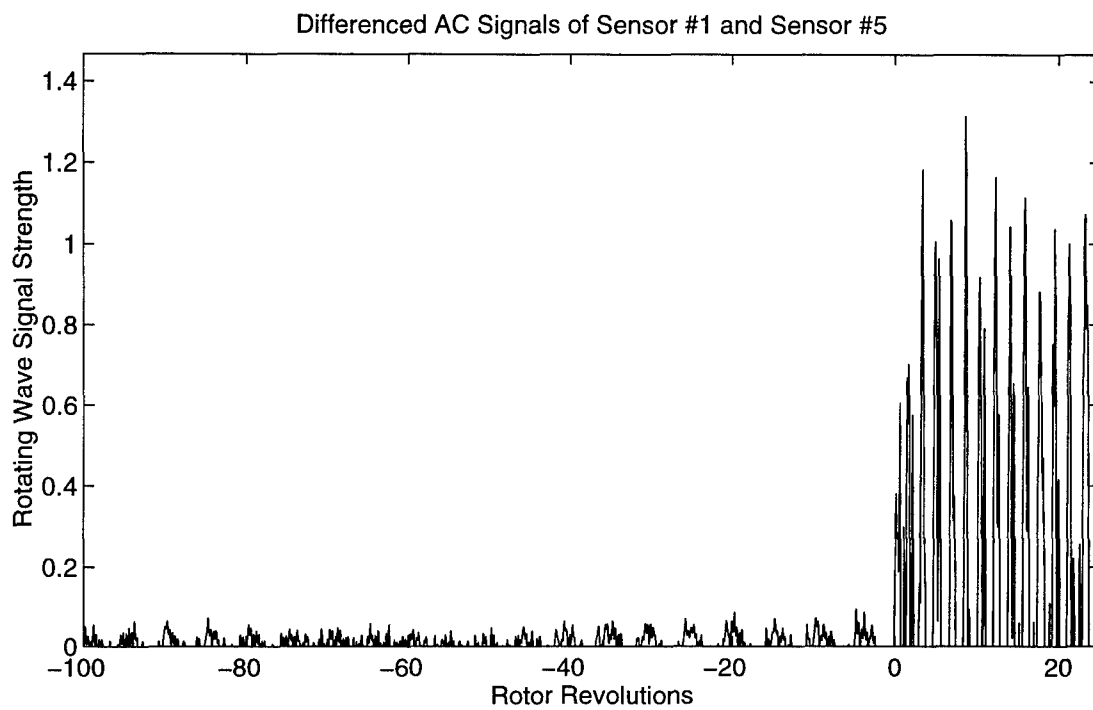
Figure 185. Onset of Rotating Stall and Surge (Case C, 95% Rotor Speed, 212.748 revs/sec)

226
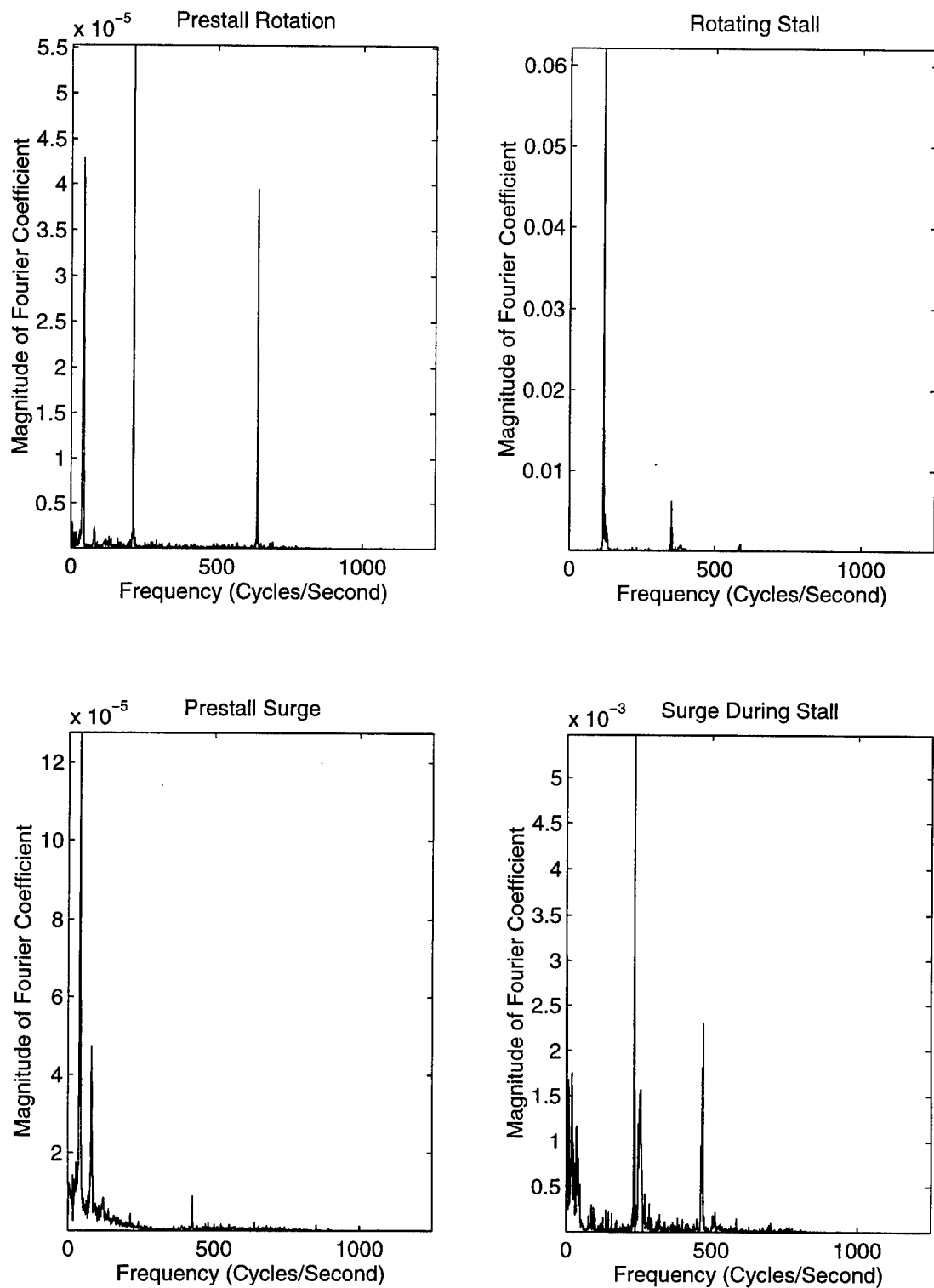
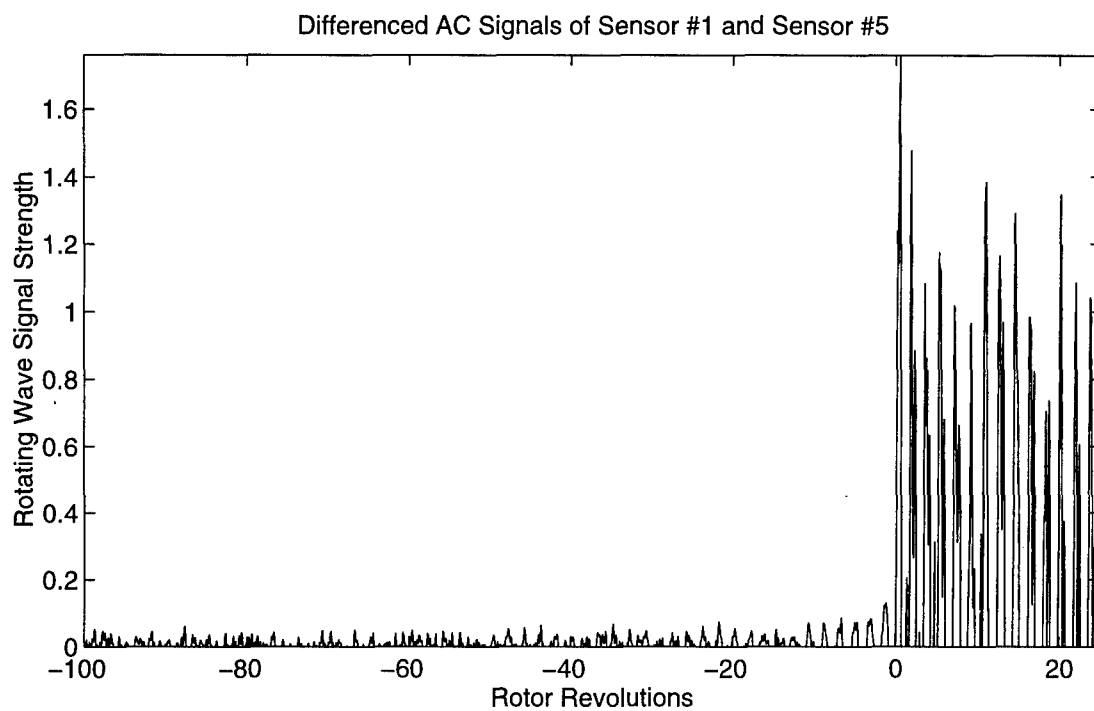Figure 186. frequency of Rotating Stall and Surge (Case C, 95% Rotor Speed, 212.748 revs/sec)

227
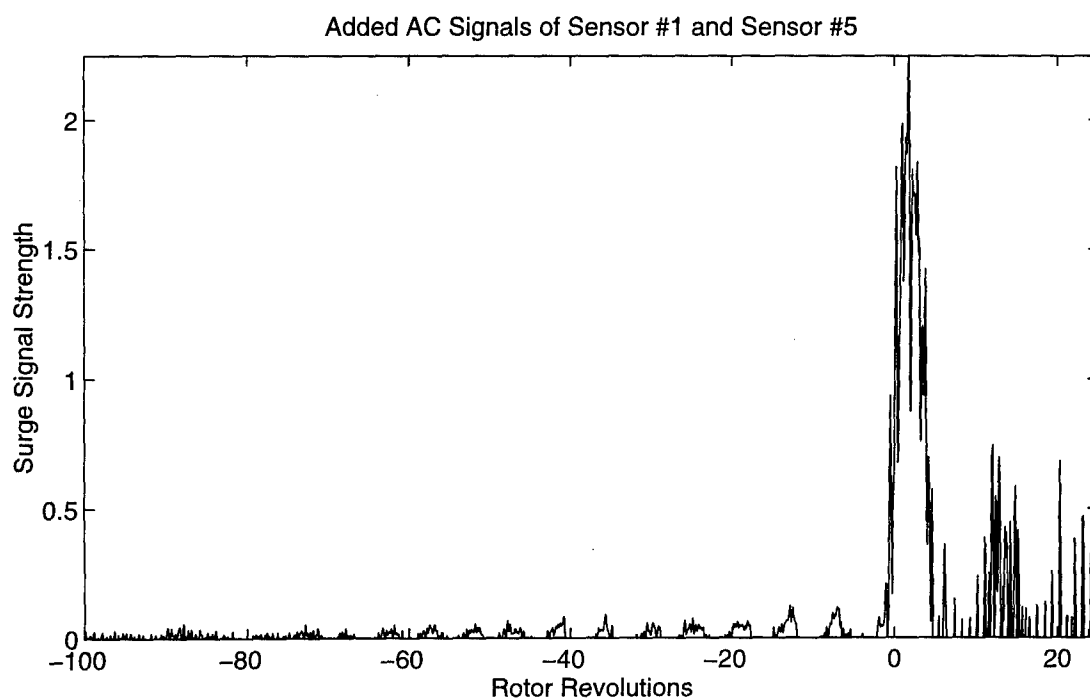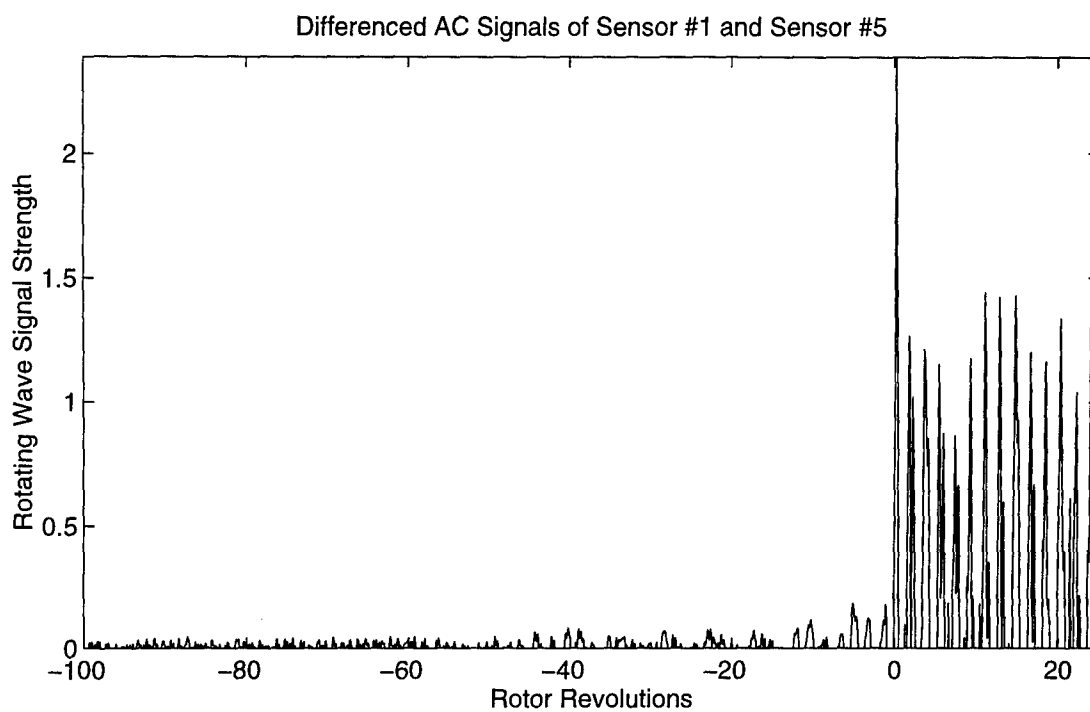
Figure 187. Onset of Rotating Stall and Surge (Case C, 100% Rotor Speed, 223.759 revs/sec)
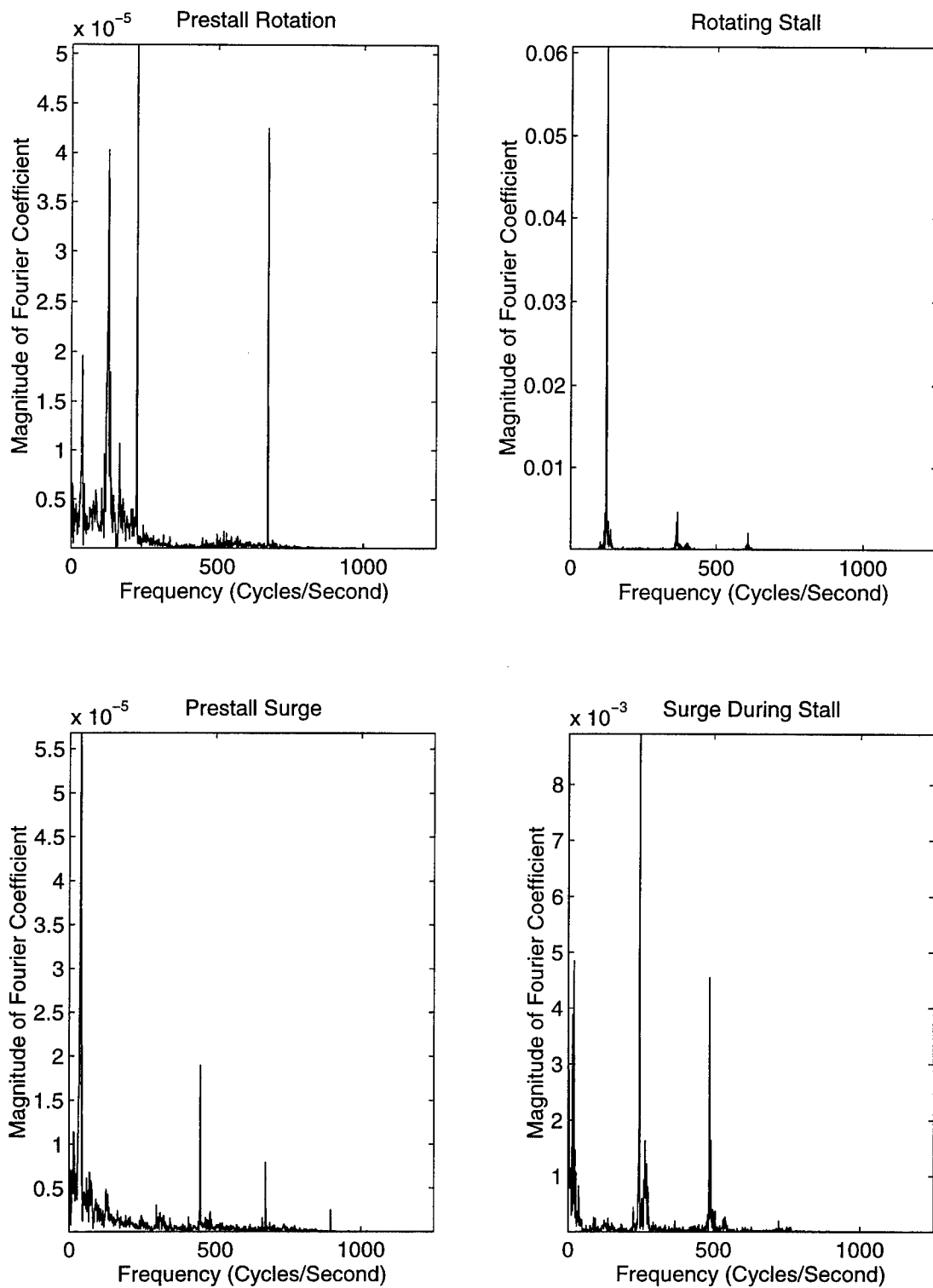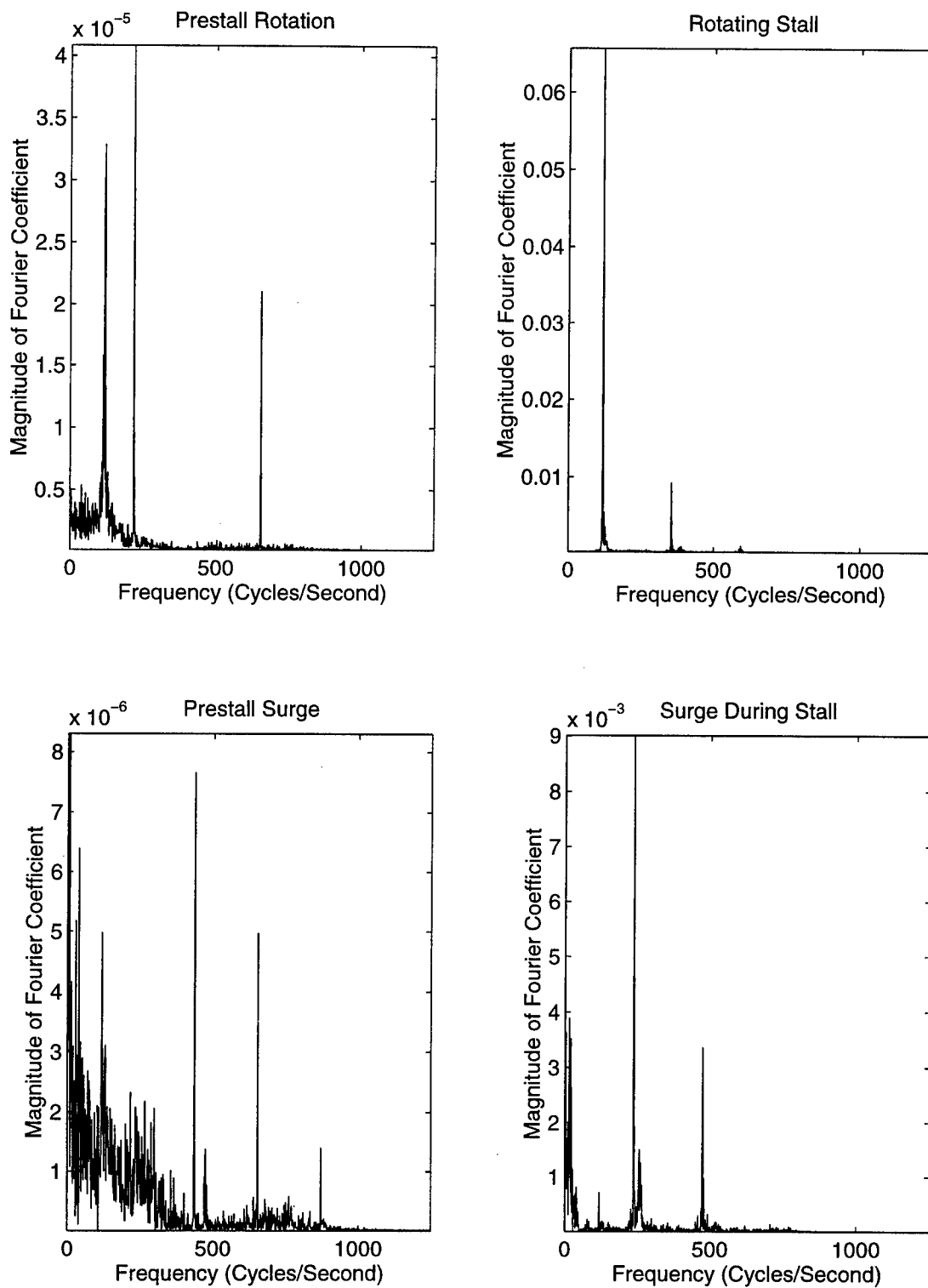
Figure 188. Frequency of Rotating Stall and Surge (Case C, 100% Rotor Speed, 223.759 revs/sec)

229
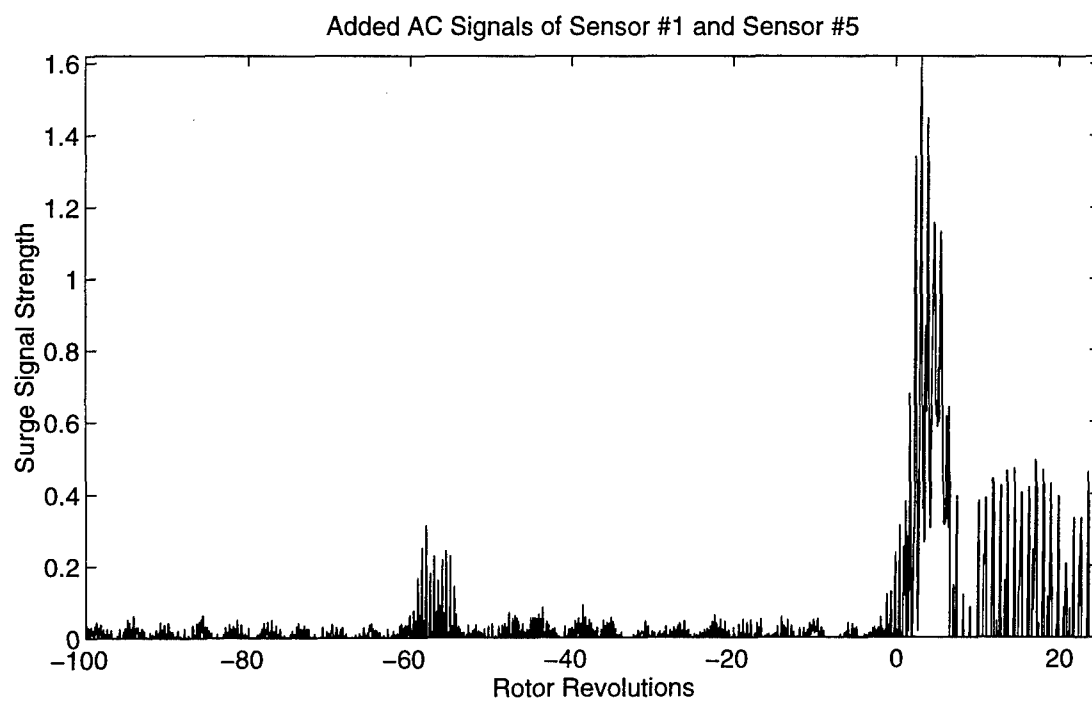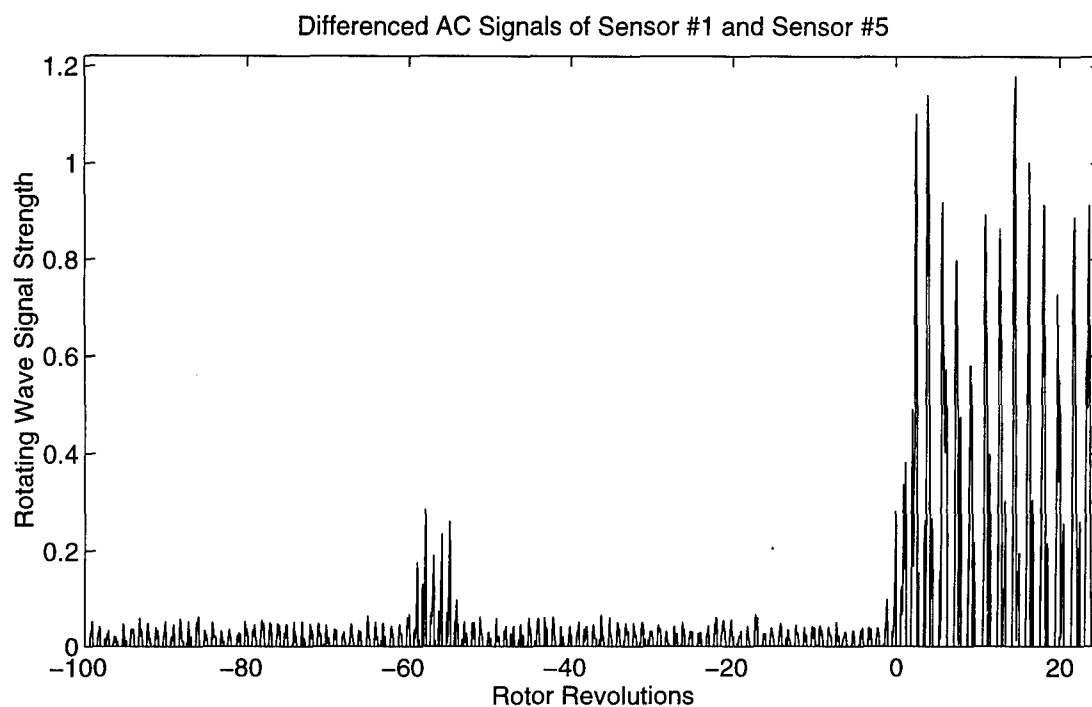
Figure 189. Onset of Rotating Stall and Surge (Case D, 85% Rotor Speed, 186.184 revs/sec)
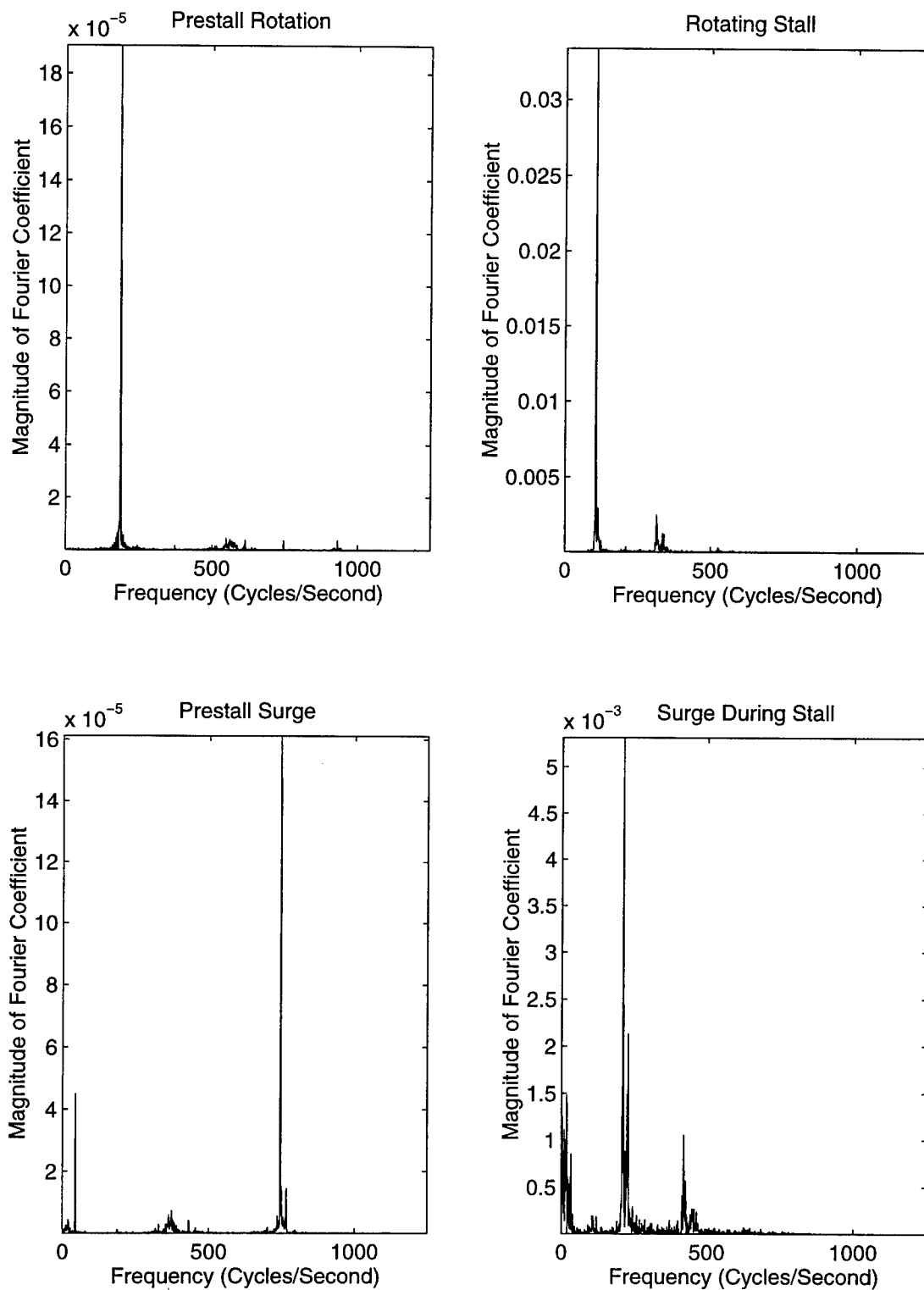
Figure 190. Frequency of Rotating Stall and Surge (Case D, 85% Rotor Speed, 186.184 revs/sec)
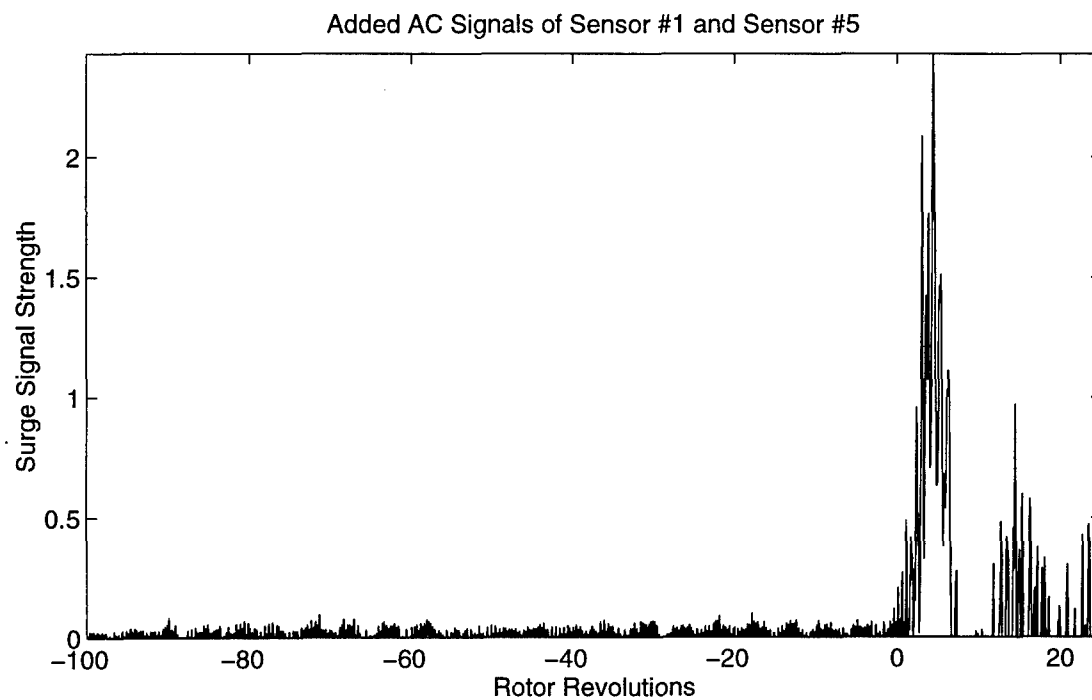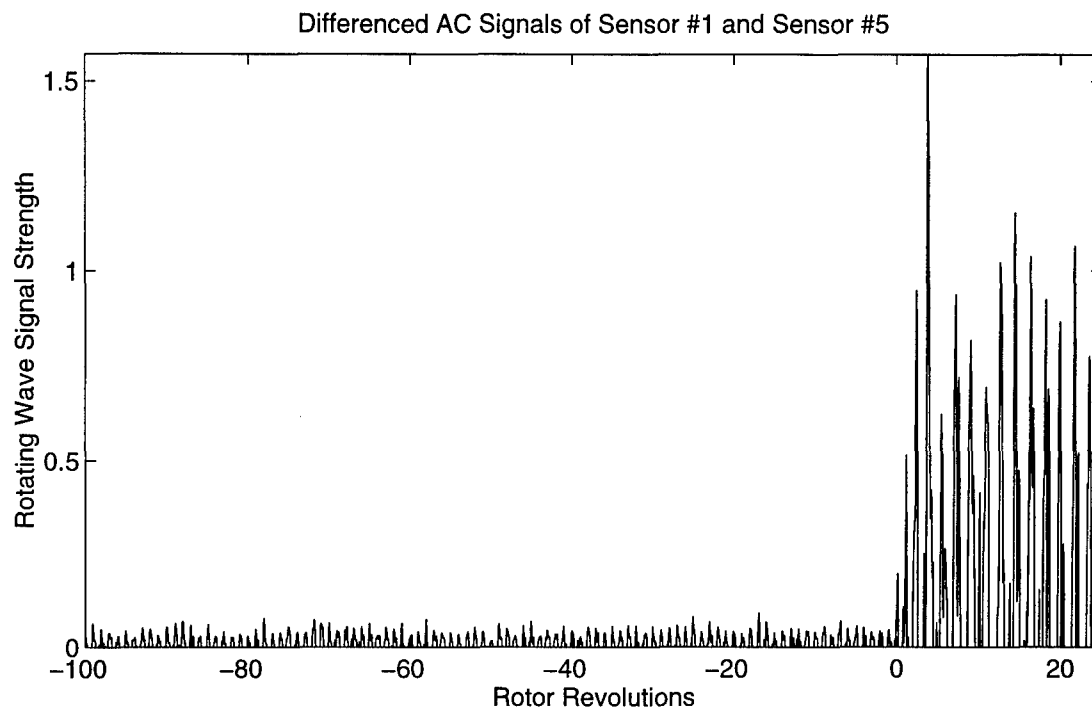
Figure 191. Onset of Rotating Stall and Surge (Case D, 90% Rotor Speed, 197.708 revs/sec)
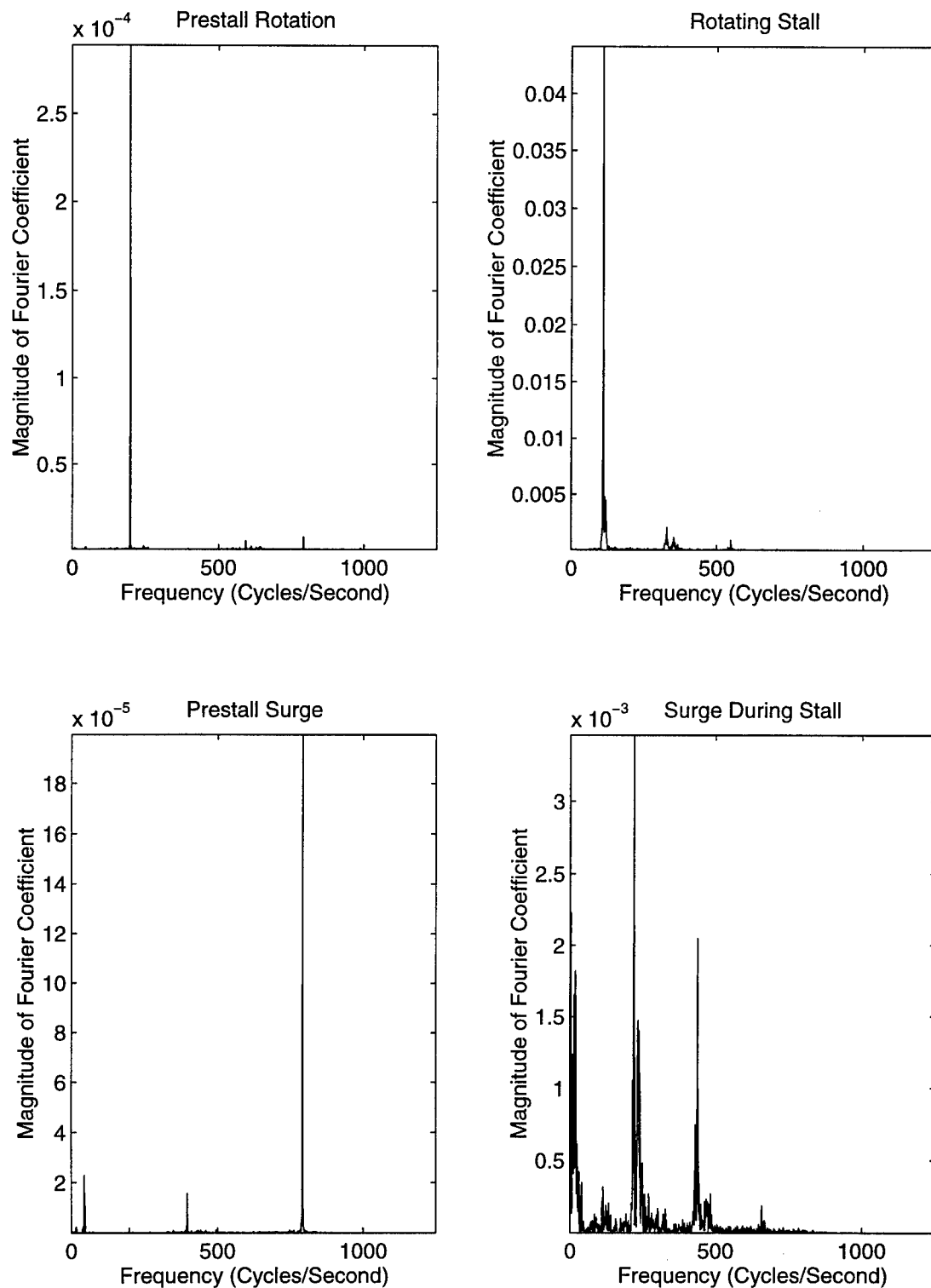
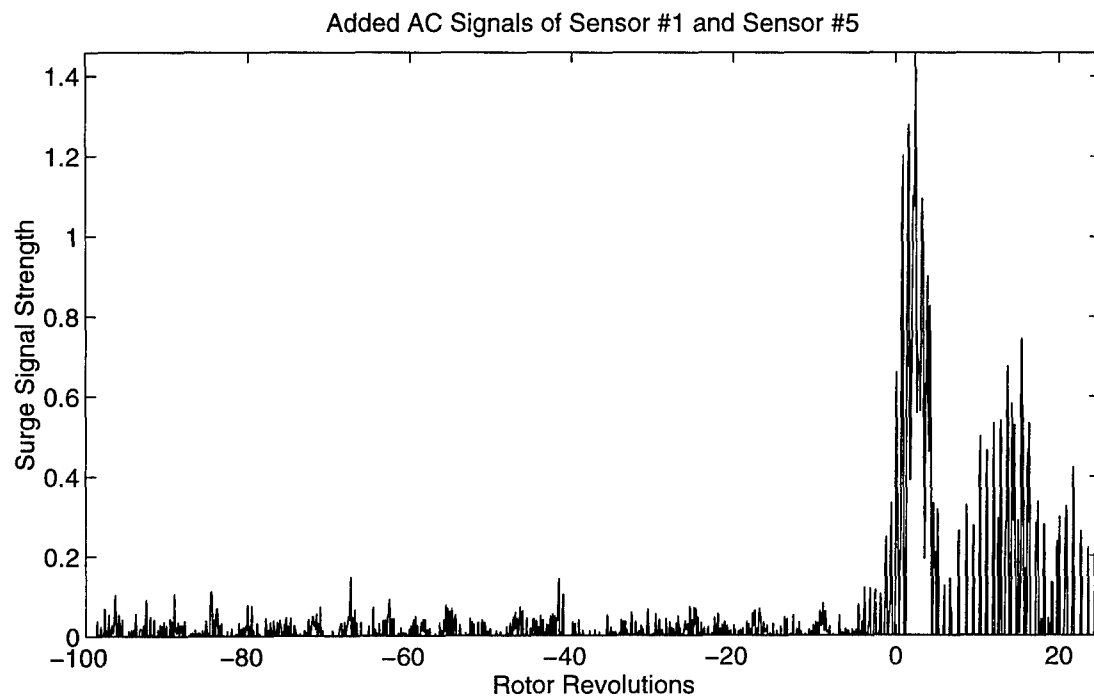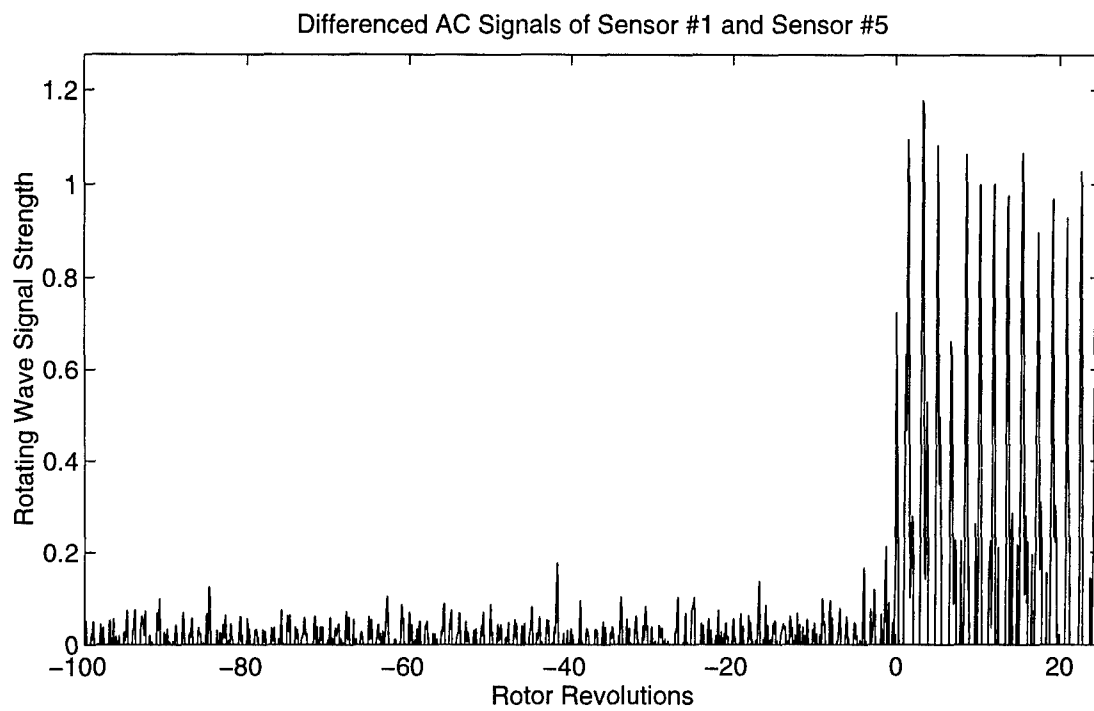Figure 192. Frequency of Rotating Stall and Surge (Case D, 90% Rotor Speed, 197.708 revs/sec)

233

Differenced AC Signals of Sensor #1 and Sensor #5

Added AC Signals of Sensor #1 and Sensor #5
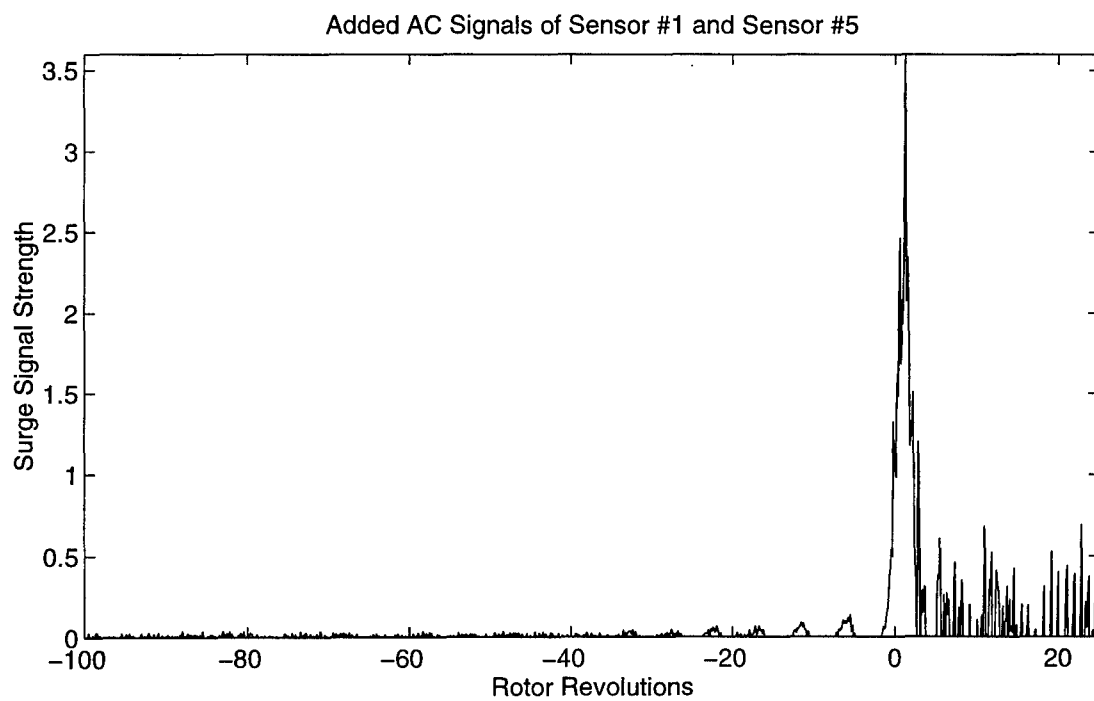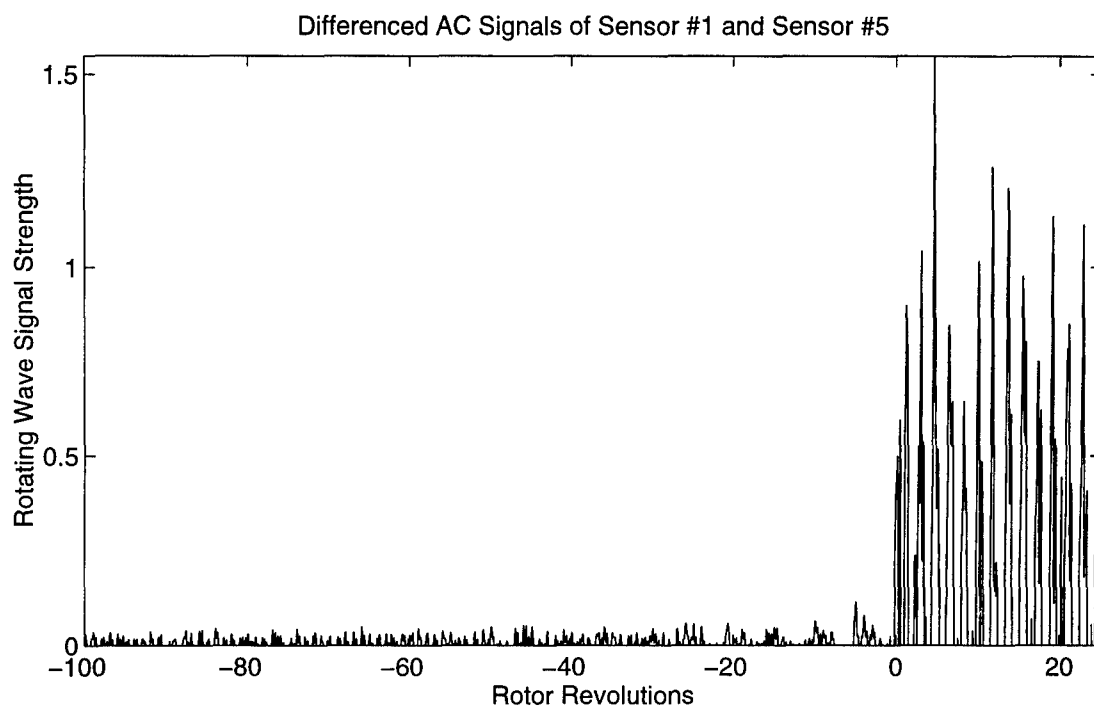
Figure 193. Onset of Rotating Stall and Surge (Case D, 95% Rotor Speed, 208.382 revs/sec)
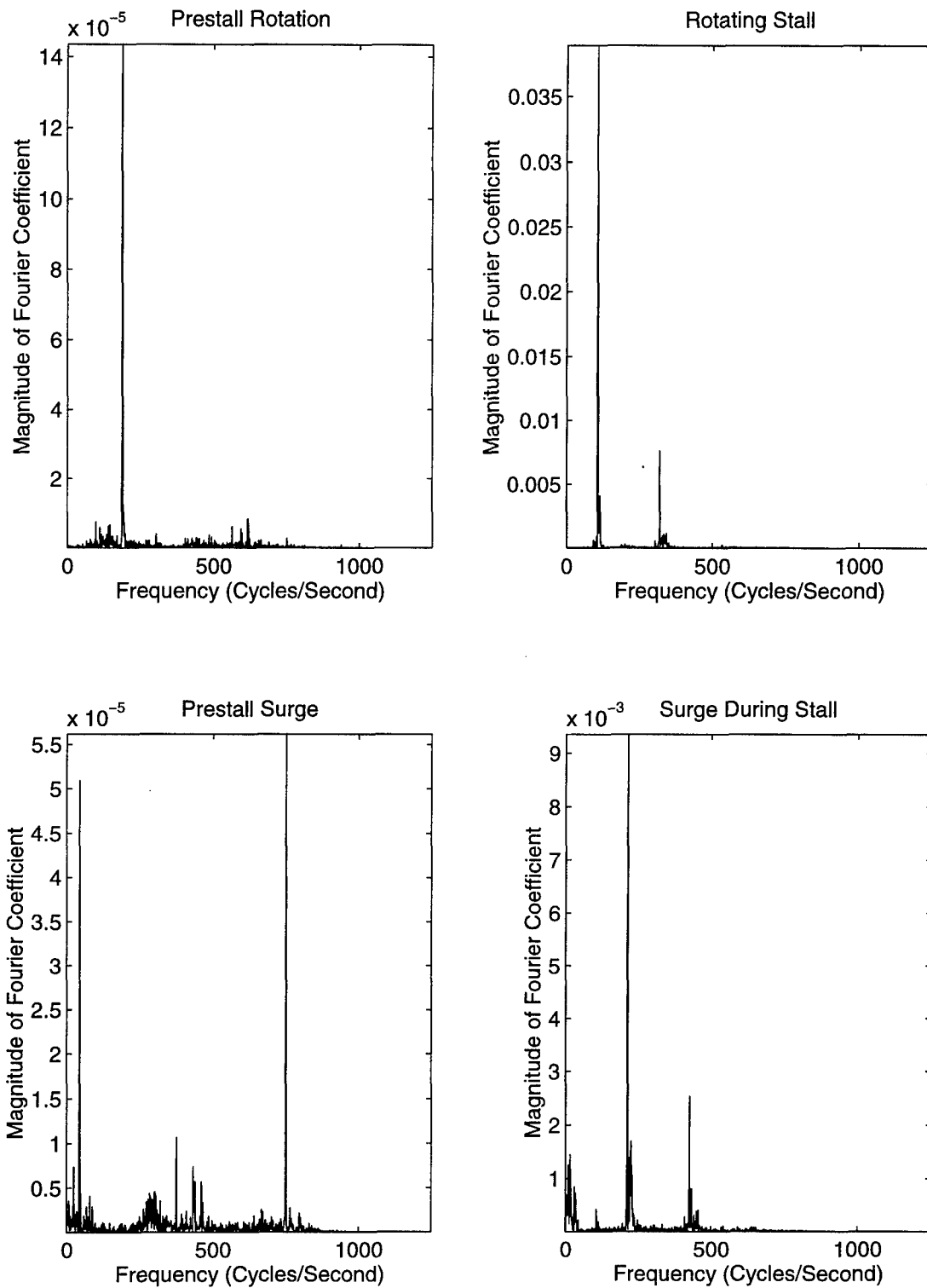
234
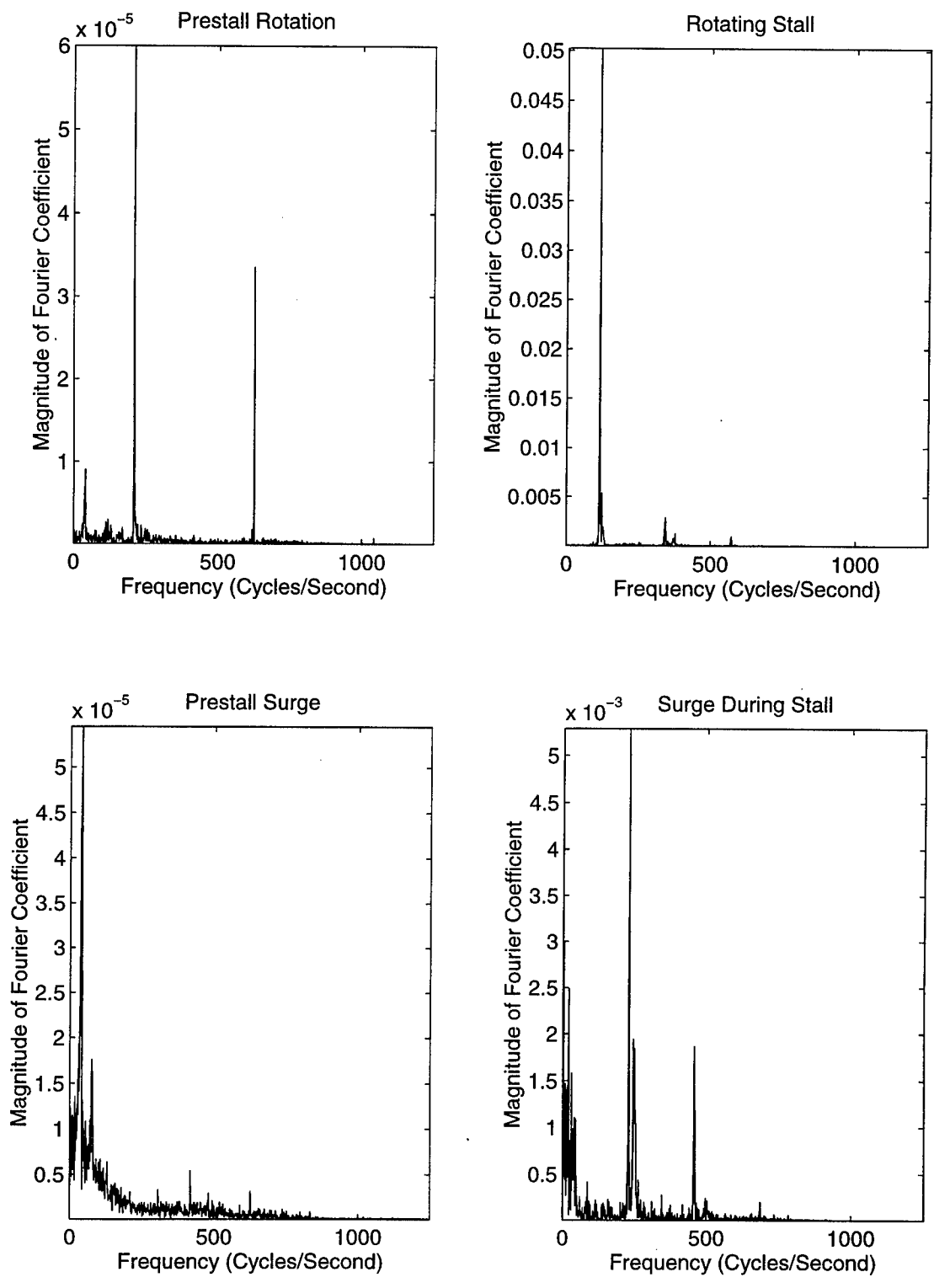
Figure 194. Frequency of Rotating Stall and Surge (Case D, 95% Rotor Speed, 208.382 revs/sec)

235
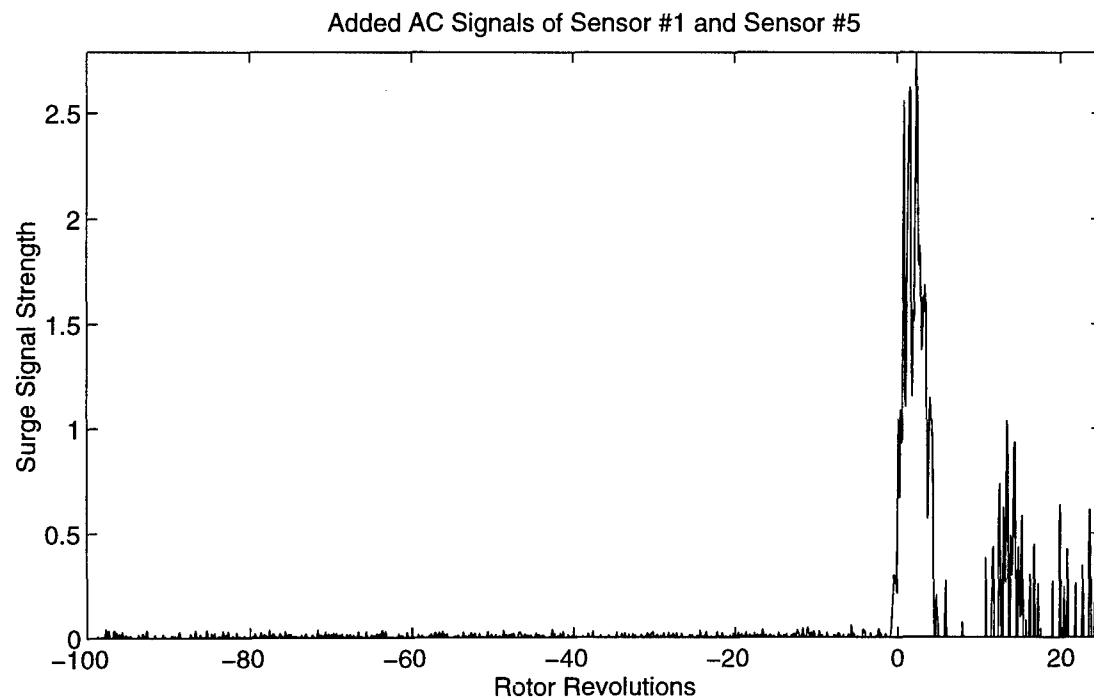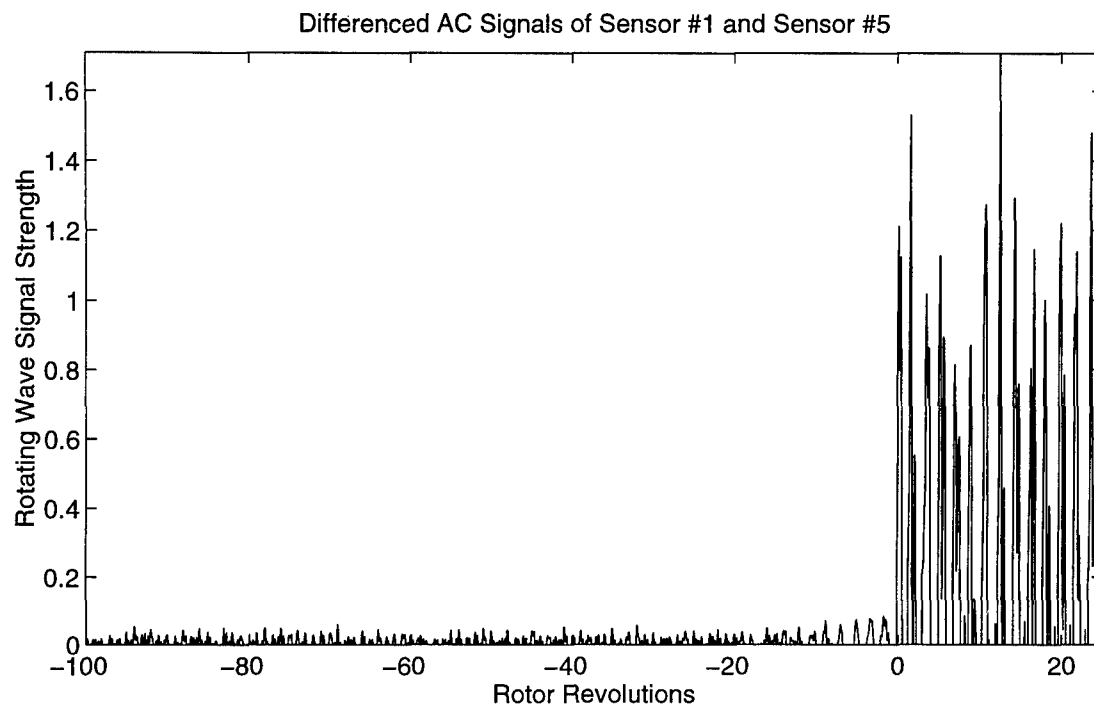
Figure 195. Onset of Rotating Stall and Surge (Case D, 100% Rotor Speed, 219.296 revs/sec)

236
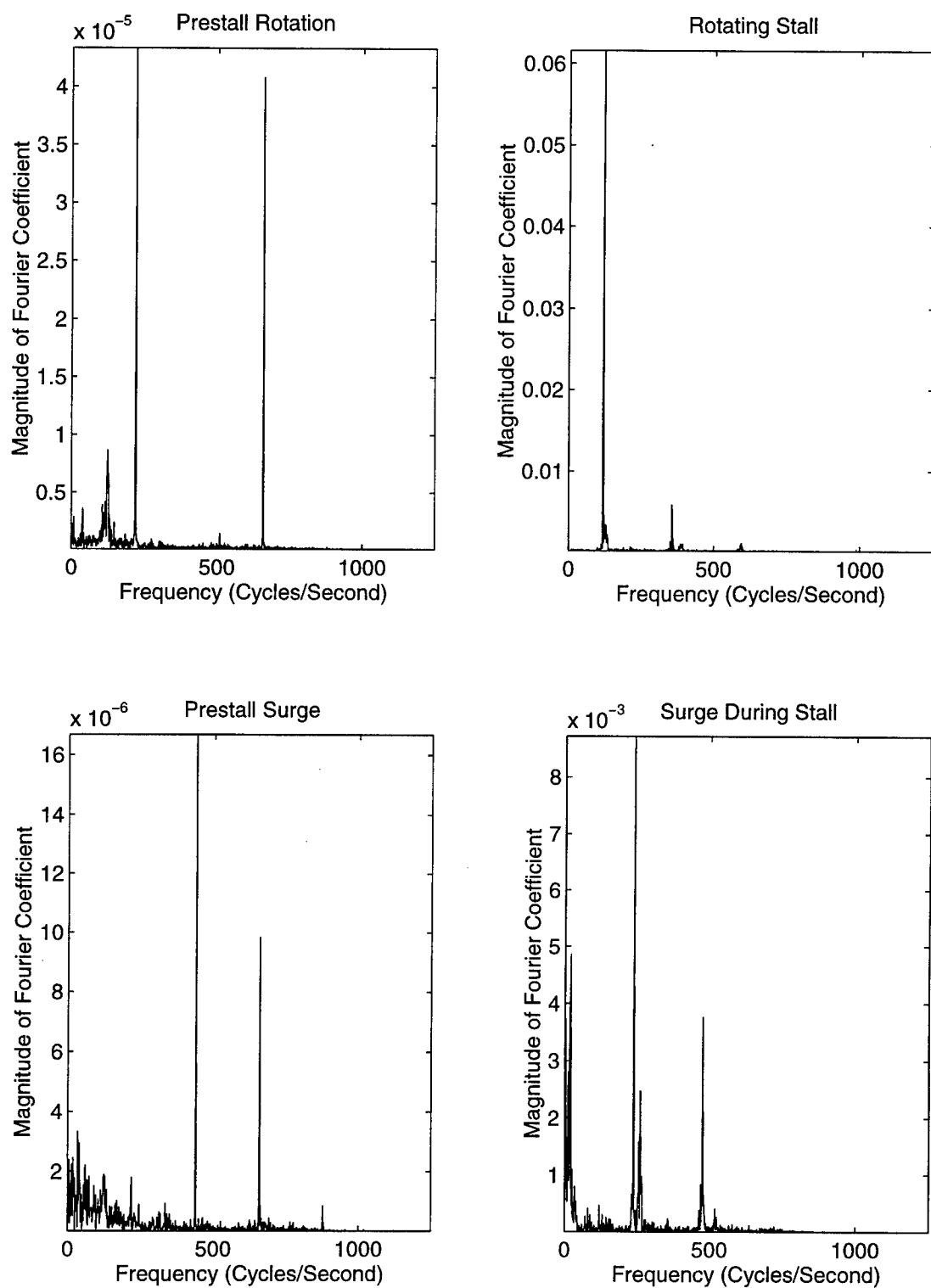
Figure 196. Frequency of Rotating Stall and Surge (Case D, 100% Rotor Speed, 219.296 revs/sec)

237
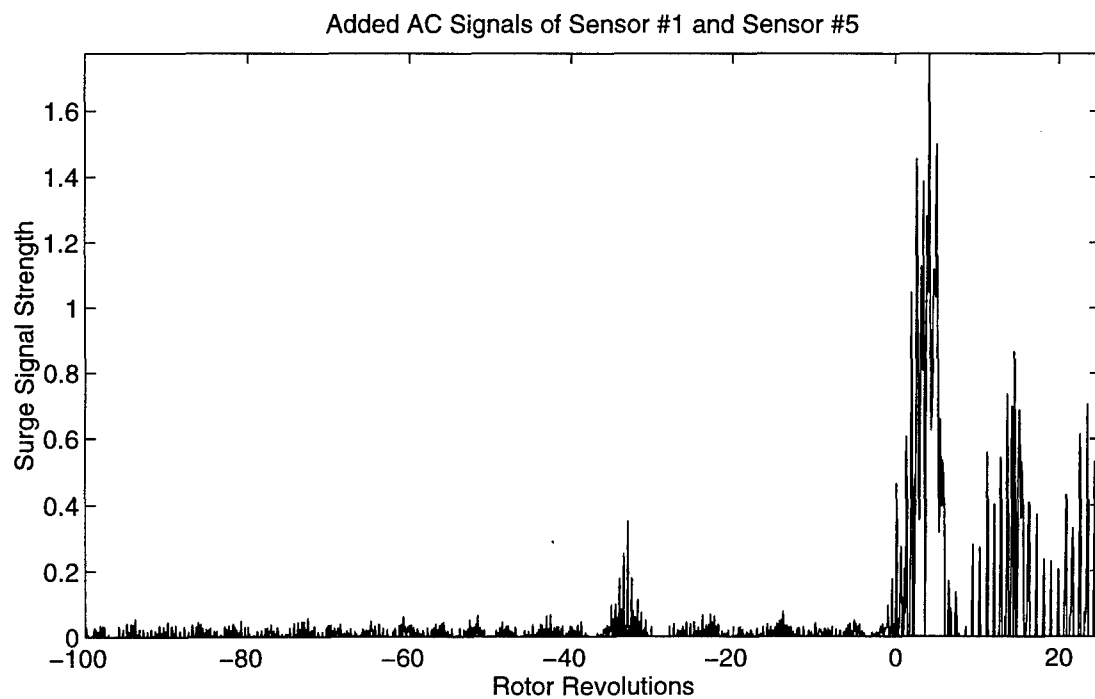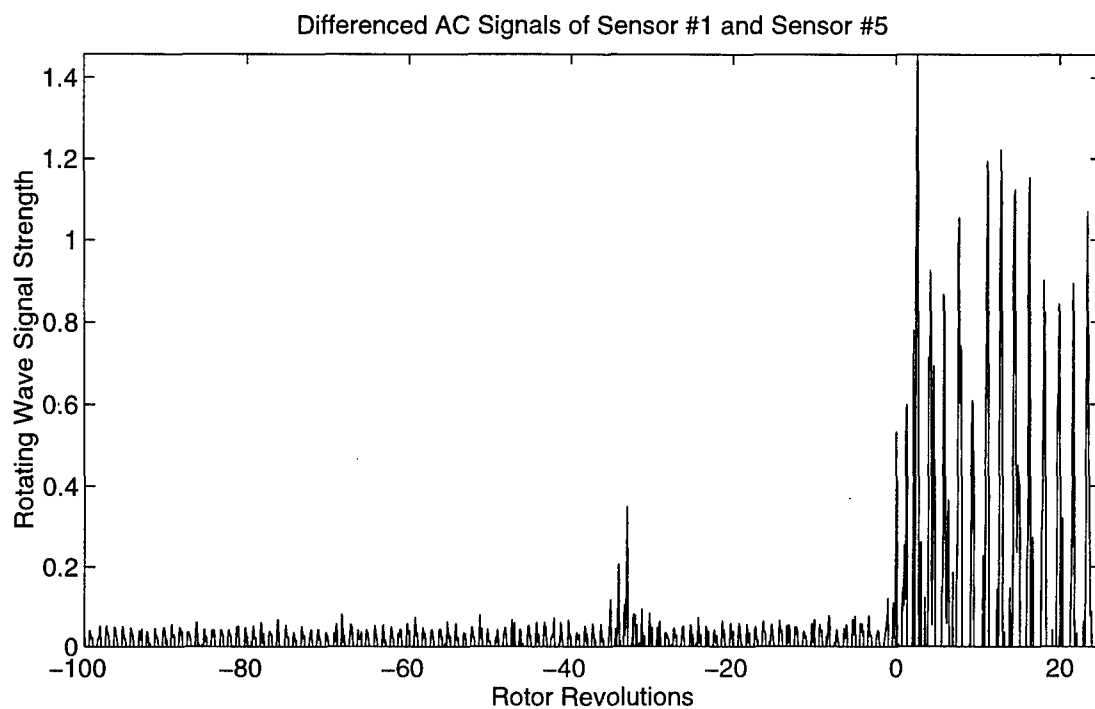
Figure 197. Onset of Rotating Stall and Surge (Case E, 85% Rotor Speed, 185.507 revs/sec)
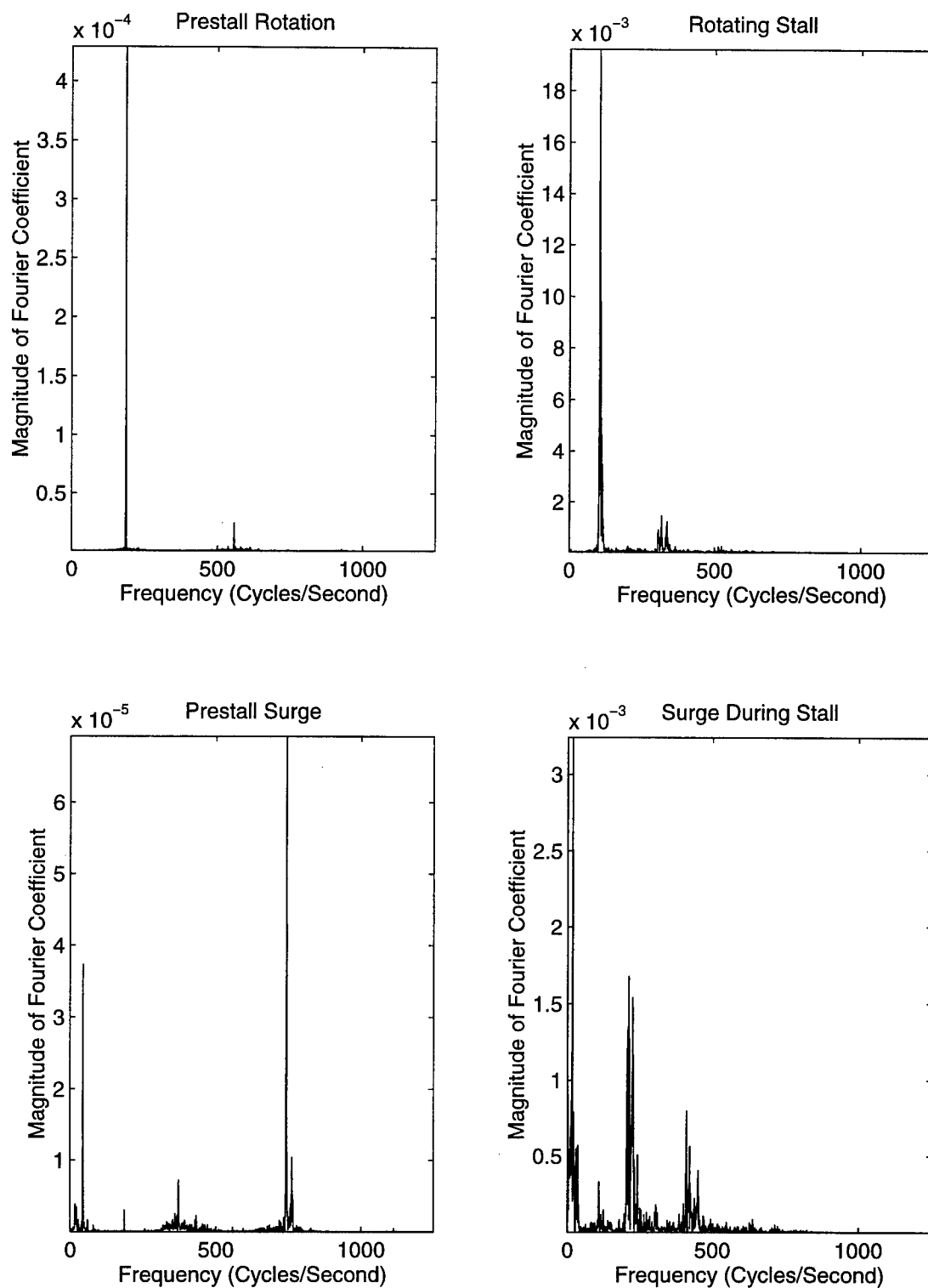
Figure 198. Frequency of Rotating Stall and Surge (Case E, 85% Rotor Speed, 185.507 revs/sec)
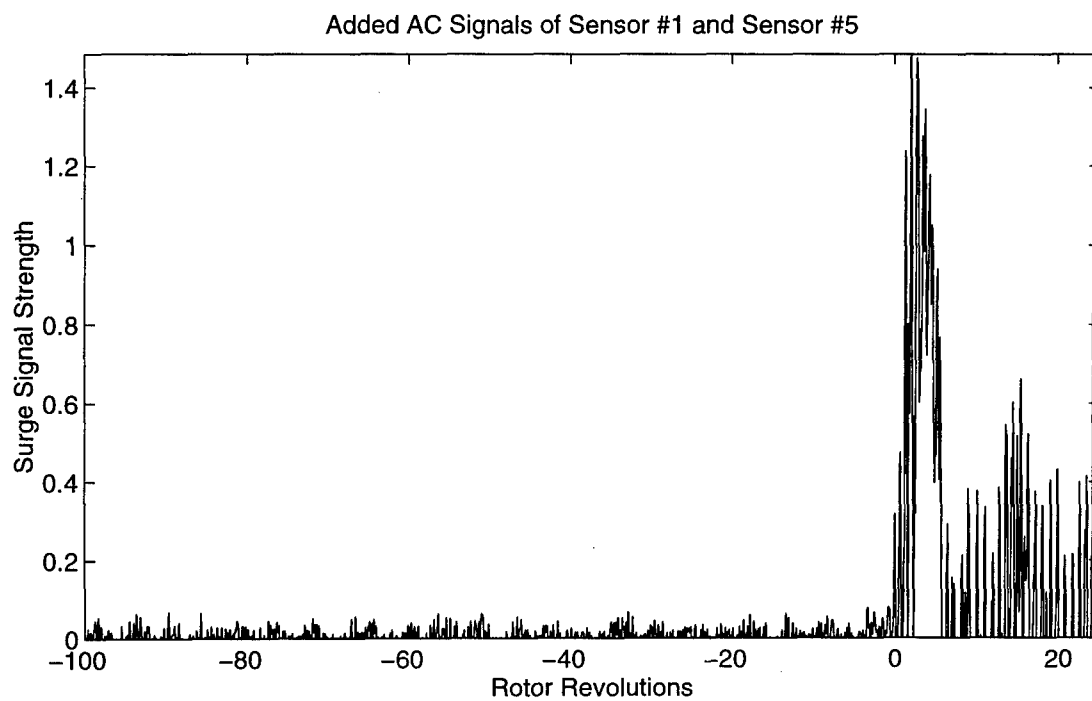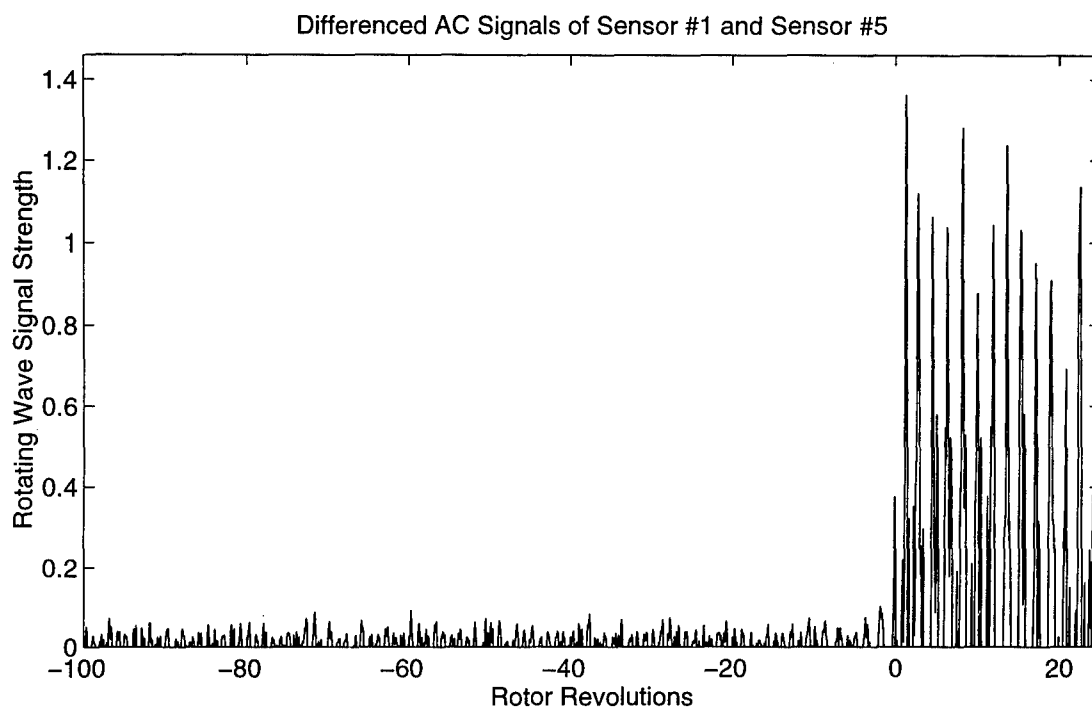
239
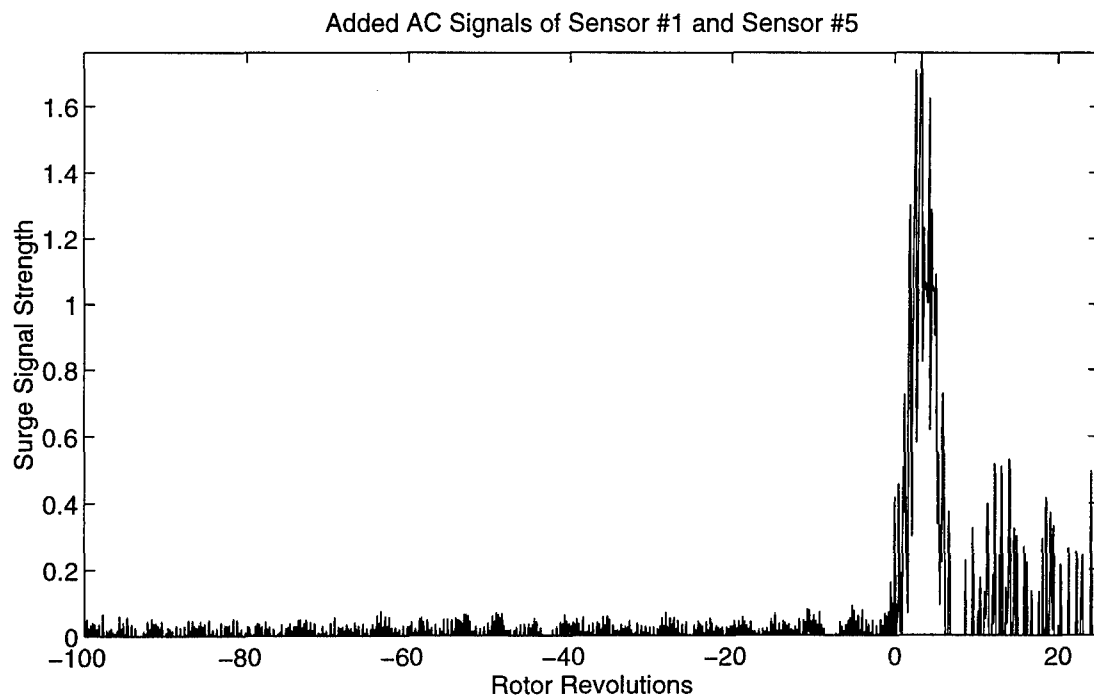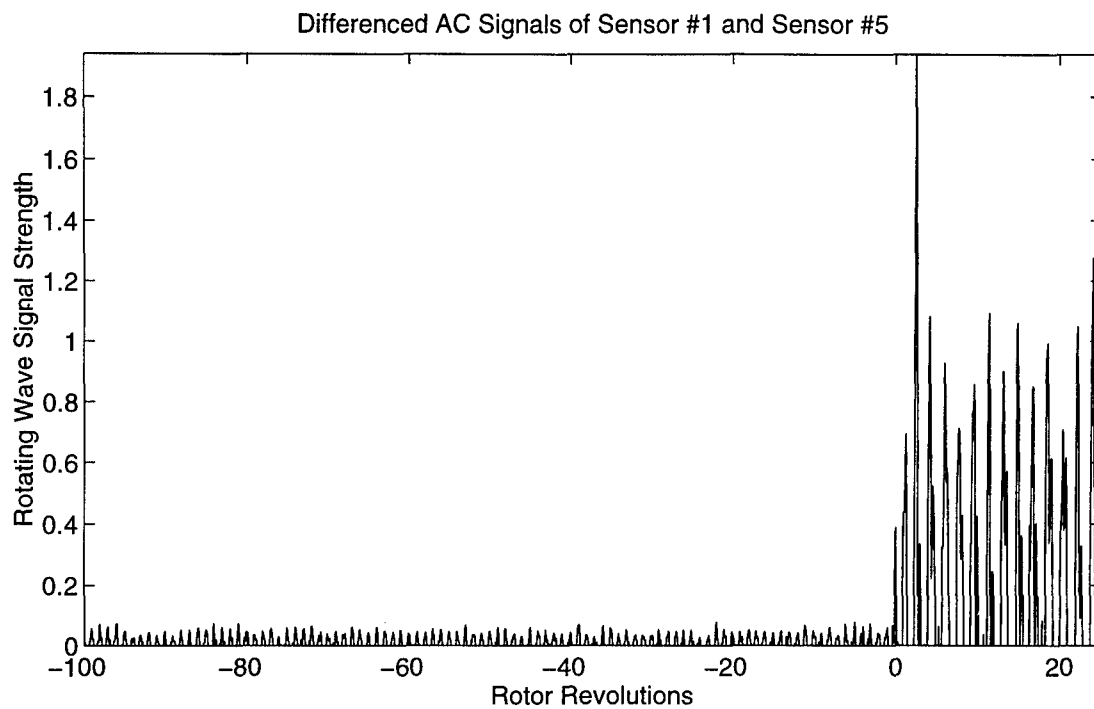
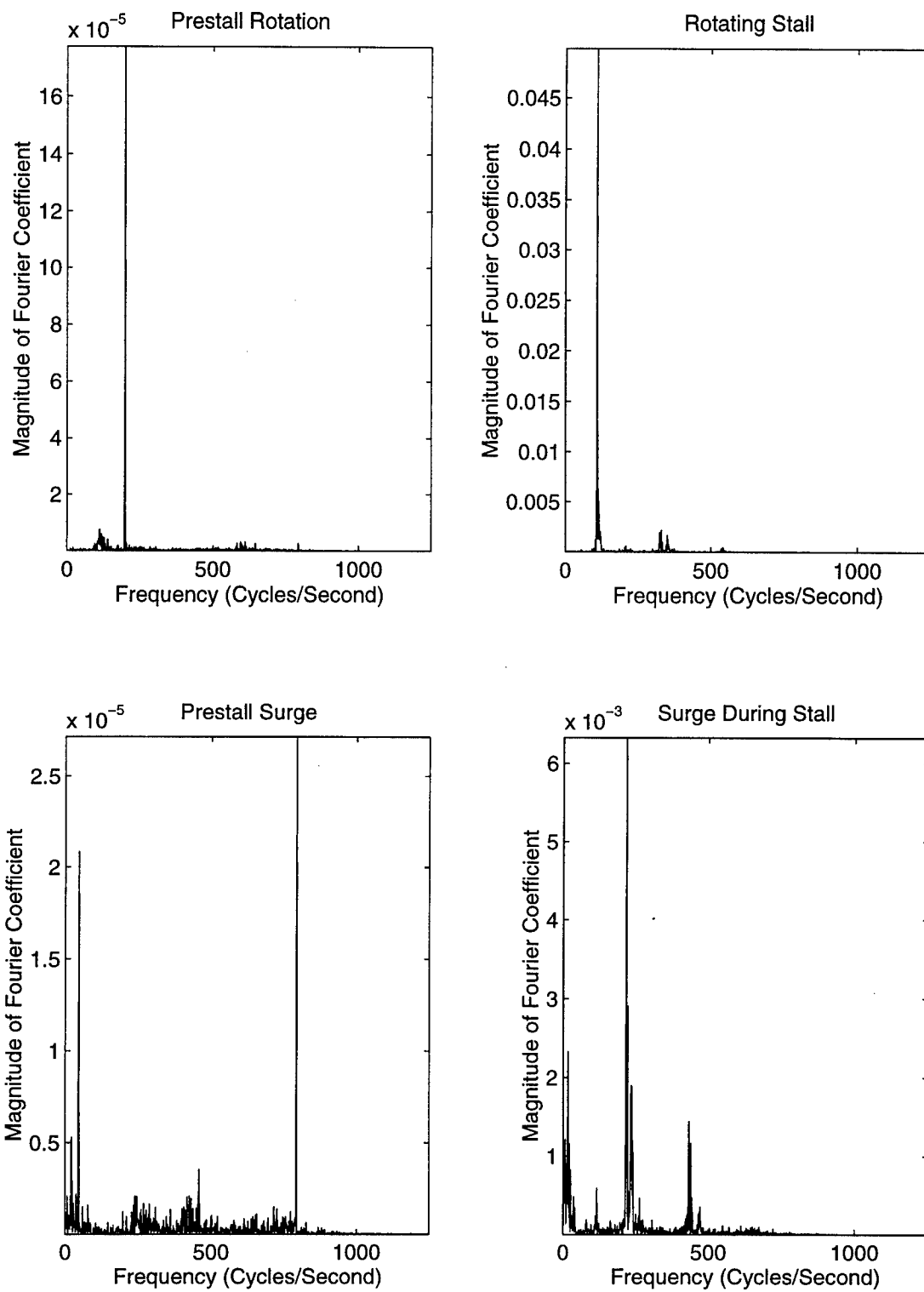Figure 199. Onset of Rotating Stall and Surge (Case E, 90% Rotor Speed, 196.308 revs/sec)
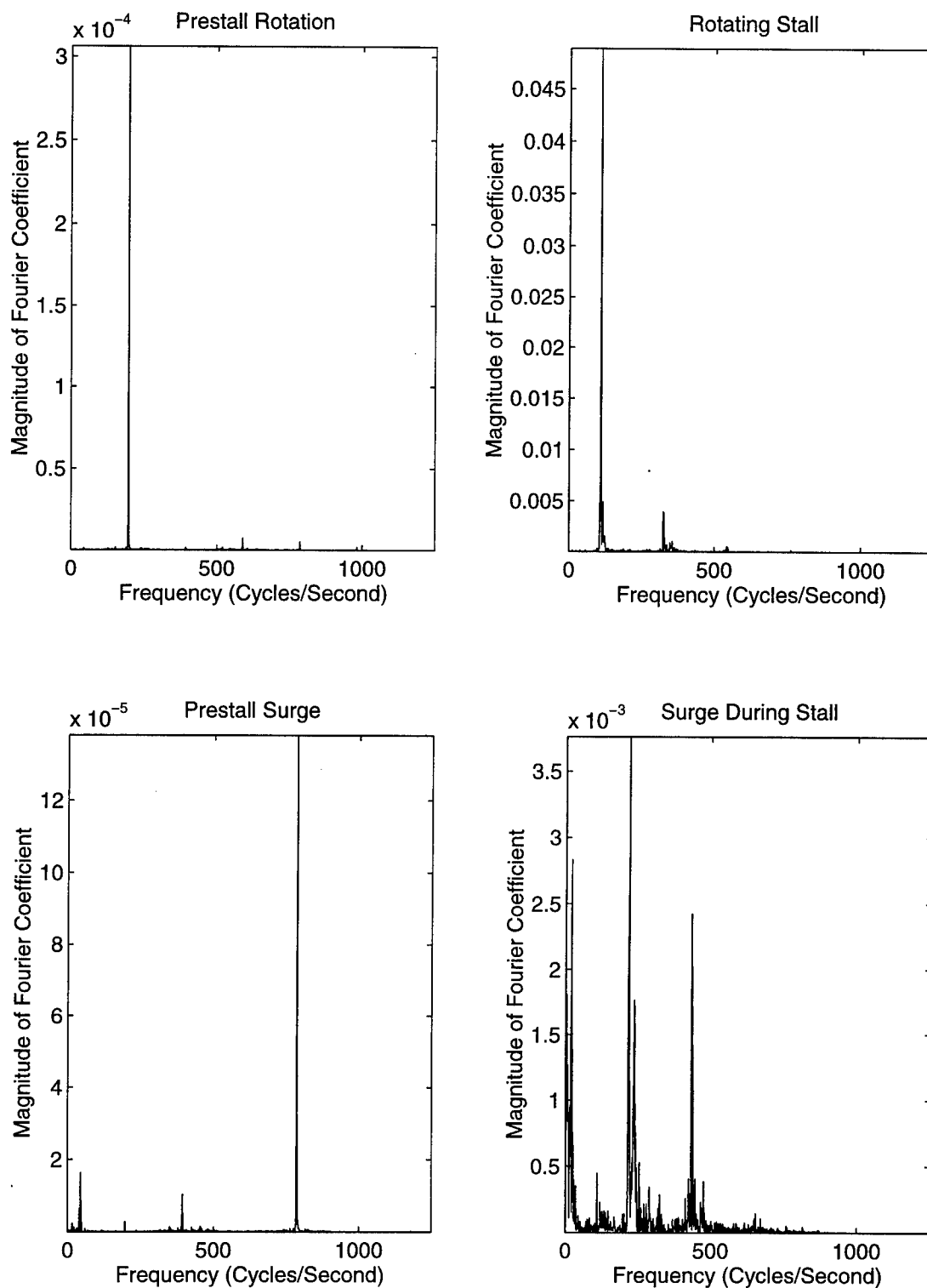
Figure 200. Frequency of Rotating Stall and Surge (Case E, 90% Rotor Speed, 196.308 revs/sec)
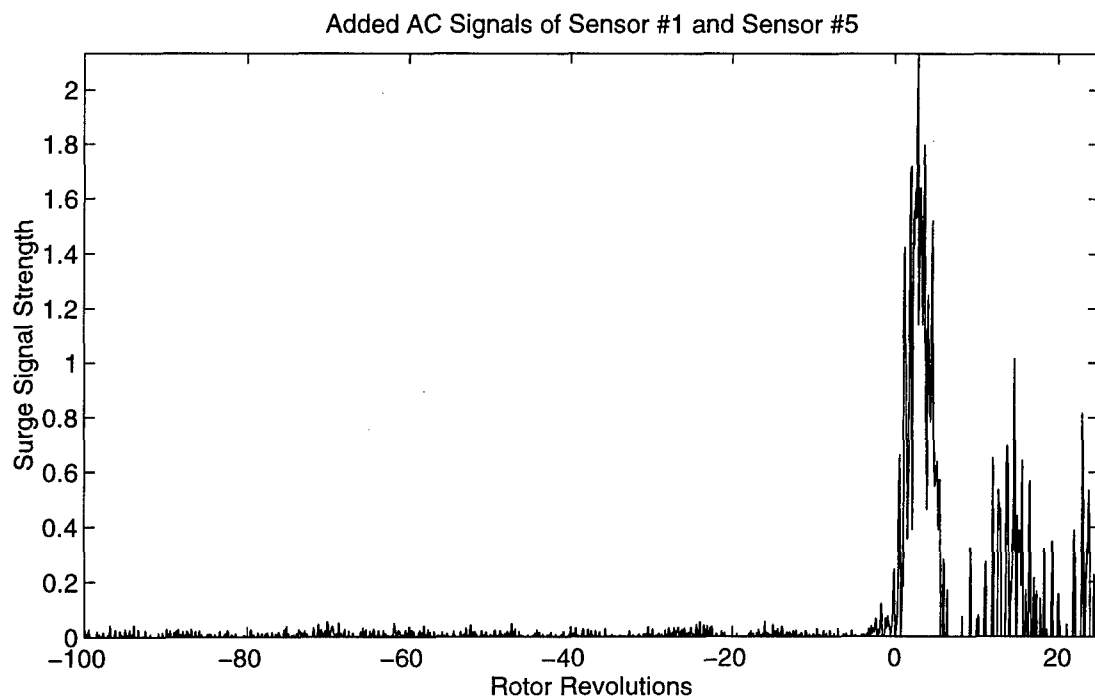
241

Differenced AC Signals of Sensor #1 and Sensor #5

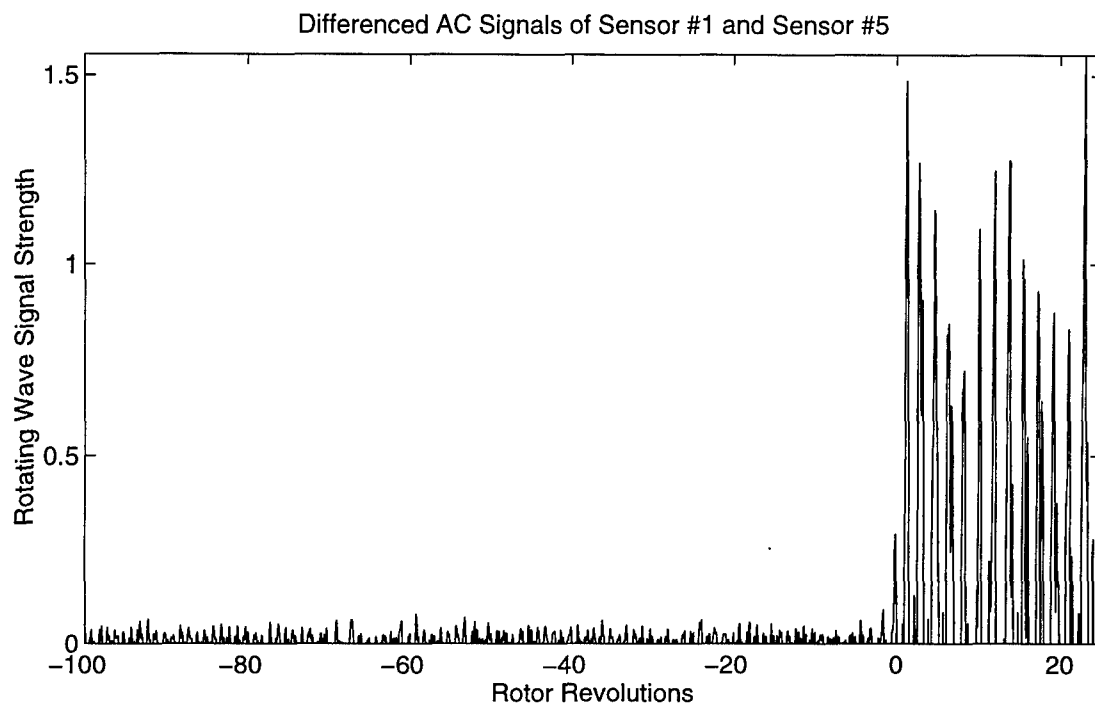Added AC Signals of Sensor #1 and Sensor #5

Figure 201. Onset of Rotating Stall and Surge (Case E, 95% Rotor Speed, 207.391 revs/sec)
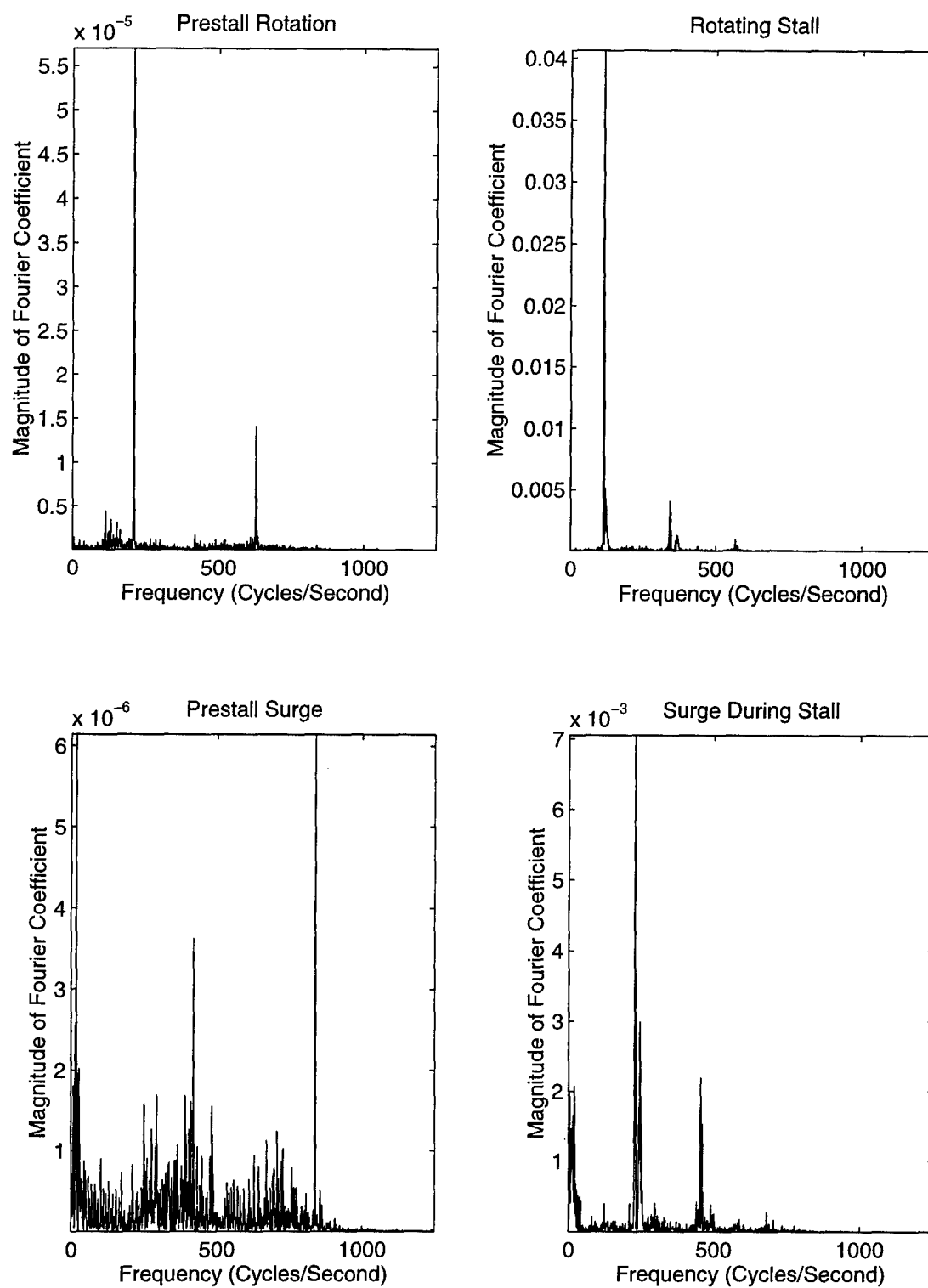
Figure 202. Frequency of Rotating Stall and Surge (Case E, 95% Rotor Speed, 207.391 revs/sec)
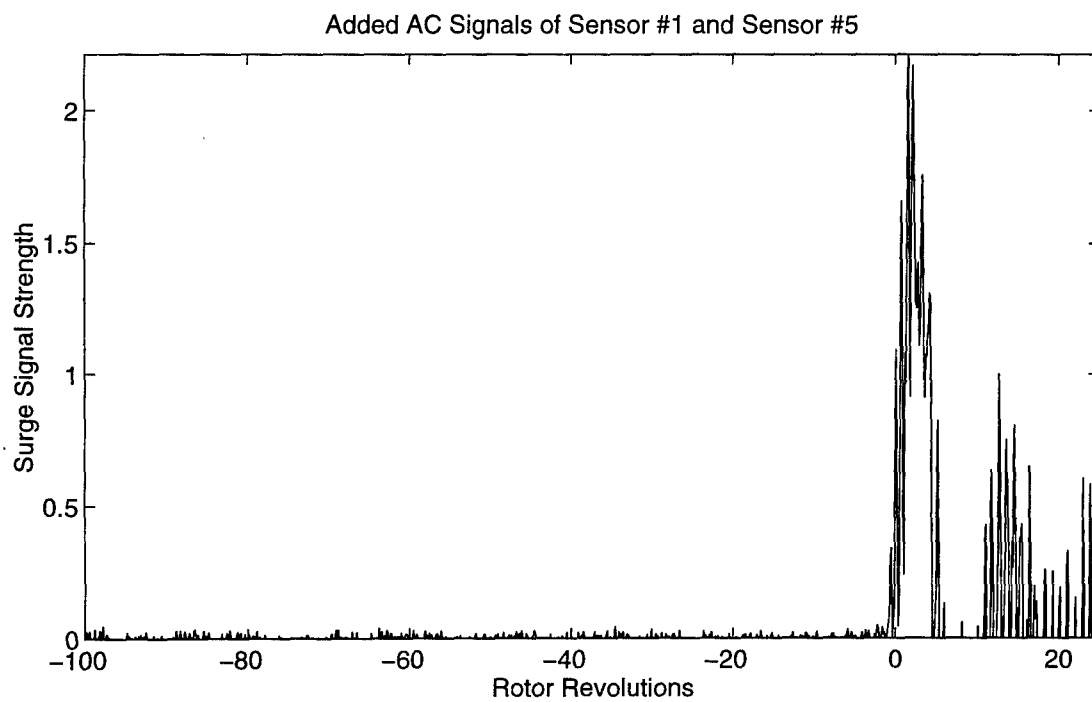
Figure 203. Onset of Rotating Stall and Surge (Case E, 100% Rotor Speed, 218.201 revs/sec)

Figure 204. Frequency of Rotating Stall and Surge (Case E, 100% Rotor Speed, 218.201 revs/sec)
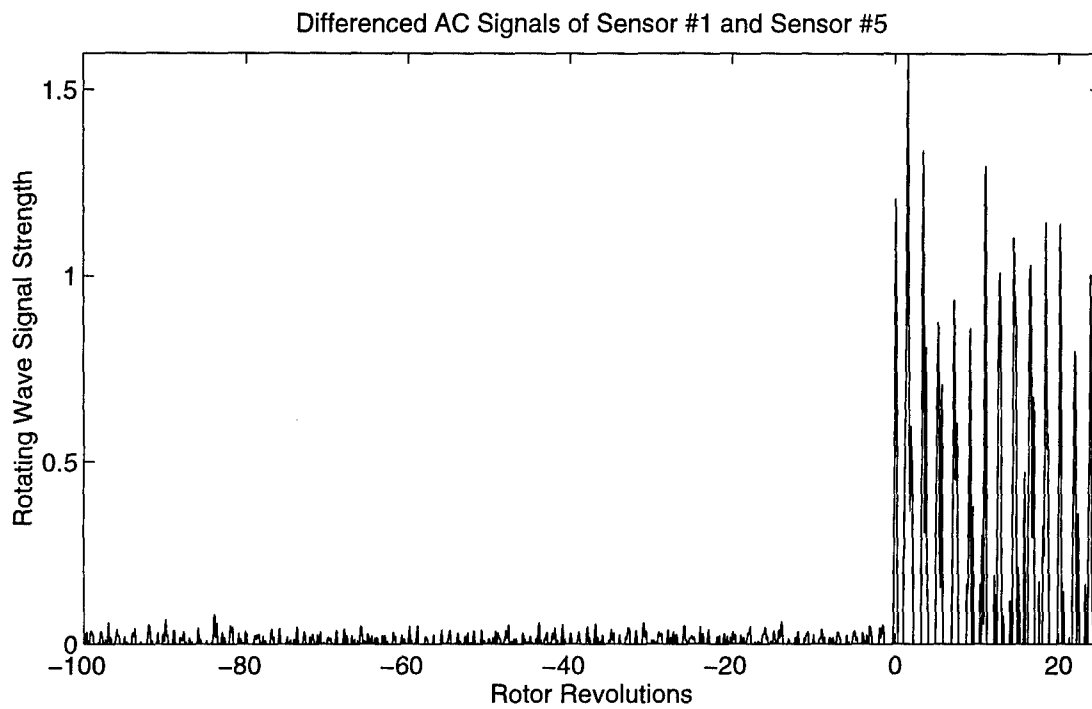
Figure 205. Onset of Rotating Stall and Surge (Case F, 85% Rotor Speed, 185.009 revs/sec)

246

Figure 206. Frequency of Rotating Stall and Surge (Case F, 85% Rotor Speed, 185.009 revs/sec)

247

Differenced AC Signals of Sensor #1 and Sensor #5

Added AC Signals of Sensor #1 and Sensor #5

Figure 207. Onset of Rotating Stall and Surge (Case F, 90% Rotor Speed, 195.966 revs/sec)

Figure 208. Frequency of Rotating Stall and Surge (Case F, 90% Rotor Speed, 195.966 revs/sec)

249

Figure 209. Onset of Rotating Stall and Surge (Case F, 95% Rotor Speed, 206.743 revs/sec)
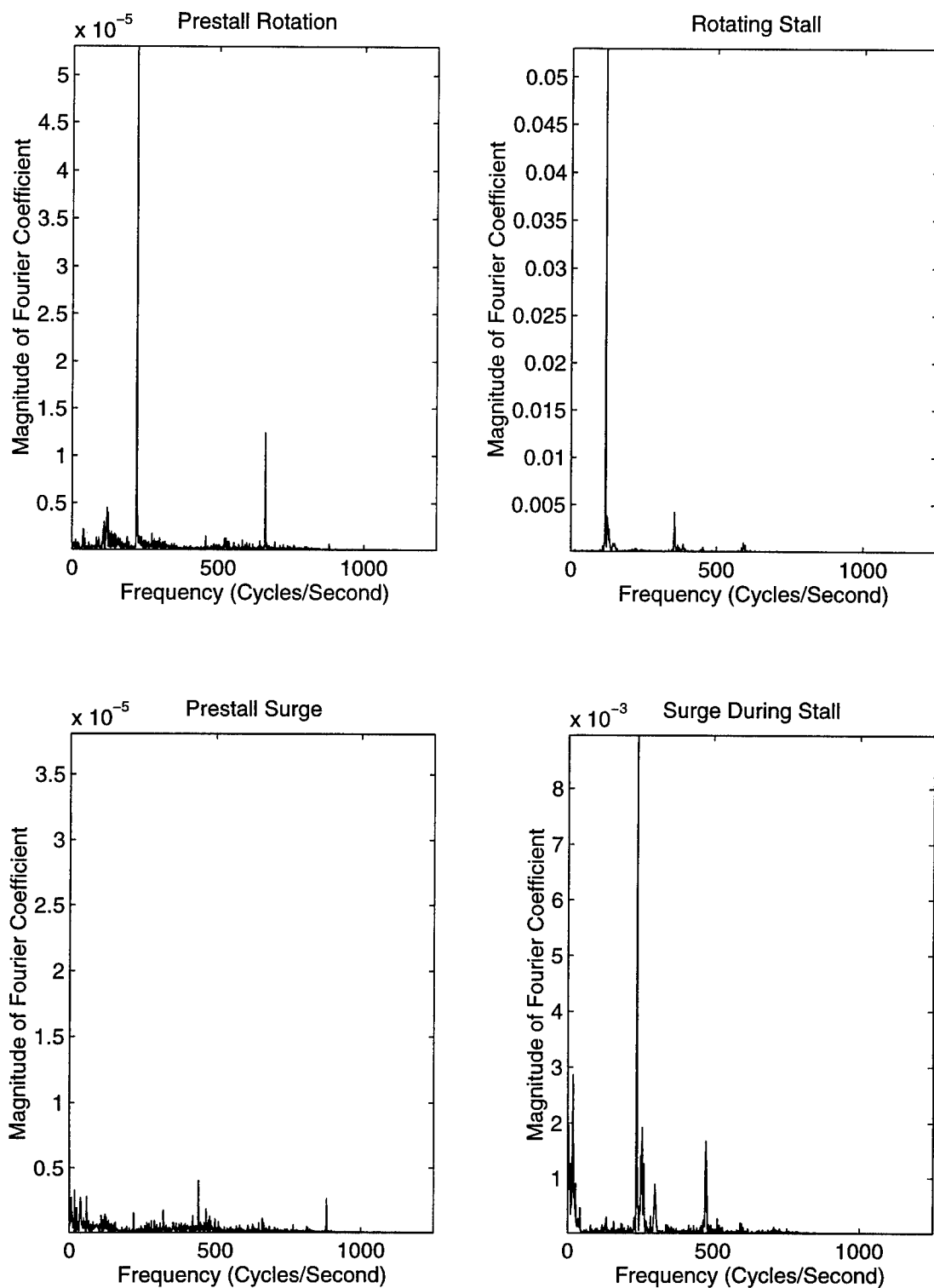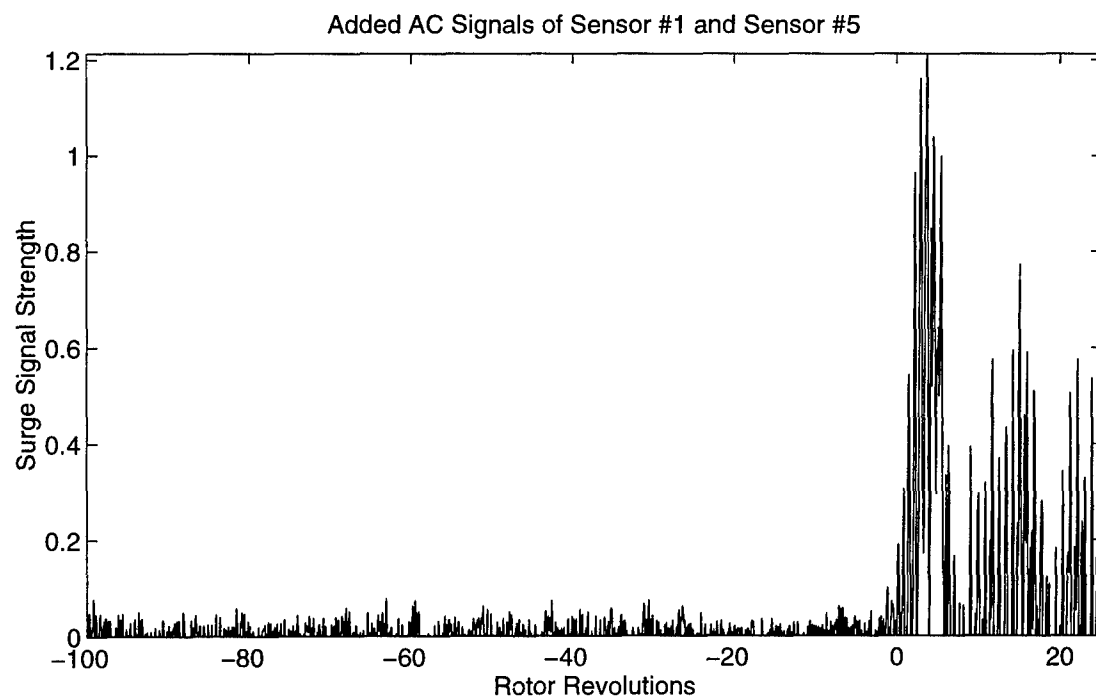
Figure 210. Frequency of Rotating Stall and Surge (Case F, 95% Rotor Speed, 206.743 revs/sec)
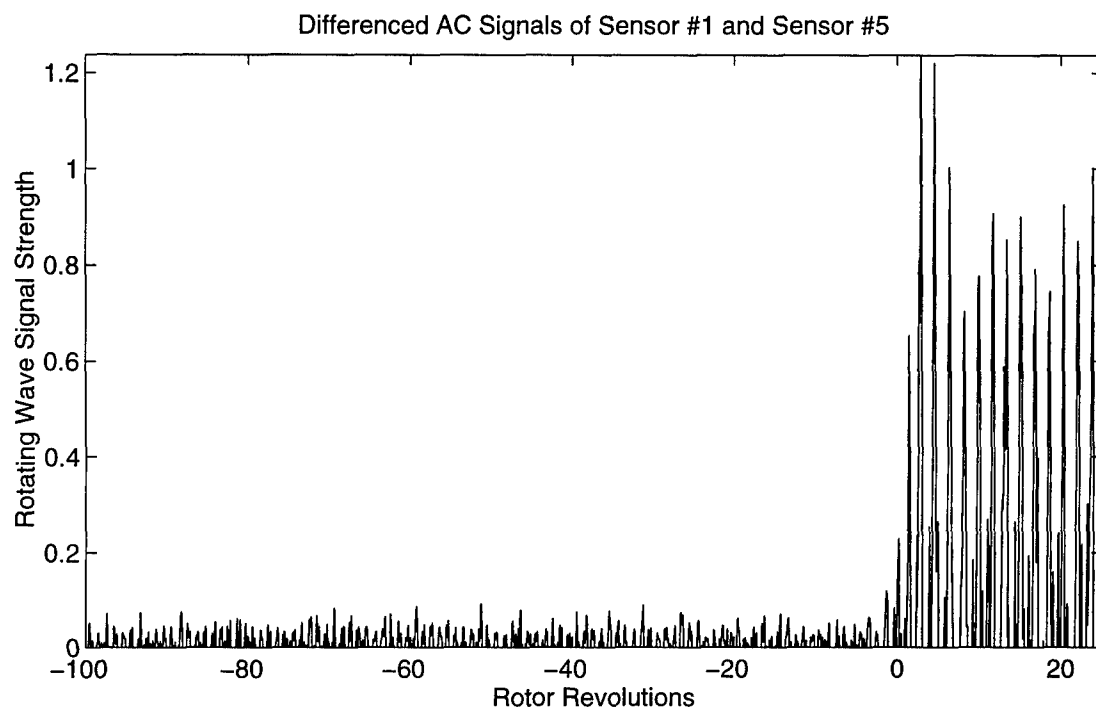
251

Figure 211. Onset of Rotating Stall and Surge (Case F, 100% Rotor Speed, 217.676 revs/sec)

252

Figure 212. Frequency of Rotating Stall and Surge (Case F, 100% Rotor Speed, 217.676 revs/sec)

253

Differenced AC Signals of Sensor #1 and Sensor #5

Added AC Signals of Sensor #1 and Sensor #5

Figure 213. Onset of Rotating Stall and Surge (Case G, 85% Rotor Speed, 187.355 revs/sec)
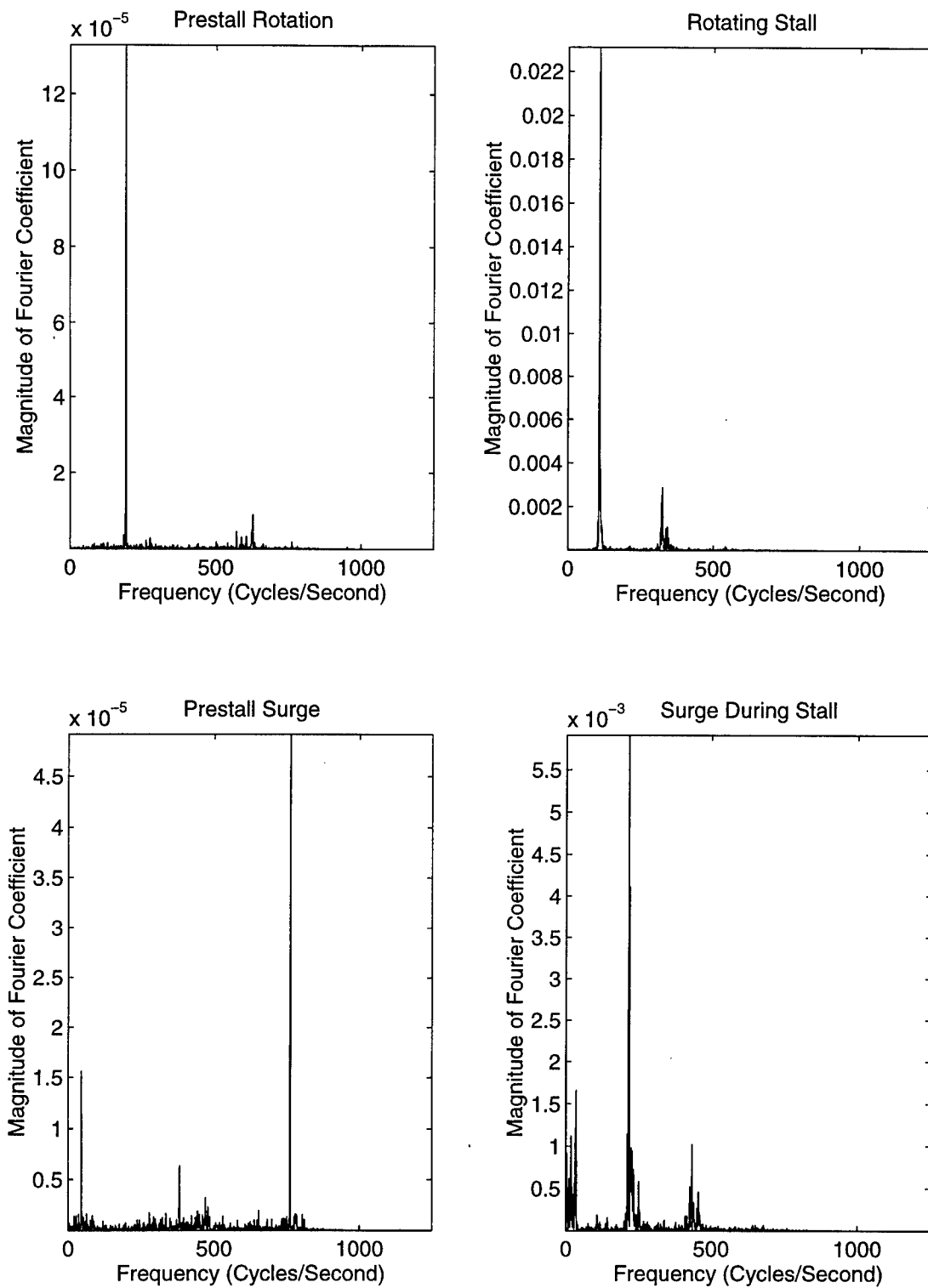
254

Figure 214. Frequency of Rotating Stall and Surge (Case G, 85% Rotor Speed, 187.355 revs/sec)
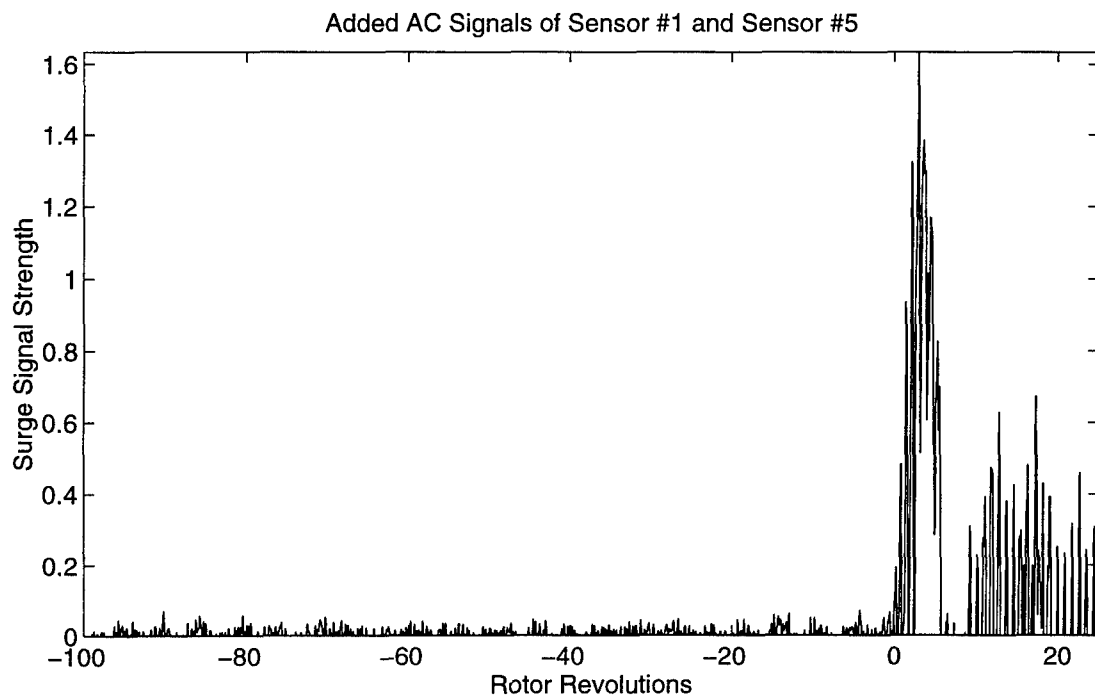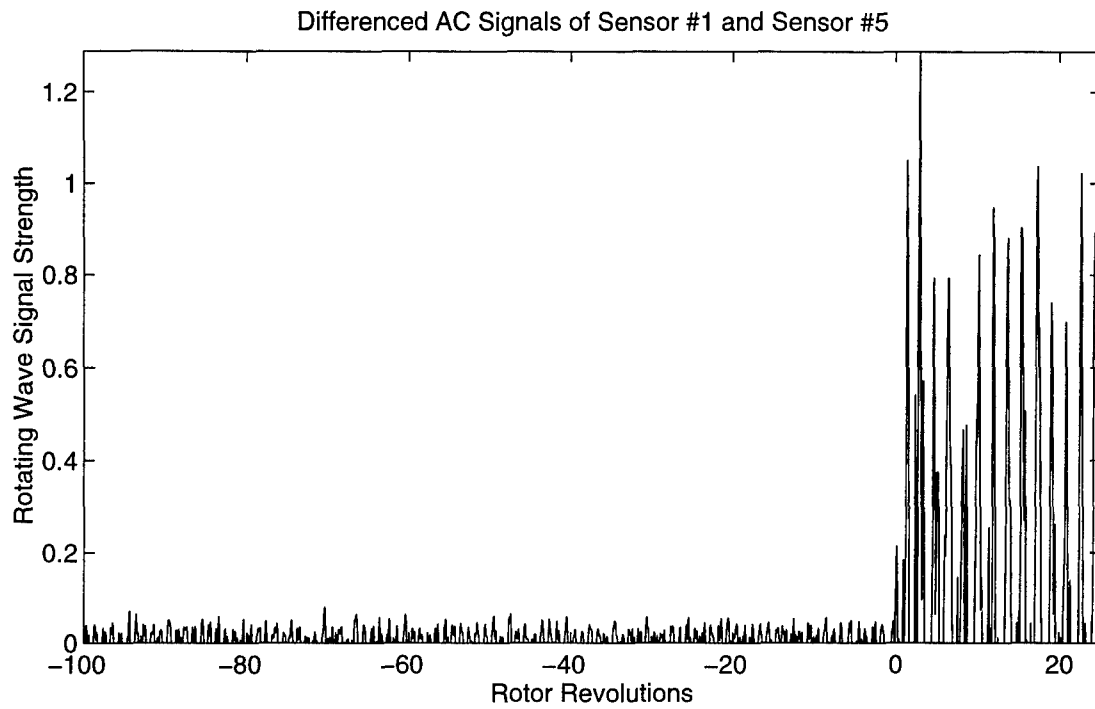
255

Figure 215. Onset of Rotating Stall and Surge (Case G, 90% Rotor Speed, 198.133 revs/sec)

Figure 216. Frequency of Rotating Stall and Surge (Case G, 90% Rotor Speed, 198.133 revs/sec)

257

Differenced AC Signals of Sensor #1 and Sensor #5

Added AC Signals of Sensor #1 and Sensor #5

Figure 217. Onset of Rotating Stall and Surge (Case G, 95% Rotor Speed, 209.253 revs/sec)

258

Figure 218. Frequency of Rotating Stall and Surge (Case G, 95% Rotor Speed, 209.253 revs/sec)

259

Figure 219. Onset of Rotating Stall and Surge (Case G, 100% Rotor Speed, 220.300 revs/sec)
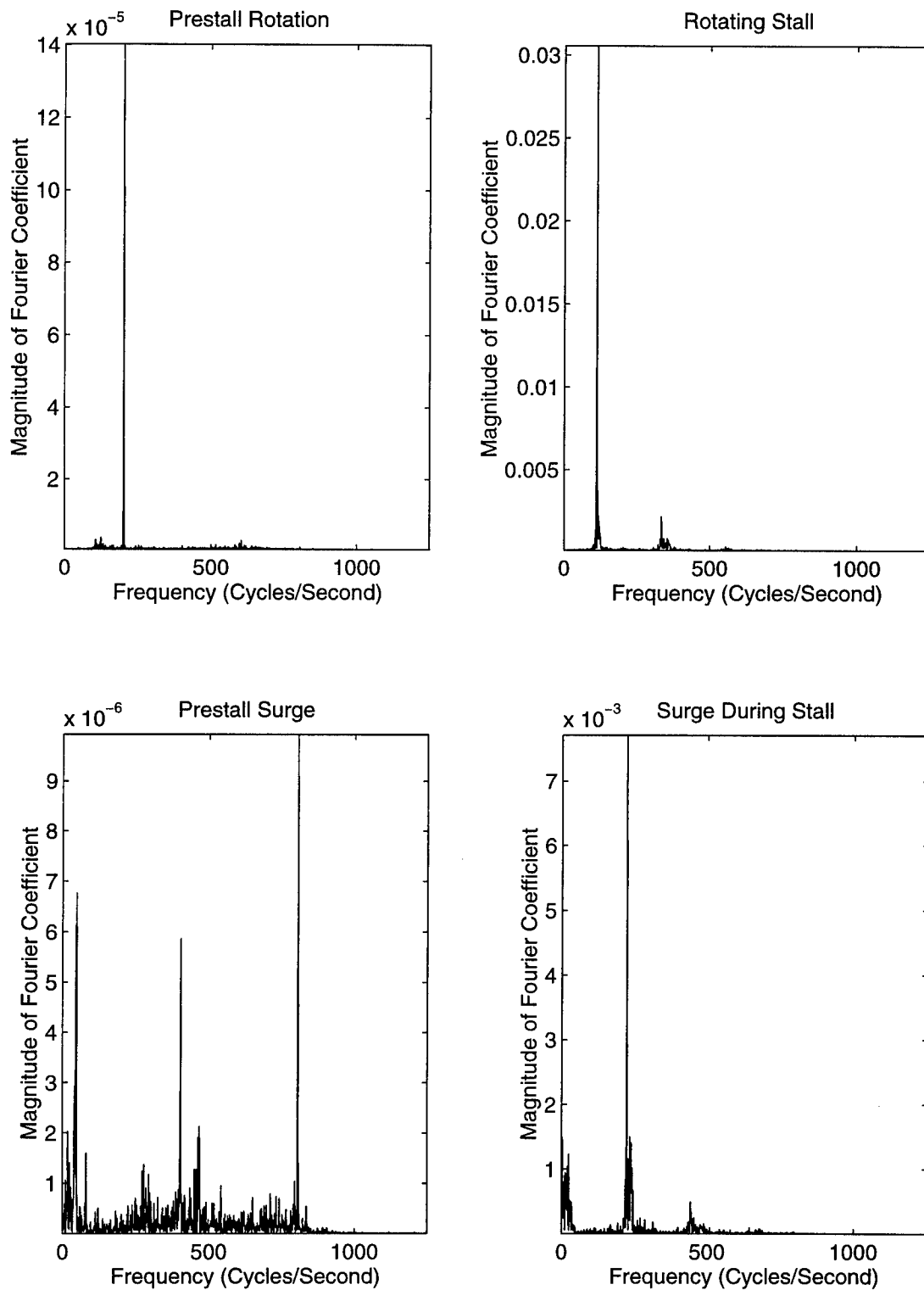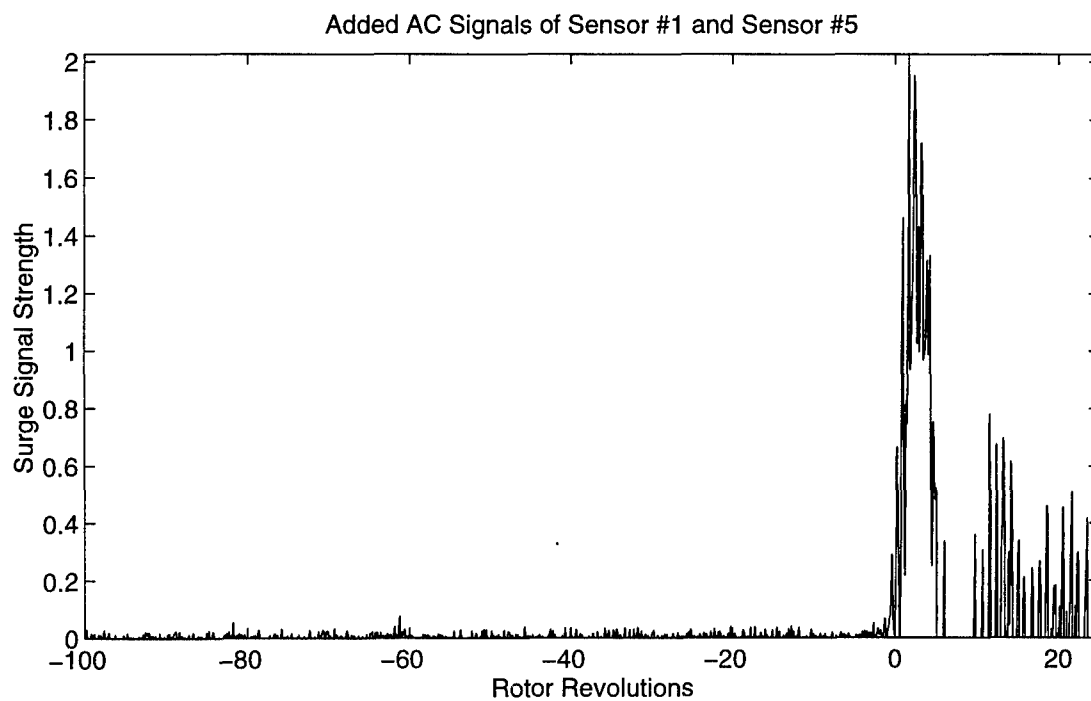
260

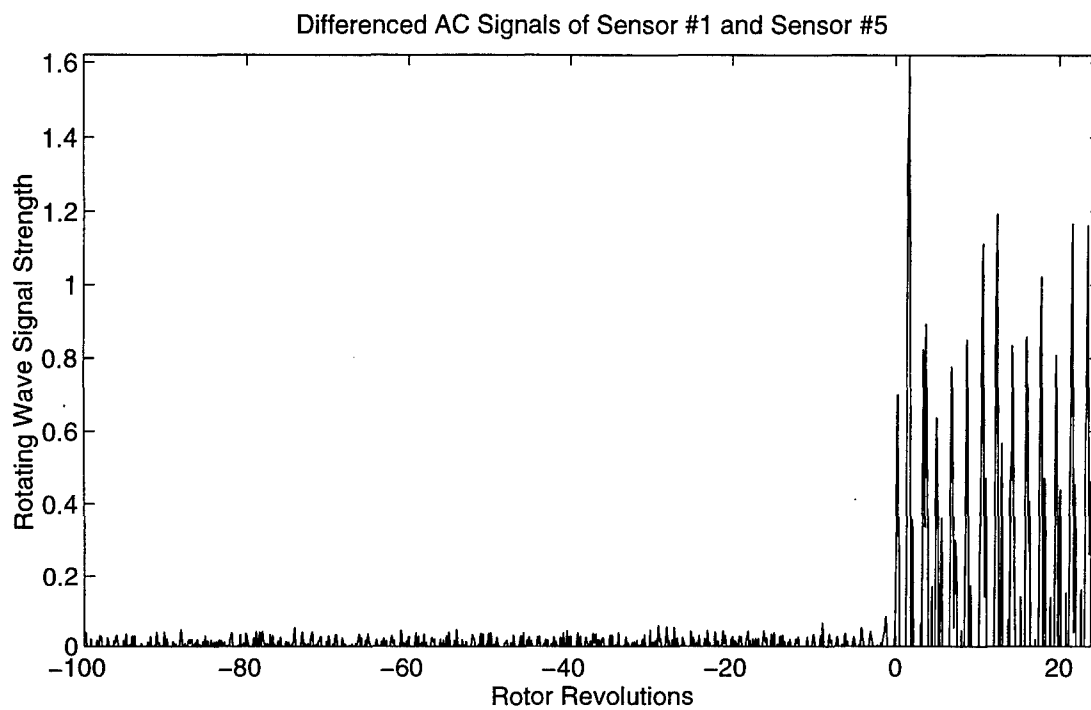Figure 220. Frequency of Rotating Stall and Surge (Case G, 100% Rotor Speed, 220.300 revs/sec)

Figure 221. Onset of Rotating Stall and Surge (Case H, 85% Rotor Speed, 190.102 revs/sec)

262

Figure 222. Frequency of Rotating Stall and Surge (Case H, 85% Rotor Speed, 190.102 revs/sec)

263

Figure 223. Onset of Rotating Stall and Surge (Case H, 90% Rotor Speed, 201.204 revs/sec)

Figure 224. Frequency of Rotating Stall and Surge (Case H, 90% Rotor Speed, 201.204 revs/sec)

Figure 225. Onset of Rotating Stall and Surge (Case H, 95% Rotor Speed, 212.555 revs/sec)
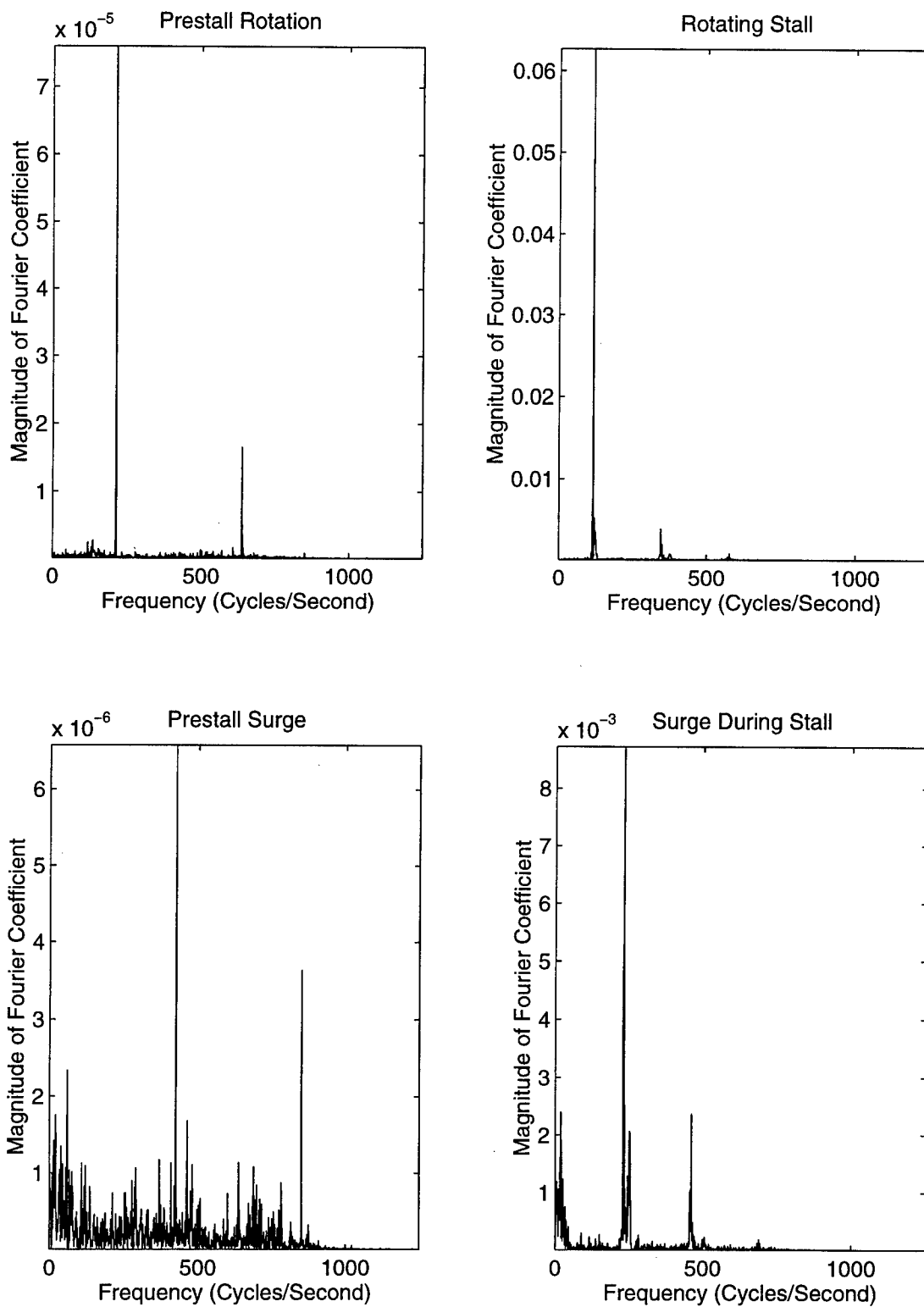
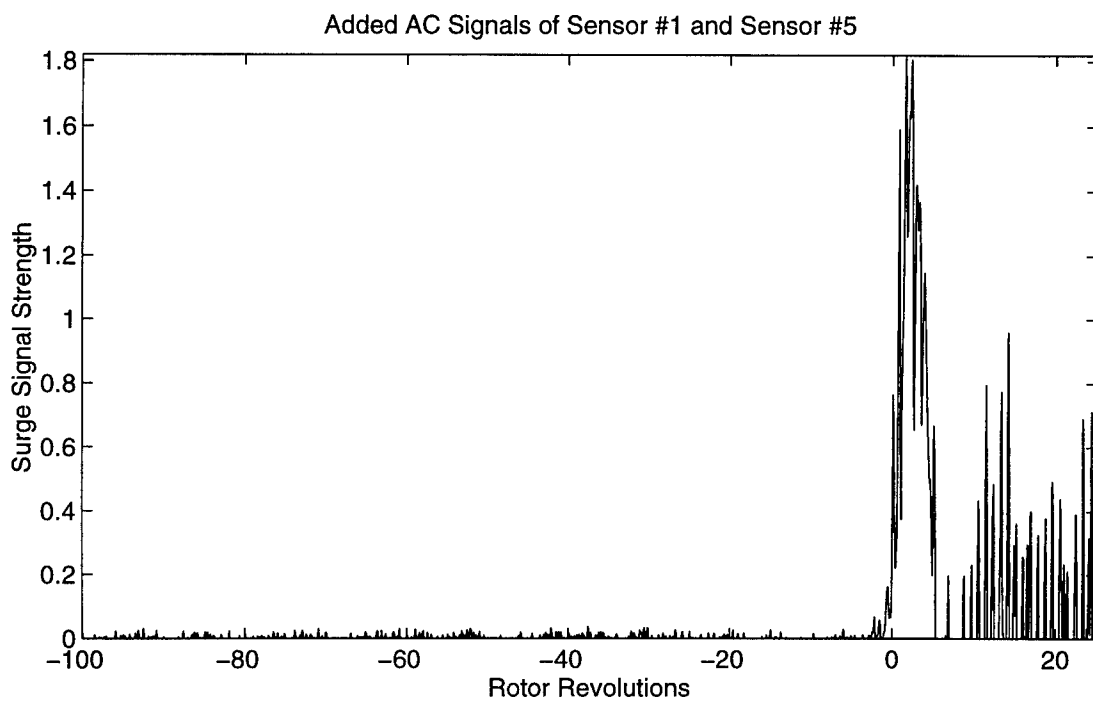Figure 226. Frequency of Rotating Stall and Surge (Case H, 95% Rotor Speed, 212.555 revs/sec)
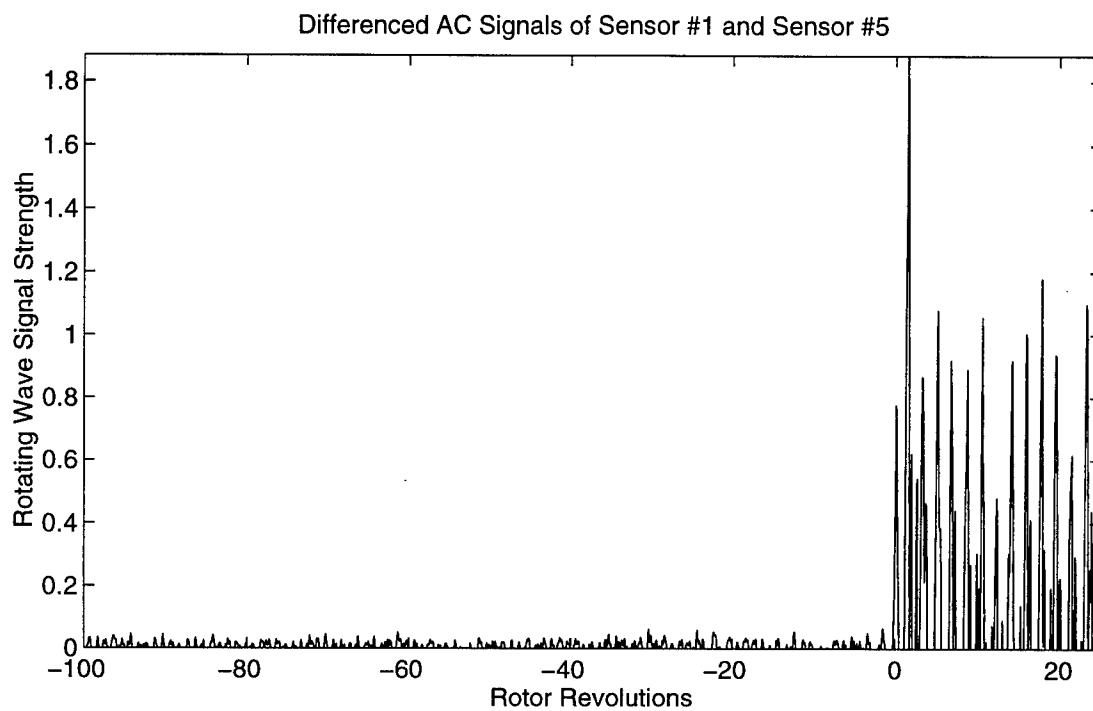
Figure 227. Onset of Rotating Stall and Surge (Case H, 100% Rotor Speed, 223.569 revs/sec)
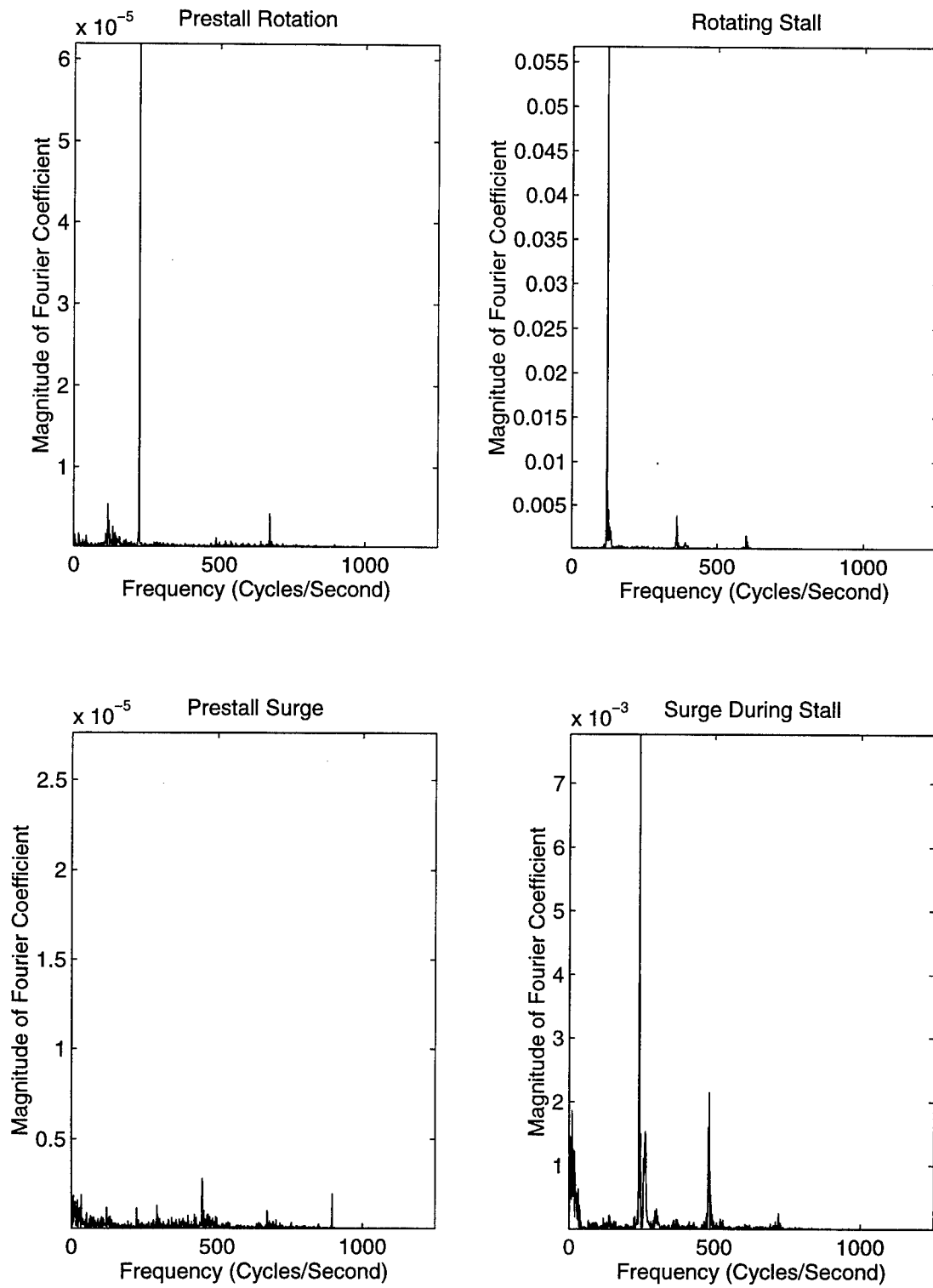
Figure 228. Frequency of Rotating Stall and Surge (Case H, 100% Rotor Speed, 223.569 revs/sec)

Differenced AC Signals of Sensor #1 and Sensor #5

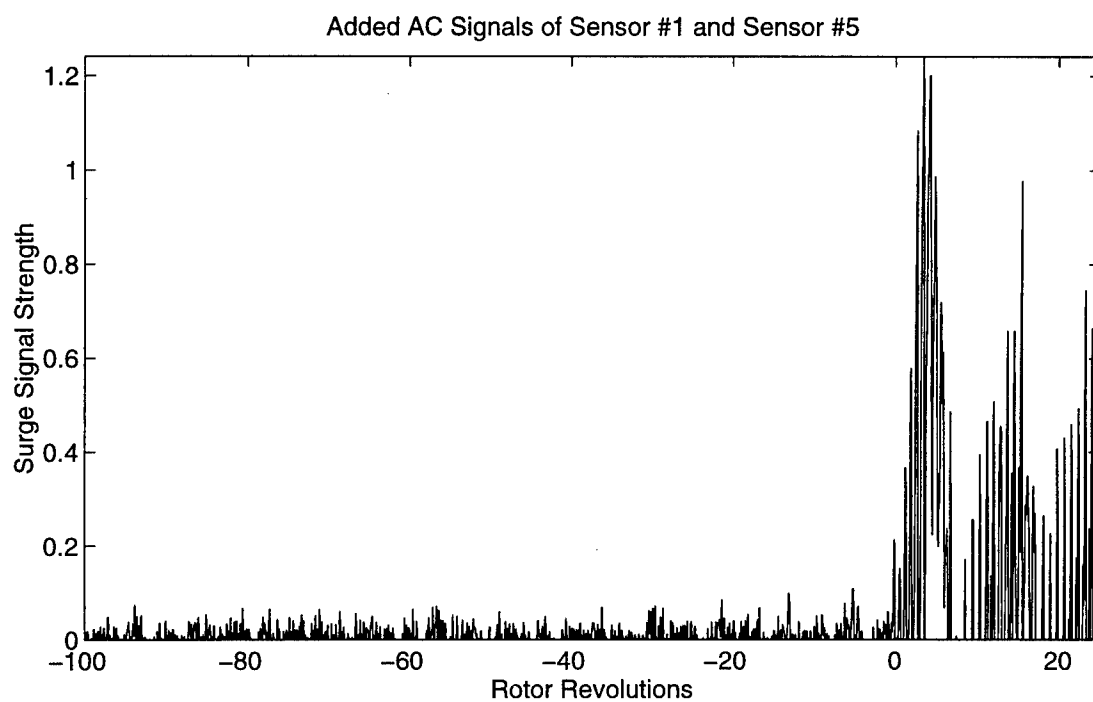

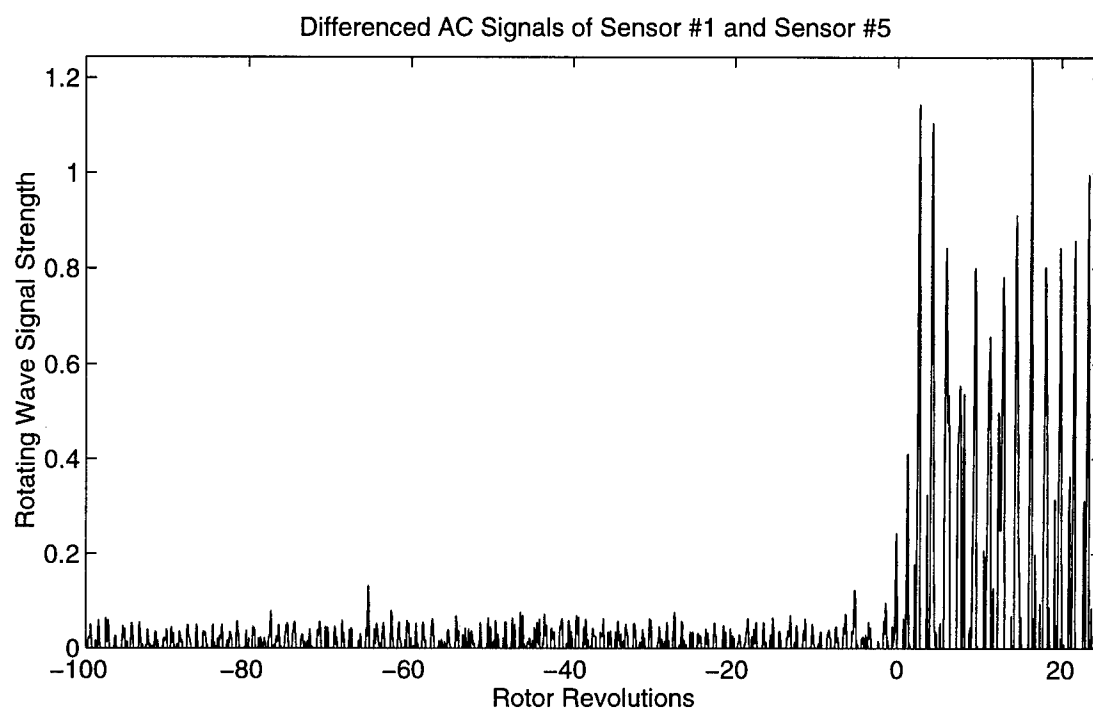Added AC Signals of Sensor #1 and Sensor #5

Figure 229. Onset of Rotating Stall and Surge (Case I, 85% Rotor Speed, 187.603 revs/sec)
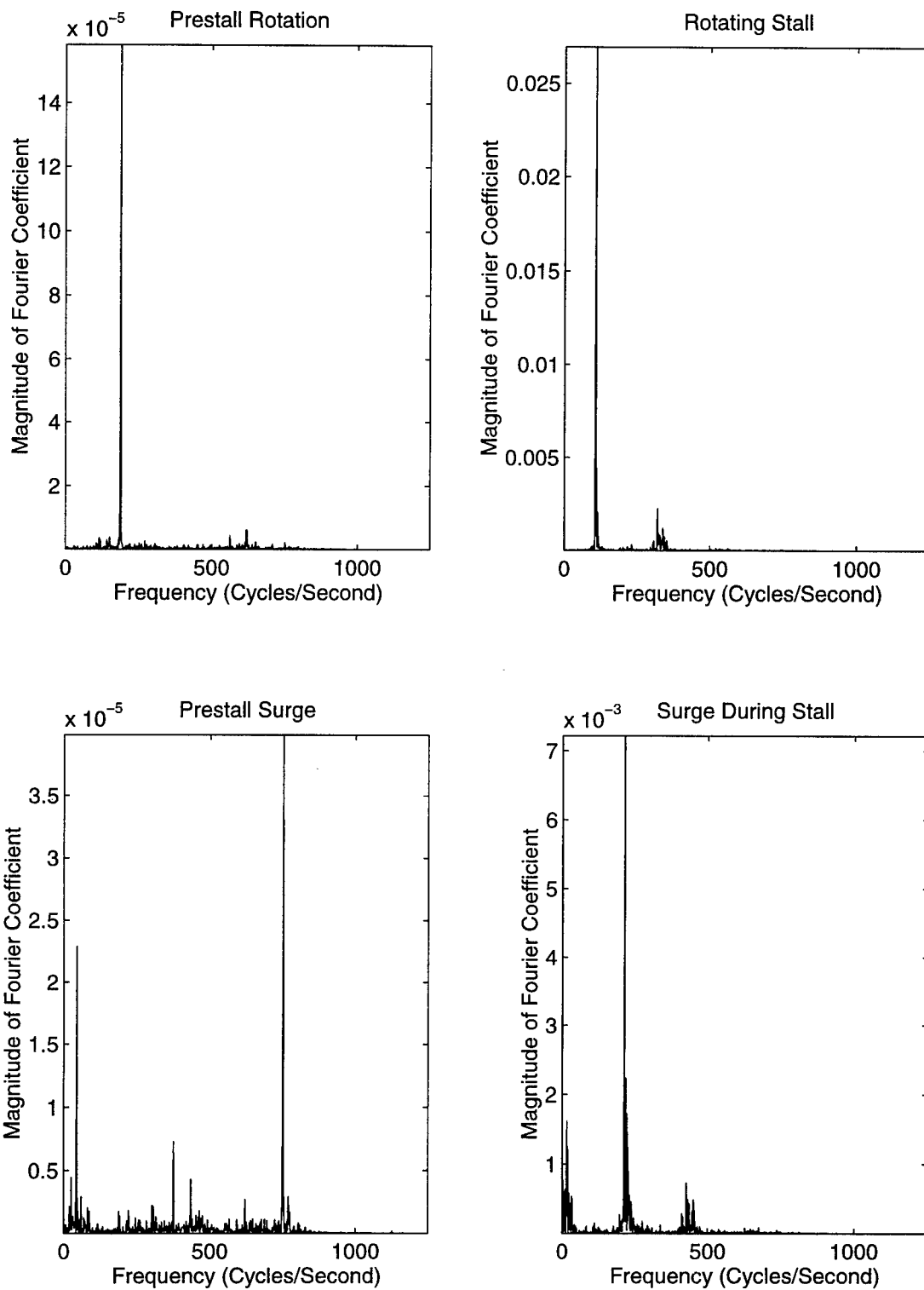
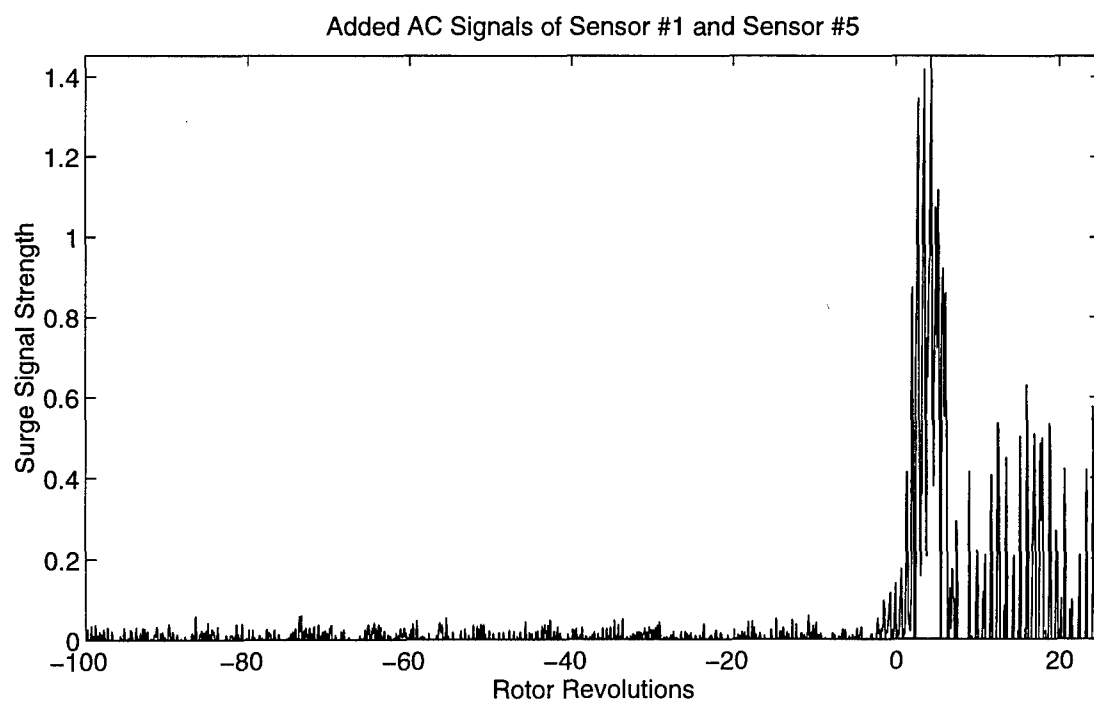Figure 230. Frequency of Rotating Stall and Surge (Case I, 85% Rotor Speed, 187.603 revs/sec)
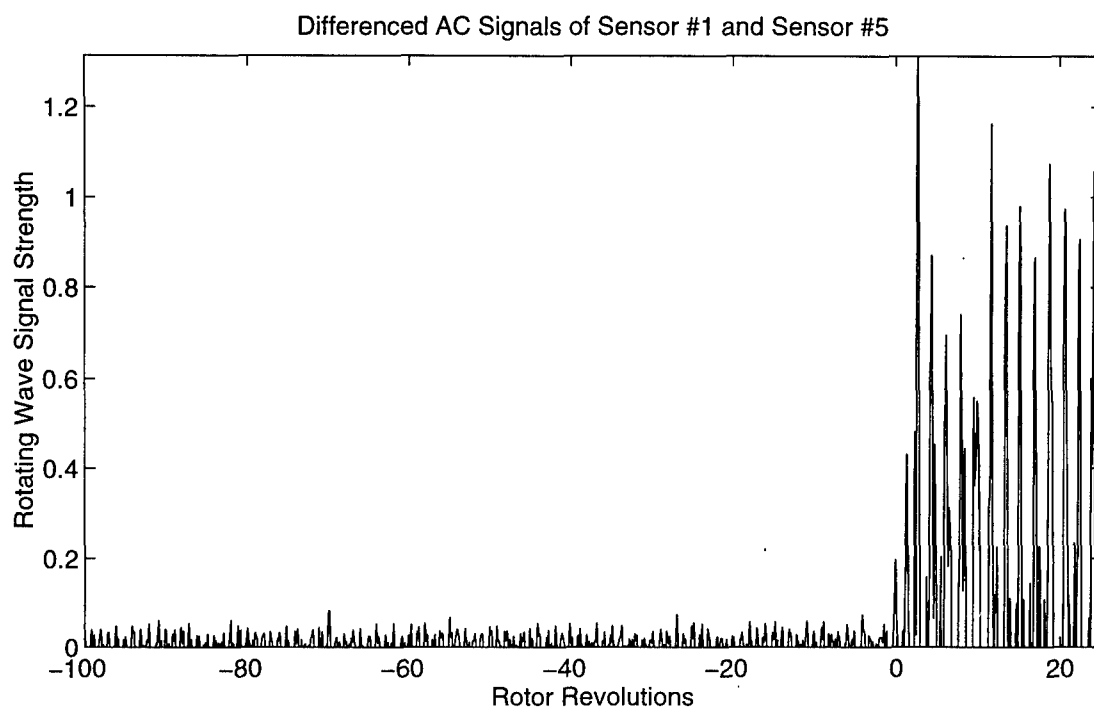
Figure 231. Onset of Rotating Stall and Surge (Case I, 90% Rotor Speed, 199.264 revs/sec)

Figure 232. Frequency of Rotating Stall and Surge (Case I, 90% Rotor Speed, 199.264 revs/sec)

273

Figure 233. Onset of Rotating Stall and Surge (Case I, 95% Rotor Speed, 209.918 revs/sec)
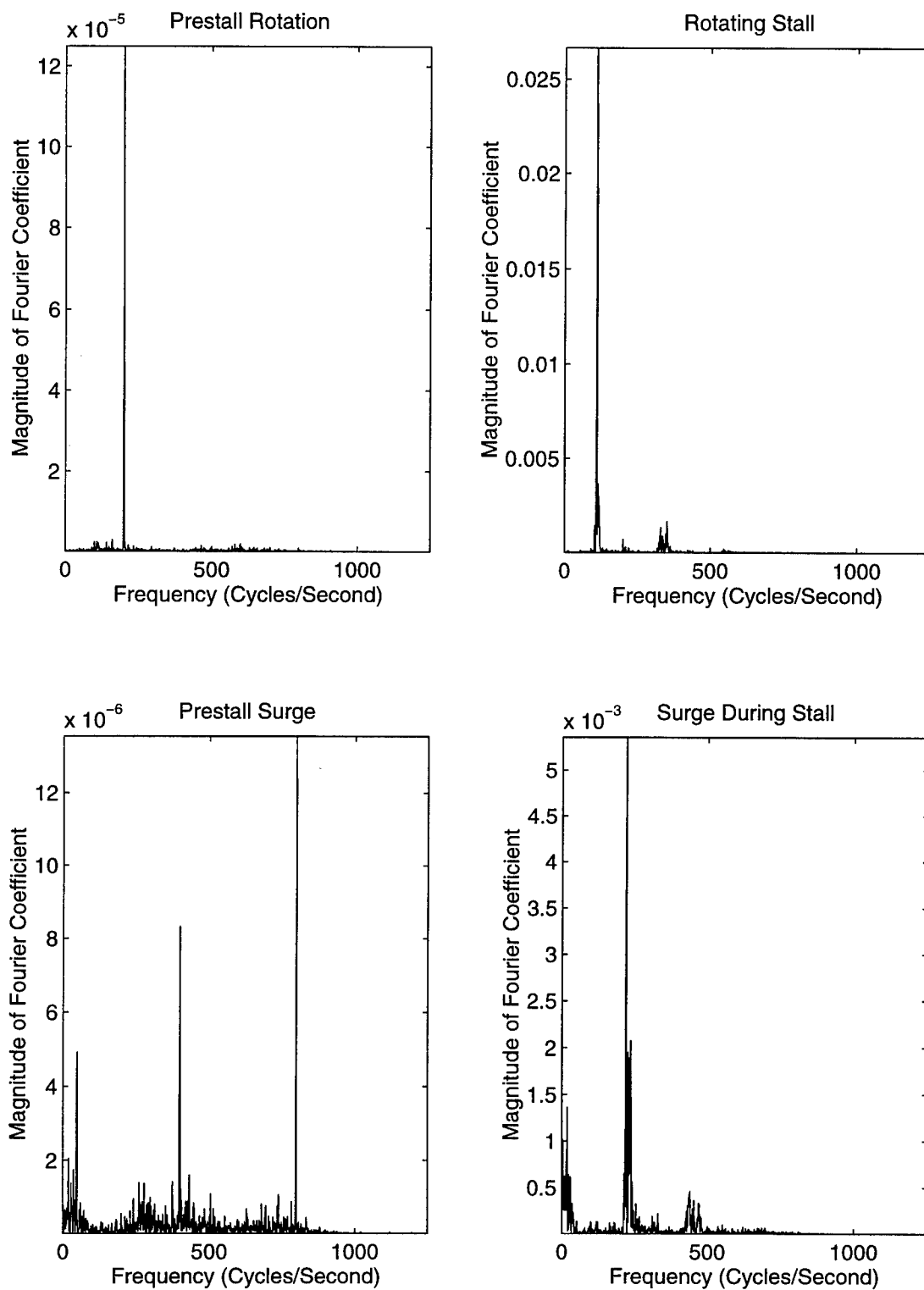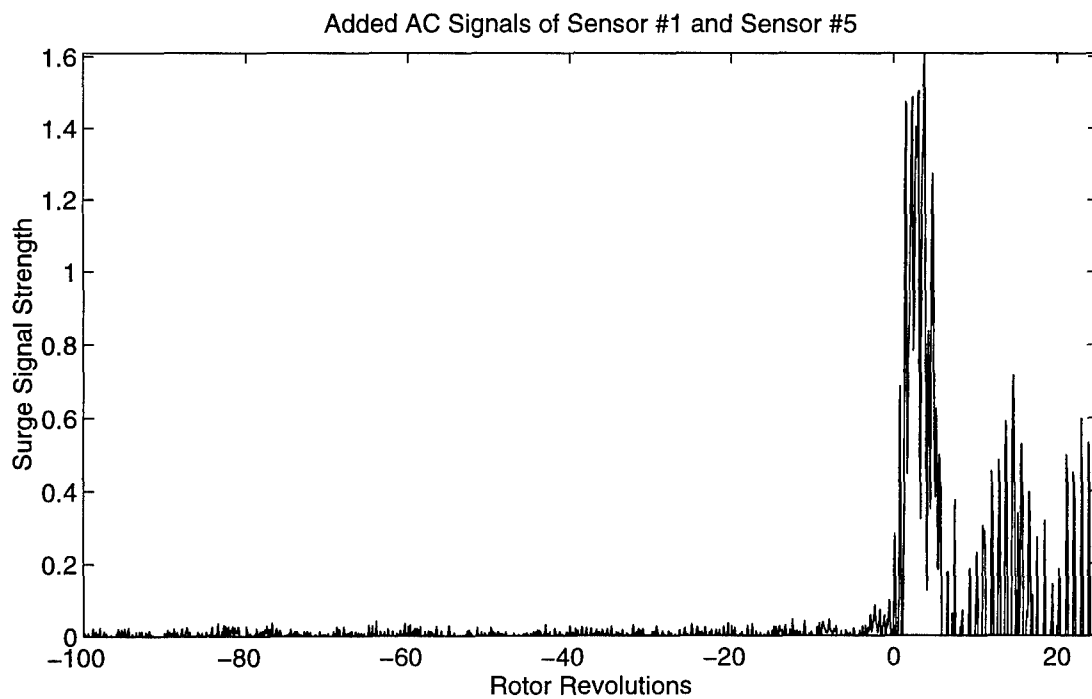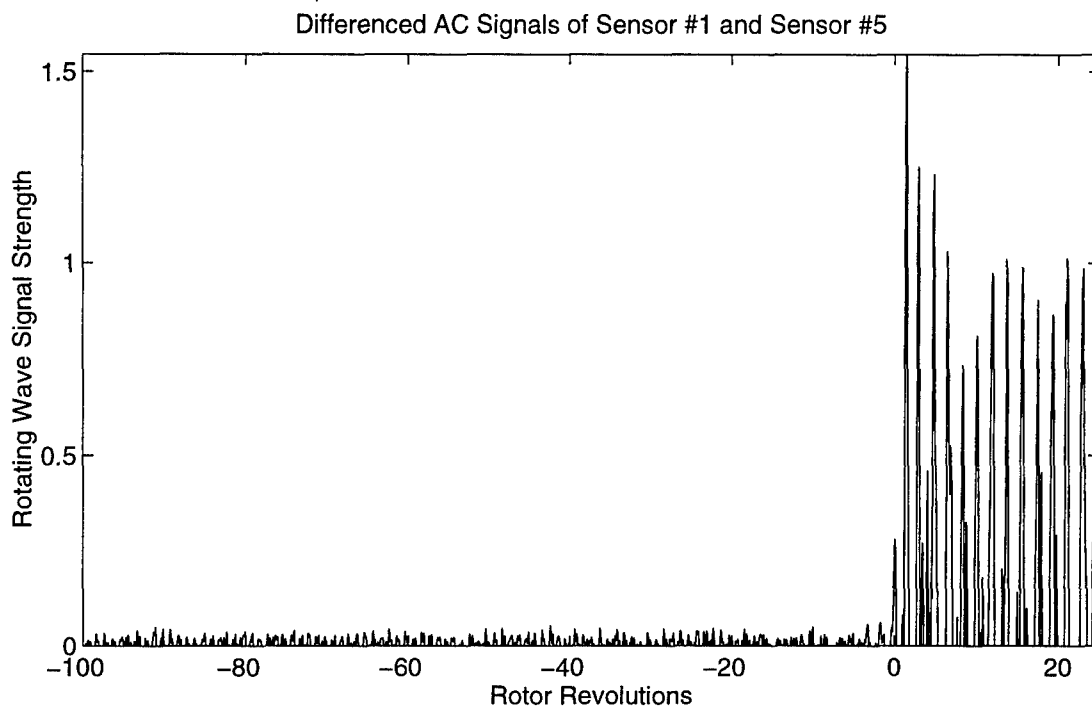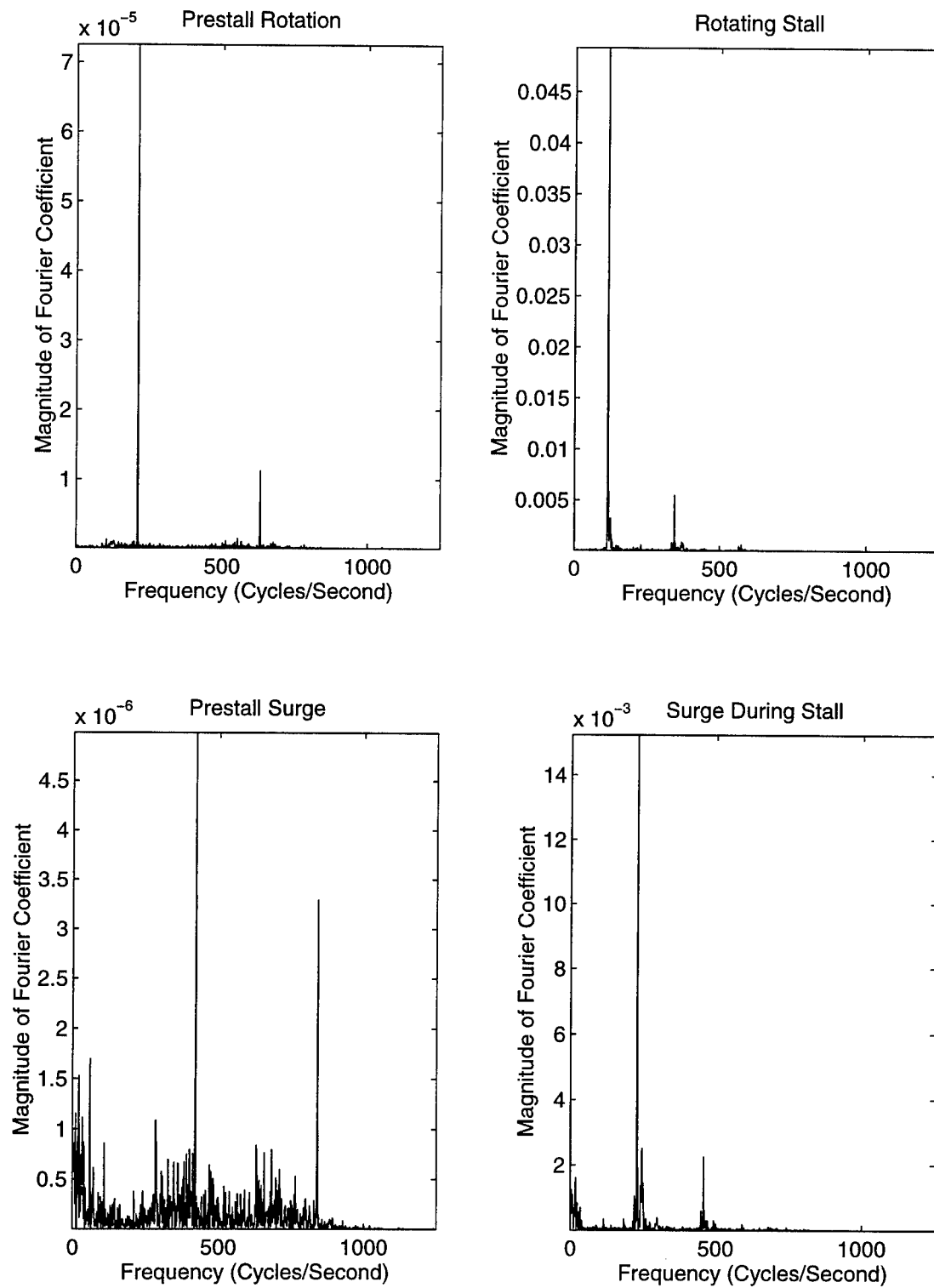
274

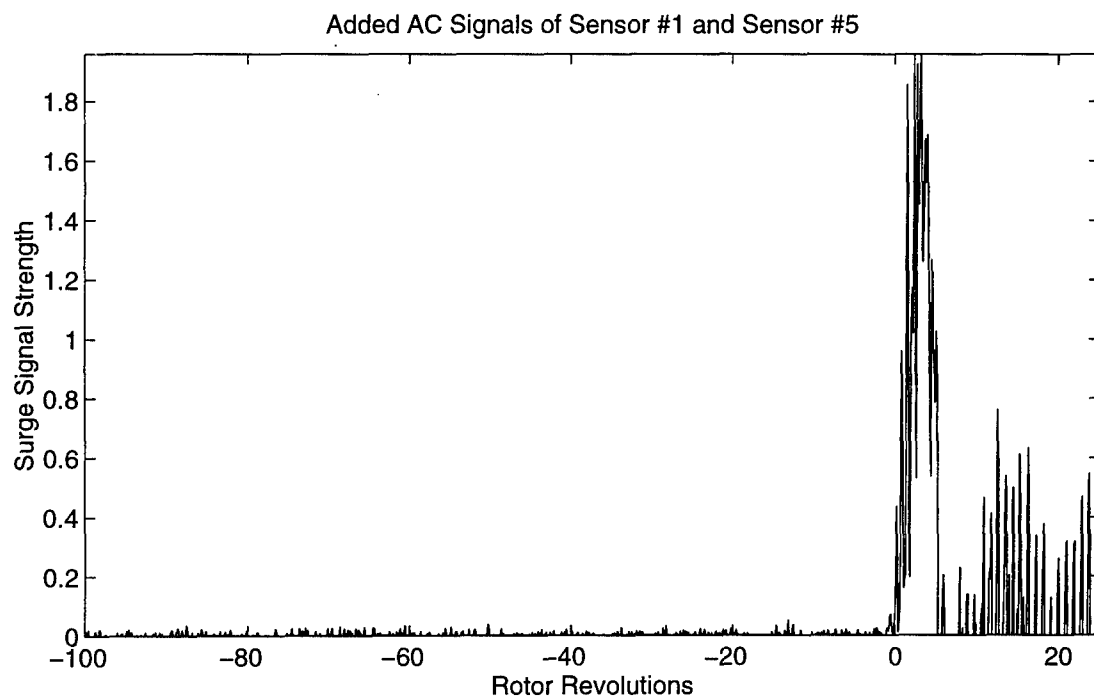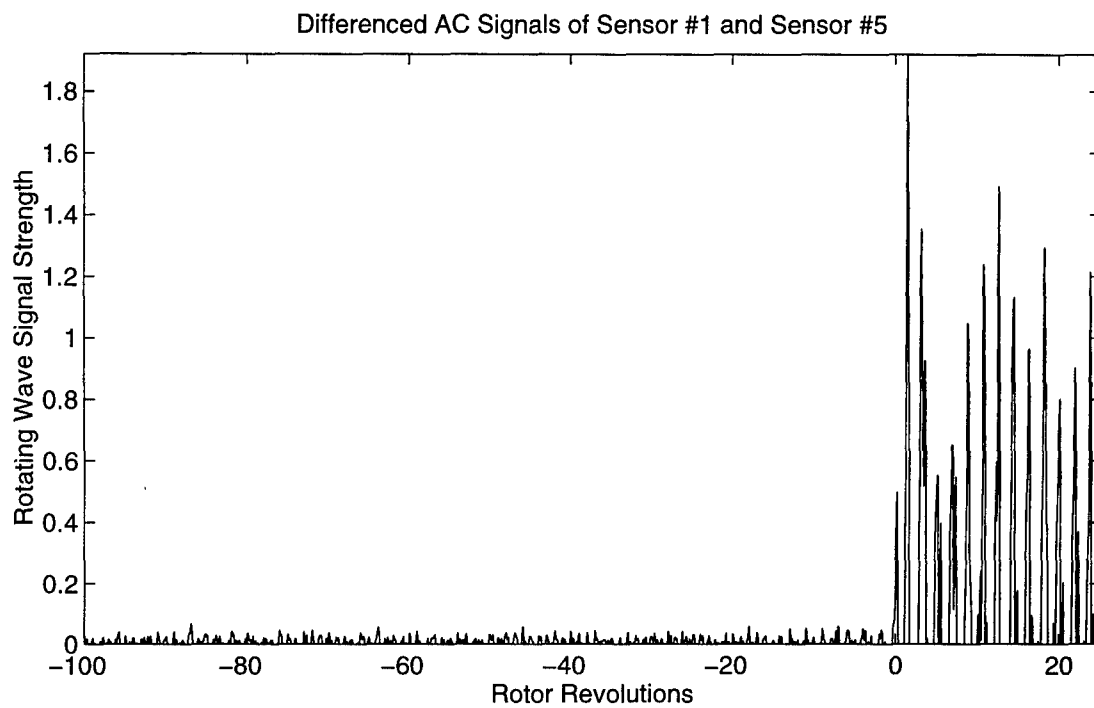Figure 234. Frequency of Rotating Stall and Surge (Case I, 95% Rotor Speed, 209.918 revs/sec)

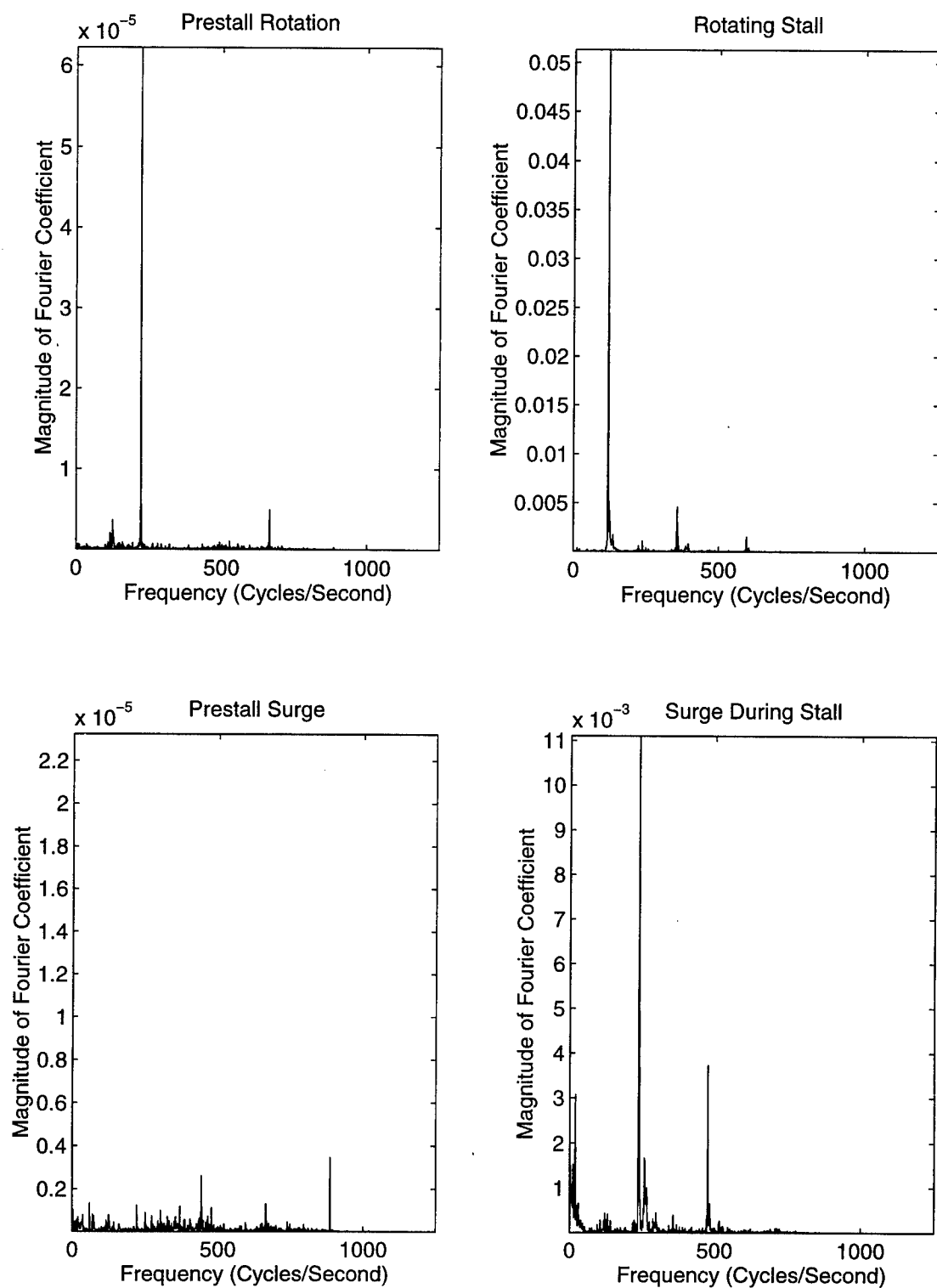Figure 235. Onset of Rotating Stall and Surge (Case I, 100% Rotor Speed, 221.280 revs/sec)

276

Figure 236. Frequency of Rotating Stall and Surge (Case I, 100% Rotor Speed, 221.280 revs/sec)

Vita

Don Thompson ████████████████████████████, his family moved to Amarillo, Texas where he spent the remainder of his youth. He graduated from Amarillo High School in 1977 and attended Texas Tech University in Lubbock, Texas. Upon graduating in 1981 with a bachelor's degree in Mechanical Engineering, he entered the active duty Air Force and attended Officer Training School at Lackland AFB, Texas.

He was assigned to the 351st Strategic Missile Wing at Whiteman AFB, Missouri where he served as the Wing/Base Mechanical Engineer and Officer-in-Charge of the Technical Engineering Branch. He earned his masters degree in Mechanical and Aerospace Engineering from the University of Missouri—Columbia in December of 1984. He attended Undergraduate Pilot Training at Reese AFB, Texas from 1984 to 1985. He was assigned as a B-52H copilot to the 325th Bomb Squadron at Fairchild AFB, Washington following initial training at Castle AFB, California. He progresssed through duties as Aircraft Commander, Instructor Pilot, Training Flight Instructor, Standardization/Evaluation Pilot, Flight Commander, and Operations Officer. He also served as interim Squadron Commander of the 325th Bomb Squadron. He was selected to pursue doctoral studies in Aeronautical and Astronautical Engineering at the Air Force Institute of Technology from 1994 to 1997.

Major Thompson is a senior pilot with more than 2800 hours of experience in the B-52, T-37, and T-38 aircraft. He also maintains FAA civilian ratings as an Airline Transport Pilot and Certificated Flight Instructor.

He is married to Rachelle Thompson, born and raised in Polson, Montana.

████████████████████████████

REPORT DOCUMENTATION PAGE

1. AGENCY USE ONLY (Leave blank)	2. REPORT DATE 25 June 1997	3. REPORT TYPE AND DATES COVERED Dissertation, April 1996 - July 1997

4. TITLE AND SUBTITLE

Stepped Tip Gap Effects on a Transonic Axial-Flow Compressor Rotor

5. FUNDING NUMBERS

6. AUTHOR(S)

Donald W. Thompson, Major, USAF

7. PERFORMING ORGANIZATION NAME(S) AND ADDRESS(ES)

Air Force Institute of Technology (AFIT/ENY)
2950 P Street, Bldg 640
Wright-Patterson AFB OH 45433-7765

8. PERFORMING ORGANIZATION REPORT NUMBER

AFIT/DS/ENY/97-5

9. SPONSORING/MONITORING AGENCY NAME(S) AND ADDRESS(ES)

Wright Laboratories Propulsion and Power Directorate, Compressor Research Facility
WL/POTX, Bldg 18D
1950 Fifth Street
Wright-Patterson AFB, OH 45433-7251

10. SPONSORING/MONITORING AGENCY REPORT NUMBER

11. SUPPLEMENTARY NOTES

12a. DISTRIBUTION/AVAILABILITY STATEMENT

APPROVED FOR PUBLIC RELEASE; DISTRIBUTION UNLIMITED

12b. DISTRIBUTION CODE

13. ABSTRACT (Maximum 200 words)

The effects of stepped tip gaps and clearance levels on the performance, flowfield, and stall characteristics of a transonic axial-flow compressor rotor were experimentally and numerically determined. A theory and mechanism for relocation of blockage in the rotor tip region was developed. A two-stage compressor with no inlet guide vanes was tested in the Wright Laboratories Compressor Research Facility located at Wright-Patterson Air Force Base, Ohio. The first-stage rotor was unswept and was tested for an optimum tip clearance with variations in stepped gaps machined into the casing near the aft tip region of the rotor. Nine casing geometries were investigated consisting of three step profiles at each of three clearance levels. For small and intermediate clearances, stepped tip gaps were found to improve pressure ratio, efficiency, and flow range for most operating conditions. At 100% design rotor speed, stepped tip gaps produced a doubling of mass flow range with as much as a 2.0% increase in mass flow and a 1.5% improvement in efficiency. The flowfield characteristics associated with performance improvements were experimentally and numerically analyzed. Stepped tip gaps were found to have no significant effect on the stall characteristics of the rotor; the stability characteristics attributable to tip geometry were determined by the clearance over the forward portion of the rotor blade. This study provides guidelines for engineers to improve compressor performance for an existing design by applying an optimum casing profile.

14. SUBJECT TERMS

Axial-Flow Compressor, Transonic Rotor, Tip Clearance, Stepped Tip Gap, Blockage, Aerodynamic Seal, Vortex Entrainment, Performance, Shock-Vortex Interaction, Stall

15. NUMBER OF PAGES

319

16. PRICE CODE

17. SECURITY CLASSIFICATION OF REPORT	18. SECURITY CLASSIFICATION OF THIS PAGE	19. SECURITY CLASSIFICATION OF ABSTRACT	20. LIMITATION OF ABSTRACT
UNCLASSIFIED	UNCLASSIFIED	UNCLASSIFIED	UL

GENERAL INSTRUCTIONS FOR COMPLETING SF 298

The Report Documentation Page (RDP) is used in announcing and cataloging reports. It is important that this information be consistent with the rest of the report, particularly the cover and title page. Instructions for filling in each block of the form follow. It is important to *stay within the lines* to meet *optical scanning requirements*.

Block 1. Agency Use Only (Leave blank).

Block 2. Report Date. Full publication date including day, month, and year, if available (e.g. 1 Jan 88). Must cite at least the year.

Block 3. Type of Report and Dates Covered. State whether report is interim, final, etc. If applicable, enter inclusive report dates (e.g. 10 Jun 87 - 30 Jun 88).

Block 4. Title and Subtitle. A title is taken from the part of the report that provides the most meaningful and complete information. When a report is prepared in more than one volume, repeat the primary title, add volume number, and include subtitle for the specific volume. On classified documents enter the title classification in parentheses.

Block 5. Funding Numbers. To include contract and grant numbers; may include program element number(s), project number(s), task number(s), and work unit number(s). Use the following labels:

C	-	Contract	PR	- Project
G	-	Grant	TA	- Task
PE	-	Program Element	WU	- Work Unit Accession No.

Block 6. Author(s). Name(s) of person(s) responsible for writing the report, performing the research, or credited with the content of the report. If editor or compiler, this should follow the name(s).

Block 7. Performing Organization Name(s) and Address(es). Self-explanatory.

Block 8. Performing Organization Report Number. Enter the unique alphanumeric report number(s) assigned by the organization performing the report.

Block 9. Sponsoring/Monitoring Agency Name(s) and Address(es). Self-explanatory.

Block 10. Sponsoring/Monitoring Agency Report Number. (If known)

Block 11. Supplementary Notes. Enter information not included elsewhere such as: Prepared in cooperation with...; Trans. of...; To be published in.... When a report is revised, include a statement whether the new report supersedes or supplements the older report.

Block 12a. Distribution/Availability Statement. Denotes public availability or limitations. Cite any availability to the public. Enter additional limitations or special markings in all capitals (e.g. NOFORN, REL, ITAR).

DOD - See DoDD 5230.24, "Distribution Statements on Technical Documents."
DOE - See authorities.
NASA - See Handbook NHB 2200.2.
NTIS - Leave blank.

Block 12b. Distribution Code.

DOD - Leave blank.
DOE - Enter DOE distribution categories from the Standard Distribution for Unclassified Scientific and Technical Reports.
NASA - Leave blank.
NTIS - Leave blank.

Block 13. Abstract. Include a brief *(Maximum 200 words)* factual summary of the most significant information contained in the report.

Block 14. Subject Terms. Keywords or phrases identifying major subjects in the report.

Block 15. Number of Pages. Enter the total number of pages.

Block 16. Price Code. Enter appropriate price code *(NTIS only)*.

Blocks 17. - 19. Security Classifications. Self-explanatory. Enter U.S. Security Classification in accordance with U.S. Security Regulations (i.e., UNCLASSIFIED). If form contains classified information, stamp classification on the top and bottom of the page.

Block 20. Limitation of Abstract. This block must be completed to assign a limitation to the abstract. Enter either UL (unlimited) or SAR (same as report). An entry in this block is necessary if the abstract is to be limited. If blank, the abstract is assumed to be unlimited.